Effect of Unbalanced Moment on Punching Shear Strength of Slab-Column Joints

by

Mikhail Laguta

A thesis
presented to the University of Waterloo
in fulfillment of the
thesis requirement for the degree of
Master of Applied Science
in
Civil Engineering

Waterloo, Ontario, Canada, 2020

Author’s declaration

I hereby declare that I am the sole author of this thesis. This is a true copy of the thesis, including any required final revisions, as accepted by my examiners.

I understand that my thesis may be made electronically available to the public.

Abstract

The design of reinforced concrete flat plate slab-column connections subjected to unbalanced moments varies greatly between national design codes. Specific to Canada and the United States (U.S.), assumptions relating to the distribution of unbalanced moments between shear and flexure stresses were introduced in the 1970s based on limited research. Research on the topic of slab-column connections subjected to eccentric loading has deviated away from the linear shear distribution assumptions of Canada, the U.S., and Europe in favour of beam, truss, membrane, and other analogies. As such, it is of value to study the performance of varying design code approaches as well as the accuracy of the stress distribution assumptions within Canadian and American design codes.

In this thesis, numerical modelling of slab-column connections subjected to eccentric loading is performed by the author using the software Abaqus (Dassault Systèmes). Finite element models were created to simulate the behaviour of laboratory-tested slab-column specimens. Preliminary finite element model parameters were based on research by Genikomsou (2015) and geometry, material, and boundary condition assumptions specific to the specimens. Calibration of the finite element models was necessary to ensure that the analyses accurately reproduced behaviour observed during testing. This was done by changing one parameter at a time and selecting the parameter value that resulted in the most accurate results. Accuracy was evaluated based on the analyses' ability to reproduce moment-rotation data, load-displacement data, and crack patterns of the experiments. To verify the calibrated parameters, finite element analyses of two edge connections of varying eccentricities and one interior connection subjected to concentric loading were conducted.

The calibrated finite element models were used to perform a parametric study on the effects of varying eccentricities on the punching shear strength of three slab-column connections with reinforcement ratios of 0.5-percent, 1.0-percent, and 1.5-percent. The study showed that the normalized moment-shear data of the three specimens is nonlinear. In contrast, all design codes assume a linear moment-shear interaction. With regard to design code performance, none of the design codes' punching shear provisions accurately predicted the capacities of the specimen with a reinforcement ratio of 0.5-percent. This is because this specimen's flexural reinforcement yielded before punching shear failure could occur. Since ACI 318-19 and CSA A23.3-19 do not

consider the contribution of flexural reinforcement to a connection's punching shear strength, each of these design codes was accurate for only one reinforcement ratio. Eurocode 2 (2004) accurately predicted the punching shear strength of specimens subjected to concentric loads. Furthermore, it underestimated the punching shear strength for eccentricities approaching infinity (i.e. only unbalanced moments). This was likely because the specimens failed in flexure, rather than punching, when subjected to large unbalanced moments. The level I, II, and IV approximations of *fib* Model Code 2010 underestimated the punching shear capacities for all eccentricities. Of the three levels of approximation, the level IV predictions best reproduced the shape of the moment-shear interaction obtained from finite element analyses.

The distribution of unbalanced moments between shear and flexural stresses at a critical section $d/2$ from the column face (as defined by ACI 318-19 and CSA A23.3-19) was found to vary depending on the magnitude of vertical loads applied and the reinforcement ratio. Both ACI 318-19 and CSA A23.3-19 describe this distribution using a coefficient γ_v. This coefficient is assumed to be equal to 0.40 for square, interior connections. From the results of specimen analyses, the coefficient γ_v was approximately equal to 0.25 for specimens subjected to low eccentricities and approximately 0.40 for specimens subjected to large eccentricities. An equation was presented to predict the coefficient γ_v specific to the specimens analysed. Further development of the equation is required to allow it to be applicable to other specimens.

Acknowledgements

I would like to thank my supervisor, Dr. Maria Anna Polak, for her guidance and supervision through the completion of this thesis. I would also like to thank Dr. Cory Zurell and Dr. Trevor Hrynyk for reviewing this thesis and providing invaluable feedback.

I would like to extend my gratitude to my colleagues and friends from the Polak research group: Liangxue Cai, André Kühl, Piotr Wiciak, Colin Van Niejenhuis, and Philip Lochan. I would also like to express my appreciation to Graeme Milligan for always being available to lend an ear, Ryan Barrage for his invaluable help with Abaqus scripting, and Nader Sleiman for always bringing laughter into the office.

I wish to thank my friends for their love and support: Asal, Arian, and Baba Montakhab for being like a second family to me; and Daniel Wai for always planning fun excursions away from research, as well as his insights into plasticity and Abaqus.

Lastly, I wish to acknowledge the support of my family, especially during the preparation of this thesis.

Table of contents

Author's declaration ii
Abstract iii
Acknowledgements v
LIST OF FIGURES xi
LIST OF TABLES xxiv
Chapter 1: Introduction 1
1.1 Problem statement 1
1.2 Thesis overview 3
Chapter 2: Literature review 5
2.1 Review of laboratory tests and analysis methods 5
2.1.1 Working stress analysis method by Di Stasio and Van Buren 5
2.1.2 Ultimate strength analysis method by Johannes Moe 7
2.1.3 Ultimate strength analysis method by ASCE-ACI Committee 326 9
2.1.4 Implementation of unbalanced moment analysis in ACI 318-65 10
2.1.5 Moment transfer coefficient γf by Hanson and Hanson 11
2.1.6 Column rectangularity on connection strength by Hawkins, Fallsen, and Hinojosa 12
2.1.7 Tests of exterior connections subjected to unbalanced moments by Zaghlool ... 13
2.1.8 Beam analogy by Hawkins and Corley 14
2.1.9 Influence of column shape on slab-column connection strength by Vanderbilt . 15
2.1.10 Connections subjected to unbalanced moments tested by Stamenkovic 16
2.1.11 Study of slab-column behaviour by Regan 18
2.1.12 Size effect on unbalanced moment specimens by Neth, de Paiva, and Long 21
2.1.13 Truss analogy analysis method by Alexander and Simmonds 23
2.1.14 Analysis of γf for edge slab-column connections by Moehle 25
2.1.15 Interior connections under unbalanced moments by Hawkins, Bao, and Yamazaki 26
2.1.16 Critical Shear Crack Theory 27
2.1.17 Minimum reinforcement and size effect coefficient by Hawkins and Ospina 30
2.2 Review of punching shear provisions in national design codes 31

2.2.1 ACI 318-19 31
2.2.2 CSA A23.3-19 37
2.2.3 Eurocode 2 (2004) 39
2.2.4 Model Code 2010 42
2.2.5 CSCT code-like formulation (2008) 49
Chapter 3: Constitutive modelling of materials using Abaqus 51
3.1 Concrete 51
3.1.1 Uniaxial compressive behaviour 51
3.1.2 Uniaxial tensile behaviour 52
3.1.3 Concrete Damaged Plasticity 53
3.2 Steel reinforcement 55
Chapter 4: Preliminary parameters of finite element models 56
4.1 Tests of interior connections by Ghali, Elmasri, and Dilger (1976) 56
4.2 Overview of parameters 57
4.3 Boundary conditions 58
4.4 Concrete properties 59
4.5 Reinforcement properties 61
Chapter 5: Calibration of finite element model parameters 63
5.1 Modelling of column concrete confinement 65
5.1.1 Results of specimen SM 0.5 analyses 66
5.1.2 Results of specimen SM 1.0 analyses 70
5.1.3 Results of specimen SM 1.5 analyses 73
5.1.4 Conclusions and recommendations 78
5.2 Study of corner boundary conditions 78
5.2.1 Results of specimen SM 0.5 analyses 80
5.2.2 Results of specimen SM 1.0 analyses 88
5.2.3 Results of specimen SM 1.5 analyses 94
5.2.4 Conclusions and recommendations 100
5.3 Preventing support failure 101
5.3.1 Option A: restraining top of failing slab edge 101
5.3.2 Option B: using elastic material at failing slab edge 109

5.3.3 Option C: changing support boundary conditions between loads 117
5.3.4 Comparison of options 126
5.3.5 Conclusions and recommendations 129
5.4 Study of fracture energy models 130
5.4.1 Results of specimen SM 0.5 analyses 131
5.4.2 Results of specimen SM 1.0 analyses 133
5.4.3 Results of specimen SM 1.5 analyses 135
5.4.4 Conclusions and recommendations 137
5.5 Equivalent versus as-tested reinforcement layout 138
5.5.1 Results of specimen SM 0.5 analyses 138
5.5.2 Results of specimen SM 1.0 analyses 140
5.5.3 Results of specimen SM 1.5 analyses 142
5.5.4 Conclusions and recommendations 144
5.6 Comparison of concrete mesh sizes 145
5.6.1 Results of specimen SM 0.5 analyses 145
5.6.2 Results of specimen SM 1.0 analyses 148
5.6.3 Results of specimen SM 1.5 analyses 152
5.6.4 Conclusions and recommendations 154
5.7 Comparison of reinforcement mesh sizes and element types 156
5.7.1 Results of specimen SM 0.5 analyses 156
5.7.2 Results of specimen SM 1.0 analyses 161
5.7.3 Results of specimen SM 1.5 analyses 164
5.7.4 Conclusions and recommendations 168
5.8 Comparison of concrete dilation angles 168
5.8.1 Results of specimen SM 0.5 analyses 169
5.8.2 Results of specimen SM 1.0 analyses 172
5.8.3 Results of specimen SM 1.5 analyses 176
5.8.4 Comparison of specimen results 179
5.8.5 Conclusions and recommendations 180
5.9 Study of effects of self-weight 181
5.9.1 Results of specimen SM 0.5 analyses 182

5.9.2 Results of specimen SM 1.0 analyses....184
5.9.3 Results of specimen SM 1.5 analyses....186
5.9.4 Conclusions and recommendations....188
5.10 Study of concrete modulus of elasticity....189
5.10.1 Calculation of tangent modulus of elasticity....189
5.10.2 Results of specimen SM 0.5 analyses....193
5.10.3 Results of specimen SM 1.0 analyses....196
5.10.4 Results of specimen SM 1.5 analyses....199
5.10.5 Conclusions and recommendations....201
5.11 Comparison of strain-hardening versus perfectly-plastic reinforcement....203
5.11.1 Strain-hardening stress-strain data....203
5.11.2 Results of specimen SM 0.5 analyses....204
5.11.3 Results of specimen SM 1.0 analyses....207
5.11.4 Results of specimen SM 1.5 analyses....209
5.11.5 Conclusions and recommendations....211
5.12 Additional possible calibration: neoprene supports....212
Chapter 6: Finite element analyses of laboratory-tested specimens....213
6.1 SM specimens by Ghali, Elmasri, and Dilger (1976)....213
6.1.1 Boundary conditions....213
6.1.2 Concrete properties....213
6.1.3 Reinforcement properties....215
6.1.4 Moment versus rotation results....216
6.1.5 Vertical displacement versus rotation results....218
6.1.6 Crack patterns....220
6.2 Specimens XXX and HXXX by El-Salakawy (1998)....222
6.2.1 Boundary conditions....223
6.2.2 Concrete properties....224
6.2.3 Reinforcement properties....226
6.2.4 Moment versus rotation results....227
6.2.5 Vertical load versus displacement results....228
6.2.6 Crack patterns....229

6.3 Specimen SB1 by Adetifa (2003) 232
6.3.1 Boundary conditions 233
6.3.2 Concrete properties 234
6.3.3 Reinforcement properties 236
6.3.4 Vertical load versus displacement results 236
6.3.5 Crack patterns 237
Chapter 7: Parametric study using numerical modelling 239
7.1 Moment versus rotation results 239
7.2 Moment versus vertical load results 243
7.3 Vertical load capacity versus eccentricity 244
7.4 Moment-shear interaction diagram 245
Chapter 8: Proposed method for predicting punching shear failure 248
8.1 Average shear stresses of critical elements versus applied moment 250
8.2 Stress-based method: vertical load contribution to average shear stress 252
8.3 Stress-based method: moment contribution to average shear stress 253
8.4 Stress-based method: ultimate shear stress 257
Chapter 9: Comparisons with current design codes 259
9.1 SM specimens by Ghali, Elmasri, and Dilger (1976) 259
9.1.1 Coefficient γv as proposed versus ACI 318-19 259
9.1.2 Moment versus vertical load results 262
9.2 Specimens XXX and HXXX by El-Salakawy (1998) 266
9.3 Specimen SB1 by Adetifa (2003) 268
Chapter 10: Conclusions and recommendations 269
10.1 Finite element model parameter calibration 269
10.2 Verification of calibrated finite element model parameters 270
10.3 Accuracy of national design codes 270
10.4 Study of shear stresses at critical perimeter of ACI 318-19 272
10.5 Recommendations 273
Letters of copyright 274
References 280

LIST OF FIGURES

Figure 2.1: Maximum vertical load used by Moe (1961) to develop limiting shear equations. Reprinted from Development Department Bulletin D47, Portland Cement Association (April 1961). Reprinted with permission. 9
Figure 2.2: Moment-shear interaction diagram by Zaghlool (1971) 14
Figure 2.3: Column of slab-column connection subjected to combined loading 15
Figure 2.4: Vertical load versus moment envelope for 6-inch square column specimens tested by Hanson and Hanson (1968) (N. Hawkins & Corley, 1971) 15
Figure 2.5: Shear capacity versus eccentricity for interior connections (Regan, 1981) 20
Figure 2.6: Critical sections located: a) $0.5d$ away from column, and b) $0.5d$ away from outermost shear reinforcement as per ACI 318-19 (ACI Committee 318, 2019) 32
Figure 2.7: Critical sections located: a) 2d away from column, and b) 1.5d away from outermost shear reinforcement as per Eurocode 2 (British Standards Institution, 2004) 40
Figure 2.8: Critical sections located: a) $0.5dv$ away from column, and b) $0.5dv$ away from outermost shear reinforcement as per Model Code 2010 (federation internationale du béton (fib), 2013) 43
Figure 3.1: Hognestad parabola for defining concrete compression uniaxial stress-strain data 52
Figure 3.2: Typical concrete tensile uniaxial stress-strain data 52
Figure 4.1: Boundary conditions used for FE analyses of SM specimens 59
Figure 4.2: Concrete mesh used for FE analyses of SM specimens 59
Figure 4.3: Compression stress-strain data used for FE analyses of SM specimens 60
Figure 4.4: Tension stress-strain data used for FE analyses of SM specimens 60
Figure 4.5: Concrete material assignments for FE analyses of SM specimens 61
Figure 4.6: Reinforcement stress-strain data used for FE analyses of SM specimens 62
Figure 5.1: Specimen SM 0.5 a) moment-rotation and b) displacement-rotation data using varying values for column modulus of elasticity 67
Figure 5.2: Specimen SM 0.5 experiment (Ghali et al., 1976) and analyses crack patterns using varying values for modulus of elasticity E. Authorized reprint of experiment photographs from ACI Journal, Volume 73, Issue 10, October 1976. 69
Figure 5.3: Specimen SM 1.0 a) moment-rotation and b) displacement-rotation data using varying values for column modulus of elasticity E 71

Figure 5.4: Specimen SM 1.0 analyses crack patterns using varying values for modulus of elasticity E 73
Figure 5.5: Specimen SM 1.5 a) moment-rotation and b) displacement-rotation data using varying values for column modulus of elasticity E 75
Figure 5.6: Specimen SM 1.5 experiment (Ghali et al., 1976) and analyses crack patterns using varying values for modulus of elasticity E. Authorized reprint of experiment photographs from ACI Journal, Volume 73, Issue 10, October 1976..... 77
Figure 5.7: Boundary conditions used for analyses a) BC1 through BC4 and b) BC1-E through BC4-E 80
Figure 5.8: Specimen SM 0.5 a) moment-rotation and b) displacement-rotation data for analyses BC1 through BC4 81
Figure 5.9: Specimen SM 0.5 analysis BC1 failure mechanism 82
Figure 5.10: Specimen SM 0.5 top face experiment (Ghali et al., 1976) and analyses crack patterns for boundary condition analyses BC1 through BC4. Authorized reprint of experiment photograph from ACI Journal, Volume 73, Issue 10, October 1976..... 83
Figure 5.11: Specimen SM 0.5 bottom face experiment (Ghali et al., 1976) and analyses crack patterns for boundary condition analyses BC1 through BC4. Authorized reprint of experiment photograph from ACI Journal, Volume 73, Issue 10, October 1976..... 84
Figure 5.12: Specimen SM 0.5 a) moment-rotation and b) displacement-rotation data for analyses BC1-E through BC4-E 85
Figure 5.13: Specimen SM 0.5 top face experiment (Ghali et al., 1976) and analyses crack patterns for boundary condition analyses BC1-E through BC4-E. Authorized reprint of experiment photograph from ACI Journal, Volume 73, Issue 10, October 1976..... 86
Figure 5.14: Specimen SM 0.5 bottom face experiment (Ghali et al., 1976) and analyses crack patterns for boundary condition analyses BC1-E through BC4-E. Authorized reprint of experiment photograph from ACI Journal, Volume 73, Issue 10, October 1976..... 87
Figure 5.15: Specimen SM 1.0 a) moment-rotation and b) displacement-rotation data for analyses BC1 through BC4 88
Figure 5.16: Specimen SM 1.0 analyses crack patterns for boundary condition analyses BC1 through BC4 90

Figure 5.17: Specimen SM 1.0 a) moment-rotation and b) displacement-rotation data for analyses BC1-E through BC4-E 92
Figure 5.18: Specimen SM 1.0 analyses crack patterns for boundary condition analyses BC1-E through BC4-E 93
Figure 5.19: Specimen SM 1.5 a) moment-rotation and b) displacement-rotation data for analyses BC1 through BC4 95
Figure 5.20: Specimen SM 1.5 top face experiment (Ghali et al., 1976) and analyses crack patterns for boundary condition analyses BC1 through BC4. Authorized reprint of experiment photograph from ACI Journal, Volume 73, Issue 10, October 1976 96
Figure 5.21: Specimen SM 1.5 bottom face experiment (Ghali et al., 1976) and analyses crack patterns for boundary condition analyses BC1 through BC4. Authorized reprint of experiment photograph from ACI Journal, Volume 73, Issue 10, October 1976 97
Figure 5.22: Specimen SM 1.5 a) moment-rotation and b) displacement-rotation data for analyses BC1-E through BC4-E 98
Figure 5.23: Specimen SM 1.5 top face experiment (Ghali et al., 1976) and analyses crack patterns for boundary condition analyses BC1-E through BC4-E. Authorized reprint of experiment photograph from ACI Journal, Volume 73, Issue 10, October 1976 99
Figure 5.24: Specimen SM 1.5 bottom face experiment (Ghali et al., 1976) and analyses crack patterns for boundary condition analyses BC1-E through BC4-E. Authorized reprint of experiment photograph from ACI Journal, Volume 73, Issue 10, October 1976 100
Figure 5.25: Boundary conditions used for option A study of preventing support failure study 102
Figure 5.26: Specimen SM 0.5 a) moment-rotation and b) displacement-rotation data for top and bottom of slab edges restrained analysis versus bottom of slab edges restrained analysis 103
Figure 5.27: Specimen SM 0.5 experiment (Ghali et al., 1976) and analyses crack patterns for option A and base case analyses. Authorized reprint of experiment photographs from ACI Journal, Volume 73, Issue 10, October 1976. 104
Figure 5.28: Specimen SM 1.0 a) moment-rotation and b) displacement-rotation data for top and bottom of slab edges restrained analysis versus bottom of slab edges restrained analysis 105
Figure 5.29: Specimen SM 1.0 analyses crack patterns for top and bottom of slab edges restrained analysis versus bottom of slab edges restrained analysis 106

Figure 5.30: Specimen SM 1.5 a) moment-rotation and b) displacement-rotation data for top and bottom of slab edges restrained analysis versus bottom of slab edges restrained analysis 107
Figure 5.31: Specimen SM 1.5 experiment (Ghali et al., 1976) and analyses crack patterns for top and bottom of slab edges restrained analysis versus bottom of slab edges restrained analysis. Authorized reprint of experiment photographs from ACI Journal, Volume 73, Issue 10, October 1976. 108
Figure 5.32: Typical a) material properties and b) meshing for option B analyses 110
Figure 5.33: Specimen SM 0.5 a) moment-rotation and b) displacement-rotation data for elastic lifting slab edge analysis versus plastic lifting slab edge restrained analysis 111
Figure 5.34: Specimen SM 0.5 experiment (Ghali et al., 1976) and analyses crack patterns for elastic lifting slab edge analysis versus plastic lifting slab edge restrained analysis. Authorized reprint of experiment photographs from ACI Journal, Volume 73, Issue 10, October 1976. .112
Figure 5.35: Specimen SM 1.0 a) moment-rotation and b) displacement-rotation data for elastic lifting slab edge analysis versus plastic lifting slab edge restrained analysis 113
Figure 5.36: Specimen SM 1.0 analyses crack patterns for elastic lifting slab edge analysis versus plastic lifting slab edge restrained analysis 114
Figure 5.37: Specimen SM 1.5 a) moment-rotation and b) displacement-rotation data for elastic lifting slab edge analysis versus plastic lifting slab edge restrained analysis 115
Figure 5.38: Specimen SM 1.5 experiment (Ghali et al., 1976) and analyses crack patterns for elastic lifting slab edge analysis versus plastic lifting slab edge restrained analysis. Authorized reprint of experiment photographs from ACI Journal, Volume 73, Issue 10, October 1976. .116
Figure 5.39: Typical boundary conditions for option C analyses in the a) apply vertical load and rest steps and b) apply moment step 117
Figure 5.40: Specimen SM 0.5 a) moment-rotation and b) displacement-rotation data for changing support boundary conditions between loads analysis versus static boundary conditions analysis 119
Figure 5.41: Specimen SM 0.5 experiment (Ghali et al., 1976) and analyses crack patterns for changing support boundary conditions between loads analysis versus static boundary conditions analysis. Authorized reprint of experiment photographs from ACI Journal, Volume 73, Issue 10, October 1976. 120

Figure 5.42: Specimen SM 1.0 a) moment-rotation and b) displacement-rotation data for changing support boundary conditions between loads analysis versus static boundary conditions analysis 121
Figure 5.43: Specimen SM 1.0 analyses crack patterns for changing support boundary conditions between loads analysis versus static boundary conditions analysis..... 122
Figure 5.44: Specimen SM 1.5 a) moment-rotation and b) displacement-rotation data for changing support boundary conditions between loads analysis versus static boundary conditions analysis 123
Figure 5.45: Specimen SM 1.5 experiment (Ghali et al., 1976) and analyses crack patterns for changing support boundary conditions between loads analysis versus static boundary conditions analysis. Authorized reprint of experiment photographs from ACI Journal, Volume 73, Issue 10, October 1976. 125
Figure 5.46: Specimen SM 0.5 a) moment-rotation and b) displacement-rotation data for the three options to prevent support failure and base case 127
Figure 5.47: Specimen SM 0.5 top face experiment (Ghali et al., 1976) and analyses crack patterns for the support failure prevention options and base case. Authorized reprint of experiment photograph from ACI Journal, Volume 73, Issue 10, October 1976..... 128
Figure 5.48: Specimen SM 0.5 bottom face experiment (Ghali et al., 1976) and analyses crack patterns for the support failure prevention options and base case. Authorized reprint of experiment photograph from ACI Journal, Volume 73, Issue 10, October 1976..... 129
Figure 5.49: Specimen SM 0.5 a) moment-rotation and b) displacement-rotation data using MC 1990 versus MC 2010 fracture energy models 132
Figure 5.50: Specimen SM 0.5 experiment (Ghali et al., 1976) and analyses crack patterns using MC 1990 versus MC 2010 fracture energy models. Authorized reprint of experiment photographs from ACI Journal, Volume 73, Issue 10, October 1976. 133
Figure 5.51: Specimen SM 1.0 a) moment-rotation and b) displacement-rotation data using MC 1990 versus MC 2010 fracture energy models 134
Figure 5.52: Specimen SM 1.0 analyses crack patterns using MC 1990 versus MC 2010 fracture energy models 135
Figure 5.53: Specimen SM 1.5 a) moment-rotation and b) displacement-rotation data using MC 1990 versus MC 2010 fracture energy models 136

Figure 5.54: Specimen SM 1.5 experiment (Ghali et al., 1976) and analyses crack patterns using MC 1990 versus MC 2010 fracture energy models. Authorized reprint of experiment photographs from ACI Journal, Volume 73, Issue 10, October 1976. 137
Figure 5.55: Specimen SM 0.5 a) moment-rotation and b) displacement-rotation data using equivalent versus as-tested reinforcement layouts 139
Figure 5.56: Specimen SM 0.5 experiment (Ghali et al., 1976) and analyses crack patterns using equivalent versus as-tested reinforcement layouts. Authorized reprint of experiment photographs from ACI Journal, Volume 73, Issue 10, October 1976. 140
Figure 5.57: Specimen SM 1.0 a) moment-rotation and b) displacement-rotation data using equivalent versus as-tested reinforcement layouts 141
Figure 5.58: Specimen SM 1.0 analyses crack patterns using equivalent versus as-tested reinforcement layouts 142
Figure 5.59: Specimen SM 1.5 a) moment-rotation and b) displacement-rotation data using equivalent versus as-tested reinforcement layouts 143
Figure 5.60: Specimen SM 1.5 experiment (Ghali et al., 1976) and analyses crack patterns using equivalent versus as-tested reinforcement layouts. Authorized reprint of experiment photographs from ACI Journal, Volume 73, Issue 10, October 1976. 144
Figure 5.61: Specimen SM 0.5 a) moment-rotation and b) displacement-rotation data using varying concrete mesh sizes 146
Figure 5.62: Specimen SM 0.5 top face experiment (Ghali et al., 1976) and analyses crack patterns using varying concrete mesh sizes. Authorized reprint of experiment photograph from ACI Journal, Volume 73, Issue 10, October 1976..... 147
Figure 5.63: Specimen SM 0.5 bottom face experiment (Ghali et al., 1976) and analyses crack patterns using varying concrete mesh sizes. Authorized reprint of experiment photograph from ACI Journal, Volume 73, Issue 10, October 1976..... 148
Figure 5.64: Specimen SM 1.0 a) moment-rotation and b) displacement-rotation data using varying concrete mesh sizes 149
Figure 5.65: Specimen SM 1.0 analyses crack patterns using varying concrete mesh sizes... 151
Figure 5.66: Specimen SM 1.5 a) moment-rotation and b) displacement-rotation data using varying concrete mesh sizes 152

Figure 5.67: Specimen SM 1.5 top face experiment (Ghali et al., 1976) and analyses crack patterns using varying concrete mesh sizes. Authorized reprint of experiment photograph from ACI Journal, Volume 73, Issue 10, October 1976.....153
Figure 5.68: Specimen SM 1.5 bottom face experiment (Ghali et al., 1976) and analyses crack patterns using varying concrete mesh sizes. Authorized reprint of experiment photograph from ACI Journal, Volume 73, Issue 10, October 1976.....154
Figure 5.69: Specimen SM 0.5 a) moment-rotation and b) displacement-rotation data using varying reinforcement mesh types and sizes.....157
Figure 5.70: Specimen SM 0.5 top face experiment (Ghali et al., 1976) and analyses crack patterns using varying reinforcement mesh types and sizes. Authorized reprint of experiment photograph from ACI Journal, Volume 73, Issue 10, October 1976.....159
Figure 5.71: Specimen SM 0.5 bottom face experiment (Ghali et al., 1976) and analyses crack patterns using varying reinforcement mesh types and sizes. Authorized reprint of experiment photograph from ACI Journal, Volume 73, Issue 10, October 1976.....160
Figure 5.72: Specimen SM 1.0 a) moment-rotation and b) displacement-rotation data using varying reinforcement mesh types and sizes.....161
Figure 5.73: Specimen SM 1.0 top face analyses crack patterns using varying reinforcement mesh types and sizes.....163
Figure 5.74: Specimen SM 1.0 bottom face analyses crack patterns using varying reinforcement mesh types and sizes.....164
Figure 5.75: Specimen SM 1.5 a) moment-rotation and b) displacement-rotation data using varying reinforcement mesh types and sizes.....165
Figure 5.76: Specimen SM 1.5 top face experiment (Ghali et al., 1976) and analyses crack patterns using varying reinforcement mesh types and sizes. Authorized reprint of experiment photograph from ACI Journal, Volume 73, Issue 10, October 1976.....166
Figure 5.77: Specimen SM 1.5 bottom face experiment (Ghali et al., 1976) and analyses crack patterns using varying reinforcement mesh types and sizes. Authorized reprint of experiment photograph from ACI Journal, Volume 73, Issue 10, October 1976.....167
Figure 5.78: Specimen SM 0.5 a) moment-rotation and b) displacement-rotation data using varying concrete dilation angles.....169

Figure 5.79: Specimen SM 0.5 a) moment versus dilation angle and b) displacement versus dilation angle data using varying concrete dilation angles.....170
Figure 5.80: Specimen SM 0.5 top face experiment (Ghali et al., 1976) and analyses crack patterns using varying concrete dilation angles. Authorized reprint of experiment photograph from ACI Journal, Volume 73, Issue 10, October 1976.....171
Figure 5.81: Specimen SM 0.5 bottom face experiment (Ghali et al., 1976) and analyses crack patterns using varying concrete dilation angles. Authorized reprint of experiment photograph from ACI Journal, Volume 73, Issue 10, October 1976.....172
Figure 5.82: Specimen SM 1.0 a) moment-rotation and b) displacement-rotation data using varying concrete dilation angles.....173
Figure 5.83: Specimen SM 1.0 a) moment versus dilation angle and b) displacement versus dilation angle data using varying concrete dilation angles.....174
Figure 5.84: Specimen SM 1.0 analyses crack patterns using varying concrete dilation angles 175
Figure 5.85: Specimen SM 1.5 a) moment-rotation and b) displacement-rotation data using varying concrete dilation angles.....176
Figure 5.86: Specimen SM 1.5 a) moment versus dilation angle and b) displacement versus dilation angle data using varying concrete dilation angles.....177
Figure 5.87: Specimen SM 1.5 top face experiment (Ghali et al., 1976) and analyses crack patterns using varying concrete dilation angles. Authorized reprint of experiment photograph from ACI Journal, Volume 73, Issue 10, October 1976.....178
Figure 5.88: Specimen SM 1.5 bottom face experiment (Ghali et al., 1976) and analyses crack patterns using varying concrete dilation angles. Authorized reprint of experiment photograph from ACI Journal, Volume 73, Issue 10, October 1976.....179
Figure 5.89: Analysis ultimate moments minus experiment ultimate moments versus dilation angles for specimens a) SM 0.5, SM 1.0, and SM 1.5; and b) SM 0.5 and SM 1.0.....180
Figure 5.90: Test orientation of SM specimens including vertical force *V*, force couple *P*, and gravity force *G*.....182
Figure 5.91: Specimen SM 0.5 a) moment-rotation and b) displacement-rotation data when including versus excluding self-weight.....183

Figure 5.92: Specimen SM 0.5 experiment (Ghali et al., 1976) and analyses crack patterns when including versus excluding self-weight. Authorized reprint of experiment photographs from ACI Journal, Volume 73, Issue 10, October 1976.....184
Figure 5.93: Specimen SM 1.0 a) moment-rotation and b) displacement-rotation data when including versus excluding self-weight.....185
Figure 5.94: Specimen SM 1.0 analyses crack patterns when including versus excluding self-weight.....186
Figure 5.95: Specimen SM 1.5 a) moment-rotation and b) displacement-rotation data when including versus excluding self-weight.....187
Figure 5.96: Specimen SM 1.5 experiment (Ghali et al., 1976) and analyses crack patterns when including versus excluding self-weight. Authorized reprint of experiment photographs from ACI Journal, Volume 73, Issue 10, October 1976.....188
Figure 5.97: Typical stress-strain curve (El-Salakawy, 1998) and Hognestad parabolas with Et equal to $5500fc'$ for specimens XXX and HXXX.....190
Figure 5.98: Strain at peak stress versus compressive strength for tested and Hognestad values 192
Figure 5.99: Typical stress-strain curve (El-Salakawy, 1998) and Hognestad parabolas with Et equal to $3150fc'$ for specimens XXX and HXXX.....193
Figure 5.100: Specimen SM 0.5 a) moment-rotation and b) displacement-rotation data using the Hognestad parabola with Et equal to $3150fc'$ and $5500fc'$.....194
Figure 5.101: Specimen SM 0.5 experiment (Ghali et al., 1976) and analyses crack patterns using the Hognestad parabola with Et equal to $3150fc'$ and $5500fc'$. Authorized reprint of experiment photographs from ACI Journal, Volume 73, Issue 10, October 1976. 196
Figure 5.102: Specimen SM 1.0 a) moment-rotation and b) displacement-rotation data using the Hognestad parabola with Et equal to $3150fc'$ and $5500fc'$.....198
Figure 5.103: Specimen SM 1.0 analyses crack patterns using the Hognestad parabola with Et equal to $3150fc'$ and $5500fc'$.....199
Figure 5.104: Specimen SM 1.5 a) moment-rotation and b) displacement-rotation data using the Hognestad parabola with Et equal to $3150fc'$ and $5500fc'$.....200

Figure 5.105: Specimen SM 1.5 experiment (Ghali et al., 1976) and analyses crack patterns using the Hognestad parabola with Et equal to $3150fc'$ and $5500fc'$. Authorized reprint of experiment photographs from ACI Journal, Volume 73, Issue 10, October 1976. 201
Figure 5.106: True and engineering stress-strain data of steel reinforcement used for SM specimens (Flathau, 1971) 204
Figure 5.107: Specimen SM 0.5 a) moment-rotation and b) displacement-rotation data using strain-hardening versus perfectly-plastic reinforcement 206
Figure 5.108: Specimen SM 0.5 experiment (Ghali et al., 1976) and analyses crack patterns using strain-hardening versus perfectly-plastic reinforcement. Authorized reprint of experiment photographs from ACI Journal, Volume 73, Issue 10, October 1976. 207
Figure 5.109: Specimen SM 1.0 a) moment-rotation and b) displacement-rotation data using strain-hardening versus perfectly-plastic reinforcement 208
Figure 5.110: Specimen SM 1.0 analyses crack patterns using strain-hardening versus perfectly-plastic reinforcement 209
Figure 5.111: Specimen SM 1.5 a) moment-rotation and b) displacement-rotation data using strain-hardening versus perfectly-plastic reinforcement 210
Figure 5.112: Specimen SM 1.5 experiment (Ghali et al., 1976) and analyses crack patterns using strain-hardening versus perfectly-plastic reinforcement. Authorized reprint of experiment photographs from ACI Journal, Volume 73, Issue 10, October 1976. 211
Figure 6.1: Concrete mesh used for FE analyses of SM specimens 214
Figure 6.2: Compression stress-strain data used for FE analyses of SM specimens 214
Figure 6.3: Tension stress-strain data used for FE analyses of SM specimens 215
Figure 6.4: Concrete material assignments for FE analyses of SM specimens 215
Figure 6.5: Reinforcement stress-strain data used for FE analyses of SM specimens 216
Figure 6.6: Specimen SM 0.5 moment versus rotation results 217
Figure 6.7: Specimen SM 1.0 moment versus rotation results 217
Figure 6.8: Specimen SM 1.5 moment-rotation results 218
Figure 6.9: Specimen SM 0.5 vertical displacement versus rotation results 219
Figure 6.10: Specimen SM 1.0 vertical displacement versus rotation results 219
Figure 6.11: Specimen SM 1.5 vertical displacement versus rotation results 220

Figure 6.12: Specimen SM 0.5 experiment (Ghali et al., 1976) and analyses crack patterns. Authorized reprint of experiment photographs from ACI Journal, Volume 73, Issue 10, October 1976. 221
Figure 6.13: Specimen SM 1.0 FE analyses crack patterns 221
Figure 6.14: Specimen SM 1.5 experiment (Ghali et al., 1976) and FE analyses crack patterns. Authorized reprint of experiment photographs from ACI Journal, Volume 73, Issue 10, October 1976. 222
Figure 6.15: Boundary conditions used for FE analyses of specimens XXX and HXXX 224
Figure 6.16: Concrete mesh used for FE analyses of specimens XXX and HXXX.....224
Figure 6.17: Compression stress-strain data used for FEA of specimens XXX and HXXX ..225
Figure 6.18: Tension stress-strain data used for FEA of specimens XXX and HXXX 225
Figure 6.19: Concrete material assignments for FE analyses of specimens XXX and HXXX 226
Figure 6.20: 5M reinforcement stress-strain data used for specimens XXX and HXXX FE analyses.....227
Figure 6.21: 10M reinforcement stress-strain data used for specimens XXX and HXXX FE analyses.....227
Figure 6.22: Moment versus rotation results for specimens XXX and HXXX.....228
Figure 6.23: Load versus displacement results for specimens XXX and HXXX 228
Figure 6.24: Top view of specimen XXX experiment (El-Salakawy, 1998) and FEA crack patterns. Photograph reprinted from *Shear behaviour of reinforced concrete flat slab-column edge connections with openings* (p.115), by E. El-Salakawy, 1998. Reprinted with permission. 229
Figure 6.25: Perspective view of specimen XXX experiment (El-Salakawy, 1998) and FEA crack patterns. Photograph reprinted from *Shear behaviour of reinforced concrete flat slab-column edge connections with openings* (p.122), by E. El-Salakawy, 1998. Reprinted with permission.....230
Figure 6.26: Perspective view of specimen HXXX experiment (El-Salakawy, 1998) and FEA crack patterns. Photograph reprinted from *Shear behaviour of reinforced concrete flat slab-column edge connections with openings* (p.143), by E. El-Salakawy, 1998. Reprinted with permission.....231

Figure 6.27: Column view of specimen HXXX experiment (El-Salakawy, 1998) and FEA crack patterns. Photograph reprinted from *Shear behaviour of reinforced concrete flat slab-column edge connections with openings* (p.146), by E. El-Salakawy, 1998. Reprinted with permission. 232
Figure 6.28: Boundary conditions used for FE analysis of specimen SB1 234
Figure 6.29: Concrete mesh used for FE analysis of specimen SB1.....234
Figure 6.30: Compression stress-strain data used for FE analysis of specimen SB1.....235
Figure 6.31: Tension stress-strain data used for FE analysis of specimen SB1 235
Figure 6.32: Concrete material assignments for FE analysis of specimen SB1 235
Figure 6.33: Reinforcement stress-strain data used for specimen SB1 analysis 236
Figure 6.34: Specimen SB1 vertical load versus vertical displacement results 237
Figure 6.35: Tension-side view of specimen SB1 experiment (Adetifa & Polak, 2005) and FEA crack patterns. Authorized reprint of experiment photograph from ACI Structural Journal, Volume 102, Issue 2, March-April 2005. 238
Figure 7.1: Moment-rotation results for specimen SM 0.5 subjected to varying vertical loads 240
Figure 7.2: Typical tension flexural failure among SM 0.5 FE analyses under larger vertical loads (160 kN analysis shown).....240
Figure 7.3: Typical compression flexural yielding among SM FE analyses under low vertical loads (60 kN analysis of SM 1.5 shown).....241
Figure 7.4: Moment-rotation results for specimen SM 1.0 subjected to varying vertical loads 242
Figure 7.5: Moment-rotation results for specimen SM 1.5 subjected to varying vertical loads 242
Figure 7.6: Moment versus vertical load results for SM specimens 244
Figure 7.7: Normalized vertical load capacities versus eccentricities for SM specimens and predictions by Regan (1981) 245
Figure 7.8: Moment-shear interaction diagram for the SM specimens 247
Figure 8.1: Critical perimeter elements used to develop stress-based analysis method.....248
Figure 8.2: Typical shear stress distribution at critical perimeter under only vertical load 249

Figure 8.3: Typical shear stress distribution at critical perimeter under combined vertical load and unbalanced moment 249
Figure 8.4: Critical elements at additive side of critical section 250
Figure 8.5: Average shear stress versus moment for specimen SM 0.5 FE analyses 251
Figure 8.6: Average shear stress versus moment for specimen SM 1.0 FE analyses 252
Figure 8.7: Average shear stress versus moment for specimen SM 1.5 FE analyses 252
Figure 8.8: Average shear stress versus vertical load from FE analyses of SM specimens subjected to only vertical loading 253
Figure 8.9: Changes in stresses given an applied strain for low and high axial forces 254
Figure 8.10: Slope α of average shear stress versus moment results from FEA (180 kN FE analysis of SM 1.5 shown) 255
Figure 8.11: Values of α coefficient versus vertical loads 256
Figure 8.12: Ultimate average shear stresses versus vertical loads for SM FE analyses 258
Figure 9.1: Average shear stress versus moment for SM specimens (V = 140 kN) 260
Figure 9.2: Average shear stress versus moment for SM specimens (V = 160 kN) 260
Figure 9.3: Average shear stress versus moment for SM specimens (V = 180 kN) 261
Figure 9.4: FEA and code-predicted moment capacities for specimen SM 0.5 subjected to various vertical loads 264
Figure 9.5: FEA and code-predicted moment capacities for specimen SM 1.0 subjected to various vertical loads 265
Figure 9.6: FEA and code-predicted moment capacities for specimen SM 1.5 subjected to various vertical loads 266

LIST OF TABLES

Table 2.1: Values of kc, ks, and kt (Stamenkovic, 1969) 18
Table 2.2: Maximum vc for two-way members with shear reinforcement (ACI Committee 318, 2019) 33
Table 2.3: Maximum vu for two-way members with shear reinforcement (ACI Committee 318, 2019) 34
Table 2.4: Maximum modified values of γf for nonprestressed two-way slabs (reproduced with permission, ACI 318-19, Section 8.4.2.2.4) 36
Table 3.1: Base values of fracture energy GFo as per Model Code 1990 53
Table 4.1: Compression reinforcement properties for FE analyses of SM specimens 61
Table 4.2: Tension reinforcement properties for FE analyses of SM specimens 61
Table 5.1: Specimen SM 0.5 analyses results using varying column moduli of elasticity E 67
Table 5.2: Specimen SM 1.0 analyses results using varying column moduli of elasticity E 71
Table 5.3: Specimen SM 1.5 analyses results using varying column moduli of elasticity E 75
Table 5.4: Support lengths analysed for corner boundary condition study 79
Table 5.5: Specimen SM 0.5 results for analyses BC1 through BC4 82
Table 5.6: Specimen SM 0.5 results for analyses BC1-E through BC4-E 86
Table 5.7: Specimen SM 1.0 results for analyses BC1 through BC4 89
Table 5.8: Specimen SM 1.0 results for analyses BC1-E through BC4-E 92
Table 5.9: Specimen SM 1.5 results for analyses BC1 through BC4 95
Table 5.10: Specimen SM 1.5 results for analyses BC1-E through BC4-E 98
Table 5.11: Specimen SM 0.5 analyses results for top of failing slab edge restrained versus top and bottom of failing slab edges restrained analyses 103
Table 5.12: Specimen SM 1.0 analyses results for top of failing slab edge restrained versus top and bottom of failing slab edges restrained analyses 105
Table 5.13: Specimen SM 1.5 analyses results for top and bottom of slab edges restrained analysis versus bottom of slab edges restrained analysis 107
Table 5.14: Specimen SM 0.5 analyses results for elastic lifting slab edge analysis versus plastic lifting slab edge restrained analysis 111
Table 5.15: Specimen SM 1.0 analyses results for elastic lifting slab edge analysis versus plastic lifting slab edge restrained analysis 113

Table 5.16: Specimen SM 1.5 analyses results for elastic lifting slab edge analysis versus plastic lifting slab edge restrained analysis 115
Table 5.17: Specimen SM 0.5 analyses results for changing support boundary conditions between loads analysis versus static boundary conditions analysis 119
Table 5.18: Specimen SM 1.0 analyses results for changing support boundary conditions between loads analysis versus static boundary conditions analysis 122
Table 5.19: Specimen SM 1.5 analyses results for changing support boundary conditions between loads analysis versus static boundary conditions analysis 124
Table 5.20: Base values of fracture energy GFo (Comité Euro-International du Béton, 1993) 130
Table 5.21: Fracture energy Gf values used in analyses of SM specimens 131
Table 5.22: Specimen SM 0.5 analyses results using MC 1990 versus MC 2010 fracture energy models 132
Table 5.23: Specimen SM 1.0 analyses results using MC 1990 versus MC 2010 fracture energy models 134
Table 5.24: Specimen SM 1.5 analyses results using MC 1990 versus MC 2010 fracture energy models 136
Table 5.25: Specimen SM 0.5 analyses results using equivalent versus as-tested reinforcement layouts 139
Table 5.26: Specimen SM 1.0 analyses results using equivalent versus as-tested reinforcement layouts 141
Table 5.27: Specimen SM 1.5 analyses results using equivalent versus as-tested reinforcement layouts 143
Table 5.28: Specimen SM 0.5 results using varying concrete mesh sizes 146
Table 5.29: Specimen SM 1.0 results using varying concrete mesh sizes 149
Table 5.30: Specimen SM 1.5 results using varying concrete mesh sizes 152
Table 5.31: Specimen SM 0.5 results using varying reinforcement mesh types and sizes 158
Table 5.32: Specimen SM 1.0 results using varying reinforcement mesh types and sizes 162
Table 5.33: Specimen SM 1.5 results using varying reinforcement mesh types and sizes 165
Table 5.34: Specimen SM 0.5 results using varying concrete dilation angles 170
Table 5.35: Specimen SM 1.0 results using varying concrete dilation angles 173

Table 5.36: Specimen SM 1.5 results using varying concrete dilation angles 176
Table 5.37: Specimen SM 0.5 analyses results when including versus excluding self-weight 183
Table 5.38: Specimen SM 1.0 analyses results when including versus excluding self-weight 185
Table 5.39: Specimen SM 1.5 analyses results when including versus excluding self-weight 187
Table 5.40: Concrete properties of specimens tested by El-Salakawy (1998) 190
Table 5.41: Required tangent modulus of elasticity coefficients for El-Salakawy's specimens 192
Table 5.42: Specimen SM 0.5 analyses results using the Hognestad parabola with Et equal to $3150fc'$ and $5500fc'$ 195
Table 5.43: Specimen SM 1.0 analyses results using the Hognestad parabola with Et equal to $3150fc'$ and $5500fc'$ 198
Table 5.44: Specimen SM 1.5 analyses results using the Hognestad parabola with Et equal to $3150fc'$ and $5500fc'$ 200
Table 5.45: Specimen SM 0.5 analyses results using strain-hardening versus perfectly-plastic reinforcement.....206
Table 5.46: Specimen SM 1.0 analyses results using strain-hardening versus perfectly-plastic reinforcement.....208
Table 5.47: Specimen SM 1.5 analyses results using strain-hardening versus perfectly-plastic reinforcement.....210
Table 6.1: Compression reinforcement properties for FE analyses of SM specimens.....216
Table 6.2: Tension reinforcement properties for FE analyses of SM specimens 216
Table 6.3: Compression reinforcement properties for FEA of specimens XXX and HXXX .226
Table 6.4: Tension reinforcement properties for FEA of specimens XXX and HXXX 226
Table 6.5: Column reinforcement properties for FEA of specimens XXX and HXXX 226
Table 6.6: Compression reinforcement properties for FE analysis of specimen SB1.....236
Table 6.7: Tension reinforcement properties for FE analysis of specimen SB1 236
Table 6.8: Column reinforcement properties for FE analysis of specimen SB1 236

Table 9.1: Proposed values of γv for SM specimens subjected to only moments or only vertical loads.....261
Table 9.2: Experiment, FEA, and code-predicted capacities for specimen XXX.....267
Table 9.3: Experiment, FEA, and code-predicted capacities for specimen HXXX.....267
Table 9.4: Experiment, FEA, and code-predicted capacities for specimen SB1.....268

Chapter 1: Introduction

1.1 Problem statement

In the 1950s, flat plate floor slab systems without drop panels or column capitals became increasingly common in office and residential buildings of substantial heights (FEMA 274, 1997). Similarly, smaller column sizes were becoming increasingly common within these systems (Di Stasio & Van Buren, 1960). The benefits of using flat plate floor slabs over spandrel beams include decreased floor thickness and more economic formwork. Decreased floor thickness allows for either larger clear distances between story heights or increased number of stories per building. More economic formwork allows for decreased construction time and cost. However, two-way shear failure of flat plate slab-column connections is brittle and little warning is provided prior to failure. Furthermore, shear failure of slab-column connections can lead to progressive collapse of entire structural systems. In the event of interior slab-column punching failure, shear stresses at adjacent connections increase by approximately 25-percent. Furthermore, additional unbalanced moments develop at adjacent connections due to inequalities in residual span lengths (Regan, 1981).

In 1971, ACI 318 introduced provisions describing the distribution of unbalanced moments between shear and flexural stresses based on the dimensions of a critical perimeter. CSA A23.3 introduced the same provisions in 1973 (CSA Group, 1973). The research in support of these design provisions was conducted by Hanson and Hanson (1968). For a square, interior column, Hanson and Hanson stated that 40-percent of unbalanced moments are transferred to shear stresses and the remaining 60-percent are transferred to flexural stresses. Although conflicting distribution percentages were shown by researchers including Moe (1961) and ACI-ASCE Committee 326 (1962), the provisions remain unchanged since the 1970s and describe the behaviour of unbalanced moments in ACI 318-19 and CSA A23.3-19.

The effects of unbalanced moments on slab-column connections have remained of interest to numerous researchers to this day. However, these researchers have commonly deviated away from the linear shear stress distribution assumptions of ACI 318 and CSA A23.3 in favour of prediction methods based on truss, beam, and membrane analogies. These methods were developed based on results of various laboratory tests in which specimens were subjected to

combined gravity loads and unbalanced moments. Due to space, cost, and load frame constraints, laboratory-tested specimens are often single slab-column sub-assemblages rather than frames consisting of multiple slab-column connections. The dimension of the slab is based on the radius of contraflexure, which is the distance away from the column at which moments within the slab are equal to zero. Furthermore, specimens are typically scaled versions of prototype structures. The behaviour observed among these scaled-specimens are assumed to be scalable to full-sized structures.

In this thesis, finite element analyses were conducted to reproduce the behaviour observed during laboratory-testing of slab-column connections without transverse reinforcement subjected to unbalanced moments and gravity loads. Numerical modelling allows for the study of stresses and strains within any region of the specimen, which would not be possible with laboratory testing. To ensure that specimen behaviour was accurately reproduced, the finite element models needed to be calibrated. Moment-rotation data, load-displacement data, and crack patterns from literature were compared to those produced by the finite element analyses. The finite element models were calibrated by changing one parameter at a time and selecting the parameter value that resulted in results closest to experimental results. Once the finite element models were calibrated, additional laboratory-tested specimens were analysed using the calibrated parameters and their results were compared to experimental results. If these finite element analyses accurately reproduced experimental behaviour, the finite element models were considered calibrated. Finally, a parametric study was conducted on the effects of moment-to-shear ratios on load capacities and stress distributions within the slab around the column.

Specimens SM 0.5, SM 1.0, and SM 1.5 tested by Ghali, Elmasri, and Dilger (1976) were used to calibrate the finite element model parameters. The preliminary parameters were selected based on research conducted by Genikomsou (2015) at the University of Waterloo as well as geometry, material, and boundary condition information provided by Ghali et al. (1976). These specimens were selected for analysis because only the slab reinforcement ratio varied between specimens. Specimens XXX and HXXX tested by El-Salakawy (1998) and specimen SB1 tested by Adetifa (2003) were analysed to verify the calibrated parameters. Specimens XXX and HXXX were used for verification as these specimens were edge slab-column connections, whereas the SM specimens were interior connections. Furthermore, specimens XXX and HXXX

differed only with respect to loading eccentricity. Specimen SB1 was used for verification as it was subjected to concentric loading whereas other analysed specimens included unbalanced moments. Finally, the SM specimens tested by Ghali et al. (1976) were used for the parametric study on the effects of moment-to-shear ratios on load capacities and stress distributions.

The specific objectives of this research are as follows:

1. summarize current code provisions and relevant historical research relating to the effect of unbalanced moments on the punching shear strength of slab-column connections,
2. develop a calibrated three-dimensional finite element model that may be used for analysing slab-column sub-assemblages subjected to combined unbalanced moments and gravity loads,
3. use the calibrated finite element model to conduct a parametric study on the effects of moment-to-shear ratios on punching shear strength and shear distributions at the critical perimeter defined by ACI 318-19 and CSA A23.3-19,
4. develop equations similar to those presented in ACI 318-19 and CSA A23.3-19 to predict the punching shear capacity of slab-column connections subjected to unbalanced moments, and
5. compare moment capacities for varying vertical loads as predicted by CSA A23.3-19, ACI 318-19, Eurocode 2 (2004), and *fib* Model Code 2010 to moment capacities determined from finite element analyses.

1.2 Thesis overview

The outline of this thesis is as follows:

Chapter 1 provides a brief introduction of the research problem, the process of developing the finite element model, and the research objectives. Chapter 2 is separated into two sections. Section 2.1 provides a review of past research in which laboratory tests were conducted and/or analysis methods were developed. Section 2.2 provides an overview of national design codes and their provisions relating to slab-column connections subjected to unbalanced moments. Chapter 3 explains the constitutive modelling of concrete and steel reinforcement in Abaqus.

Chapter 4 outlines the preliminary finite element model parameters for specimens SM 0.5, SM 1.0, and SM 1.5 prior to calibration. Chapter 5 explains the process of calibrating the finite element models and the effects of each parameter on finite element analysis results. Chapter 6 presents the calibrated finite element model parameters and the results of applying those parameters to specimens SM 0.5, SM 1.0, SM 1.5, XXX, HXXX, and SB1. Chapter 7 presents the results of the parametric study on the effects of moment-to-shear ratios (i.e. eccentricity) on the punching shear strength of the SM specimens. In Chapter 8, equations for the average shear stress and limiting average shear stress are developed based on the linear shear stress distribution assumption of CSA A23.3-19 and ACI 318-19. Chapter 9 compares the proposed equation for calculating the distribution of unbalanced moment between shear and flexural stresses (from Chapter 8) to the equation in CSA A23.3-19 and ACI 318-19. Also, a comparison of the moment versus vertical load data obtained from finite element analyses is made to the predictions of various national design codes and the proposed method. Chapter 10 presents a summary of the research herein and provides recommendations for future work.

Chapter 2: Literature review

2.1 Review of laboratory tests and analysis methods

2.1.1 Working stress analysis method by Di Stasio and Van Buren

Di Stasio and Van Buren (1960) developed a working stress analysis method based on laboratory tests they had conducted. Di Stasio and Van Buren were among the first to suggest that the ACI 318-56 (ACI Committee 318, 1956) concrete shear stress equation should include an additional term to account for the shear stress created by unbalanced moments. This change was implemented in ACI 318-63 (ACI Committee 318, 1965) and in all subsequent design code releases.

Di Stasio and Van Buren presented equations to calculate critical concrete shear stresses for exterior columns with and without spandrel beams, as well as interior columns without spandrel beams. These concrete shear stresses were examined at a periphery a distance $t - 1\frac{1}{2}$" from the column faces. For exterior columns without spandrel beams, the critical shear stress when the moment axis was parallel to the free edge, was presented as

$$v = \frac{8t}{7d}\left[\frac{V}{A} - \frac{(Hh - M - Ve)\alpha_1}{J}\right] \tag{2.1}$$

where t is the slab thickness, d is the effective slab depth, V is the applied vertical force, A is the area of the peripheral section given by

$$A = (2c + b)t \tag{2.2}$$

Hh is a force-couple moment produced by the column horizontal shear force H multiplied by the story height h, M is the resisting moment of the section, Ve is the moment produced by eccentrically-applied vertical loads, α_1 is the distance from the centroid of the peripheral section area to the extreme fibers given by

$$\alpha_1 = \frac{c}{2} + g\ , \tag{2.3}$$

and J is the polar moment of inertia given by

$$J_c = \frac{2tc^3}{12} + \frac{2ct^3}{12} + 2ctg^2 + bt\left[\frac{c}{2} - g\right]^2 . \quad (2.4)$$

The dimension c is the length of the critical perimeter orthogonal to the free edge and g is given by

$$g = \frac{bc}{2(2c + b)} \quad (2.5)$$

where b is the length of the critical perimeter parallel to the free edge.

For interior columns, the critical shear stress was presented as

$$v = \frac{8t}{7d}\left[\frac{V}{A} \pm \frac{Hh - (M_1 + m) - (M_2 - m)}{J}\frac{c}{2}\right] \quad (2.6)$$

where M_1 and M_2 are the flexural moments on opposite sides of the column, and m is the resultant unbalanced moment. For interior columns, the critical perimeter area is

$$A = 2(c + b)t \quad (2.7)$$

and the polar moment of inertia is

$$J = \frac{2tc^3}{12} + \frac{2ct^3}{12} + 2bt\left[\frac{c}{2}\right]^2 . \quad (2.8)$$

The Di Stasio and Van Buren method multiples both the vertical load and unbalanced moment shear stress contributions by $8t/7d$. This comes from the assumption that shear stresses are resisted over the lever arm jd, where j is equal to $7/8$. This was the assumption found within the ACI 318 design code (ACI Committee 318, 1956) at time that this method was published.

Multiplying by t/d reduces the shear-resisting area, which was previously calculated using the entire slab thickness, to account for the concrete tension side cover that ruptures and does not carry shear stresses.

This method assumes that longitudinal reinforcement increases the punching shear strength of the connection through dowel action. This is done by increasing the shear-resisting area of the peripheral section and the polar moment of inertia. The modified peripheral section area is

$$A' = A[1 + (n - 1)\rho] \quad (2.9)$$

where n is the ratio between the modulus of elasticity of the steel to that of the concrete, and ρ is the reinforcement ratio.

Similarly, the modified polar moment of inertia is

$$J' = J[1 + (n - 1)\rho] . \quad (2.10)$$

The maximum shear stress used by Di Stasio and Van Buren was based on the ACI 318-56 standard. This standard stated that the maximum shear stress is $0.03f_c'$ when at least 50-percent of the required column strip reinforcement passes through the shear-resisting critical section. This capacity is reduced proportionately to $0.025f_c'$ as the column strip reinforcement that passes through the critical section approaches 25 percent. This was the minimum reinforcement required to pass through the critical section based on ACI 318-56.

2.1.2 Ultimate strength analysis method by Johannes Moe

Johannes Moe produced an ultimate strength model for determining the punching shear capacity of slab-column connections subjected to combined moment and vertical loading (1961). Moe tested 43 slab-column connections that were simply supported along the slab edges and loaded axially through the column. Of these 43 slabs, 12 slabs were loaded with eccentric column loads to produce both a vertical load and a moment. These loads were applied at a point along a beam attached to the top column stub. The eccentricity varied between 2.4-inches and 24.2-inches. The reinforcement ratios of these specimens were either 1.34 or 1.50 percent.

At the time of publication, previous research by Elstner and Hognestad (1956) suggested that the concrete punching strength did not change when the vertical load eccentricity was increased up to one-half of the column size nor did it change when the amount of compression reinforcement was increased. Their tested specimens had eccentricities, e, of 7-inches and column side lengths, r, of 14-inches ($e/r = 0.5$). Moe commented that the test setup used by Elstner and Hognestad likely did not produce eccentricities as the specimen columns were not allowed to move horizontally (1961).

Moe later stated that specimens with e/r ratios less than 0.5 behaved similarly to concentrically-loaded specimens. Although the behaviour was similar, Moe measured additional concrete strains adjacent the column face on the same side as the imposed eccentricity. Furthermore,

specimens without negative moment reinforcement failed under lower loads than specimens with negative moment reinforcement.

Moe concluded that placing bending reinforcement in narrow bands across the column did not increase the connection's shear strength but did increase the slab's flexural rigidity (1961).

Moe stated that the maximum shear stress, v, for a square column could be determined using

$$v = \frac{P}{A_c} + \frac{\beta M}{J_c}\left(\frac{r}{2}\right) \tag{2.11}$$

where P is the vertical load,

$$A_c = 4rd\,, \tag{2.12}$$

r is the column side length, d is the effective depth, β is the percent of moment that is resisted by shear, M is the unbalanced moment, and

$$J_c = \frac{2r^3 d}{3}\,. \tag{2.13}$$

Contrary to other mechanical models, Moe assumed that the punching shear critical perimeter is located at the column rather than at a periphery some distance away. Moe determined that using a value of 0.33 for β produced an average P_{test}/P_{calc} value of 1.026 with a standard deviation of 0.103.

Moe presented a limiting shear stress of

$$v = (9.23 - 1.12\,d/r)\sqrt{f_c'} \qquad \text{(US customary units: psi, in.)} \tag{2.14}$$

when $r/d \leq 3$ and

$$v = (2.5 + 10\,d/r)\sqrt{f_c'} \qquad \text{(US customary units: psi, in.)} \tag{2.15}$$

when $r/d > 3$. The limiting shear stress prediction for $r/d \leq 3$ was based on empirical data while the limiting shear stress for $r/d > 3$ was based on theoretical assumptions. Equations 2.14 and 2.15 were developed based on limiting shear forces from concentrically-loaded specimens. As shown in Figure 2.1, Moe selected limiting shear forces such that the governing failure mode would be in flexure rather than shear. Moe stated that the punching shear capacity

could be increased by adding flexural reinforcement but that this approach to increasing the shear capacity would be uneconomical.

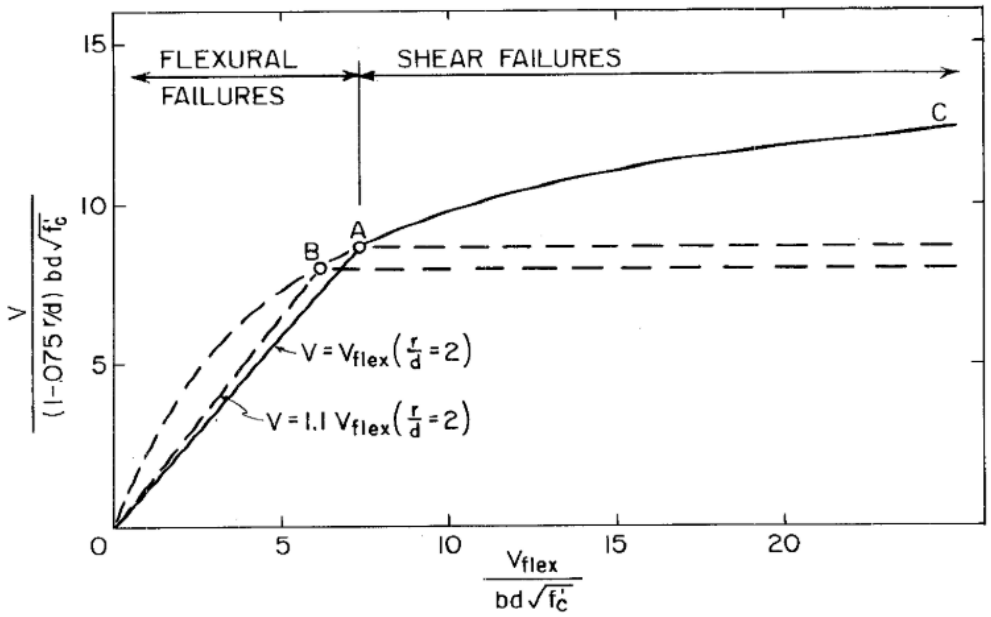

Figure 2.1: Maximum vertical load used by Moe (1961) to develop limiting shear equations. Reprinted from Development Department Bulletin D47, Portland Cement Association (April 1961). Reprinted with permission.

2.1.3 Ultimate strength analysis method by ASCE-ACI Committee 326

Based on the work of Di Stasio and Van Buren (1960) and Moe (1961), ASCE-ACI Committee 326 (1962) proposed the following equation for determining the maximum concrete shear stress at a periphery section $d/2$ from the column:

$$v_u = \frac{V}{A_c} + \frac{KM}{J_c}\left(\frac{c}{2}\right) \tag{2.16}$$

where V is the vertical load,

$$A_c = 2(c+b)d = b_o d\,, \tag{2.17}$$

K is the portion of unbalanced moment transferred to concrete shear stress,

$$J_c = \frac{2dc^3}{12} + \frac{2cd^3}{12} + 2bd\left(\frac{c}{2}\right)^2\,, \tag{2.18}$$

c and b are the critical section lengths parallel and orthogonal to the moment axis, respectively. As proposed by Di Stasio and Van Buren (1960), the committee stated that A_c and J_c could be

multiplied by $[1 + (n - 1)\rho]$ to account for the effects of dowel action. Based on empirical data, the committee suggested that K equal 0.2 rather than 0.33 as suggested by Moe.

ASCE-ACI Committee 326 (1962) modified Moe's limiting shear stress equations to provide a conservative fit to tested specimen data. They proposed two different equations for determining the limiting shear stress. The first equation was to use a limiting shear stress of

$$v = 4\left(1 + \frac{d}{r}\right)\sqrt{f_c'} \qquad \text{(US customary units: psi, in.)} \quad (2.19)$$

calculated at the periphery section adjacent to the column, where r is the side length of a square column. The second equation was to use a limiting stress of

$$v = 4\sqrt{f_c'} \qquad \text{(US customary units: psi, in.)} \quad (2.20)$$

calculated at the periphery section a distance $d/2$ from the column.

ASCE-ACI Committee 326 recommended using Equation 2.20 as it does not depend on the length r, which would be ambiguous for column shapes other than a square.

2.1.4 Implementation of unbalanced moment analysis in ACI 318-65

The Commentary on Building Code Requirements for Reinforced Concrete ACI 318-63 (ACI Committee 318, 1965) suggested predicting shear at a periphery section defined by lengths a and c in instances where the connection is loaded under combined moment, torsion, and vertical load. Length a is parallel to the moment axis and equals $1.5t$ plus the column dimension parallel to the moment axis (where t is the slab depth). Length c is perpendicular to the moment axis and equals d plus the column dimension perpendicular to the moment axis. ACI Committee 318 suggest predicting the shear stress using:

$$v = \frac{V}{A_c} \pm \frac{M_T(c/2)}{J_c} \quad (2.21)$$

where

$$A_c = 2(a + c)\,, \quad (2.22)$$

and

$$J_c = \frac{dc^3}{6} + \frac{ct^3}{6} + 2ad\left(\frac{c}{2}\right)^2 . \quad (2.23)$$

Similar to the method proposed by Di Stasio and Van Buren (1960), only the torsional moment M_T is transferred to concrete shear stress (i.e. the remaining moment not resisted by flexure at the critical section). ACI Committee 318 suggested using a limiting shear stress of $2\sqrt{f_c'}$.

2.1.5 Moment transfer coefficient γ_f by Hanson and Hanson

In 1968, Hanson and Hanson tested 16 interior slab-column specimens and 1 edge slab-column specimen. All of the specimens shared the same slab depth, concrete cover, reinforcement spacing, and reinforcement size but had one of three different columns. Hanson and Hanson studied the effect of column rectangularity and orientation on the transfer of unbalanced moment to flexural and shear stresses. The specimens were loaded with either: only unbalanced moments, only gravity loads, or a combination of unbalanced moments and gravity loads. Additionally, Hanson and Hanson investigated how holes adjacent to the columns affected the transfer of unbalanced moment between slabs and columns. These specimens had 1-inch wide holes that were on opposite sides of the column and the lengths of these holes were along the same direction (i.e. either parallel or orthogonal to the moment axis).

Hanson and Hanson compared their test results to the prediction methods of Di Stasio and Van Buren (1960), Moe (1961), ACI-ASCE Committee 326 (1962), and the Commentary on ACI 318-63 (ACI Committee 318, 1965). Of these methods, Hanson and Hanson determined that the method recommended by ACI-ASCE Committee 326 produced good predictions when K, the portion of moment carried by shear, was increased from 0.2 to 0.4. Moreover, Hanson and Hanson found that using a 12-inch by 6-inch column, with its short edge about the moment axis, resulted in an ultimate moment increase between 33 and 60 percent over using a 6-inch by 6-inch square column. Similarly, using a 12-inch by 6-inch column, with its long edge about the moment axis, resulted in an ultimate moment increase between 20 and 40 percent over using a 6-inch by 6-inch square column. This research was later used by ACI Committee 318 (1970) to develop an equation to predict γ_v, the portion of moment carried by concrete shear stresses:

$$\gamma_v = 1 - \frac{1}{1 + \frac{2}{3}\sqrt{\frac{c_1 + d}{c_2 + d}}} \quad (2.24)$$

Equation 2.24 uses critical section lengths rather than column side lengths. It was implemented in ACI 318-71 (ACI Committee 318, 1971) and kept in subsequent releases of the ACI 318 design code.

On the effect of holes on slab-column moment transfer, Hanson and Hanson observed that holes adjacent to the column and orthogonal to the moment axis had little effect on the punching shear capacity. Contrarily, holes adjacent to the column and parallel to the moment axis reduced the shear capacity between 30 to 35 percent. Also, Hanson and Hanson found that existing code provisions underestimated the punching shear capacity of slab-column connections with holes adjacent to the column. They noted that the reinforcement passing through their specimens' holes likely contributed to the specimens' increased punching shear capacities (Hanson & Hanson, 1968).

2.1.6 Column rectangularity on connection strength by Hawkins, Fallsen, and Hinojosa

Hawkins, Fallsen, and Hinojosa (1971) investigated the influence of column rectangularity on the punching shear strength of slab-column connections. Hawkins et al. tested 9 concentrically loaded interior slab-column specimens with short-to-long edge ratios between 1.0 and 4.3. Hawkins et al. found that ACI 318-71 (ACI Committee 318, 1971) predicted accurate shear capacities for specimens with column long-to-short side length ratios of less than 2. For specimens with ratios greater than 2, the shear capacities decreased as the ratio was increased. Hawkins et al. proposed the equation:

$$\frac{V_u}{b_o d\sqrt{f_c'}} = (2.5 + 3.0\, s/l) \leq 4.0 \quad \text{(US customary units: psi, in.)} \quad (2.25)$$

where s and l are the column short and long side lengths, respectively. The inequality in Equation 2.25 limits the calculated maximum shear stress to $4\sqrt{f_c'}$, which was the governing maximum shear stress in ACI 318-71. As per the inequality, this maximum shear stress is $4\sqrt{f_c'}$ for s/l values greater than 0.5.

In 1974, ASCE-ACI Committee 426 proposed an alternative to Equation 2.25:

$$\frac{V_u}{b_o d\sqrt{f_c'}} = (2.0 + 3.0\, s/l) \leq 4.0\,, \quad \text{(US customary units: psi, in.)} \quad (2.26)$$

which would limit the maximum shear stress to $2\sqrt{f_c'}$ for large l/s ratios (ASCE-ACI Committee 426, 1974).

The research of Hawkins et al. led to the following maximum shear stress equation within ACI 318-77 (ACI Committee 318, 1977) and subsequent ACI 318 releases:

$$V_c = \left(2 + \frac{4}{\beta}\right)\sqrt{f_c'}b_o d \qquad \text{(US customary units: psi, in.) (2.27)}$$

where β is the ratio of the long-to-short column side lengths.

2.1.7 Tests of exterior connections subjected to unbalanced moments by Zaghlool

In 1971, Zaghlool tested 11 corner and 9 edge slab-column connections under both unbalanced moments and gravity loading. For edge connections, moments were applied about the axis parallel to the free edge. Zaghlool's tests were separated into different series to test how different parameters affected the strength and behaviour of slab-column connections. These parameters included: r/d ratio, reinforcement ratio, and M/V ratio. The r/d specimens used square columns with dimensions of either 7-inch by 7-inch, 10.5-inch by 10.5-inch, or 14-inch by 14-inch. The reinforcement ratio specimens used reinforcement ratios of either 1.23-percent, 1.65-percent, or 2.23-percent. For the M/V specimens, moment-to-vertical-load ratios of infinite (i.e. only unbalanced moment), 2.48-feet, 1.28-feet, or zero (i.e. only vertical load) were used.

Zaghlool showed that the measured ultimate shear stresses were consistently higher than the predictions of ACI 318-63. Increasing either the r/d ratio or reinforcement ratio resulted in increased ultimate shear stress. Contrarily, increasing the M/V ratio resulted in decreased ultimate shear stress.

Zaghlool produced the moment-shear interaction diagram reproduced in Figure 2.2. Specimens subjected to both unbalanced moments and gravity loads had higher moment capacities than specimens subjected to only unbalanced moments. Zaghlool suggested that the gravity loads increased the moment capacity for two reasons. First, the gravity load (applied through the column) increased the confinement within the concrete compression region. Second, the gravity load produced an eccentric moment acting in the opposite direction to the applied moment. Based on these results, Zaghlool suggested the use of a bilinear moment-shear relation. He

suggested that an applied moment does not influence a connection's vertical load capacity and vice versa (Zaghlool, 1971).

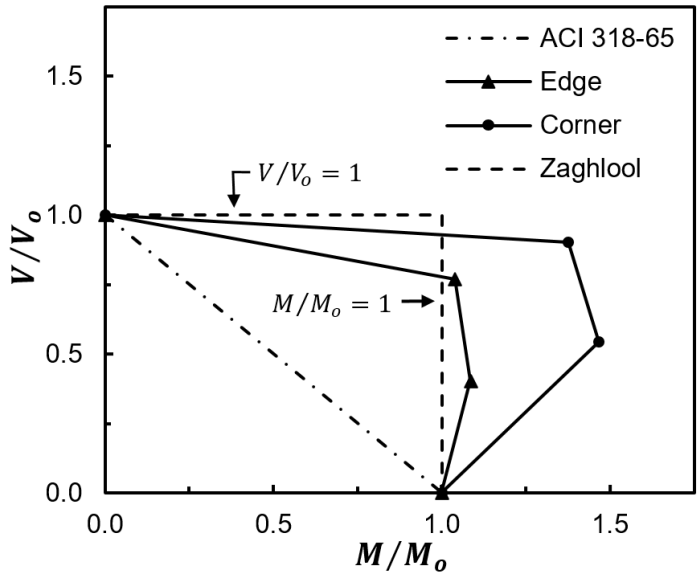

Figure 2.2: Moment-shear interaction diagram by Zaghlool (1971)

2.1.8 Beam analogy by Hawkins and Corley

In 1971, Hawkins and Corley published a method of evaluating the strength of slab-column connections by treating slabs as beams framing into the column. It is assumed that each beam can deform enough to develop their ultimate strengths. By this beam analogy, connections can fail either in shear-torsion, flexure, shear, or moment-torsion. Figure 2.3 shows a column subjected to both an unbalanced moment and a vertical load. Shear-torsion failure occurs when all faces except face BC reach their shear or torsional capacities. Moment-torsion failure occurs when face CB (additionally, AD for interior connections) develops its flexural capacities and the remaining moment is resisted through torsion by adjacent faces. This failure mode would typically govern for cases where little shear is applied to the connection. Hawkins and Corley showed that their method accurately predicted the ultimate capacities of tests by Hanson and Hanson (1968), Anderson (1966), and themselves (Corley & Hawkins, 1968). Figure 2.4 shows the failure envelope produced by Hawkins and Corley for the interior 6-inch by 6-inch square columns tested by Hanson and Hanson (1968).

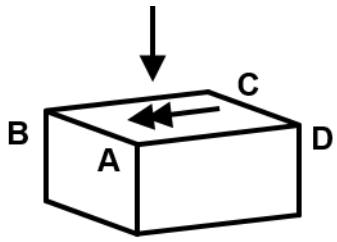

Figure 2.3: Column of slab-column connection subjected to combined loading

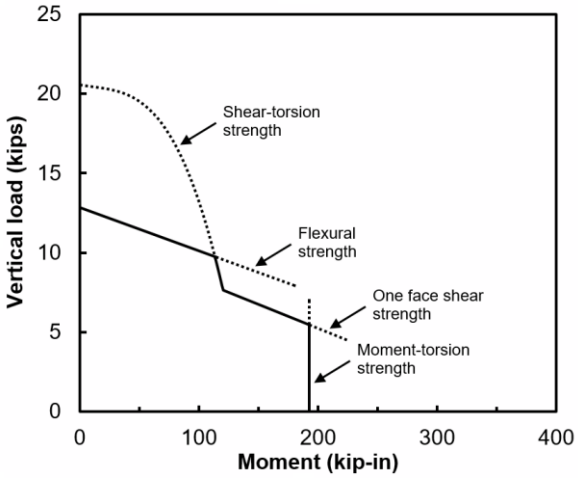

Figure 2.4: Vertical load versus moment envelope for 6-inch square column specimens tested by Hanson and Hanson (1968) (N. Hawkins & Corley, 1971)

2.1.9 Influence of column shape on slab-column connection strength by Vanderbilt

In 1972, Vanderbilt presented test results of 15 interior slab-column specimens. The specimens had varying r/d ratios with a column shape of either a square or a circle and a negative moment reinforcement ratio of either 1-percent or 2-percent. For circular columns, the column side length, r, assumed was that of a square column with equal column area. Vanderbilt showed that circular columns had higher shear capacities than square columns of equal column area and reinforcement ratio. Vanderbilt attributed this strength difference to stress concentrations at the corners of square columns.

For the same reinforcement ratio and column area, Vanderbilt observed minimal shear strength increases for r/d values of 2 and 8 and larger shear strength increases at intermediate r/d values. The largest observed shear strength increase was 35-percent for specimens with r/d equal to 4 (ASCE-ACI Committee 426, 1974; Vanderbilt, 1972).

Vanderbilt's research led to the following maximum shear stress equation within ACI 318-89 (ACI Committee 318, 1989) and subsequent ACI 318 releases:

$$V_c = \left(\frac{\alpha_s d}{b_o} + 2\right)\sqrt{f_c'}\, b_o d \,. \qquad \text{(US customary units: psi, in.) (2.28)}$$

In Equation 2.25, α_s is equal to 40 for interior columns, 30 for edge columns, and 20 for corner columns. Confinement is likely reduced as b_o/d is increased, which would result in reduced maximum shear stresses (Moehle, Kreger, & Leon, 1988).

The variable α_s was implemented in Equation 2.25 to predict similar maximum shear stresses for all column locations, while incorporating the b_o/d effects observed by Vanderbilt. For example, consider a 12-inch by 12-inch square column with an effective depth, d, of 3-inches. Assuming that the column is $d/2$ away from the free edges in edge and corner configurations, the critical perimeter, b_o, would be 60-inches, 45-inches, and 30-inches for interior, edge, and corner locations, respectively. Equation 2.25 would predict a maximum shear stress of $4\sqrt{f_c'}$ for all locations, which is consistent with the existing ACI 318-89 limiting shear stress based on Moe's research (ACI Committee 318, 1989; 1961).

2.1.10 Connections subjected to unbalanced moments tested by Stamenkovic

In 1969, Stamenkovic published the results of their study on the effects of gravity loading and unbalanced moments on the strength of slab-column connections. He tested 52 half-scale slab-column connections of varying column location, column shape, and loading. Gravity loads were applied axially through column stubs and unbalanced moments were applied as opposing forces at the ends of top and bottom column stubs. All specimens used 3-foot by 3-foot square slabs of 3-inch thickness, which were supported by tie-rods around the perimeter of the slabs. All slabs were reinforced with Grade 60, 5/16-inch diameter bars with a reinforcement ratio of 1.17-percent.

Ten interior connections were subjected to M/V ratios of infinite (i.e. only vertical load), 2.58 feet, 1.29 feet, 0.52 feet, and 0.26 feet. Five of these specimens used 5-inch by 5-inch square columns and the remaining five used 3-inch by 6-inch square columns. Similarly, ten edge connections with 5-inch by 5-inch square columns were subjected to the same M/V ratios as the interior columns. For five of these specimens, the moment was applied about an axis parallel to

the free edge. For the remaining five specimens, the moment was applied about an axis perpendicular to the free edge. Lastly, five corner connections with 5-inch by 5-inch square columns were subjected to M/V ratios of 5.17 feet, 2.58 feet, 1.29 feet, and 0.81 feet.

Stamenkovic normalized and plotted moment-shear data for each column location and loading. Based on this data, Stamenkovic suggested that the capacity of interior connections and edge connections with moments about the axis perpendicular to the free edge could be predicted using the equation

$$\frac{V}{V_u} + \frac{M}{M_u} = 1\,. \tag{2.29}$$

Similarly, Stamenkovic suggested that the capacity of corner connections and edge connections with moments about the axis parallel to the free edge could be predicted using the equation

$$\left(\frac{V}{V_u}\right)^2 + \left(\frac{M}{M_u}\right)^2 = 1\,. \tag{2.30}$$

In Equations 2.44 and 2.45, the ultimate vertical load without any moment applied, V_u, for interior connections is

$$V_u = 0.9\left(4rd_1\sqrt{U_{cyl}}\,\frac{15(1-0.075\,r/d_1)}{1+5.25\,\dfrac{4rd_1\sqrt{U_{cyl}}}{V_{flex}}}\right). \tag{2.31}$$

The ultimate vertical load without any moment applied, V_u, for edge connections is

$$V_u = 0.9\frac{3r+4d}{4r+8d}\left(4rd_1\sqrt{U_{cyl}}\,\frac{15(1-0.075\,r/d_1)}{1+5.25\dfrac{3rd_1\sqrt{U_{cyl}}}{V_{flex}}}\right). \tag{2.32}$$

The ultimate vertical load without any moment applied, V_u, for corner connections is

$$V_u = 0.9\frac{2r+2d}{4r+8d}\left(4rd_1\sqrt{U_{cyl}}\,\frac{15(1-0.075\,r/d_1)}{1+5.25\dfrac{2rd_1\sqrt{U_{cyl}}}{V_{flex}}}\right). \tag{2.33}$$

In Equations 2.46, 2.47, and 2.48, r is the column side length orthogonal to the moment axis, d is the slab thickness, d_1 is the effective slab depth, U_{cyl} is the concrete cylinder strength, and V_{flex} is the slab flexural strength using the yield-line theory.

In Equations 2.44, the ultimate moment without any vertical load applied, M_u, is given by

$$M_u = k_c U_w r \left(\frac{d}{2}\right)^2 + 0.13 U_w \Sigma_o b a_s + k_s U_w r d_1 b + 0.5 n k_t \left(\frac{A_{st} f_y}{bd}\right) d^2 \left(b - \frac{d}{3}\right). \quad (2.34)$$

In Equations 2.45, the ultimate moment without any vertical load applied, M_u, is given by

$$M_u = 0.9 A_s f_y d_1 \left(1 - 0.59 \frac{\rho f_y}{U_{cyl}}\right) + 0.5 n k_t \left(\frac{A_{st} f_y}{bd}\right) d^2 \left(b - \frac{d}{3}\right). \quad (2.35)$$

In Equations 2.34 and 2.35: U_w is the concrete cube strength or $0.85U_{cyl}$; k_c, k_s, and k_t are provided in Table 2.1; Σ_o is the minimum of the top and bottom reinforcement circumference; and b is the column side length parallel to the moment axis. In Equation 2.34, $0.13U_w\Sigma_o$ cannot exceed twice the reinforcement yield stress.

Table 2.1: Values of k_c, k_s, and k_t (Stamenkovic, 1969)

Column location	k_c	k_s	k_t
Interior	1.00	0.10	1.00
Edge (span parallel to free edge)	0.80	0.07	1.00
Edge (span orthogonal to free edge)	—	—	0.70
Corner	—	—	0.70

2.1.11 Study of slab-column behaviour by Regan

In 1981, Regan developed various design equations using experimental data relating to flexure, shear, and deflections. With respect to punching shear, Regan studied how various parameters influenced the punching capacity of slab-column connections. These parameters included concrete strength, reinforcement area and layout, r/d ratio, size effect, load and support conditions, and unbalanced moments.

Based on research by Elstner and Hognestad (1956), Regan proposed that the ultimate punching shear stress is proportional to the cube-root of the concrete compressive strength. Similarly, this stress is proportional to the cube-root of $100A_s/bd$.

Regan stated that adding flexural steel increases the punching shear strength for two reasons. First, additional reinforcement increases the compression zone which means more uncracked concrete to carry shear. Second, additional reinforcement reduces crack widths which means more aggregate interlock to carry shear. On the topic of concentrating reinforcement toward the column, Regan stated that existing data showed a 6-percent decrease in punching shear capacity when the concentration of steel was increased from a uniform distribution. This difference was negligible. On the topic of compression reinforcement, Regan stated that existing data in which the area of compression steel was between 0.3 to 1.0 times the area of tension steel, the punching shear capacity increased only up to 12-percent. Regan commented that many punching shear predictions consider the reinforcement yield stress in their formulations. However, Moe's tests (1961) showed no differences in capacity when using reinforcement with a yield stress of 330 megapascals (MPa) compared to using reinforcement with a yield stress of 480 MPa. Furthermore, Regan commented that using a reinforcement parameter within mechanical models may not adequately capture behaviour since only a portion of the reinforcement is yielding. Lastly, Regan stated that specimens with reinforcement fanning outward from the column had punching capacities 30-percent less than specimens with orthogonal reinforcement mats but equivalent flexural strength.

With respect to r/d ratios, Regan suggested that circular columns provide a 15-percent increase in shear capacity compared to square columns of equal area. Regan stated that the nominal ultimate shear stress is inversely proportional to the fourth-root of a slabs effective depth. However, this effect is reduced if the maximum aggregate size is scaled in proportion with the effective depth. On the topic of load and boundary conditions, Regan commented that specimens typically do not include in-plane restraints at slab edges to recreate the compressive membrane effects observed in practical flat slab systems. Furthermore, some experiments had slab edges that were restrained from rotating. Regan stated that these effects were likely negligible.

For an interior slab-column connection, Regan showed that the reduction in vertical load capacity when the connection is subjected to an unbalanced moment could be approximated using

$$\frac{V_{ue}}{V_{uo}} = \frac{1}{1 + 1.5e/\sqrt{(c_1 + 2d)(c_2 + 2d)}} \tag{2.36}$$

where V_{ue} is the ultimate shear capacity with a load eccentricity, V_{uo} is the ultimate concentric shear capacity, and e is the load eccentricity (or M/V). Regan proposed that the 1.5 coefficient in Equation 2.36 could be modified to 1.0 or 2.0 to better correlate to some experimental data. Equation 2.36 using coefficients of 1.0, 1.5, and 2.0 is plotted in Figure 2.5.

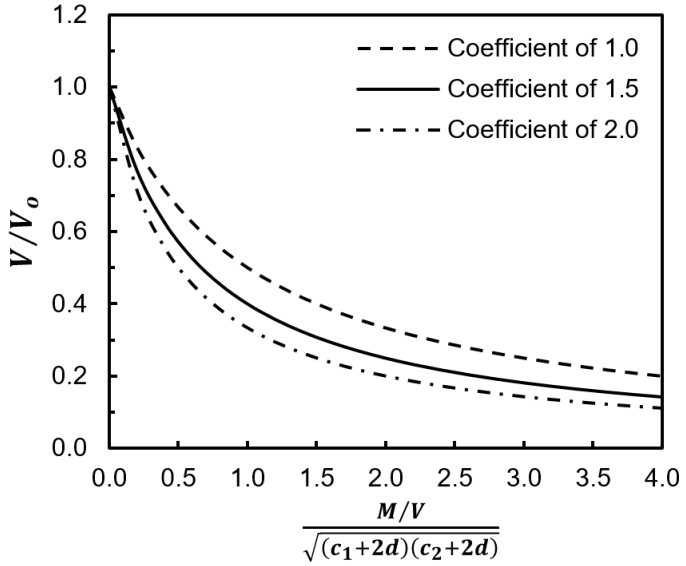

Figure 2.5: Shear capacity versus eccentricity for interior connections (Regan, 1981)

Considering all aforementioned effects, Regan proposed that the ultimate load for interior connections subjected to concentric loads could be predicted using

$$V_{Rd} = 0.1K_{sc}\xi_s \sqrt[3]{\frac{100A_s}{bd}f_{cu}}A_c \tag{2.37}$$

where

$$K_{sc} = 1.15\sqrt{\frac{4\pi \cdot column\ area}{(column\ perimeter)^2}} \tag{2.38}$$

and

$$\xi_s = \sqrt[4]{\frac{300}{d}} \tag{2.39}$$

and

$$A_c = 2.69d(\Sigma c + 7.85d) \tag{2.40}$$

where Σc is the perimeter a distance $2.5d$ from the column.

Regan proposed the following equation for determining the ultimate vertical load for interior connections with unbalanced moments:

$$V_{Rde} = V_{Rd} \cdot \frac{1}{1 + \frac{1.5(e_x + e_y)}{\sqrt{(c_x + 2d)(c_y + 2d)}}} \tag{2.41}$$

where e_x and e_y are the load eccentricities (i.e. M/V) in the x and y directions and c_x and c_y are the column dimensions in the x and y directions.

For edge connections, Regan proposed the following equation to predict the punching load:

$$V_{Rd,edge} = 0.1K_{sc}\xi_s \sqrt[3]{\frac{100A_s}{bd} f_{cu}} \left(\frac{A_c}{1.25 + \frac{1.5e}{c + 2d}} \right). \tag{2.42}$$

For corner connections, Regan proposed the following equation to predict the punching load:

$$V_{Rd,corner} = 0.8 \cdot 0.1K_{sc}\xi_s \sqrt[3]{\frac{100A_s}{bd} f_{cu}} A_c \,. \tag{2.43}$$

2.1.12 Size effect on unbalanced moment specimens by Neth, de Paiva, and Long

In 1981, Neth, de Paiva, and Long tested four flat plate subsystem configurations. The four subsystems were scaled versions of a full-size design: one-half, one-quarter, one-sixth, and one-eight scale specimens. The one-half scaled specimen had a 20-foot by 10-foot flat slab with two columns spaced 10-feet apart along each of the longer slab edges. Each of these four columns was located 5-feet from the shorter slab edges. The remaining specimens used square flat slabs

with two columns total placed opposite one another at the center of the slab width. For all specimens, the slab edges with columns present were unrestrained, while the slab edges without columns were allowed to deform in all directions and rotate only about the axis parallel to the edge. The flat plates of all specimens were loaded using 16 point loads to simulate combined unbalanced moment and gravity loading conditions. All specimens had a reinforcement ratio of 1-percent with similar concrete mixes.

Neth et al. found that all specimens showed similar plate deflections, as well as rotations, flexural cracking, and failure behaviour near slab-column connections (1981). Neth et al. showed that the specimens deformed similarly but smaller-scale specimens had larger load capacities compared to larger-scale specimens. They proved this by addressing similarities among load-deflection data once all data had been normalized. Furthermore, they suggested testing specimens scaled to no less than one-quarter of the full-sized specimen to avoid overestimating a connections load capacity.

Regardless of size, all specimens developed the same types of cracks throughout testing. First, flexural cracks began to form at a distance from the free edge equal to two-thirds of the orthogonal-to-free-edge column dimension. These cracks formed at the tension slab-column interface and propagated at an angle toward the compression slab face. These cracks continued toward the interior column of the specimens. The slab plate adjacent the column would rotate rigidly about the apex of the crack in a hinge-like manner. Although similar flexural cracks formed at distances away from the column, the initial flexural cracks increased in width through testing and ultimately governed the behaviour of the connections. Approaching the ultimate loads of the connections, cracks formed orthogonal to the flexural cracks which developed as punching shear failure began to occur. Neth et al. described these orthogonal cracks as secondary failure cracks that formed after the crushing of the concrete compression zone (1981).

Based on slab deflections, Neth et al. doubted that dowel action contributed to punching shear strength. However, they noted that compression reinforcement strains suddenly increased as tension reinforcement began to yield. This meant that the compression reinforcement provided additional confinement and capacity to the concrete compression zone. Furthermore, based on compression reinforcement strains, Neth et al. found that the radius of contraflexure moved toward the column as the load was increased (1981).

2.1.13 Truss analogy analysis method by Alexander and Simmonds

In 1987, Alexander and Simmonds published a truss analogy for modelling internal forces within slab-column connections under combined gravity loading and unbalanced moment. Their truss analogy was developed for slab-column connections without transverse reinforcement. They stated that existing models that assume a linear distribution of vertical shear stresses across a critical section are problematic for three reasons. First, the vertical shear stresses within the slab are part of a diagonal tension field. However, this tension field no longer exists after diagonal cracks form within the slab. These cracks typically form under gravity loads equal to 50 to 70 percent of the ultimate gravity load. If the slabs are unloaded after cracking then reloaded until failure, the load capacity is the same as if the slab had been monotonically loaded. Alexander and Simmonds stated that the linear distribution model should apply only to uncracked regions of compressed concrete which have diagonal tension fields that could carry shear stresses. Second, the linear distribution model considers shear stresses adjacent to column faces located orthogonal to the moment axis. Alexander and Simmonds stated that these faces fail in torsion rather than shear and, therefore, should not be analysed using a shear distribution model. Third, the failure surface changes with different moment-to-vertical load ratios; however, the critical section location is based on a constant reinforcement depth instead of a varying uncracked concrete depth.

The truss analogy proposed by Alexander and Simmons relies on a different set of assumptions. The truss is made up of inclined concrete struts and horizontal steel ties. One end of each concrete strut equilibrates the tensile force from an adjacent steel tie and the other end connects to the column. The inclined concrete struts can be defined as anchoring struts, uplift struts, or gravity struts. Anchoring struts are in-plane with the reinforcement and help to develop the reinforcement. Uplift struts tie to bottom mat reinforcement and oppose upward movement of the slab. Gravity struts tie to top mat reinforcement and oppose downward movement of the slab. Gravity struts are present when only gravity loading is applied. These gravity struts are replaced with anchoring struts as the moment-to-vertical-load ratio is increased. Under large enough moments, uplift struts and gravity struts will oppose one another on opposite column faces where both faces are parallel to the moment axis.

The truss failure is based on the yielding of steel ties rather than the concrete struts. Alexander and Simmonds stated that a flexural compression failure is outside the limits of practical design. The steel tie failure occurs when the concrete struts reach a certain angle α relative to the slab. Alexander and Simmonds proposed the equation

$$\tan\alpha = 1.0 - e^{-0.85K} \tag{2.44}$$

where

$$K = \frac{s_{eff} \cdot d' \cdot \sqrt{f_c'}}{A_{bar} \cdot f_y \cdot (c/d_s)^{0.25}}. \tag{2.45}$$

In Equation 2.44, $\tan\alpha$ is the out-of-plane shear force carried by the concrete strut divided by the in-plane force carried by the yielding steel tie. This equation implies that the concrete strut angle α cannot exceed 45 degrees. In Equation 2.45, d' is the concrete cover, s_{eff} is the effective bar spacing which is equal to the maximum of the bar spacing or $3d'$, A_{bar} is the area of the reinforcing bar, c is the column dimension perpendicular to the bar being analysed, and d_s is the slab effective depth (i.e. distance from the compression face to the reinforcement centroid). The term c/d_s is based on research by Hawkins et al. (1971) which accounts for reductions in concrete shear strength as column rectangularity is increased.

To produce Equation 2.44, Alexander and Simmonds performed a regression using $\tan\alpha$ and K values for 43 concentrically-loaded test specimens. Concentrically-loaded specimens were used to ensure that only gravity struts were present rather than anchoring or lifting struts. However, Alexander and Simmonds stated that the truss analogy can be applied to each column face independently regardless of geometry, reinforcement, or loading. This is justified by crack pattern similarities between interior and edge slab-column connections under combined loading.

Alexander and Simmonds stated that describing slab-column failure as either shear or flexural failure based on ductility is misleading. Instead, failure should be described as either local connection failure or slab failure. Furthermore, they stated both local and slab failures can be ductile or brittle, and that ductile failures occur in connections with high strain gradients. These gradients can occur if: low reinforcement ratios are used, uplift struts are adjacent to gravity struts, or anchoring struts connect to shear struts at a node (Alexander & Simmonds, 1987).

2.1.14 Analysis of γ_f for edge slab-column connections by Moehle

In 1988, Moehle suggested that the ACI 318 (ACI Committee 318, 1986) code provisions relating to unbalanced moment transfer at edge slab-column connections did not agree with published test data. He suggested that existing test data correlated well to a bilinear V_u/V_o versus M_u/M_o interaction diagram. The variable V_u is the ultimate vertical load without any applied moment, V_o is equal to $v_c A_{cs}$, M_u is the tested ultimate moment, and M_o is the ultimate moment without any applied vertical load. In other words, there is no significant interaction between shear and moment and connections fail in either shear or flexure.

Using the provisions from ACI 318-86, Moehle plotted Strength Ratio versus V_u/V_o data for 27 edge slab-column connections. These specimens were loaded with both gravity loads and moments about an axis parallel to the free edge. Moehle defined Strength Ratio as the maximum of v/v_c at the inner column face, v/v_c at the outer column face, and M_u/M_o (where v is the linearly-varying shear stress about the connection). Moehle stated that failure should occur when the Strength Ratio is equal to 1. The plotted Strength Ratios varied between 1.05 and 2.53 with a coefficient of variation of 0.25.

Moehle reduced the coefficient of variation to 0.19 by assuming only vertical loads were resisted by shear stresses and moments were resisted entirely by flexural stresses (i.e. γ_f equal to one). However, the data still did not correlate well for specimens with V_u/V_o values greater than 0.75. The mean Strength Ratio (i.e. M_u/M_o) was equal to 1.28.

To reduce the mean Strength Ratio to 1.0, Moehle increased M_o by increasing the moment transfer width from

$$c_2 + 3h \tag{2.46}$$

to

$$c_2 + 2c_t\,, \tag{2.47}$$

where c_t is the distance from the column faces (oriented orthogonal to the free edge) to the extents of torsional cracks measured after punching failure has occurred.

The crack width c_t is given by

$$c_t = c_1\sqrt{\rho_t/\rho_l} \tag{2.48}$$

where ρ_t and ρ_l are the transverse and longitudinal reinforcement ratios. Equation 2.48 was derived assuming that both transverse and longitudinal reinforcement mats are yielding when slab-column connection failure occurs.

Using Equation 2.47, the mean Strength Ratio reduced to 1.07 with a coefficient of variation of 0.16. To simplify the calculation, he suggested using a moment transfer width of

$$c_2 + 2c_1 \tag{2.49}$$

which assumes that the torsional cracks are oriented 45 degrees from the free edge of the connection. Equation 2.49 increased the mean Strength Ratio to 1.15 without changing the coefficient of variation.

Moehle presented a design procedure in which shear and moment forces are first calculated. Then, the column is sized such that the shear force is resisted by $0.75v_cA_{sc}$. Finally, the reinforcement required to resist the applied moment is placed across a width of $c_2 + 2c_1$. Moehle stated the reinforcement ratio should be less than $0.5\rho_b$ to ensure the reinforcement around the column fully develops (1988).

In 1995, ACI 318 allowed for γ_f modifications based on Moehle's suggestions but did not increase the moment transfer width (ACI Committee 318, 1995). ACI 318-95 stated that γ_f could be increased up to 1.0 if the vertical load is limited to 40-percent of the vertical load capacity and the reinforcement ratio does not exceed $0.375\rho_b$. In ACI 318-08, the reinforcement ratio condition was replaced with a reinforcement tensile strain condition. ACI 318-08 stated that the reinforcement tensile strain within the moment transfer width had to be at least 0.010.

2.1.15 Interior connections under unbalanced moments by Hawkins, Bao, and Yamazaki

In 1989, Hawkins, Bao, and Yamazaki tested 36 interior slab-column connections subjected to both unbalanced moments and gravity loads. The specimens were grouped into seven different series to test the influence of various parameters on the connection strength and stiffness. These parameters included reinforcement ratio and concentration, slab depth, concrete strength and type, shear reinforcement, and column rectangularity. Within each series, specimens were tested

with M/V ratios of 5.1-inches and 22.7-inches and reinforcement ratios between 0.60-percent and 1.42-percent.

Hawkins et al. found that ACI 318-83 over-predicted the punching shear capacity of six specimens, all of which had reinforcement ratios not greater than 0.73-percent. One of these six specimens had an ultimate shear lower than the concrete limiting shear and a higher $\gamma_f M$ than the moment resistance of the slab section. This suggests that differently proportioned γ_f and γ_v parameters could predict ultimate shear and moment values equal to their respective limits. Another two of these six specimens exhibited wide beam flexural failures. Each of these failures occurred at the column face across the width of the slab. The remaining three of the six specimens failed due to pullout before their flexural strengths could develop.

For specimens with reinforcement ratios greater than 0.73-percent, ACI 318-83 predicted capacities that were increasingly conservative with increasing reinforcement ratio. Specimens with higher reinforcement ratios were less ductile and their punching failures were more sudden. Concentrating the reinforcement toward the column increased the stiffness but decreased the ultimate vertical load. When subjected to a M/V loading of 22.7-inches, specimen slabs would lift at one slab end and lower at the opposite slab end. When subjected to a M/V loading of 5.1-inches, all specimens deflected downwards along their slab edges.

2.1.16 Critical Shear Crack Theory

Through the use of a strut-and-tie model, Muttoni and Schwartz proposed that shear failure in slabs without shear reinforcement is caused by the propagation of a critical shear crack through the slab compression strut at the column (1991). Muttoni and Schwartz stated that the punching shear capacity could be increased by moving the critical shear crack away from the column. For example, Bollinger (1985) tested circular specimens with circular columns which were reinforced with radial flexural reinforcement around the edges of the slabs. When additional reinforcement was placed in the vicinity of the column, the ultimate vertical load decreased. The addition of this reinforcement produced cracks tangent to the column at the location of the reinforcement. Without this reinforcement, only cracks perpendicular to the column face were present in this location.

Muttoni and Schwartz stated that force transfer across cracks is dependent on the width and roughness of the crack surfaces. Muttoni and Schwartz presented crack width versus transverse displacement data from a test beam, which showed the crack width after which force transfer is no longer possible. Since the crack width is proportional to slab rotation, Muttoni and Schwartz developed a semi-empirical expression to relate the nominal shear strength to the product of slab rotation and depth:

$$\frac{V_R}{b_0 d^3 \sqrt{f_c}} = \frac{1}{1 + \left(\frac{\psi d}{4\ \text{mm}}\right)^2}. \qquad \text{(SI units: N, mm)} \quad (2.50)$$

Equation xx showed a significant decrease in punching shear capacity with increasing slab depth. This suggested that size-effect has a strong effect on the punching shear capacity. In 2003, Muttoni revised Equation 2.50 to include the influence of the maximum aggregate size on the shear capacity (through affecting the roughness of the critical shear crack):

$$\frac{V_R}{b_0 d^3 \sqrt{f_c'}} = \frac{3/4}{1 + 15\frac{\psi d}{d_{g0} + d_g}} \quad (2.51)$$

where d_{g0} is a reference size equal to 16 millimetres (mm) and d_g is the maximum aggregate size. This revision was based on research conducted by Vecchio and Collins (1986) and Walraven (1981).

In 2008, Muttoni presented a direct relationship for predicting slab rotations of axisymmetric isolated slabs in lieu of nonlinear numerical modelling. This load-rotation relationship was developed based on a quadrilinear moment-curvature relationship. Muttoni offered a simpler bilinear relationship by neglecting the concrete tensile stress and the effects of tension stiffening. Additionally, Muttoni developed a simplified design method for determining slab rotation:

$$\psi = 1.5\frac{r_s}{d}\frac{f_y}{E_s}\left(\frac{V}{V_{flex}}\right)^{3/2} \quad (2.52)$$

where r_s is the radius of contraflexure equal to $0.22L$ (based on linear-elastic calculations), and

$$V_{flex} = 2\pi m_R \frac{r_s}{r_q - r_c} \quad (2.53)$$

where r_q is the radius of the load introduction and r_c is the radius of a circular column. Muttoni stated that the strength reduction due to size effect is a function of slenderness rather than thickness as reflected by the radius of contraflexure, r_s.

Muttoni showed that the quadrilinear and simplified formulations accurately predicted vertical load and rotation capacities of 87 laboratory tests, except for connections with thick slabs and low reinforcement ratios. For these connections, the effects of the concrete tensile strength and tension stiffening needed to be considered through the use of the quadrilinear relationship.

For the same experimental data, ACI 318-05 predicted a constant punching shear capacity of $0.33\sqrt{f_c'}$ for all specimens with varying values of $\psi d/(d_{g0} + d_g)$. These predictions had a large coefficient of variation of 0.20. Muttoni showed that ACI 318 does not consider the effects of various parameters on the punching shear strength including reinforcement ratio, size effect, and slenderness. ACI 318 considers the effects of b_0/d by reducing the punching shear strength for columns with aspect ratios greater than 2:1. However, its punching shear strength predictions were increasingly conservative with decreasing b_0/d.

Relative to ACI 318-05, Eurocode 2 produced more accurate predictions with a coefficient of variation of 0.12. It considered the effects of reinforcement ratio and size effect on the punching shear strength. However, it did not consider the effects of slenderness. Eurocode 2 predicted the effects of b_0/d accurately by considering the critical section at a distance of $2d$ from the column instead of $0.5d$.

Muttoni's simplified design method considered all aforementioned effects on the punching shear strength in addition to the effects of the reinforcement yield stress; however, this effect is minimal. The simplified design method produced accurate predictions with a coefficient of variation of 0.09. This design method is currently being used in the Swiss design code (SIA, 2003) and Model Code (federation internationale du béton (fib), 2013).

In addition to two-way slabs without transverse reinforcement, the Critical Shear Crack Theory was extended to apply to two-way slabs with transverse reinforcement (Fernández Ruiz &

Muttoni, 2009), continuous slabs (Einpaul, Ruiz, & Muttoni, 2015), prestressed slabs (Clément, Pinho Ramos, Fernández Ruiz, & Muttoni, 2014), and concentrated loads in linearly supported slabs (Natário, Fernández Ruiz, & Muttoni, 2014) (Muttoni A., Fernández Ruiz M., 2018). In 2018, Drakatos, Muttoni, and Beyer presented a mechanical model to predict the moment-rotation relationship for connections subjected to combined gravity loads and lateral drifts (2018). This model was developed based on the Critical Shear Crack Theory for slab-column connections without transverse reinforcement (Drakatos et al., 2018).

2.1.17 Minimum reinforcement and size effect coefficient by Hawkins and Ospina

In 2017, Hawkins and Ospina proposed revisions to address two issues with ACI 318-14 punching shear design provisions. The first issue was that lightly-reinforced slab-column connections could undergo flexure-driven punching failure (rather than "pure" punching failure) as a result of flexural reinforcement yielding. In these flexure-driven failures, laboratory-tested specimens did not develop their full shear capacities. The second issue with ACI 318-14 was that it did not account for punching shear strength reductions with increasing slab depth (N. M. Hawkins & Ospina, 2017).

Hawkins and Ospina's solution to the first issue began by analysing test data for 48 interior slab-column sub-assemblages and 12 frames containing at least one interior slab-column connection. They showed that specimens with reinforcement ratios less than 1-percent commonly failed at shear capacities lower than predicted by ACI 318-14. Hawkins and Ospina stated that the punching shear resistance of a slab-column connection is the lesser of V_c and the flexural strength of the slab near the column, V_{ly}, based on the yield-line theory. This was also observed by Peiris and Ghali (2011). Hawkins and Ospina defined V_{ly} as:

$$V_{ly} = 8m = 8\rho f_y d^2 \,. \tag{2.54}$$

For connections subjected to concentric loading, Hawkins and Ospina showed that defining the punching shear resistance as the lesser of V_c and V_{ly} resulted in tested-to-calculated capacities close to unity.

Similarly, the tested-to-calculated strength of specimens subjected to gravity loads and unbalanced moments as per ACI 318-14 is

$$\frac{Test}{Calc} = \max\left(\frac{V_T}{V_o} + \frac{M_T}{M_o}, \frac{\gamma_f M_T}{M_R}\right). \tag{2.55}$$

Hawkins and Ospina showed that the ACI 318-14 tested-to-calculated specimen strength produced values less than unity for M/Vc ratios less than 2 (where c is the square column dimension). For specimens with M/Vc ratios less than 2, modifying Equation 2.55 such that

$$\frac{Test}{Calc} = \max\left(\frac{V_T}{V_o} + \frac{M_T}{M_o}, \frac{V_T}{V_{ly}} + \frac{M_T}{M_o}, \frac{\gamma_f M_T}{M_R}\right) \tag{2.56}$$

resulted in tested-to-calculated strengths closer to unity.

Equation 2.54 was implemented within Section 8.6.1.2 of ACI 318-19. In Section 8.6.1.2, $A_s/(b_{slab}d)$ was substituted in place of ρ, $\alpha_s/5$ was substituted in place of 8 (to scale the constant 8 for different column locations), and the equation was rearranged to solve for the minimum required area A_s.

On the topic of size effect, Hawkins and Ospina showed good agreement between tested and calculated shear strengths when V_c was reduced by a factor k_v for depths greater than 10-inches:

$$k_v = \frac{1.4}{\sqrt{1 + \frac{d}{10}}}. \tag{2.57}$$

Equation 2.57 with a constant $\sqrt{2}$ instead of 1.4 was implemented in Section 22.5.5.1.3 of ACI 318-19.

2.2 Review of punching shear provisions in national design codes

2.2.1 ACI 318-19

2.2.1.1 Critical sections

ACI 318-19 states that two-way shear strength must be analysed at critical sections at perimeters $d/2$ from: column faces and, if applicable, changes in slab thickness (Section 22.6.4.1). For slabs with shear reinforcement, two-way shear strength must also be checked at a critical section

$d/2$ from the outermost peripheral line of shear reinforcement (Section 22.6.4.2). The critical perimeter, b_o, for Section 22.6.4.1 and Section 22.6.4.2 is presented in Figure 2.6. The dimension b_1 defines the length of the critical perimeter parallel to the axis of the unbalanced moment. Similarly, the dimension b_2 defines the critical perimeter length orthogonal to the unbalanced moment axis. This figure applies to CSA A23.3-19 as the critical section definitions are the same for both CSA A23.3-19 and ACI 318-19.

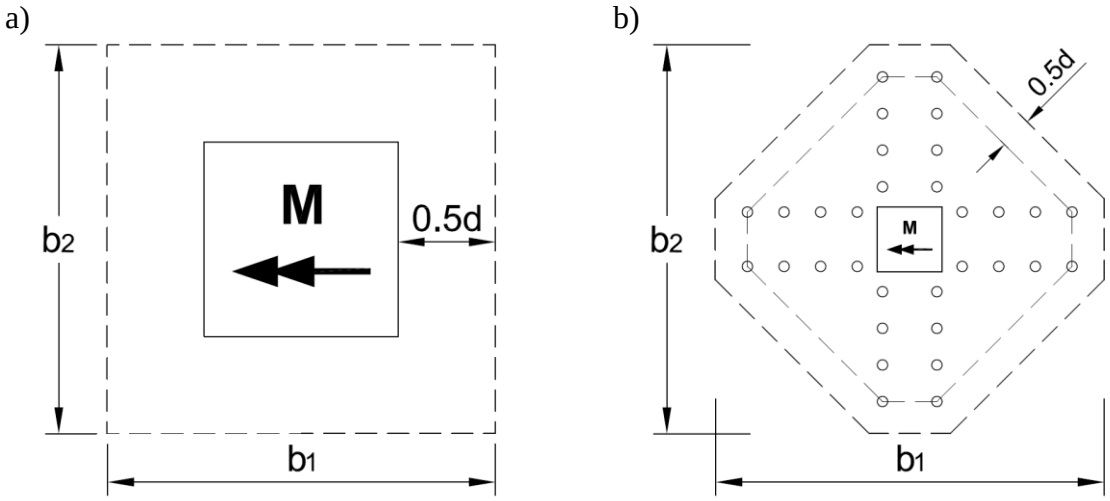

Figure 2.6: Critical sections located: a) $0.5d$ away from column, and b) $0.5d$ away from outermost shear reinforcement as per ACI 318-19 (ACI Committee 318, 2019)

2.2.1.2 Two-way shear strength

Section 22.6.5.2 governs the concrete two-way strength, v_c, for a slab without shear reinforcement

$$v_c = \min \begin{Bmatrix} 0.33 \\ 0.17\left(1 + \frac{2}{\beta}\right) \\ 0.083\left(2 + \frac{\alpha_s d}{b_o}\right) \end{Bmatrix} \lambda_s \lambda \sqrt{f_c'} \quad \text{(SI units: N, mm)} \quad (2.58)$$

where β is the ratio of the longer column edge length to the shorter column edge length; α_s is 40 for interior columns, 30 for edge columns, and 20 for corner columns; d is the effective slab depth (from the compression fiber to the centroid of flexural reinforcement); and λ is 1.0 for normal density concrete and ranges between 0.75 and 1.0 for lightweight concrete.

The size effect coefficient, λ_s, is given by:

$$\lambda_s = \sqrt{\frac{2}{1+\frac{d}{250}}}. \qquad \text{(SI units: N, mm)} \quad (2.59)$$

In the case of slabs with shear reinforcement, Section 22.6.6.1 outlines the appropriate values of two-way concrete strength to use depending on the critical section and type of shear reinforcement. Table 2.2 presents Section 22.6.6.1 as presented in the ACI code.

Table 2.2: Maximum v_c for two-way members with shear reinforcement (ACI Committee 318, 2019)

Type of shear reinforcement	**Maximum v_c at section $d/2$ from column**	**Maximum v_c at section $d/2$ from last row of shear reinforcement**
Stirrups	$0.17\lambda_s\lambda\sqrt{f_c'}$	$0.17\lambda_s\lambda\sqrt{f_c'}$
Headed shear stud reinforcement	$\min\left\{\begin{matrix}0.25\\0.17\left(1+\frac{2}{\beta}\right)\\0.083\left(2+\frac{\alpha_s d}{b_o}\right)\end{matrix}\right\}\lambda_s\lambda\sqrt{f_c'}$	$0.17\lambda_s\lambda\sqrt{f_c'}$

The two-way shear strength provided by shear reinforcement is provided by Section 22.6.7.2:

$$v_s = \frac{A_v f_{yt}}{b_o s} \quad (2.60)$$

where A_v is the area of shear reinforcement that lies on a perimeter peripheral to the column, f_{yt} is the yield strength of transverse reinforcement, and s is the spacing between adjacent rows of reinforcement.

The two-way shear strength contributions of the concrete and shear reinforcement may be summed, as per Section 22.6.1.3, to determine the nominal two-way strength of the slab:

$$v_n = v_c + v_s\,. \quad (2.61)$$

It is important to note that a strength reduction factor, ϕ, of 0.75 (Section 21.2.1) must be used as a safety factor to account for slab understrength due to variations in material strengths and

dimensions, to account for inaccuracies in equations, to reflect available ductility and required reliability, and to reflect the importance of the member (R21.1.1).
The nominal two-way strength capacity is reduced as per Section 14.5.1.1:

$$\phi v_n \geq v_u \,. \tag{2.62}$$

In determining the shear capacity of the shear-reinforced specimens, two more sections must be considered: Section 22.6.4.2 and Section 22.6.6.2.

Section R22.6.4.2 indicates to "check shear stress in concrete at a critical section located at a distance d/2 beyond the point where shear reinforcement is discontinued. Calculated shear stress at this section must not exceed the limits given in expressions (b) and (d) in Table 22.6.6.1". The code requires this check because the shear reinforcement will not contribute to the nominal resistance at a perimeter d/2 from the perimeter containing the last row of shear reinforcement. This section provides the lowest v_c and will produce the lowest punching shear force.

Section 22.6.6.3 provides limiting factors on v_u at sections d/2 from the column face as shown in Table 2.3.

Table 2.3: Maximum v_u for two-way members with shear reinforcement (ACI Committee 318, 2019)

Type of shear reinforcement	**Maximum v_u at critical section $d/2$ from column face**
Stirrups	$\phi 0.5\sqrt{f_c'}$
Headed shear stud reinforcement	$\phi 0.66\sqrt{f_c'}$

Although the specimens analysed are loaded concentrically without unbalanced moments, Section R8.4.4.2.3 provides a means of determining the factored shear stress, v_u, as:

$$v_u = v_{uv} + \frac{\gamma_v M_{sc} c}{J_c} \tag{2.63}$$

where v_{uv} is the stress resulting from the controlling load combination without moment transfer, γ_v is a coefficient representing the portion of unbalanced moment distributed to shear, M_{sc} is the unbalanced moment, c is the eccentricity, and J_c is analogous to the polar moment of inertia. If unbalanced moments exist in two orthogonal axes, another unbalanced moment term may be added and each term would correspond to one of the axes.

The parameter γ_v is given by Section 8.4.4.2.2

$$\gamma_v = 1 - \gamma_f \tag{2.64}$$

and γ_f is given by Section 8.4.2.3.2

$$\gamma_f = \frac{1}{1 + \left(\frac{2}{3}\right)\sqrt{\frac{b_1}{b_2}}} \, . \tag{2.65}$$

Therefore,

$$\gamma_v = 1 - \frac{1}{1 + \left(\frac{2}{3}\right)\sqrt{\frac{b_1}{b_2}}} \tag{2.66}$$

where b_1 is the critical perimeter dimension parallel to the axis of the applied moment and b_2 is the critical perimeter dimension orthogonal to the axis of the applied moment.

Section 8.4.2.2.4 of ACI 318-19 states that the value of γ_f can be increased (and, therefore, the value of γ_v to be decreased) if criteria shown in Table 2.4 are met. The maximum allowable γ_f depends on the connection location and span direction and can only be increased if: the factored nominal shear stress, v_{uv}, does not exceed a percentage of the two-way shear strength v_c, and the net tensile strain within the effective slab width, ε_t, exceeds the reinforcement yield strain, ε_{ty}, plus a given constant.

For a square column, the maximum allowable γ_f is 1.0 for edge connections analysed in the span parallel to the free edge and corner connections in either span. For edge connections analysed perpendicular to the free edge and interior connections in either span, the maximum allowable γ_f is 0.75. Recall that the unmodified γ_f for a square column is 0.6.

The commentary provided on this code provision is limited. Outside of cases where lateral drifts are imposed, the net tensile strain, ε_t, could be determined by performing a slab sectional analysis. However, the unbalanced moment resisted by slab flexural stresses should be known to perform this analysis. Also, the provision allows γ_f to be increased up to a maximum value but does not suggest a method for determining intermediate values of γ_f.

Table 2.4: Maximum modified values of γ_f for nonprestressed two-way slabs (reproduced with permission, ACI 318-19, Section 8.4.2.2.4)

Column location	Span direction	v_{uv}	ε_t (within b_{slab})	Max modified γ_f
Corner column	Either direction	$\leq 0.5\phi v_c$	$\geq \varepsilon_{ty} + 0.003$	1.0
Edge column	Perpendicular to edge	$\leq 0.75\phi v_c$	$\geq \varepsilon_{ty} + 0.003$	1.0
	Parallel to edge	$\leq 0.4\phi v_c$	$\geq \varepsilon_{ty} + 0.008$	$\frac{1.25}{1+\left(\frac{2}{3}\right)\sqrt{\frac{b_1}{b_2}}} \leq 1.0$
Interior column	Either direction	$\leq 0.4\phi v_c$	$\geq \varepsilon_{ty} + 0.008$	$\frac{1.25}{1+\left(\frac{2}{3}\right)\sqrt{\frac{b_1}{b_2}}} \leq 1.0$

The polar moment of inertia, J_c, is given by

$$J_c = \frac{d(c_1+d)^3}{6} + \frac{(c_1+d)d^3}{6} + \frac{d(c_2+d)(c_1+d)^2}{2} \tag{2.67}$$

where c_1 is the column face length in the direction of analysis and c_2 is the column face length in the plane perpendicular to analysis.

New to the 2019 edition of ACI 318, Section 8.6.1.2 states that if

$$v_{uv} > \phi 0.17\lambda_s\lambda\sqrt{f_c'} \tag{2.68}$$

then, the minimum area of reinforcement over the width b_{slab} must be greater than $A_{s,min}$:

$$A_{s,min} = \frac{5v_{uv}b_{slab}b_o}{\phi\alpha_s f_y} \quad . \tag{2.69}$$

According to the ACI 318-19 commentary, Section 8.6.1.2 was introduced based on research by Peiris and Ghali (Peiris & Ghali, 2011), Hawkins and Ospina (N. M. Hawkins & Ospina, 2017), Bayrak and Jirsa (2009), Muttoni (2008), and Dam and Wight (2017).

2.2.2 CSA A23.3-19

2.2.2.1 Critical sections

Section 13.3.3.1 of CSA A23.3-19 defines the critical two-way shear section at a distance d/2 from the perimeter of a concentrated load or reaction area (CSA Group, 2019). This is similar to the definition provided by ACI 318-19.

2.2.2.2 Two-way shear strength

Section 13.3.4.1 governs the concrete two-way strength, v_c, for a slab without shear reinforcement,

$$v_c = \min \begin{Bmatrix} 0.38 \\ 0.19\left(1 + \frac{2}{\beta}\right) \\ 0.19 + \frac{\alpha_s d}{b_o} \end{Bmatrix} \lambda \phi_c \sqrt{f_c'} \qquad \text{(SI units: N, mm) (2.70)}$$

where β is the ratio of the longer column edge length to the shorter column edge length; α_s is 4 for interior columns, 3 for edge columns, and 2 for corner columns; d is the depth from the compression fiber to the centroid of flexural reinforcement; λ is 1.0 for normal density concrete; and ϕ_c is the resistance factor for concrete, which is taken as 0.65. Section 13.3.1.2 states that the effective depth, d, when used for two-way shear calculations, is to be taken as the average effective depth between the two directions of reinforcement.

In the case of slabs with headed shear reinforcement, Section 13.3.8.3 provides an equation for two-way concrete strength:

$$v_c = 0.28 \lambda \phi_c \sqrt{f_c'} \qquad \text{(SI units: N, mm) (2.71)}$$

The two-way shear strength provided by shear reinforcement is provided by Section 13.3.8.3:

$$v_s = \frac{\phi_s A_{vs} f_{yv}}{b_o s} \qquad (2.72)$$

where ϕ_s is the resistance factor of steel, A_{vs} is the area of shear reinforcement that lies on a perimeter peripheral to the column, f_{yv} is the yield strength of shear reinforcement, and s is the spacing between adjacent rows of reinforcement.

The two-way shear strength contributions of the concrete and shear reinforcement may be summed, as per Section 11.3.3, to determine the nominal two-way strength of the slab:

$$v_r = v_c + v_s \, . \tag{2.73}$$

Unlike the ACI code, there is no additional section for the reduction of the shear resistance as resistance factors for concrete and steel were already considered in the previous equations.
In determining the shear capacity of the shear-reinforced specimens, three more sections must be considered: Section 13.3.7.4, Section 13.3.8.2 and Section 13.3.8.6.

Section 13.3.7.4 specifies that shear resistance must be placed where the factored shear is not greater than $0.19\lambda\phi_c\sqrt{f_c'}$ but at least 2d from the column face. Similar to ACI, CSA implemented this check to ensure that at a distance of d/2 away from the shear reinforcement, where shear reinforcement is inactive, the concrete alone can sustain the applied loads. The CSA provisions differ from ACI 318 only by using 0.19 instead of 0.17.

Section 13.3.8.2 limits the factored shear stress, v_f, to

$$v_f = 0.75\lambda\phi_c\sqrt{f_c'} \, . \qquad \text{(SI units: N, mm)} \tag{2.74}$$

ACI has a near-identical limit of $\phi 0.66\sqrt{f_c'}$ (as previously presented) when appropriate reduction factors are considered.

Section 13.3.8.6 is not a typical analysis check as it provides values for spacing using factored loads. In order to have a spacing of 0.75d between rows of shear bolts, the factored shear stress, d/2 from the column face, must be less than or equal to:

$$v_f = 0.56\lambda\phi_c\sqrt{f_c'} \, . \qquad \text{(SI units: N, mm)} \tag{2.75}$$

Section R22.6.4.2 indicates to “check shear stress in concrete at a critical section located at a distance d/2 beyond the point where shear reinforcement is discontinued. Calculated shear stress at this section must not exceed the limits given in expressions (b) and (d) in Table 22.6.6.1”. The code requires this check because the shear reinforcement will not contribute to the nominal resistance at a perimeter d/2 from the perimeter containing the last row of shear reinforcement. This provision provides the lowest v_c and will produce the lowest punching shear force.

Although the specimens analysed are loaded concentrically without unbalanced moments, Section 13.3.5.5 provides a means of determining the factored shear stress, v_f, as:

$$v_f = \frac{V_f}{b_o d} + \left(\frac{\gamma_v M_f e}{J}\right)_x + \left(\frac{\gamma_v M_f e}{J}\right)_y \tag{2.76}$$

where V_f is the force resulting from vertical gravity loads, γ_v is a coefficient representing the portion of unbalanced moment distributed to shear, M_f is the unbalanced moment, e is the eccentricity, and J is analogous to the polar moment of inertia.

The parameter γ_f is given in Section 13.3.5.3:

$$\gamma_f = \frac{1}{1 + \left(\frac{2}{3}\right)\sqrt{\frac{b_1}{b_2}}} \quad . \tag{2.77}$$

where b_1 is the critical perimeter dimension parallel to the axis of the applied moment and b_2 is the critical perimeter dimension orthogonal to the axis of the applied moment.

2.2.3 Eurocode 2 (2004)

2.2.3.1 Critical sections

Similar to ACI 318-19 and CSA A23.3-19, there are two critical shear sections that need to be considered. As per Section 6.4.2(1), a critical section at a distance of 2d from the column faces is considered with rounded corners. Section 6.4.5(4) states to consider another critical section of distance kd (k varies between countries but a value of 1.5 is recommended) from the peripheral perimeter that intersects the outermost row of shear reinforcement. Both critical perimeters have rounded corners versus the right-angle corners of ACI and CSA. The critical perimeters defined by Section 6.4.2(1) and Section 6.4.5(4) are presented in Figure 2.7. Unlike ACI 318-19 and CSA A23.3-19, Eurocode 2 limits the critical perimeter between adjacent transverse reinforcing bars to $2d$.

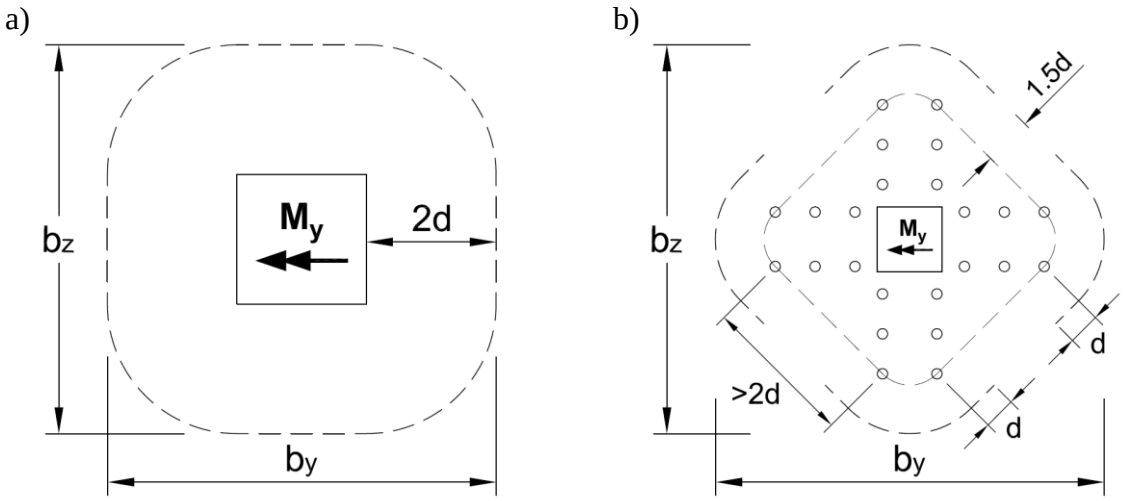

Figure 2.7: Critical sections located: a) 2d away from column, and b) 1.5d away from outermost shear reinforcement as per Eurocode 2 (British Standards Institution, 2004)

2.2.3.2 Two-Way Shear Strength

Section 6.4.4(1) governs the concrete two-way strength, v_c, for a slab without shear reinforcement (note that SI units are used within all equations presented in this section),

$$v_{Rd,c} = C_{Rd,c}k(100\rho_l f_{ck})^{\frac{1}{3}} \geq v_{min} \tag{2.78}$$

where

$$C_{Rd,c} = \frac{0.18}{\gamma_c} = \frac{0.18}{1.5} = 0.12 \tag{2.79}$$

and

$$k = 1 + \sqrt{\frac{200}{d}} \leq 2.0 \tag{2.80}$$

and

$$\rho_l = \sqrt{\rho_y \rho_z} \leq 0.02 \tag{2.81}$$

and

$$v_{min} = 0.035k^{\frac{3}{2}}f_{ck}^{\frac{1}{2}} \tag{2.82}$$

and f_{ck} is the concrete cylinder compression strength (MPa), ρ_y is the flexural reinforcement ratio in the y-direction, and ρ_z is the flexural reinforcement in the z-direction.

The punching shear resistance of a slab with shear reinforcement is given by Section 6.4.5(1):

$$v_{Rd,cs} = 0.75v_{Rd,c} + 1.5\left(\frac{d}{s_r}\right)A_{sw}f_{ywd,ef}\left(\frac{1}{u_1 d}\right)\sin\alpha \tag{2.83}$$

where s_r is the radial spacing between rows of shear reinforcement; A_{sw} is the area of shear reinforcement in a perimeter peripheral to the column; $f_{ywd,ef}$ is given by

$$f_{ywd,ef} = 250 + 0.25d \leq f_{ywd} \tag{2.84}$$

where f_{ywd} is the yield stress of the shear reinforcement; u_1 is the perimeter of the critical section; and α is the angle between the flexural reinforcement and the shear reinforcement.

The factored shear stress is given by Section 6.4.5(3):

$$v_{Ed} = \frac{\beta V_{Ed}}{u_o d} \leq v_{Rd,max} \tag{2.85}$$

where

$$\beta = 1 + 1.8\sqrt{\left(\frac{e_y}{b_z}\right)^2 + \left(\frac{e_z}{b_y}\right)^2} \tag{2.86}$$

and u_o is the length of column periphery, e_y and e_z are M_{Ed}/V_{Ed} along the y- and z- axes, and b_y and b_z are the widths of the critical section in the y- and z- axis, respectively. The β coefficient accounts for any shear contributions attributed to unbalanced moments.

Similar to ACI and CSA, factored shear stress at a distance of 1.5d from the peripheral perimeter intersecting the shear reinforcement must be less than the shear capacity contributions of concrete alone:

$$v_{Rd,c} = \frac{\beta V_{Ed}}{u_{out,ef} d}. \quad (2.87)$$

The maximum shear resistance, $v_{Rd,max}$, as per Section 6.2.2(6) is:

$$v_{Rd,max} = 0.5 v f_{cd} \quad (2.88)$$

where

$$v = 0.6\left(1 - \frac{f_{ck}}{250}\right) \quad (2.89)$$

and

$$f_{cd} = \frac{\alpha_{cc} f_{ck}}{\gamma_c}. \quad (2.90)$$

2.2.4 Model Code 2010

2.2.4.1 Critical sections

Model Code 2010 considers that punching shear is resisted by perimeter b_o and depth d_v. The perimeter b_o is the shear-resisting control perimeter, which is determined based on geometry and loading, and d_v is the shear-resisting effective depth, which is the distance from the centroid of the tension reinforcement mats to the supported area.

To determine the shear-resisting control perimeter, b_o, the basic control perimeter, b_1, is first determined then reduced based on geometry and loading. Similar to other design codes, the punching shear capacity is to be checked at two sections: a distance of $0.5d_v$ from the column and, if shear reinforcement is present, a distance of $0.5d_v$ from the outer perimeter of shear reinforcement. The basic control perimeter, b_1, is shown for these sections in Figure 2.8. Model Code 2010 limits the straight portions of the basic control perimeters to $3d_v$. This is relevant to connections with large column side lengths or connections with shear reinforcement.

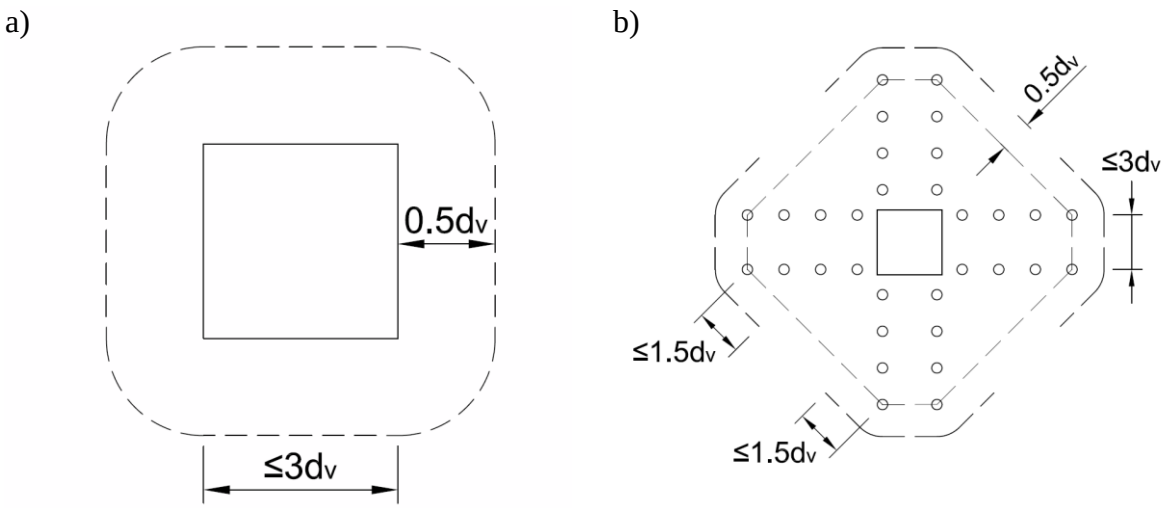

Figure 2.8: Critical sections located: a) $0.5d_v$ away from column, and b) $0.5d_v$ away from outermost shear reinforcement as per Model Code 2010 (federation internationale du béton (fib), 2013)

If gravity loads greater than $0.2V_{Ed}$ are present closer than $3d_v$ from the edge of the column, b_o is calculated as

$$b_o = \frac{V_{Ed}}{v_{perp,d,max}} \tag{2.91}$$

where V_{Ed} is the resultant shear force and $v_{perp,d,max}$ is the maximum shear force per unit length perpendicular to the basic control perimeter.

The basic control perimeter, b_1, is reduced to $b_{1,red}$ by considering non-uniform distributions of shear forces caused by geometrical slab discontinuities such as cast-in pipes, pipe bundles, slab inserts, or openings are present and are within a distance of $5d_v$ from the column.

Once $b_{1,red}$ is determined, it is multiplied by the coefficient of eccentricity k_e to determine the shear-resisting control perimeter b_o:

$$b_o = k_e b_{1,red} \, . \tag{2.92}$$

When adjacent slabs differ by no more than 25-percent in length, k_e may be approximated as 0.90 for inner slabs, 0.70 for edge slabs, 0.65 for corner slabs, and 0.75 for corners of walls.

The coefficient of eccentricity, k_e, may be more accurately calculated as

$$k_e = \frac{1}{1 + e_u/b_u} \tag{2.93}$$

where e_u is the eccentricity of the resultant of shear forces with respect to the centroid of the basic control perimeter, and b_u is the diameter of a circular column that produces the same area within the basic control perimeter, b_o, as the designed column shape.

The eccentricity, e_u, is determined by

$$e_u = \sqrt{(e_{ux})^2 + \left(e_{uy}\right)^2} = \sqrt{\left(M_{Ed,x}/V_{Ed}\right)^2 + \left(M_{Ed,y}/V_{Ed}\right)^2} \tag{2.94}$$

where e_{ux} and e_{uy} are the eccentricities in the x and y directions, respectively; and $M_{Ed,x}$ and $M_{Ed,y}$ are the moments applied in the x and y directional spans, respectively.

2.2.4.2 Two-way shear strength

The punching shear resistance is calculated as

$$V_{Rd} = V_{Rd,c} + V_{Rd,s} \leq V_{Ed} \tag{2.95}$$

where $V_{Rd,c}$ is the design shear resistance of concrete and $V_{Rd,s}$ is the design shear resistance of shear reinforcement. Note that SI units are used within all equations presented in this section.

The design shear resistance of concrete is

$$V_{Rd,c} = k_\psi \frac{\sqrt{f_{ck}}}{\gamma_c} b_o d_v \tag{2.96}$$

where k_ψ is the parameter that considers rotations of the slab, and f_{ck} is the characteristic value of compression strength of concrete determined from testing.

The parameter k_ψ is determined as

$$k_\psi = \frac{1}{1.5 + 0.9k_{dg}\psi d} \leq 0.6 \tag{2.97}$$

where k_{dg} is a parameter dependent on aggregate size, ψ is the slab rotation around the supported area, and d is the mean value (in mm) of the flexural effective depth for the x and y direction.

If $d_g$is less than 16 mm, d_g is equal to 1. If d_g is not less than 16 mm, $k_{dg}$is taken as

$$k_{dg} = \frac{32}{16 + d_g} \geq 0.75 \tag{2.98}$$

where d_g is in mm. For high strength and lightweight concrete, d_g is assumed 0 due to the possibility of aggregate particles breaking, which would reduce aggregate interlock.

The design shear resistance of shear reinforcement is

$$V_{Rd,s} = \Sigma A_{sw} k_e \sigma_{swd} \tag{2.99}$$

where $\Sigma A_{sw}$is the sum of the cross-sectional area of all shear reinforcement within the zone bounded by $0.35d_v$ and d_v from the edge of the supported area, and

$$\sigma_{swd} = \frac{E_s \psi}{6}\left(\frac{f_{bd}}{f_{ywd}}\frac{d}{\phi_w}\right) \leq f_{ywd} \tag{2.100}$$

and f_{bd} is assumed 3 MPa for corrugated bars or by Section 6.1.3.2 and f_{ywd} denotes the design yield strength of shear reinforcement. Section 6.1.3.2 states that

$$f_{bd,o} = \frac{n_1 n_2 n_3 n_4 \left(\frac{f_{ck}}{25}\right)^{0.5}}{\gamma_c} \tag{2.101}$$

where $n_1$is 1.75 for ribbed bars, 1.4 for fusion epoxy coated ribbed bars; $n_2$is based on the casting position of the shear reinforcement bars during concreting, which is 1.0 when all bars are 45 to 90 degrees to horizontal or all bars less than 45 degrees to horizontal are greater than 250 millimetres from the bottom face and 300 millimeters from the top face, $n_2$is 0.7 for all other cases where ribbed bars are used; n_3 is dependent on the bar diameter and is assumed 1.0 for diameters not less than 25 millimeters and $(25/\phi)^{0.3}$ for diameters less than 25 millimeters; n_4 is 1.2 for f_{yk}= 400 MPa, 1.0 for f_{yk} = 500 MPa, 0.85 for f_{yk}= 600 MPa, 0.75 for f_{yk}= 700 MPa, 0.65 for f_{yk}= 800 MPa, and may be interpolated for intermediate values.

f_{bd} may use the value determined for $f_{bd,o}$ or modified based on confinement from transverse pressure as outlined by Section 6.1.3.3.

The required minimum amount of punching shear reinforcement is such that

$$\Sigma A_{sw} k_e f_{ywd} \geq 0.5 V_{Ed} \tag{2.102}$$

If inclined shear reinforcement is used

$$V_{Rd,s} = \Sigma A_{sw} k_e \sigma_{swd} \sin\alpha \tag{2.103}$$

where

$$\sigma_{swd} = \frac{E_s \psi}{6}(\sin\alpha + \cos\alpha)\left(\sin\alpha + \frac{f_{bd}}{f_{ywd}}\frac{d}{\phi_w}\right) \leq f_{ywd} \tag{2.104}$$

and α is the angle between the shear reinforcement and horizontal.

The maximum punching shear resistance is

$$V_{Rd,max} = k_{sys} k_\psi \frac{\sqrt{f_{ck}}}{\gamma_c} b_o d_v \leq \frac{\sqrt{f_{ck}}}{\gamma_c} b_o d_v \tag{2.105}$$

where k_{sys}accounts for "performance of punching shear reinforcement systems to control shear cracking and to suitably confine compression struts at the soffit of the slab", and γ_c is the partial safety factor for concrete material properties.

The parameter k_{sys} is assumed 2.4 for stirrups with sufficient development length at the compression face and bent (no anchorages or development length) at the tension face; or k_{sys} is assumed 2.8 for studs (diameter of heads larger or equal than three times the bar diameter).

The slab rotation ψ is determined by one of four levels of approximation: Level I, Level II, Level III or Level IV.

2.2.4.2.1 Level I approximation

Level I is used for regular flat slabs designed according to an elastic analysis without significant redistribution of internal forces.

The slab rotation around the column is determined as

$$\psi = 1.5 \frac{r_s}{d} \frac{f_{yd}}{E_s} \tag{2.106}$$

where r_s is the position where radial bending moment is zero with respect to the support axis, f_{yd} is the design yield strength of reinforcing steel in tension, E_s is the modulus of elasticity of reinforcing steel. The variable r_s can be approximated as the larger of $0.22L_x$ or $0.22L_y$ for the x and y directions, respectively, for flat slabs where the ratio of spans (L_x/L_y) is between 0.5 and 2.0.

2.2.4.2.2 Level II approximation

Level II is used when significant bending moment redistribution is considered in design.

The slab rotation around the column is determined as

$$\psi = 1.5 \frac{r_s}{d} \frac{f_{yd}}{E_s} \left(\frac{m_{Ed}}{m_{Rd}}\right)^{1.5} \tag{2.107}$$

where m_{Ed} is the average moment per unit length for calculation of the flexural reinforcement in the support strip, and m_{Rd} is the design average flexural strength per unit length in the support strip.

For inner columns,

$$m_{Ed} = V_{Ed}\left(\frac{1}{8} + \frac{|e_{u,i}|}{2b_s}\right). \tag{2.108}$$

For edge columns when considering the tension reinforcement is parallel to the slab edge,

$$m_{Ed} = V_{Ed}\left(\frac{1}{8} + \frac{|e_{u,i}|}{2b_s}\right) \geq \frac{V_{Ed}}{4}. \tag{2.109}$$

For edge columns when considering the tension reinforcement is perpendicular to the slab edge,

$$m_{Ed} = V_{Ed}\left(\frac{1}{8} + \frac{|e_{u,i}|}{b_s}\right). \tag{2.110}$$

For corner columns,

$$m_{Ed} = V_{Ed}\left(\frac{1}{8} + \frac{|e_{u,i}|}{b_s}\right) \geq \frac{V_{Ed}}{2}. \tag{2.111}$$

In these equations, $e_{u,i}$ refers to the eccentricity of the resultant shear forces with respect to the centroid of the basic control perimeter (i is equal to x and y for the x and y directions, respectively), and

$$b_s = 1.5\sqrt{r_{s,x} \cdot r_{s,y}} \leq L_{min} \tag{2.112}$$

where $r_{s,x}$ and $r_{s,y}$ are calculated as per Level I, and L_{min} is the smaller of the spans.

2.2.4.2.3 Level III approximation

Level III is recommended for irregular slabs or for flat slabs where l_x/l_y is not between 0.5 and 2.0.

The slab rotation around the column is determined as

$$\psi = 1.2\frac{r_s}{d}\frac{f_{yd}}{E_s}\left(\frac{m_{Ed}}{m_{Rd}}\right)^{1.5} \tag{2.113}$$

where r_s and m_{Ed} are calculated using linear elastic modelling. m_{Ed} is the average value of the moment for design of the flexural reinforcement over the width of the support strip b_s.

2.2.4.2.4 Level IV approximation

Level IV uses analytical or numerical methods to determine slab rotation. These methods should consider cracking, tension-stiffening effects, yielding of reinforcement, and other non-linear effects relevant to punching shear capacity prediction.

2.2.5 CSCT code-like formulation (2008)

The code-like formulation of the critical shear crack theory (Muttoni, 2008) is presented alongside the various national design code provisions as it does not require analyses or laboratory test results when determining a connection's punching shear capacity. The original critical shear crack theory (CSCT) was presented by Muttoni and Schwartz in 1991 as a model for determining the punching shear capacity of slab-column connections without transverse reinforcement. Over the years, it was extended to describe one-way slab failures (Muttoni, 2003), punching shear failures of slab-column connections with transverse reinforcement (Fernández Ruiz & Muttoni, 2009), and punching shear failures of slab column connections without transverse reinforcement subjected to unbalanced moments (Drakatos et al., 2018). The CSCT model states that under an applied vertical load, a critical shear crack develops around the column. This crack propagates on an incline through the slab and the slabs compression strut. As this compression strut is responsible for transferring shear between the column and the slab, the formation of the crack decreases the slabs shear carrying capacity.

The code-like formulation of the CSCT presents the load-rotation relationship as

$$\psi = 0.33 \frac{L}{d} \frac{f_y}{E_s} \left(\frac{V_d}{8 m_{Rd}} \right)^{\frac{3}{2}} \tag{2.114}$$

where L is the slab span; d is the depth from the slab to the centroid of the flexural reinforcement; f_y and E_s are the yield stress and modulus of elasticity of the flexural reinforcement, respectively; V_d is the factored shear force; and m_{Rd} is the flexural capacity of the slab in the column region. The coefficient in front of m_{Rd} is 8 for interior, 4 for edge, and 2 for corner slab-column connections.

The column-region flexural capacity, m_{Rd}, can be calculated using

$$m_{Rd} = \rho d^2 f_{yd} \left(1 - 0.5 \rho \, f_{yd} / f_{cd}\right) \quad \text{(SI units: N, mm)} \tag{2.115}$$

where ρ is the average reinforcement ratio between the two layers of longitudinal reinforcement, f_{yd} is the reinforcement design yield stress, and f_{cd} is the design concrete compressive stress (Muttoni, Ruiz, Bentz, Foster, & Sigrist, 2013).

The punching shear capacity, V_R, is determined using the equation

$$V_R = \frac{3/4}{1 + 15 \frac{\psi d}{d_{g0} + d_g}} b_0 d \sqrt{f_c'} \quad \text{(SI units: N, mm)} \tag{2.116}$$

where b_0 is the critical perimeter at a distance of d/2 from the column, d_{g0} is the reference aggregate size of 16 mm, and d_g is the aggregate size. A modified version of this equation was used in the Swiss Code for structural concrete SIA 262 (2003). The equation was modified to obtain a distribution fractile of 5-percent to account for geometry and load irregularities. The modified equation presents the design punching shear capacity, V_{Rd}, as

$$V_{Rd} = \frac{2}{3\gamma_c} \frac{1}{1 + 20 \frac{\psi d}{d_{g0} + d_g}} b_0 d \sqrt{f_c'} \, . \quad \text{(SI units: N, mm)} \tag{2.117}$$

In 2018, Drakatos, Muttoni, and Beyer extended the CSCT mechanical model to account for the effects of unbalanced moments. This mechanical model requires that rotations be determined from finite element analyses. At this time, there is no code-like formulation that considers unbalanced moments without completing finite element analyses.

Chapter 3: Constitutive modelling of materials using Abaqus

The constitutive modelling of materials using Abaqus is explained in Section 3.1 and Section 3.2 for the concrete and steel reinforcement, respectively.

3.1 Concrete

Section 3.1.1 explains the Hognestad parabola used to describe the uniaxial compression behaviour of the concrete. Section 3.1.2 describes the fracture energy model and the bilinear stress-strain data assumed to describe the uniaxial tension behaviour of the concrete. Section 3.1.3 presents the Concrete Damaged Plasticity material model used to describe the plastic behaviour of the concrete.

3.1.1 Uniaxial compressive behaviour

The uniaxial compressive behaviour of concrete was modelled using the Hognestad parabola (Hognestad, 1951). The uniaxial compressive stress-strain data modelled by the Hognestad parabola is shown in Figure 3.1. The stress-strain data is assumed linear-elastic until 40-percent of the compressive strength, f_c', which is denoted by σ_{co}. The modulus of elasticity for the linear-elastic stress-strain data, E_c, is given by

$$E_c = 5000\sqrt{f_c'} \quad . \qquad \text{(SI units: N, mm)} \quad (3.1)$$

Past the linear-elastic region, the stresses given by the Hognestad parabola are calculated as a function of strain by

$$\sigma_c = f_c' \left[2\left(\frac{\varepsilon_c}{\varepsilon_o}\right) - \left(\frac{\varepsilon_c}{\varepsilon_o}\right)^2 \right] \quad (3.2)$$

where ε_o is the strain at peak stress given by

$$\varepsilon_o = 2\frac{f_c'}{E_t} \quad . \quad (3.3)$$

The modulus of elasticity tangent to the parabola at the origin, E_t, is given by

$$E_t = 5500\sqrt{f_c'} \quad . \qquad \text{(SI units: N, mm)} \quad (3.4)$$

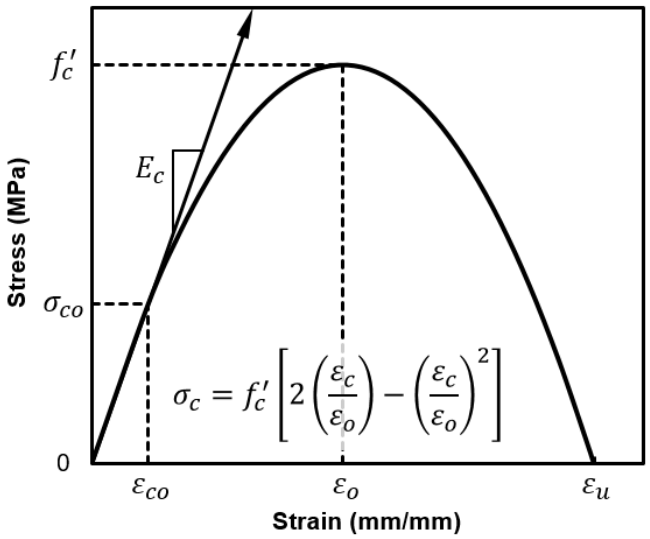

Figure 3.1: Hognestad parabola for defining concrete compression uniaxial stress-strain data

3.1.2 Uniaxial tensile behaviour

The uniaxial tensile behaviour of concrete was assumed linear-elastic until the concrete reaches its tensile strength, f_t', as shown in Figure 3.2. The linear-elastic modulus of elasticity E_c is the same as that calculated for linear-elastic concrete in compression. The strain-softening stress-strain data was assumed to be bilinear as proposed by Petersson (1981). The area under the strain-softening stress-strain data was assumed to be equal to the concrete's fracture energy, G_f. The fracture energy model as proposed by Hillerborg, Modeer, and Petersson (1976) is the energy required for a unit area of concrete to fracture in tension.

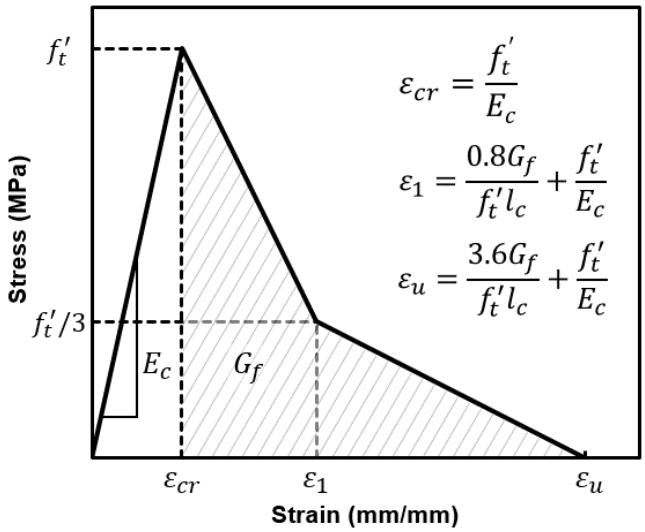

Figure 3.2: Typical concrete tensile uniaxial stress-strain data

Two fracture energy models were explored in analyses that were provided in Model Code 1990 and Model Code 2010. Model Code 1990 predicts the fracture energy based on the equation

$$G_f = G_{F_o}\left(\frac{f_{cm}}{f_{cmo}}\right)^{0.7} \qquad \text{(SI units: N, mm) (3.5)}$$

where G_{F_o} is the base value of the fracture energy which is dependent on the maximum aggregate size d_{max}, f_{cm} is the mean value of concrete compressive strength, and f_{cm} is equal to 10 MPa. The base value of the fracture energy, G_{F_o}, is determined using Table 3.1.

Table 3.1: Base values of fracture energy G_{F_o} as per Model Code 1990

d_{max} (mm)	G_{F_o} (Nmm/mm^2)
8	0.025
16	0.030
32	0.058

The mean value of concrete compressive strength, f_{cm}, is expressed as a function of the characteristic compressive strength, f_{ck}:

$$f_{cm} = f_{ck} + \Delta f \qquad (3.6)$$

where Δf is equal to 8 MPa. The characteristic compressive strength, f_{ck}, was calculated using the relationship proposed by Reineck, Kuchma, Kim, and Marx (2003):

$$f_{ck} = f_c' - 1.6 \text{ MPa}\,. \qquad \text{(SI units: N, mm) (3.7)}$$

Model Code 2010 predicts the fracture energy using the expression

$$G_f = 73(f_{cm})^{0.18}\,. \qquad \text{(SI units: N, mm) (3.8)}$$

3.1.3 Concrete Damaged Plasticity

The Concrete Damaged Plasticity model from Abaqus was used to model the concrete's plastic behaviour. This model assumes a non-associated potential plastic flow. The Concrete Damaged Plasticity model uses the yield function proposed by Lubliner, Oliver, and Oñate (1989) with modifications by Lee and Fenves (1998). The modifications account for different evolutions of strength under tension compared to compression through hardening variables $\tilde{\varepsilon}_t^{pl}$ and $\tilde{\varepsilon}_c^{pl}$, which

are the equivalent plastic tensile and compression strains, respectively (Dassault Systèmes, 2012).

The yield function is expressed as

$$F = \frac{1}{1-\alpha}\left(\bar{q} - 3\alpha\bar{p} + \beta\left(\widetilde{\varepsilon^{pl}}\right)\langle\hat{\bar{\sigma}}_{max}\rangle - \gamma\langle-\hat{\bar{\sigma}}_{max}\rangle\right) - \bar{\sigma}_c\left(\tilde{\varepsilon}_c^{pl}\right) = 0 \tag{3.9}$$

where

$$\alpha = \frac{(\sigma_{b0}/\sigma_{c0}) - 1}{2(\sigma_{b0}/\sigma_{c0}) - 1}; 0 \le \alpha \le 0.5\,, \tag{3.10}$$

$$\beta = \frac{\bar{\sigma}_c\left(\tilde{\varepsilon}_c^{pl}\right)}{\bar{\sigma}_t\left(\tilde{\varepsilon}_t^{pl}\right)}(1-\alpha) - (1+\alpha)\,, \tag{3.11}$$

$$\gamma = \frac{3(1-K_c)}{2K_c - 1}. \tag{3.12}$$

In these expressions: $\hat{\bar{\sigma}}_{max}$ is the maximum principal effective stress; σ_{b0}/σ_{c0} is the ratio of initial equibiaxial compressive yield stress to initial uniaxial compressive yield stress; K_c is the ratio of the second stress invariant on the tensile meridian, $q_{(TM)}$, to the second stress invariant on the compressive meridian, $q_{(CM)}$, which is calculated at initial yield for any hydrostatic stress provided that the maximum principal stress is negative; $\bar{\sigma}_t\left(\tilde{\varepsilon}_t^{pl}\right)$ is the effective tensile cohesion stress; and $\bar{\sigma}_c\left(\tilde{\varepsilon}_c^{pl}\right)$ is the effective compressive cohesion stress (Dassault Systèmes, 2012).

The flow potential function, G, uses the Drucker-Prager hyperbolic function

$$G = \sqrt{(\epsilon\sigma_{t0}\tan\psi)^2 + \bar{q}^2} - \bar{p}\tan\psi \tag{3.13}$$

where $\epsilon(\theta, f_i)$ is the eccentricity which defines the rate at which the function approaches its asymptote, $\sigma_{t0}(\theta, f_i) = \sigma_t|_{\tilde{\varepsilon}_t^{pl}=0, \dot{\tilde{\varepsilon}}_t^{pl}=0}$ is the uniaxial failure tensile stress obtained from user-defined tension-stiffening data, $\psi(\theta, f_i)$ is the dilation angle in the hydrostatic versus deviatoric (i.e. p versus q) stress plane at high confining pressures, $\bar{p}$ is the average of hydrostatic stresses, and $\bar{q}$ is the equivalent effective stress.

3.2 Steel reinforcement

The steel reinforcement stress-strain data used for finite element analyses was that which was provided alongside published unbalanced moment specimen test data. When stress-strain data was not provided, it was obtained from other publications that used reinforcing bars that were manufactured to the same or equivalent specification (e.g. ASTM A615-68).

The stress-strain data was converted from engineering stress-strain to true stress-strain before it was for analysis in Abaqus. For a stress-strain data set, the true strain was obtained using the equation

$$\varepsilon_t = \ln(1 + \varepsilon_e) \tag{3.14}$$

where ε_t is the true strain and ε_e is the engineering strain. The true stress was obtained using the equation

$$\sigma_t = \sigma_e(1 + \varepsilon_e) \tag{3.15}$$

where σ_t is the true stress and σ_e is the engineering stress.

The hardening rule used for the steel reinforcement was isotropic. This was done by user error. The kinematic hardening rule would have been more appropriate to account for the Bauschinger effect in which tensile strain hardening would cause a decrease in compressive strength. Similarly, compressive strain hardening would cause a decrease in tensile strength. Although steel reinforcement may occasionally be loaded, unloaded, then reloaded in the opposite direction, the reinforcement would not yield until the final load step. As such, the finite element analyses were not sensitive to the type of hardening rule used. If the finite element model is further developed to analyse cyclically-loaded specimens (e.g. when simulating a seismic event), a kinematic hardening rule should be used.

The steel reinforcement was perfectly bonded to the concrete using the embedded constraint within Abaqus. This constraint interpolates the reinforcement's translational degrees of freedom (DOF) using the values of the concrete's corresponding DOF. The embedded constraint accounts for concrete-steel bond-slip through the failure of concrete elements adjacent to the reinforcing bars (Earij, Alfano, Cashell, & Zhou, 2017).

Chapter 4: Preliminary parameters of finite element models

To calibrate parameters for the numerical modelling of slab-column connections, a preliminary set of parameters were selected and used to model interior slab-column sub-assemblages tested by Ghali et al. (1976). The preliminary parameters were either assumed based on information published by Ghali et al. or based on previous numerical modelling research conducted by Genikomsou (2015) at the University of Waterloo. These parameters were subsequently changed and their effects were studied. Final values for the finite element model parameters were chosen that best reproduced behaviour observed during laboratory testing.

In Section 4.1, background information is provided on the specimens tested by Ghali et al. (1976). Section 4.2 provides an overview of the preliminary parameters within the finite element models as well as the reasoning for each parameter. Section 4.3, Section 4.4, and Section 4.5 describe the boundary conditions, concrete properties, and reinforcement properties used within the finite element models.

4.1 Tests of interior connections by Ghali, Elmasri, and Dilger (1976)

Ghali et al. (1976) tested six specimens to study the effects of dynamic lateral loading on slab-column connection strength and deformation. They tested three specimens named SM 0.5, SM 1.0, and SM 1.5 which had tension reinforcement ratios of 0.5-percent, 1.0-percent, and 1.5-percent, respectively. For each specimen, the compression reinforcement ratio was one-third of the tension reinforcement ratio. The columns of these specimens were subjected to a constant axial force of 129 kilonewtons (kN). While maintaining this axial force, a moment displacement-couple was applied through the column and gradually increased until failure. The applied moment was increased by 6.4 centimeters at 6 minute intervals. The remaining three specimens were named DM 0.5, DM 1.0, and DM 1.5. The DM specimens were identical to the SM specimens except the moment was applied at a rate of 6.4 centimeters every 0.1 seconds. In this work, only specimens SM 0.5, SM 1.0, and SM 1.5 are studied.

All specimens used 1830 mm by 1830 mm square slabs without transverse reinforcement. The slabs were 152 mm thick with a cover of 19 mm. The edges of the slabs represented the lines of contraflexure within a flat plate system when subjected to uniform gravity loading. The specimens were tested on their sides such that their column axis was parallel to the laboratory

floor. Little information about the support conditions was provided. Ghali et al. stated that the four slab edges were allowed to rotate but not translate. The corners of the slabs were unrestrained to allow for lifting under axial loading. However, it was not stated how much of each corner was unrestrained. Other specimens tested at the University of Calgary by Langohr, Ghali, and Dilger (1976) showed neoprene bearing pads between the load frame and the slab. It was assumed that neoprene bearing pads were also used when testing the SM specimens.

Each specimen used a 305 mm by 305 mm square column with a reinforcement ratio of 4.25-percent. The spacing and size of the columns' transverse reinforcement were not stated in the publication by Ghali et al. The distance between the two ends of the column stubs was 1170 mm. Specimens SM 0.5, SM 1.0, and SM 1.5 had concrete compressive strengths of 36.8 MPa, 33.4 MPa, and 40.0 MPa, respectively. No. 4, Grade 60 deformed bars with a yield stress of 475.7 MPa were used for both slab and column longitudinal reinforcement.

4.2 Overview of parameters

The specimen geometries were modelled as described by Ghali et al. (1976), which included: the column dimensions; slab dimensions; and the slab longitudinal reinforcement areas, depths and spacings. The compressive strength and yield stress of the concrete and steel reinforcement, respectively, were provided. These parameters were not modified or studied.

The preliminary concrete uniaxial compression and tension stress-strain data were obtained using the same material models used by Genikomsou (2015). A concrete density of 2,400 kg/m^3. The Hognestad parabola (Hognestad, 1951) was used to produce uniaxial compression stress-strain data using only the concrete's compression strength. The concrete uniaxial tension stress-strain data was assumed linear-elastic until reaching the concrete's tensile strength, which was assumed to be equal to $0.33\lambda\sqrt{f_c'}$. This tensile strength expression was selected because it was used to derive the concrete web-shear strength equation within Section 22.5.8.3.2 of ACI 318-19. This derivation is presented in *SP-010: Commentary on Building Code Requirements for Reinforced Concrete (ACI 318-63)* (ACI Committee 318, 1965). The concrete's tension stiffening stress-strain data was modelled using Petersson's bilinear model (1981) and the fracture energy was determined using the equation from Model Code 1990 (Comité Euro-

International du Béton, 1993). The preliminary steel stress-strain data was assumed to be linear-elastic-perfectly-plastic.

The loads acting on the column were as provided by Ghali et al. (1976) and were not modified. In the preliminary finite element models, half of the length of the slab sides were restrained from vertical translation. The corners of the slabs were unrestrained to allow for the corners to lift under loading. The low tensile strength of the restrained concrete elements meant that the elements would fail under low loads and allow the slab to lift and rotate. However, the failure of these elements influenced the shape of the crack patterns. As such, different support lengths were studied to determine the length that produced crack patterns that best resembled those observed during laboratory testing.

As per Genikomsou's research (2015), the concrete geometries were meshed with C3D8R (continuum three-dimensional, 8-noded elements with reduced integration) with an element size of 20 mm. The longitudinal reinforcement mats were meshed with T3D2 (truss three-dimensional, 2-noded elements) with an element size of 20 mm to match the element size of the concrete. A reinforced concrete one-way slab example from the Abaqus documentation stated that if reduced-integration linear elements were used (such as the C3D8R element type) then at least four elements should be used through the depth of the slab to adequately capture the bending response within the model (Dassault Systèmes, 2012). As such, various concrete element sizes were selected to produce different numbers of elements through the depths of the slabs. The element size which best captured the bending response was selected.

4.3 Boundary conditions

The boundary conditions used for the FE analyses of all SM specimens are presented in Figure 4.1. Only half of each specimen was analysed due to specimen symmetry. At the plane of symmetry, rotation about the x- and z- axes were restrained and displacement in the y-direction was restrained. In the same plane, the centroid of the concrete was restrained from translating in the x-direction. This was done to prevent any lateral movement of the concrete. Half of each slab edge was restrained from translating in the z-direction. In the first analysis step, a pressure equivalent to 64.5 kN was linearly ramped and applied to the top face of the top column stub. In the second analysis step, the vertical load was maintained and no additional forces were

applied. In the third analysis step, 30 mm displacements were linearly ramped at the top and bottom ends of the column stubs in equal and opposite directions until failure. The distance between the ends of the two column stubs was 1.17 meters. The column dimension was 305 mm by 305 mm. The dimension of the slab was 1830 mm by 1830 mm.

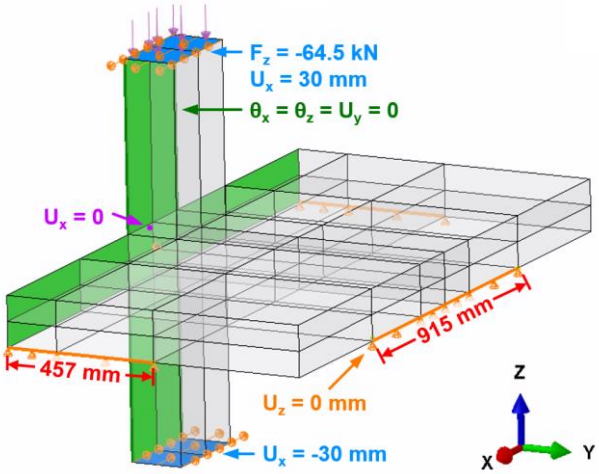

Figure 4.1: Boundary conditions used for FE analyses of SM specimens

4.4 Concrete properties

The concrete mesh used for the FE analyses of the SM specimens is shown in Figure 4.2. The concrete slab and column were meshed with C3D8R continuum elements with an element size of 20 mm.

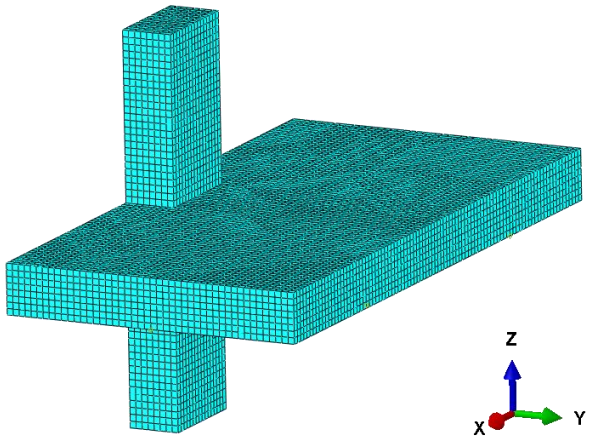

Figure 4.2: Concrete mesh used for FE analyses of SM specimens

A Poisson's ratio of 0.2 was used for the concrete. The concrete compression and tension stress-strain data are presented in Figure 4.3 and Figure 4.4, respectively.

Linear-elastic data

Specimen	E_c (MPa)	ε_{co}	σ_{co} (MPa)
SM 0.5	30,319	0.0005	14.71
SM 1.0	28,879	0.0005	13.34
SM 1.5	31,614	0.0005	15.99

Plastic data

Specimen	E_t (MPa)	ε_o	f_c' (MPa)
SM 0.5	33,351	0.0022	36.77
SM 1.0	31,767	0.0021	33.36
SM 1.5	34,776	0.0023	39.98

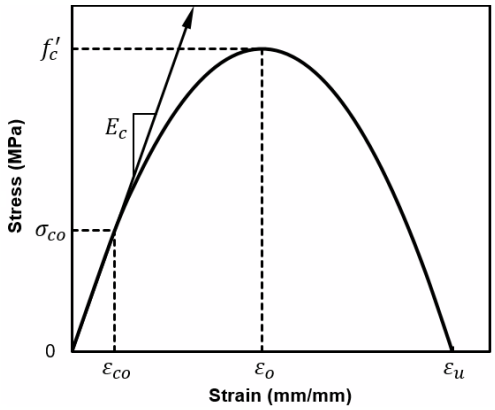

Figure 4.3: Compression stress-strain data used for FE analyses of SM specimens

Linear-elastic data

Specimen	E_c (MPa)	ε_{cr}	f_t' (MPa)
SM 0.5	30,319	0.0001	2.00
SM 1.0	28,879	0.0001	1.91
SM 1.5	31,614	0.0001	2.09

Plastic data

Specimen	G_f (N/mm)	ε_1	ε_u
SM 0.5	0.139	0.0029	0.0127
SM 1.0	0.136	0.0030	0.0131
SM 1.5	0.141	0.0028	0.0124

Note: Element length l_c is equal to 19.70 mm

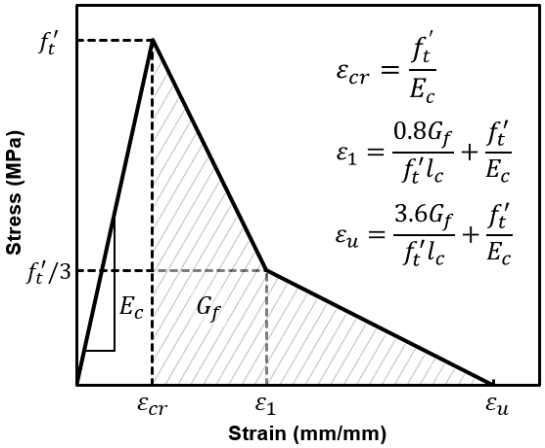

Figure 4.4: Tension stress-strain data used for FE analyses of SM specimens

The concrete material assignments used for all SM specimens are shown in Figure 4.5. Most of the concrete slab elements included the Concrete Damaged Plasticity material model. A dilation angle ψ of 40-degrees was used based on research by Genikomsou (2015). Default values from Abaqus were used for: the default flow potential eccentricity, ϵ, was equal to 0.1, the ratio of initial equibiaxial compressive yield stress to initial uniaxial compressive yield stress, σ_{b0}/σ_{c0}, was equal to 1.16, and the ratio of the second stress invariant on the tensile meridian to that on the compressive meridian, K_c, was equal to $2/3$ (Dassault Systèmes, 2012). More information about these parameters is presented in Section 3.1.3.

The edge of the slab used linear-elastic elements to prevent tension failures of the restrained elements. Tension stresses were present within these elements because the slab edge lifted when moments were applied. The concrete column used stiffened linear-elastic elements to reproduce

the confinement effects of the stirrups on the concrete. For each specimen, the column E_c values were the same as those presented in Figure 4.3.

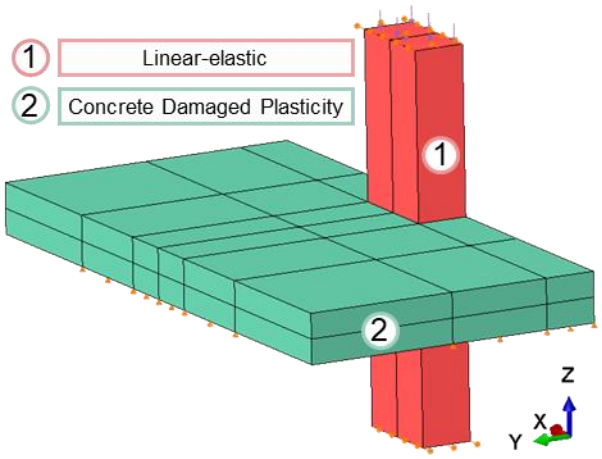

Figure 4.5: Concrete material assignments for FE analyses of SM specimens

4.5 Reinforcement properties

All steel reinforcement was meshed using T3D2 truss elements with an element size of 20 mm. The compression and tension slab flexural reinforcement properties, including reinforcement spacing and areas, are presented in Table 4.1 and Table 4.2, respectively. The column longitudinal reinforcement ratio was 4.25-percent. The column stirrups were not modelled using truss elements because the size and spacing of the stirrups were not included in the publication by Ghali et al. (1976). Instead, the confining effects of the stirrups were reproduced using linear-elastic concrete elements with higher modulus of elasticity values (i.e. ten times the modulus of elasticity of the slab concrete).

Table 4.1: Compression reinforcement properties for FE analyses of SM specimens

Specimen	x-direction			y-direction		
	Depth	Spacing	Area	Depth	Spacing	Area
SM 0.5	25 mm	600 mm	127 mm^2	38 mm	534 mm	127 mm^2
SM 1.0		300 mm			264 mm	
SM 1.5		198 mm			171 mm	

Table 4.2: Tension reinforcement properties for FE analyses of SM specimens

Specimen	x-direction			y-direction		
	Depth	Spacing	Area	Depth	Spacing	Area
SM 0.5	127 mm	200 mm	127 mm^2	114 mm	178 mm	127 mm^2
SM 1.0		100 mm			88 mm	
SM 1.5		66 mm			57 mm	

The steel reinforcement stress-strain data is shown in Figure 4.6.

Linear-elastic data	
Poisson's ratio	Modulus of elasticity
0.3	183,686 MPa

Plastic data		
	Strain (mm/mm)	Stress (MPa)
Yield	0.0026	476
Rupture	0.1135	476

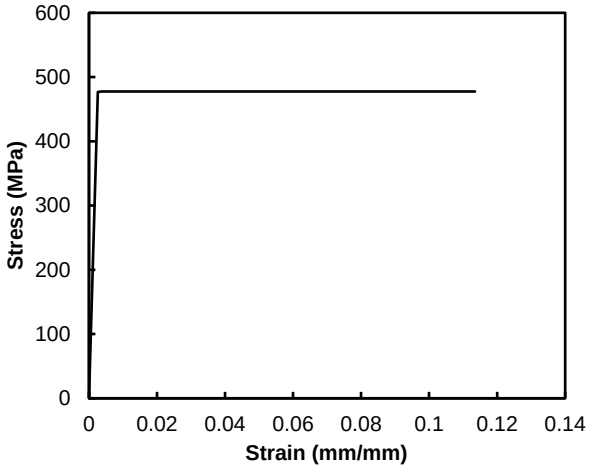

Figure 4.6: Reinforcement stress-strain data used for FE analyses of SM specimens

Chapter 5: Calibration of finite element model parameters

The calibration of the finite element models was completed by changing model parameters and features and studying how each change affected the finite element analyses results. The parameters studied were specific to either the concrete, the steel reinforcement, or the overall model. The concrete parameters included the compressive stress-strain data, fracture energy models, dilation angles, and meshing (i.e. element sizes). The steel reinforcement parameters included stress-strain data, reinforcement layout, and meshing (i.e. element sizes and types). For the overall model, changes to the boundary conditions and materials at the boundary conditions were studied.

Calibration was necessary to ensure that each model accurately reproduced the behaviours observed during testing. Since the models would later be used for parametric studies, calibration ensured that errors in the parametric studies were minimized and the trends observed were correct.

The process of calibration was completed in three steps. The first step was to create finite element models of specimens SM 0.5, SM 1.0, and SM 1.5 using the experimental data published by Ghali et al. (1976). The starting parameters with respect to element types and sizes, concrete material model, and dilation angle were those Genikomsou (2015) used to numerically model specimens tested at the University of Waterloo. More information about these parameters is provided in Chapter 4.

The second step was to change one parameter at a time and study how each change affected the results of the models. After each study, the parameter that most accurately reproduced experimental behaviour among the three models was selected and used in subsequent studies. Accuracy of the models was determined by comparing the crack patterns, displacement-rotation plots, and moment-rotation plots of the finite element analyses to those obtained through laboratory-testing. The displacement presented is the vertical displacement of the column, which was calculated by averaging the displacements of the nodes at the top of the column. The rotation presented is that of the column relative to the gravity axis. Once the model parameters were selected, the next step was to validate these parameters. This was done by creating finite element models of other tested specimens using the calibrated parameters. Similarly, the finite

element analyses results were compared to their respective experimental results. The parameters were confirmed to be calibrated if the finite element analyses accurately reproduced the results of the experiments.

Three different specimens were used to validate the model parameters: specimens XXX and HXXX tested by El-Salakawy (1998); and specimen SB1 tested by Adetifa (2003). All three specimens were tested at the University of Waterloo. Specimens XXX and HXXX were edge slab-column connections loaded with a vertical load and a moment applied simultaneously on the column. Specimen SB1 was an interior slab-column connection subjected to concentric loading.

In this chapter, the results of the following calibration studies are presented:

1. Within the column, the effect of the concrete modulus of elasticity on the FEA results was studied. This was done to determine the modulus of elasticity that best reproduced the effects of the stirrups' confinement on the concrete.
2. The effects of the slab edge restraint length on the FEA results was studied. This was done to determine the restraint length that allowed the slab corners to lift without adversely affecting the transfer of stresses from the column to the supports.
3. The FEA results of three possible boundary condition modifications were studied. This was done to determine the optimal boundary conditions that would prevent failure of the restrained elements along the lifting slab edge.
4. The effects of using different fracture energy models on the FEA results were studied.
5. The effects of using a reinforcement layout (i.e. depth and spacing) of equivalent moment resistance on the FEA results were studied.
6. The effects of the concrete element size on the FEA results were studied.
7. The effects of the reinforcement element size and type on the FEA results were studied.
8. The effects of the concrete dilation angle on the FEA results were studied.
9. The effects of self-weight on the FEA results were studied.
10. The effects of reducing the concrete tangent modulus of elasticity, E_t, on the FEA results were studied.
11. The effects of defining the reinforcement plasticity using strain-hardening versus perfectly-plastic stress-strain data on the FEA results were studied.

5.1 Modelling of column concrete confinement

The first study was done to determine how to model the column concrete confinement provided by the column stirrups. Without stirrups, the column concrete expands transversely under axial loading as per the Poisson effect. When stirrups are present, the stirrups restrict this expansion. This restriction increases aggregate interlock, which increases the column's stiffness and shear capacity.

Stirrups were not included in any of the three finite element models for two reasons. First, the stirrup sizes and spacings were not provided in the publication by Ghali et al. (1976). Second, the increased stiffness resulting from transverse concrete confinement is not possible to model solely using embedded stirrups. The embedded stirrups are able to reproduce the lateral confining pressures caused by axial loads. However, the confining pressures do not affect the concrete's stiffness in the column's longitudinal direction. As a result, it is common practice to use different stress-strain models to define the confined concrete's uniaxial behaviour (e.g. Dabaon, El-Khoriby, El-Boghdadi, & Hassanein, 2009; Hu, Huang, Wu, & Wu, 2003).

In this work, the increased stiffness and capacity is modelled by modifying the column concrete material properties. The stiffness is increased by defining a higher modulus of elasticity. The column capacity limit is removed by modelling the column concrete as a linear elastic material. Using linear elastic column concrete ensures that the column does not fail even under the large moments applied during the parametric studies. Also, fewer computational resources are used by defining elastic elements instead of plastic elements. This means that analyses can be completed in a shorter duration.

Three different values for the column concrete modulus of elasticity were analysed and compared. It was expected that increasing the modulus of elasticity would only affect the FEA results up to a certain value. At this value, rigid body motion of the column would occur. The first modulus of elasticity analysed was the unmodified modulus of elasticity calculated using the Hognestad compression material model (i.e. one times the unstiffened modulus of elasticity). The second modulus of elasticity analysed was 200 gigapascals (GPa), which is the typical modulus of elasticity of steel. The third modulus of elasticity analysed was ten times the modulus elasticity calculated using the Hognestad compression material model. The latter two modulus of elasticity values were chosen arbitrarily.

5.1.1 Results of specimen SM 0.5 analyses

For specimen SM 0.5, three values for the column modulus of elasticity were studied: 30,319 MPa; 200,000 MPa; and 303,191 MPa. The moment-rotation and displacement-rotation data for the three analyses are presented in Figure 5.1. The moment-rotation data is expressed in kilonewton-meters (kNm) and milliradians (mrad). The displacement-rotation data is expressed in millimeters (mm) and milliradians (mrad). A summary of these results are shown in Table 5.1.

The three finite element analyses showed greater rotational stiffness compared to the laboratory-tested specimen. All three analyses underestimated the moment capacity of the experiment. The percentage differences between analyses E = 30,319 MPa, E = 200,000 MPa, and E = 303,191 MPa and the experiment were 3.5-percent, 7.6-percent, and 7.8-percent, respectively.

All three analyses showed similar rotational responses under the applied moment. However, the E = 30,319 MPa analysis curve plateaued past 13 mrad. This indicated that the steel had yielded. The E = 200,000 MPa and E = 303,191 MPa models produced near-identical moment-rotation data. The moment capacity difference between the two stiffer analyses was negligible. The percentage differences in moment capacities between analyses E = 30,319 MPa, E = 200,000 GPa, and E = 303,191 MPa and the experiment were 18.8-percent, 13.9-percent, and 14.9-percent, respectively. The experiment moment-rotation data showed less rotational stiffness compared to the three analyses. The differences in moment capacity and rotational stiffness indicated that further model calibration was required.

All three models produced displacement-rotation results with near-identical slopes. The E = 30,319 MPa analysis had a lower ultimate displacement of 9.4 mm as it failed at a lower applied moment compared to the two other analyses.

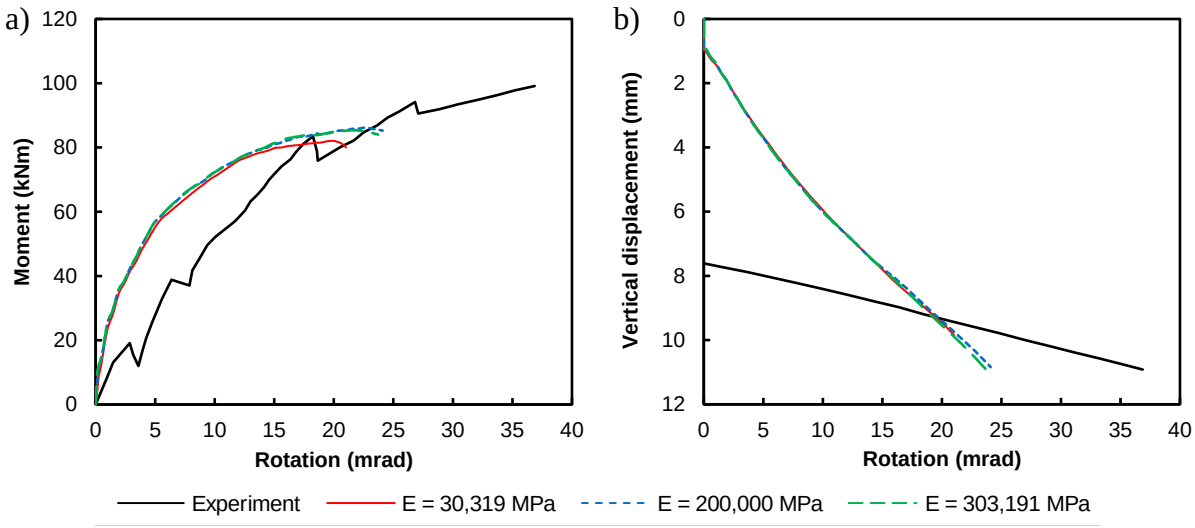

Figure 5.1: Specimen SM 0.5 a) moment-rotation and b) displacement-rotation data using varying values for column modulus of elasticity

Table 5.1: Specimen SM 0.5 analyses results using varying column moduli of elasticity *E*

	Ultimate moment (kNm)	Displacement (mm) at ultimate moment	Rotation (mrad) at ultimate moment
Analyses			
E = 30,319 MPa	82.1	9.4	19.9
E = 200,000 MPa	86.2	10.3	22.6
E = 303,191 MPa	85.4	10.0	21.4
Experiment	99.1	10.9	36.9

The experiment crack patterns and the crack patterns of the three analyses are shown in Figure 5.2. The crack patterns of the analyses were studied using the maximum principal plastic strain contour plots. These contour plots are useful for studying concrete cracks because any value greater than zero indicates that a crack has formed. This is because cracking occurs as soon as a concrete element in tension meets the yield criterion. Furthermore, an elements maximum principal plastic strain is proportional to the elements crack width. This is convenient for differentiating between small cracks, which are caused by the redistribution of tension stresses from the concrete to reinforcement, and large cracks, which caused by stress concentrations. For any analysis, using the largest strain value for the contour plot upper limit makes it difficult to see the smaller cracks represented by smaller strains. The upper limit was reduced independently for each contour plot to better observe both small and large cracks. For each analysis, the strains plotted are those produced when the 129 kN vertical load and the ultimate moment are applied.

Based on the cracks that formed around the column on the top face, using a softer column (E = 30,319 MPa) resulted in lower shear stresses within the compression region and higher shear stresses within the tension region compared to using a stiffer column (E = 200,000 MPa and E = 303,191 MPa). These higher tensile stresses caused the steel reinforcement to yield under a lower applied moment within the softer column analysis compared to the stiffer column analyses. The flexural failure mode of these analyses is consistent with the failure mode described by Ghali et al. (1976) of the laboratory-tested specimen.

All FEA crack patterns for the slab top faces showed cracks propagating from the column faces toward the supports and the slab corners. These diagonal cracks matched those observed during laboratory-testing. All FEA crack patterns showed concentrations of cracks around the columns, which are also part of the experiment crack patterns.

On the bottom face, the analyses showed cracks propagating from the tension column face towards the bottom left and bottom right edges. Additional vertical cracks were visible from the tension column face to the slab supports. These cracks were present in the experiment crack patterns. All FEA crack patterns showed cracking around the column that matched the experiment crack patterns. The stiffer column analyses showed similar cracking to the softer column analysis except with larger crack widths (i.e. larger strains).

a) Top face, experiment

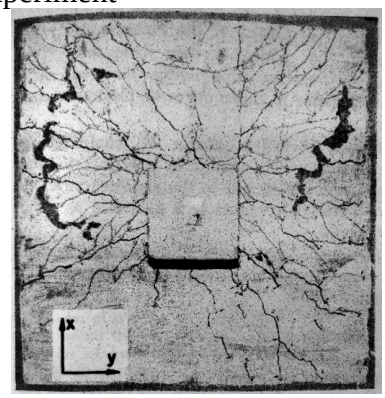

b) Bottom face, experiment

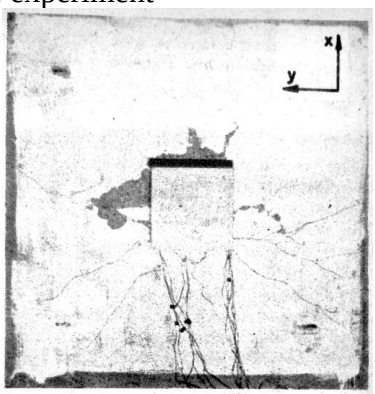

c) Top face, analysis E = 30,319 MPa

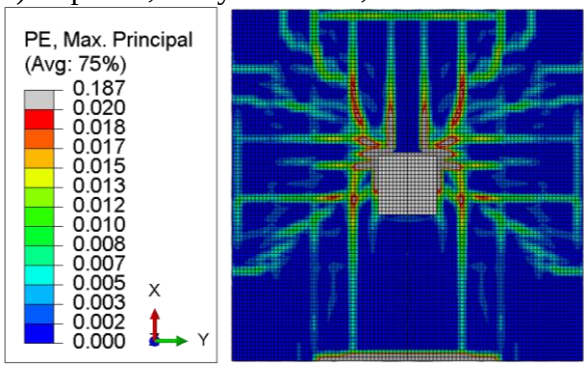

d) Bottom face, analysis E = 30,319 MPa

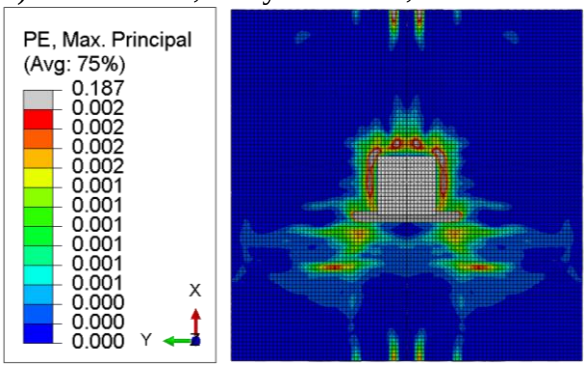

e) Top face, analysis E = 200,000 MPa

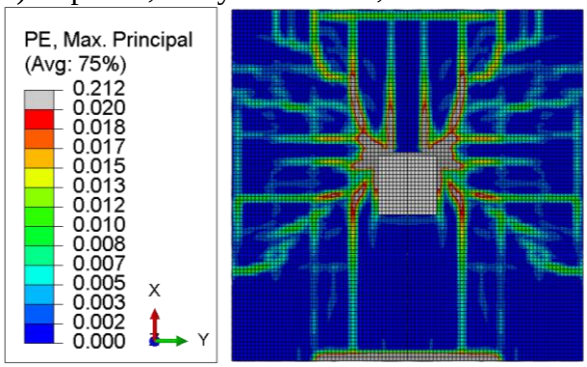

f) Bottom face, analysis E = 200,000 MPa

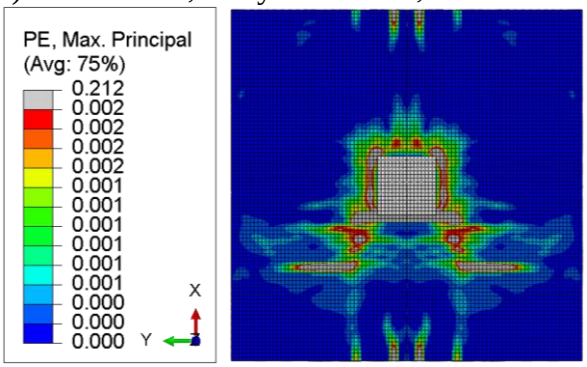

g) Top face, analysis E = 303,191 MPa

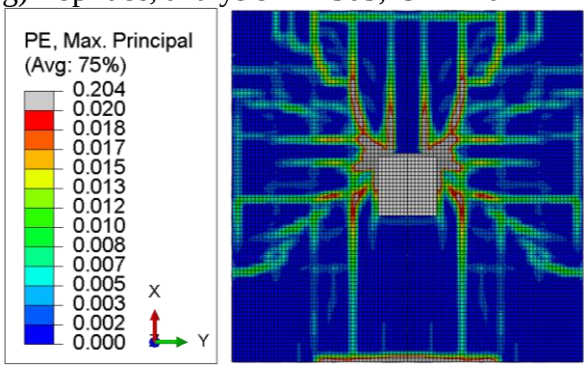

h) Bottom face, analysis E = 303,191 MPa

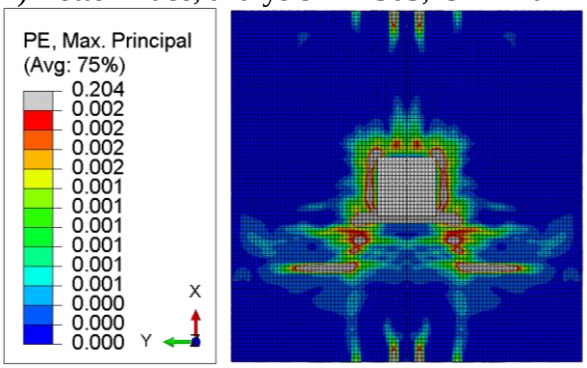

Figure 5.2: Specimen SM 0.5 experiment (Ghali et al., 1976) and analyses crack patterns using varying values for modulus of elasticity E. Authorized reprint of experiment photographs from ACI Journal, Volume 73, Issue 10, October 1976.

5.1.2 Results of specimen SM 1.0 analyses

For specimen SM 1.0, three values for the column modulus of elasticity were studied: 28,880 MPa; 200,000 MPa; and 288,795 MPa. The moment-rotation and displacement-rotation data for the three analyses are presented in Figure 5.3. A summary of these results are shown in Table 5.2.

The moment-rotation data of the three analyses had similar slopes to one another. The higher moment capacity attained when using a softer column (rather than a stiffer column) was due to differences in stress distribution. The softer column produced higher shear stresses on the top face tension region and lower shear stresses on the top face compression region. These same stress distribution differences were observed among the SM 0.5 analyses. Contrary to the SM 0.5 analyses, the SM 1.0 analyses showed an increase in moment capacity when a softer column was used. This was because the SM 1.0 specimen had more reinforcement present to resist larger moments before yielding. The added reinforcement changed the failure mode from steel yielding to concrete crushing.

For the softer column analysis, the slope of the moment-rotation data decreased at a higher rate compared to the stiffer column analyses. This is due to the progressive failure of the restrained concrete elements along the slab edges. Under an applied moment, the elements on one side of the slab resist stresses caused by the slab lifting and the elements on the other side of the slab resist stresses caused by the slab lowering. Elements resisting lifting stresses would fail early due to concrete's low tensile strength. As an element would fail, additional stresses would be carried by adjacent elements. The stiffness of this slab edge decreased as the number of failed elements increased. This decreased stiffness caused the edge to lift more in the softer column analysis compared to the stiffer column analyses under the same applied moment. The slope discontinuity visible at 7.6 mrad was caused by lifting stresses being redistributed from the lifting slab edge to the adjacent slab edge. This redistribution is reflected in the displacement-rotation data as the displacement-rotation slope appears to decrease after 7.6 mrad. This was because the vertical displacement, which until 7.6 mrad only considered downward displacement of the column stub, now being offset by the upward displacement of the lifting slab edge. Possible solutions to prevent lifting edge failure are presented in later sections.

The three finite element analyses showed greater rotational stiffness compared to the laboratory-tested specimen. All three analyses underestimated the moment capacity of the experiment. The moment capacity percentage differences between analyses E = 28,880 MPa, E = 200,000 MPa, and E = 288,795 MPa and the experiment were 3.5-percent, 7.6-percent, and 7.8-percent, respectively.

All three analyses produced similar displacement-rotation results. At the ultimate moments, the E = 28,880 MPa, E = 200,000 MPa, and E = 288,795 MPa analyses had displacements within 0.2 mm of each other. However, these analyses underestimated displacements by over three times compared to the experiment. With respect to rotations, the softer column analysis had the highest rotation of 13.2 mrad as it failed under a larger moment compared to the stiffer column analyses. However, the ultimate rotation percentage difference between the softer column analysis and the experiment was 68.7-percent.

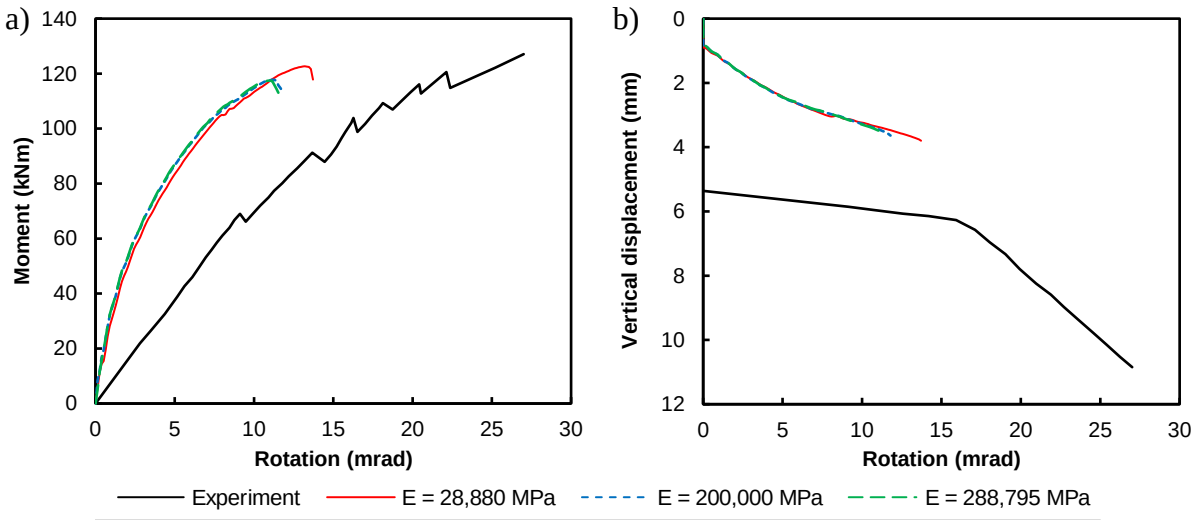

Figure 5.3: Specimen SM 1.0 a) moment-rotation and b) displacement-rotation data using varying values for column modulus of elasticity *E*

Table 5.2: Specimen SM 1.0 analyses results using varying column moduli of elasticity *E*

	Ultimate moment (kNm)	Displacement (mm) at ultimate moment	Rotation (mrad) at ultimate moment
Analyses			
E = 28,880 MPa	122.7	3.7	13.2
E = 200,000 MPa	117.8	3.5	11.2
E = 288,795 MPa	117.5	3.5	11.0
Experiment	127.1	10.8	27.0

The crack patterns of the three analyses are shown in Figure 5.4. Experimental crack patterns for specimen SM 1.0 were not published. However, since the failure mode was the same for specimens SM 1.0 and SM 1.5, the crack patterns were expected to be similar. This prediction will be verified when analysing the SM 1.5 crack patterns.

Few differences were evident between the softer column analysis and the stiffer column analyses. All the analyses formed crack concentrations around the columns. On the top face, all analyses showed cracks propagating from the top column face in an "x" shape toward the slab edges. On the bottom face, all analyses showed that cracks had formed from the bottom face in the direction of the bottom slab corners. These cracks stopped one-third of the distance from the column to the slab corners.

The softer column analysis had higher strains at the lift-resisting slab edge (0.099) compared to the stiffer column analyses (0.065 and 0.073 for analyses E = 200,000 MPa and E = 288,785 MPa, respectively).

a) Top face, analysis E = 28,880 MPa

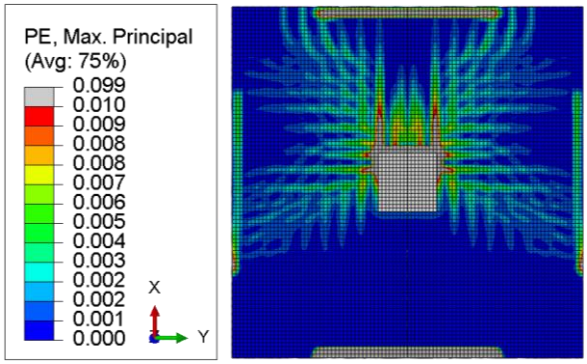

b) Bottom face, analysis E = 28,880 MPa

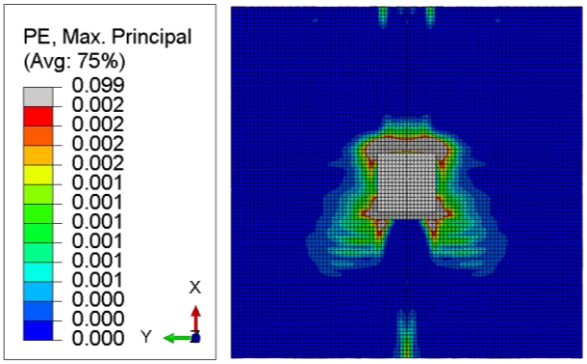

c) Top face, analysis E = 200,000 MPa

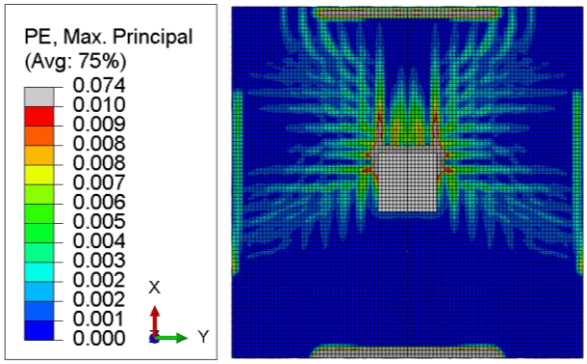

d) Bottom face, analysis E = 200,000 MPa

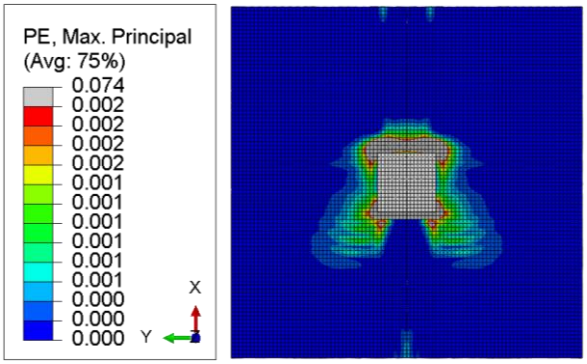

e) Top face, analysis E = 288,795 MPa

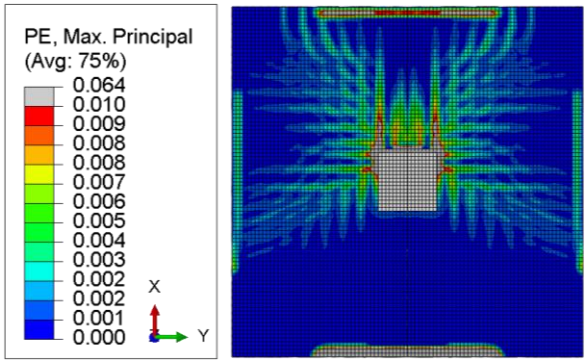

f) Bottom face, analysis E = 288,795 MPa

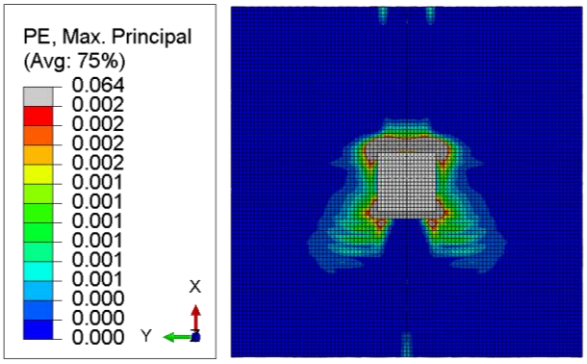

Figure 5.4: Specimen SM 1.0 analyses crack patterns using varying values for modulus of elasticity *E*

5.1.3 Results of specimen SM 1.5 analyses

For specimen SM 1.5, three values for the column modulus of elasticity were studied: 31,615 MPa; 200,000 MPa; and 316,145 MPa. The moment-rotation and displacement-rotation data for the three analyses are presented in Figure 5.5. A summary of these results are shown in Table 5.3.

The same trends among the SM 1.0 analyses were observed for the SM 1.5 analyses. First, the moment-rotation data of the three analyses had similar slopes to one another. Second, the softer

column analysis had the highest moment capacity among the analyses. The reason for this was the same as it was for the SM 1.0 analyses: a softer column produced higher shear stresses in the top face tension region and lower shear stresses in the top face compression region. Third, the lift-resisting slab edge failed due to these increased stresses in both the E = 31,615 MPa and E = 200,000 MPa analyses. As with the SM 1.0 analyses, this failure caused a decrease in rotational stiffness. The moment capacities of all analyses were similar; all moment capacities were within 1.5-percent of one another. All three analyses over-predicted the moment capacities of the laboratory-tested specimen. The largest percentage difference was 18.7-percent for analysis E = 31,615 MPa and the smallest percentage difference was 17.2-percent for analysis E = 200,000 MPa. Each of the three analyses had a rotational stiffness greater than that of the laboratory-tested specimen.

All three analyses produced similar displacement-rotation results. At the ultimate moments, all three analyses had displacements within 0.3 mm of each other. All analyses had much lower displacements when their respective ultimate moments were applied. The E = 316,145 MPa analysis had the largest displacement of 2.0 mm, while the laboratory-tested specimen had a displacement of 11.3 mm.

As discussed, the analyses had stiffer moment-rotation data compared to the laboratory-tested specimen. This resulted in lower rotations at ultimate moments. The softer column analysis had the highest rotation among the analyses of 14.1 mrad since it failed under a higher applied moment. However, this is almost half of the laboratory-tested rotation at ultimate moment which was 20.1 mrad.

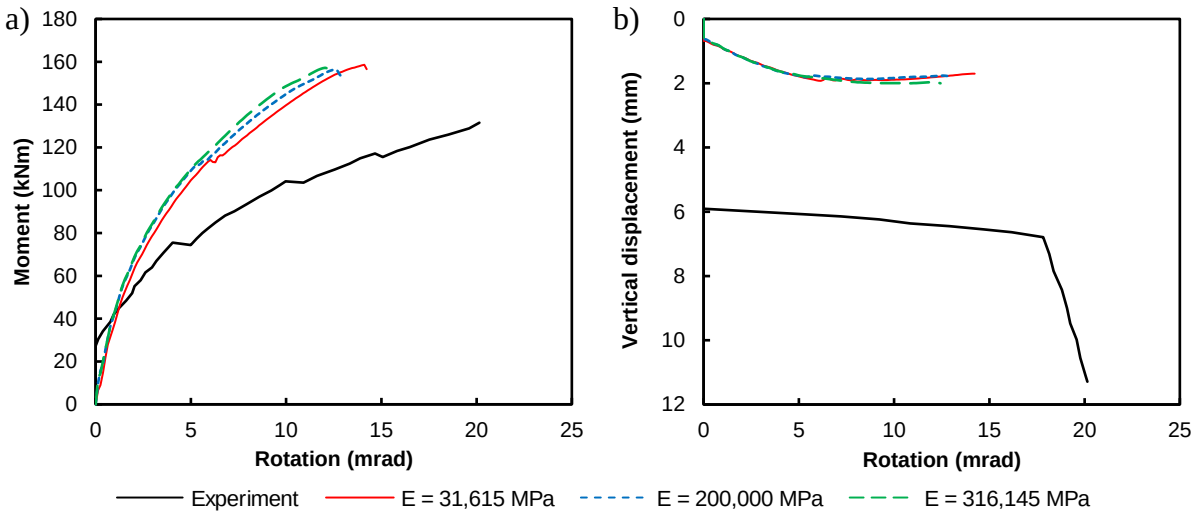

Figure 5.5: Specimen SM 1.5 a) moment-rotation and b) displacement-rotation data using varying values for column modulus of elasticity E

Table 5.3: Specimen SM 1.5 analyses results using varying column moduli of elasticity E

	Ultimate moment (kNm)	Displacement (mm) at ultimate moment	Rotation (mrad) at ultimate moment
Analyses			
E = 31,615 MPa	158.6	1.7	14.1
E = 200,000 MPa	156.3	1.8	12.6
E = 316,145 MPa	157.2	2.0	12.1
Experiment	131.5	11.3	20.1

The experiment and analyses crack patterns are shown in Figure 5.6. Among the top face crack patterns, all analyses showed cracks propagating from the left, top, and right column faces toward the slab edges and corners. These cracks were present in the experiment crack patterns. Each analysis had crack concentrations around the column. The maximum principal plastic strain occurred at the lift-resisting slab edge for all analyses. Based on these strains, all analyses observed failure of some, if not all, lift-resisting concrete elements. The softer column analysis (E = 31,615 MPa) had the highest maximum strain of 0.182. This was expected based on previous observations: softer column analyses have different slab stress distributions compared to stiffer column analyses.

Among the bottom face crack patterns, all analyses had cracks form from the bottom column face to the bottom slab edge. Additional cracks were visible forming from the bottom column face toward the bottom left and right corners; however, these cracks stopped one-third of the

distance between the column and slab edge. The bottom face experiment crack pattern published focused on the top face of the column. Therefore, it is not known if the observed crack patterns are representative of experiment crack patterns. However, all analyses did have crack concentrations at the top column as shown in the experimental crack patterns.

The crack patterns of the SM 1.5 analyses showed many similarities to the crack patterns of the SM 1.0 analyses in Figure 5.6. This was expected as the two specimens shared the same failure mode.

a) Top face, experiment

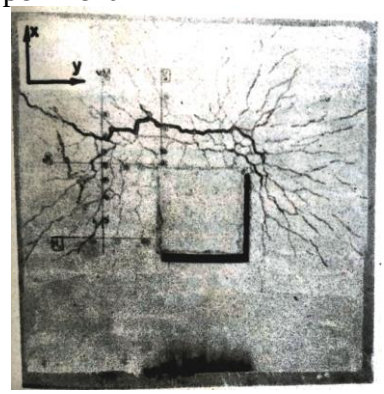

b) Bottom face, experiment

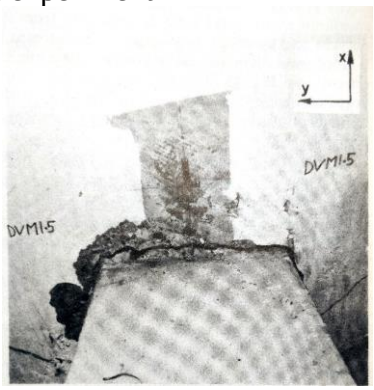

c) Top face, analysis E = 31,615 MPa

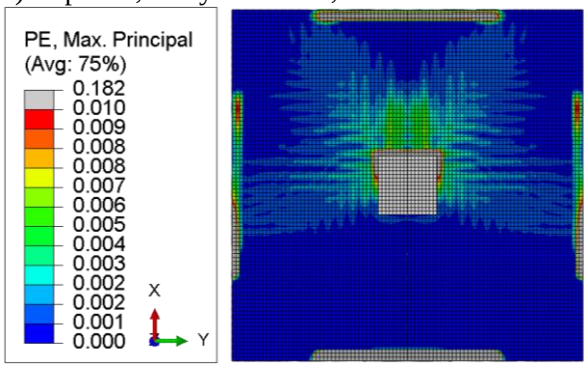

d) Bottom face, analysis E = 31,615 MPa

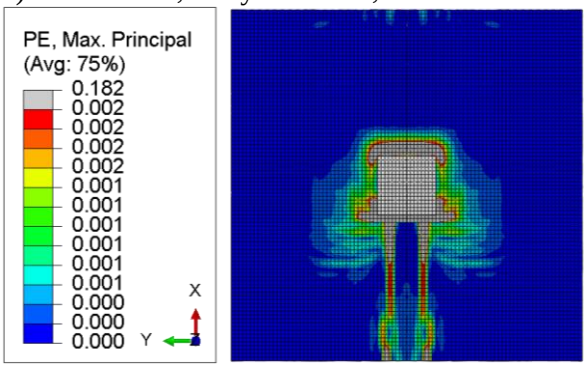

e) Top face, analysis E = 200,000 MPa

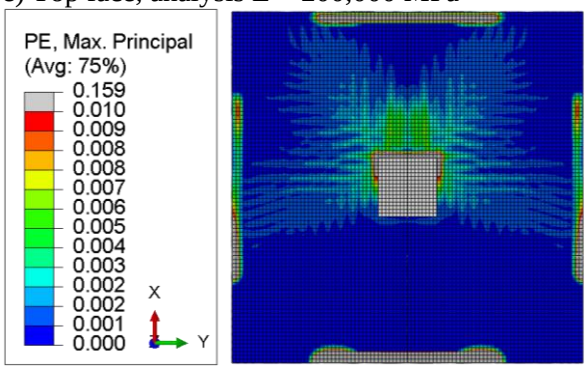

f) Bottom face, analysis E = 200,000 MPa

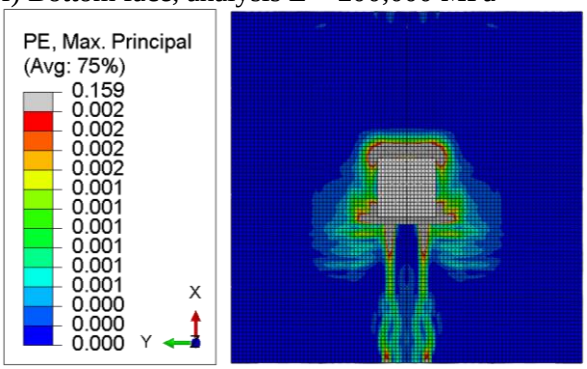

g) Top face, analysis E = 316,145 MPa

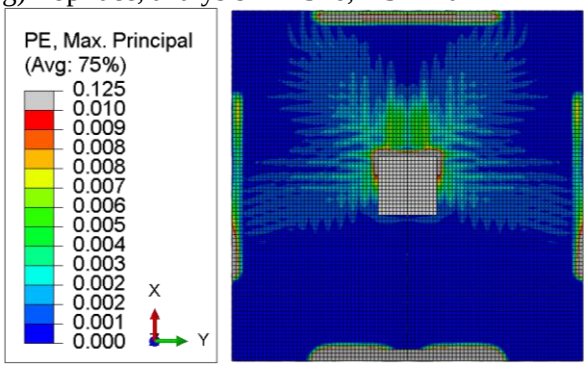

h) Bottom face, analysis E = 316,145 MPa

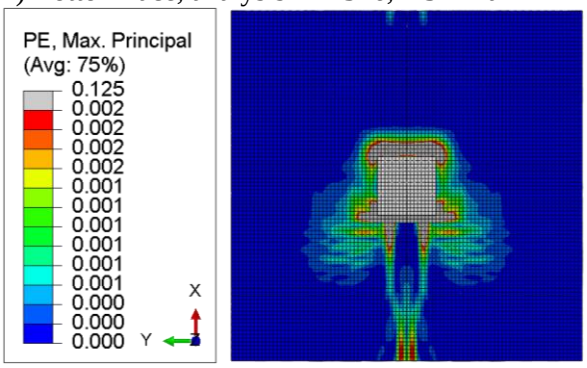

Figure 5.6: Specimen SM 1.5 experiment (Ghali et al., 1976) and analyses crack patterns using varying values for modulus of elasticity E. Authorized reprint of experiment photographs from ACI Journal, Volume 73, Issue 10, October 1976.

5.1.4 Conclusions and recommendations

The concrete confinement of the column concrete was adequately modelled by increasing the modulus of elasticity of the concrete. There were clear differences in moment-rotation data and crack patterns between using a lower modulus of elasticity compared to a higher one.

Using a modulus of elasticity equal to that calculated using the Hognestad material model resulted in higher shear stresses in the top face tension region and lower shear stresses in the top face compression region. This stress distribution resulted in a lower moment capacity for specimen SM 0.5. This was because specimen SM 0.5 failed due to flexural yielding and the increased tensile stresses caused flexural yielding to occur under a lower applied moment. The opposite effect was had for specimens SM 1.0 and SM 1.5. The failure mode of these specimens is concrete crushing. Since these specimens had more flexural reinforcement compared to specimen SM 0.5, the increased tensile stresses were not enough to cause the steel to yield before the concrete crushed. Furthermore, the decreased compression stresses when using a softer column meant that more moment could be applied before the compression elements around the column failed.

The difference in stress distribution when using a softer column compared to a stiffer column resulted in increased stresses among the lift-resisting slab edge elements. This lead to failures in the support elements for the softer column analyses of specimens SM 0.5 and SM 1.0. The specimen SM 1.5 analyses experienced partial or full failure of the support elements regardless of the column modulus of elasticity. The possible boundary conditions to prevent this failure are studied in later sections.

There were negligible differences between using a modulus of elasticity of 200,000 MPa and using a modulus of elasticity that is ten-times the modulus of elasticity calculated using the Hognestad material model. Both moduli of elasticity adequately replicated the effects of concrete confinement. Therefore, ten-times the Hognestad modulus of elasticity was used to model the column concrete for subsequent analyses.

5.2 Study of corner boundary conditions

A number of finite element analyses were conducted to determine how to best model the boundary conditions at the slab corners. Ghali et al. (1976) stated that the corners of the slabs

were unrestrained to allow them to lift under load. This meant that the support restraints along the slab edges stopped some distance short of the slab corners. However, the length of the support restraints was not provided. This length is henceforth referred to as the support length.

To determine the support length, eight finite element models were analysed using four different support lengths. The support lengths were chosen arbitrarily and expressed as fractions of the total slab edge. The names of the analyses and their support lengths, expressed both as lengths and as fractions of the slab edge, are presented in Table 5.4. The BC1 through BC4 analyses and the BC1-E through BC4-E analyses used the same set of support lengths. However, the analyses with the "-E" suffix did not have any restraints on the slab edge perpendicular to the moment axis. The boundary conditions of the analyses are presented in Figure 5.7.

The reason for conducting analyses BC1-E through BC4-E was to observe how the analysis rotational stiffness changed when the slab edge was free to follow the curvature produced by the applied moment.

Table 5.4: Support lengths analysed for corner boundary condition study

Analysis name	Support length L_s (mm)	Fraction of slab edge supported
BC1 and BC1-E	915	1/2
BC2 and BC2-E	1373	3/4
BC3 and BC3-E	1525	5/6
BC4 and BC4-E	1830	1

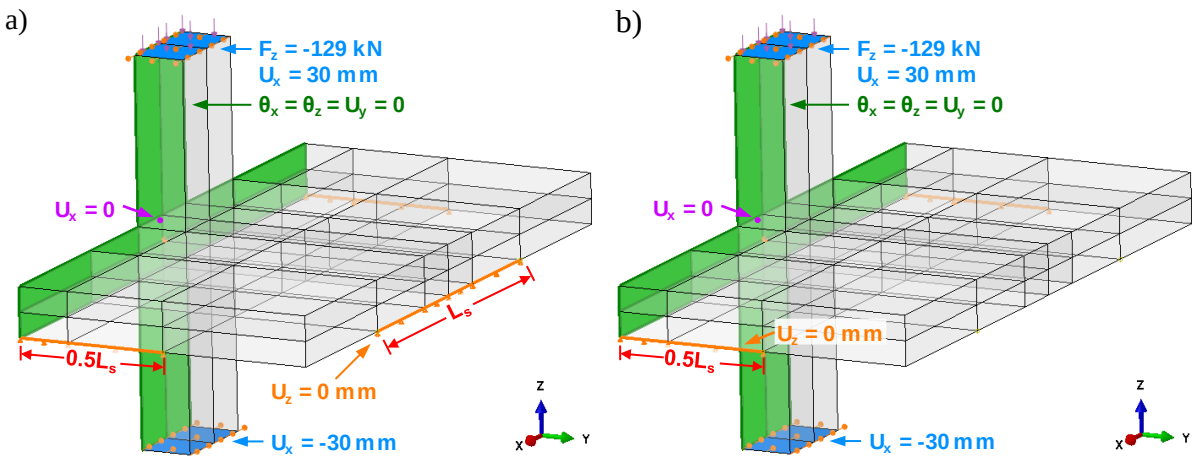

Figure 5.7: Boundary conditions used for analyses a) BC1 through BC4 and b) BC1-E through BC4-E

The expectation among these analyses was that neither the moment-rotation nor the displacement-rotation would change with varying support lengths. However, the crack patterns were expected to change. The reason for this is attributed to the low tensile strength of the concrete. The restrained corner elements would fail under a low applied moment and would become inactive. As inactive elements, they would not prevent the lifting of the slab corners. For this reason, the boundary conditions that produced crack patterns most similar to the experiment were selected and used in subsequent studies.

5.2.1 Results of specimen SM 0.5 analyses

5.2.1.1 Results of analyses BC1 through BC4

The moment-rotation and displacement-rotation data for specimen 0.5 analyses BC1 through BC4 are presented in Figure 5.8. A summary of this data is provided in Table 5.5.

All four analyses produced similar moment-rotation data. During analysis BC1, flexural failure occurred under a lower applied moment compared to the other analyses. This was because analysis BC1 did not have enough restrained support elements to resist the lifting forces caused by the applied moment. The failure of the lift-resisting support elements lead to the formation of a plastic hinge at the column face away from the failing elements. Along the plane of symmetry, there were concentrations of maximum principal plastic strains at the failing slab edge and the plastic hinge. The maximum principal plastic strain contour plot of the specimen symmetry plane under the ultimate moment is shown in Figure 5.9. The ultimate failure of analysis BC1 was due to the flexural reinforcement failure within this plastic hinge.

All analyses had stiffer moment-rotation responses compared to the experiment when the moment was only starting to be applied. Under higher moments, analyses BC2 through BC4 had moment-rotation responses of similar stiffness to the experiment. Furthermore, the ultimate moments were similar between analyses BC2 through BC4 and the experiment. Among these three analyses, analysis BC4 had the largest percentage difference compared to the experiment. Analysis BC4 had an ultimate moment of 93.5 kNm and the experiment had an ultimate moment of 99.1 kNm, which is a percentage difference of 5.8-percent.

The displacement-rotation data for analyses BC1 through BC4 were identical. All analyses showed higher initial stiffness. Under only the vertical load, all analyses columns displaced a distance of 0.7 mm. The experiment column displaced a distance of 7.7 mm. Throughout the application of the moment, the analyses showed a lower displacement-rotation slope compared to the experiment. At the ultimate moments, all analyses showed similar displacements to the experiment. The largest difference between the analyses and the experiment was observed for analysis BC4. The column of analysis BC4 displaced a distance of 9.9 mm while the column of the experiment displaced a distance of 10.9 mm. This is a percentage difference of 10.1-percent.

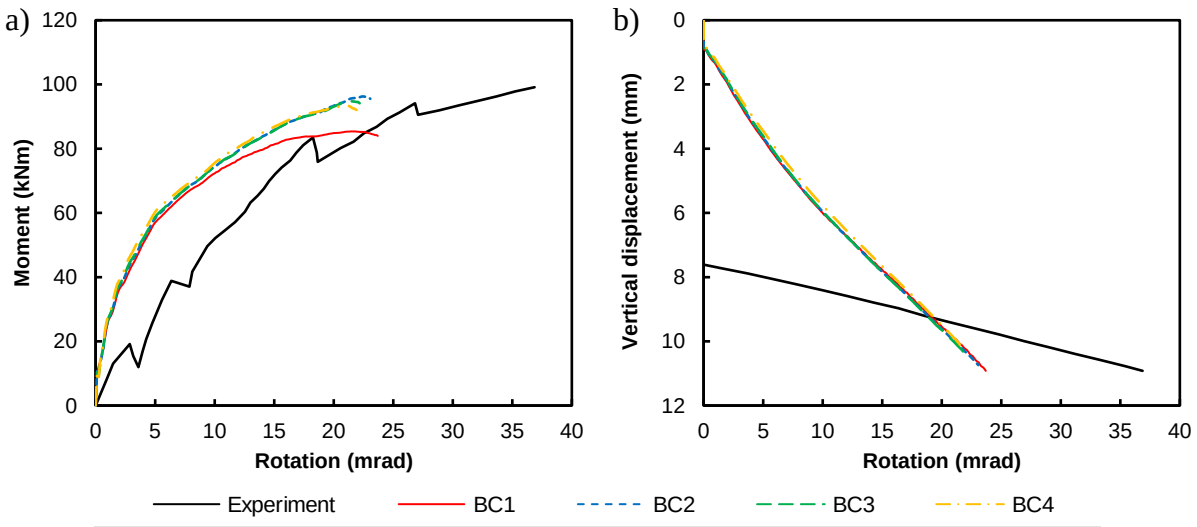

Figure 5.8: Specimen SM 0.5 a) moment-rotation and b) displacement-rotation data for analyses BC1 through BC4

Table 5.5: Specimen SM 0.5 results for analyses BC1 through BC4

	Ultimate moment (kNm)	Displacement (mm) at ultimate moment	Rotation (mrad) at ultimate moment
Analyses			
BC1	85.4	10.0	21.4
BC2	96.3	10.5	22.4
BC3	94.8	10.2	21.4
BC4	93.5	9.9	21.0
Experiment	99.1	10.9	36.9

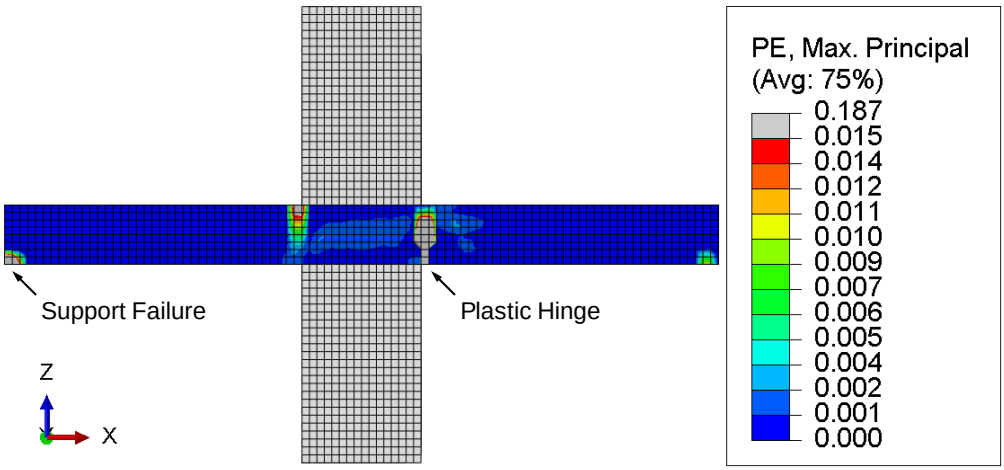

Figure 5.9: Specimen SM 0.5 analysis BC1 failure mechanism

The top face crack patterns of the experiment and analyses BC1 through BC4 for specimen SM 0.5 are shown in Figure 5.10. Among the top face crack patterns, cracks formed from the column faces to the outermost support elements on each slab edge. Analyses BC1 and BC2 showed cracking similar to the experiment as the cracks did not propagate to the corners. Analysis BC3 showed strain concentrations in the support elements by the slab corners. This indicated that those outermost elements were failing due to the corner lifting under the applied moment. Similar to analysis BC3, analysis BC4 showed significant strain concentrations in the slab corner regions. These concentrations were not present in the experiment crack patterns.

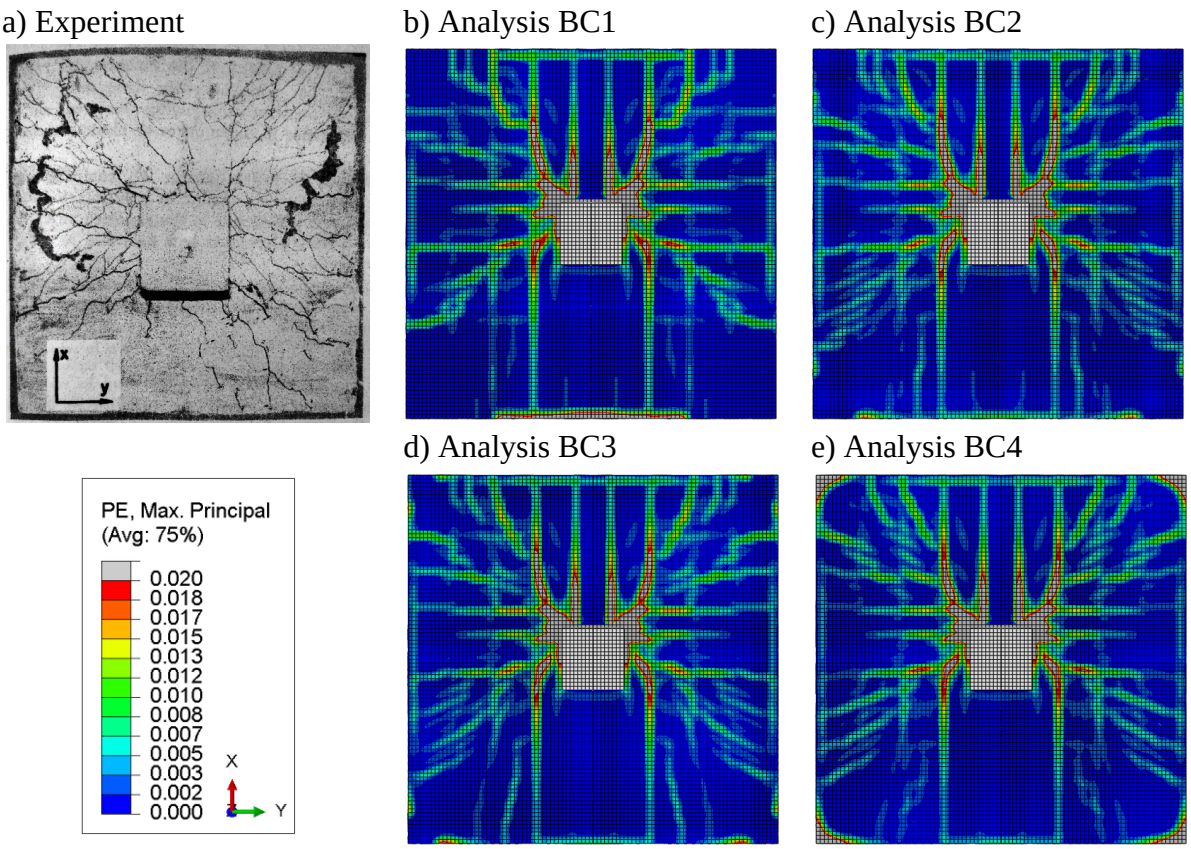

Figure 5.10: Specimen SM 0.5 top face experiment (Ghali et al., 1976) and analyses crack patterns for boundary condition analyses BC1 through BC4. Authorized reprint of experiment photograph from ACI Journal, Volume 73, Issue 10, October 1976.

The bottom face crack patterns of the experiment and analyses BC1 through BC4 for specimen SM 0.5 are shown in Figure 5.11. All analyses had cracks form from the bottom column face towards the slab edges and bottom corners. All analyses showed cracks forming from the column faces toward the edges and the outermost restrained slab elements. As the support lengths increase from analysis BC1 through BC4, two trends were evident. First, the maximum principal plastic strains (i.e. cracks) forming from the bottom column face toward the left and right slab edges decreased. Second, higher maximum principal plastic strains were present diagonally from the bottom column face toward the outer restrained slab elements. With increased support lengths, more edge elements were restrained, stresses to the supports were redistributed, and therefore, the crack patterns changed.

All analyses produced bottom face crack patterns that resembled those produced during the laboratory experiment. From the bottom column face, all analyses had the same lateral, diagonal, and vertical cracks; only the magnitude of each of these cracks (strains) differed between

analyses. These differences are negligible. Although larger strain magnitudes indicate larger crack widths, the photographed experiment cracks would be closed since the specimen would be unloaded before photographing.

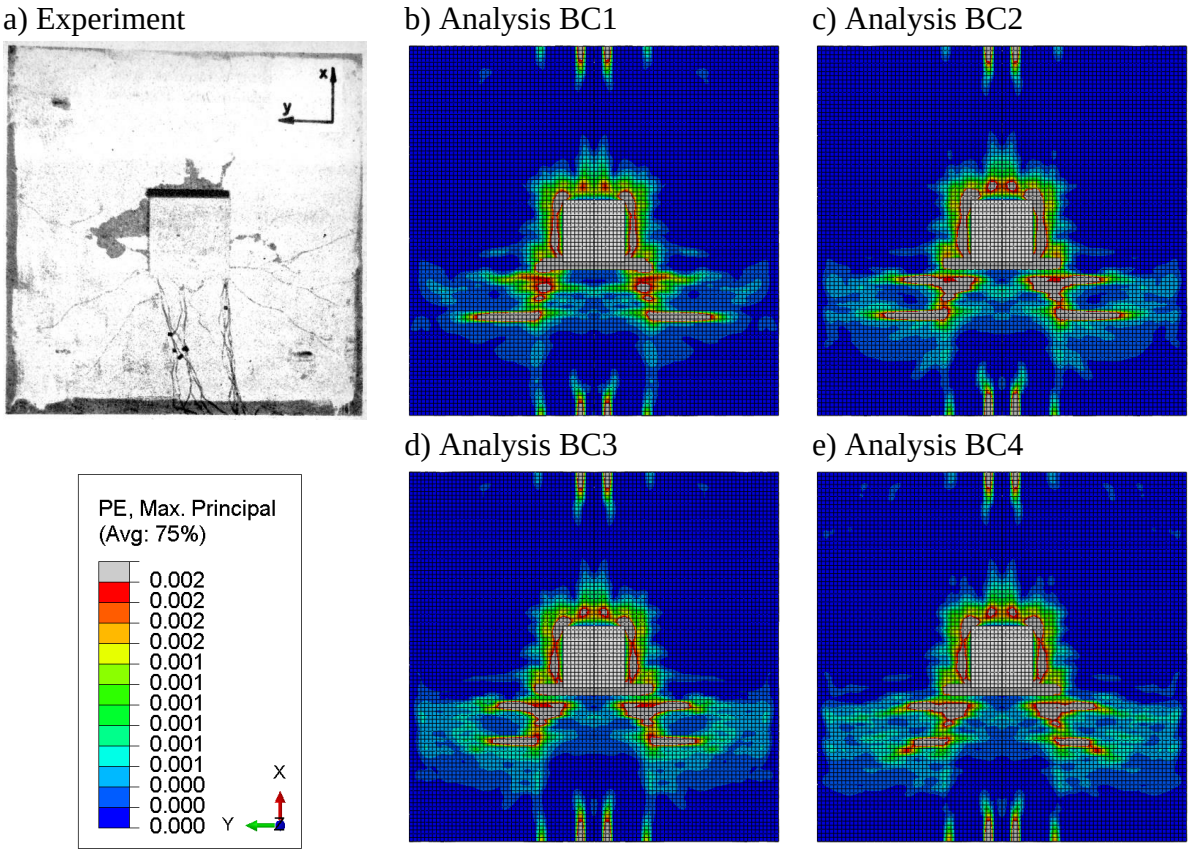

Figure 5.11: Specimen SM 0.5 bottom face experiment (Ghali et al., 1976) and analyses crack patterns for boundary condition analyses BC1 through BC4. Authorized reprint of experiment photograph from ACI Journal, Volume 73, Issue 10, October 1976.

5.2.1.2 Results of analyses BC1-E through BC4-E

The moment-rotation and displacement-rotation data for specimen 0.5 analyses BC1-E through BC4-E are presented in Figure 5.12. A summary of this data is provided in Table 5.6. Analyses BC1-E through BC4-E had moment-rotation data discontinuities that were caused by failures in the flexural reinforcement. The removal of the slab edge restraint made it such that only one direction of reinforcement was active throughout analyses. The added stresses in the active reinforcement resulted in reinforcement failure occurring at a lower applied moment. The moment-rotation slopes are similar between the "E" and non-"E" analyses until approximately 20 kNm. Past 20 kNm, it is likely that the two sets of analyses would be similar had the restrained

slab elements used a linear-elastic material and were not able to fail. Analyses BC1-E through BC4-E ultimately failed under lower applied moments compared to their respective BC1 through BC4 analyses. On average, the "E" analyses had ultimate moments 33-percent lower than their non-"E" counterparts and 38-percent lower than the experiment. The moment-rotation data of all analyses plateaued toward the end of the analyses. Unlike the non-"E" analyses, these analyses failed in flexure. The analyses showed lower rotations at ultimate moments due to their lower moment capacities.

Analyses BC1-E through BC4-E had higher displacements at the start of moment application compared to analyses BC1 through BC4. Furthermore, the displacement-rotation slopes were softer throughout the application of moment compared to the non-"E" analyses. A softer response was expected as fewer elements were restrained to resist stresses. However, additional softening was caused by support elements becoming inactive due to the aforementioned crushing failure.

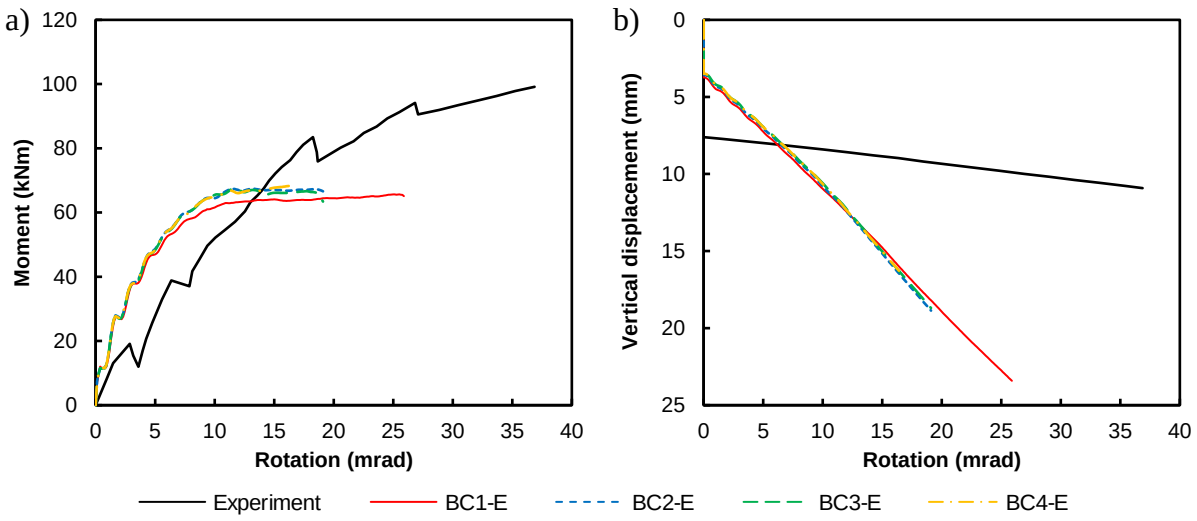

Figure 5.12: Specimen SM 0.5 a) moment-rotation and b) displacement-rotation data for analyses BC1-E through BC4-E

Table 5.6: Specimen SM 0.5 results for analyses BC1-E through BC4-E

	Ultimate moment (kNm)	Displacement (mm) at ultimate moment	Rotation (mrad) at ultimate moment
Analyses			
BC1-E	65.6	23.1	25.5
BC2-E	67.4	13.5	13.2
BC3-E	67.5	12.0	11.7
BC4-E	68.4	16.3	16.4
Experiment	99.1	10.9	36.9

The top face crack patterns of the experiment and analyses BC1-E through BC4-E for specimen SM 0.5 are shown in Figure 5.13. When the two slab edge restraints were removed, the specimen changed from a two-way slab to a one-way slab. As such, diagonal cracking was reduced and horizontal cracking increased. The crack patterns of analysis BC1-E most clearly show the compressive support failure common to all analyses.

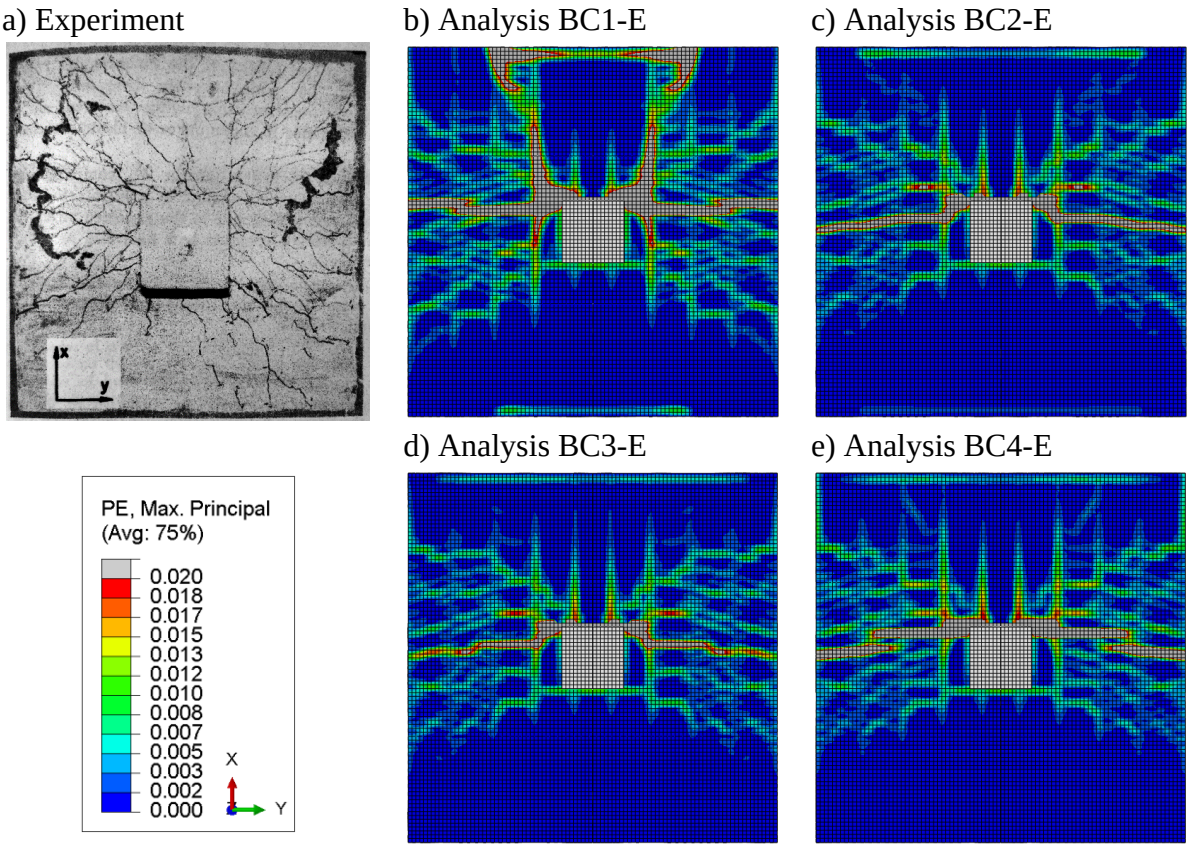

Figure 5.13: Specimen SM 0.5 top face experiment (Ghali et al., 1976) and analyses crack patterns for boundary condition analyses BC1-E through BC4-E. Authorized reprint of experiment photograph from ACI Journal, Volume 73, Issue 10, October 1976.

The bottom face crack patterns of the experiment and analyses BC1-E through BC4-E for specimen SM 0.5 are shown in Figure 5.14. Apart from compression support failure, the cracks from the bottom face towards the slab edges seen among the non-“E” analyses and within the experiment did not form among the “E” analyses.

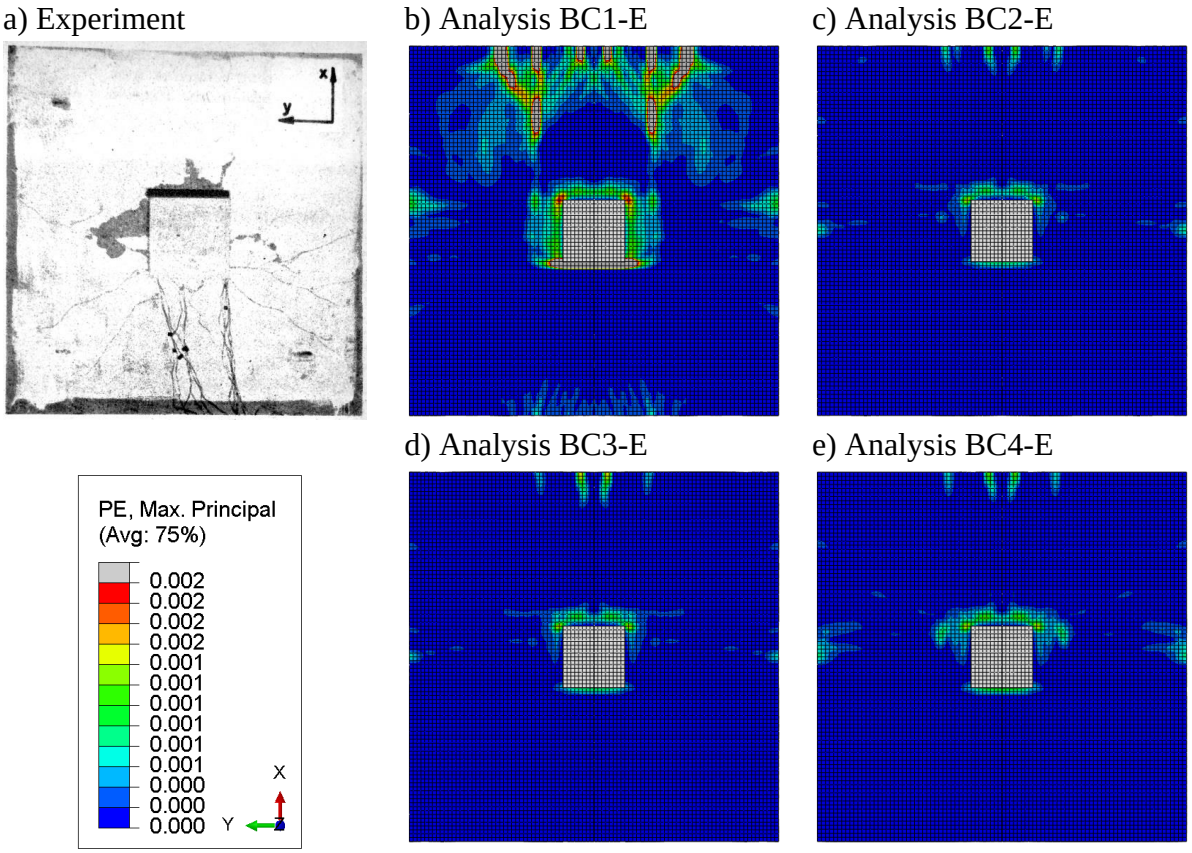

Figure 5.14: Specimen SM 0.5 bottom face experiment (Ghali et al., 1976) and analyses crack patterns for boundary condition analyses BC1-E through BC4-E. Authorized reprint of experiment photograph from ACI Journal, Volume 73, Issue 10, October 1976.

5.2.2 Results of specimen SM 1.0 analyses

5.2.2.1 Analyses BC1 through BC4

The moment-rotation and displacement-rotation data for specimen 1.0 analyses BC1 through BC4 are presented in Figure 5.15. A summary of this data is provided in Table 5.7.

All analyses but BC1 showed identical behaviour to one another. The dissimilarities in the analysis BC1 results were caused by the failure of the supports along its lift-resisting slab edge. As with specimen SM 0.5, analysis BC1 had a lower ultimate moment compared to analyses BC2 through BC4. However, this difference in ultimate moment was not as large for specimen SM 1.0 as it was for specimen SM 0.5. This was because specimen SM 1.0 had more reinforcement compared to specimen SM 0.5. The additional reinforcement within the slab-column plastic hinge allowed for higher moments to be applied before ultimate failure.

Similar displacement-rotation behaviour was observed for specimen SM 1.0 as for specimen SM 0.5. The failure of the lift-resisting slab edge elements caused the slab edge to lift. This decreased the displacement-rotation slope because the upward column displacement due to support failure counteracted the downward column displacement due to the column loading.

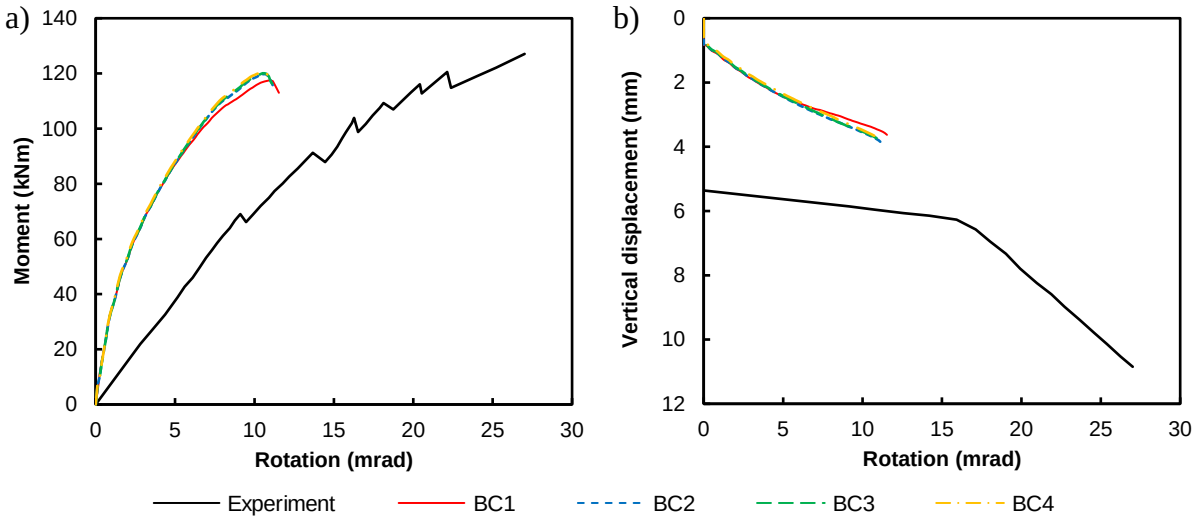

Figure 5.15: Specimen SM 1.0 a) moment-rotation and b) displacement-rotation data for analyses BC1 through BC4

Table 5.7: Specimen SM 1.0 results for analyses BC1 through BC4

	Ultimate moment (kNm)	Displacement (mm) at ultimate moment	Rotation (mrad) at ultimate moment
Analyses			
BC1	117.5	3.5	11.0
BC2	119.8	3.7	10.6
BC3	120.1	3.7	10.6
BC4	120.5	3.6	10.5
Experiment	127.1	10.8	27.0

The crack patterns of the experiment and analyses BC1 through BC4 for specimen SM 1.0 are shown in Figure 5.16. The cracks propagated from the column toward the outermost restrained elements on each side of the slab. As the support length was increased, the angles between these cracks increased. This trend was easier to observe among the bottom face crack patterns than the top face crack patterns. The bottom face crack patterns of analysis BC1 show two groups of cracks from the bottom column face outward toward the center of the bottom slab edge. The angle between these groups of cracks increases in analysis BC2 through BC4 as the support length is increased.

a) Top face, analysis BC1

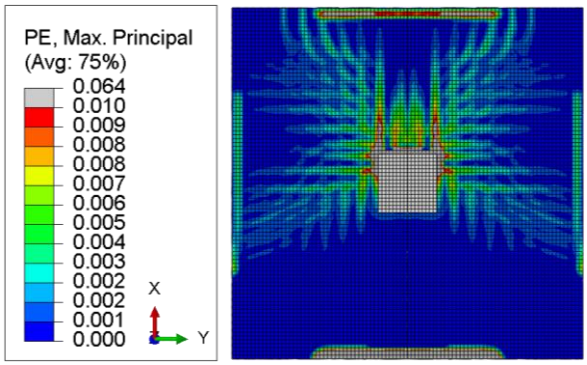

b) Bottom face, analysis BC1

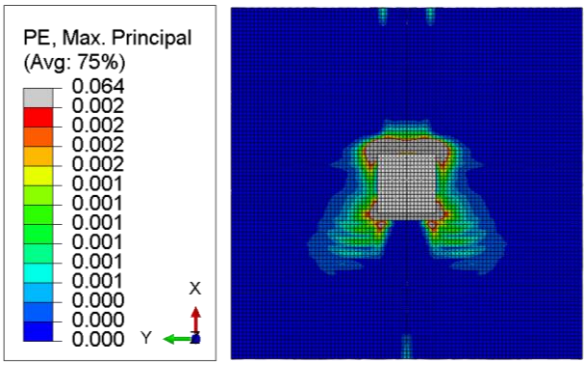

c) Top face, analysis BC2

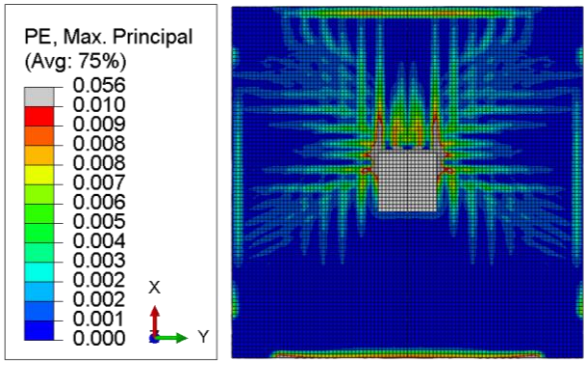

d) Bottom face, analysis BC2

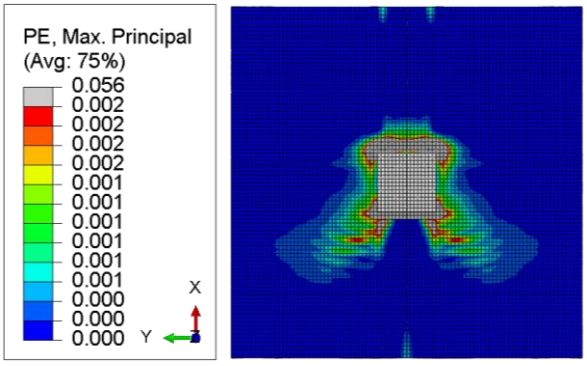

e) Top face, analysis BC3

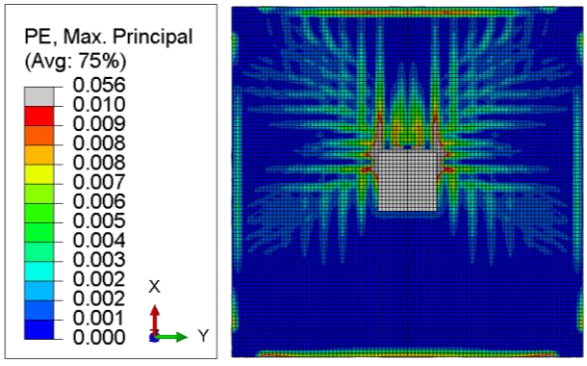

f) Bottom face, analysis BC3

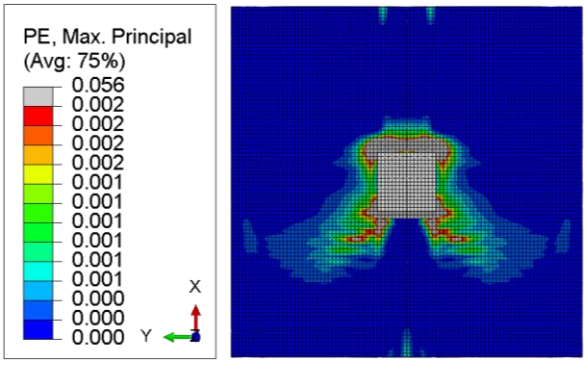

g) Top face, analysis BC4

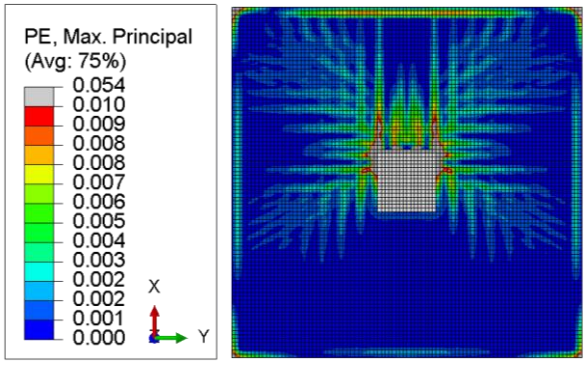

h) Bottom face, analysis BC4

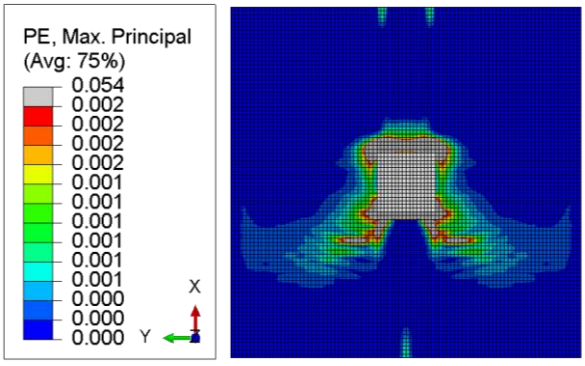

Figure 5.16: Specimen SM 1.0 analyses crack patterns for boundary condition analyses BC1 through BC4

5.2.2.2 Analyses BC1-E through BC4-E

The moment-rotation and displacement-rotation data for specimen 1.0 analyses BC1-E through BC4-E are presented in Figure 5.17. A summary of this data is provided in Table 5.8.

Removing the edge restraints orthogonal to the moment axis had little influence on the moment-rotation data of the analyses. The stiffness differences between the "E" analyses and their respective non-"E" analyses were negligible. A 5 kNm ultimate moment decrease was observed when the edge restraints were removed. The removal of the edge restraints lead to larger downward column displacements. As a result, some slab-column connection elements failed due to excessive strains. This lead to a lower rotational stiffness and ultimate moment as fewer elements were active to prevent rotations and resist forces caused by the applied moment.

All analyses showed similar displacement-rotation data to one another. Analyses BC1-E through BC4-E showed larger vertical displacements prior to the application of moment compared to analyses BC1 through BC4. This was expected as fewer restrained elements were present to increase the stiffness of the slab-column connection. The displacement-rotation slopes of these analyses were steeper than their non-"E" counterparts. The removal of support restraints changed the specimen from a two-way slab to a one-way slab. The stresses within the elements between the column and the now unrestrained slab edge were redistributed to the elements between the column and the two remaining slab edge restraints. These additional stresses resulted in more strain-softening. These decreases in element stiffness resulted in a softer displacement-rotation response.

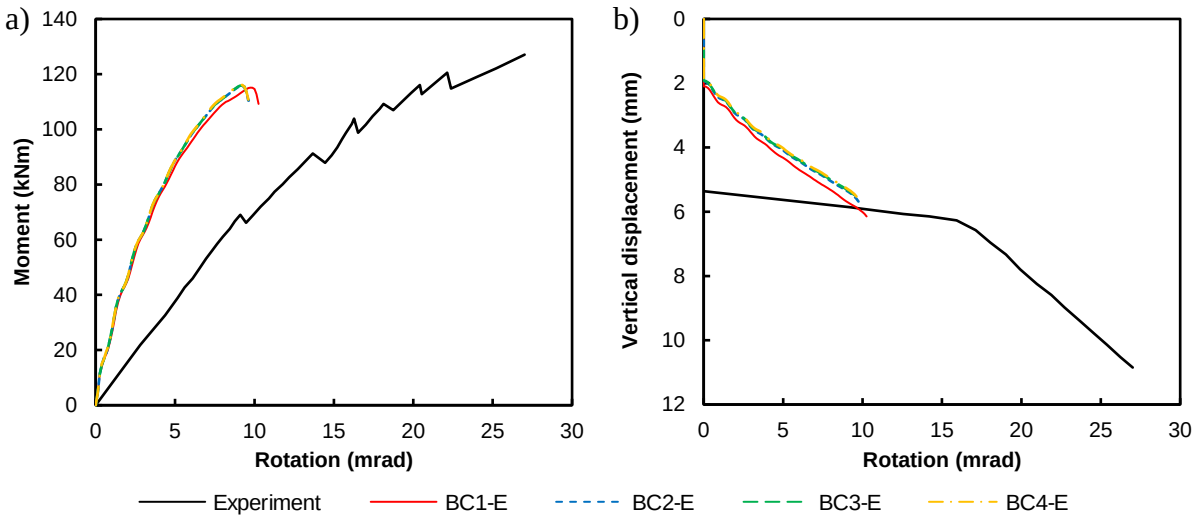

Figure 5.17: Specimen SM 1.0 a) moment-rotation and b) displacement-rotation data for analyses BC1-E through BC4-E

Table 5.8: Specimen SM 1.0 results for analyses BC1-E through BC4-E

	Ultimate moment (kNm)	Displacement (mm) at ultimate moment	Rotation (mrad) at ultimate moment
Analyses			
BC1-E	115.1	5.9	9.7
BC2-E	115.7	5.4	9.1
BC3-E	115.8	5.3	9.1
BC4-E	116.1	5.3	9.2
Experiment	127.1	10.8	27.0

The top face crack patterns of the experiment and analyses BC1-E through BC4-E for specimen SM 1.0 are shown in Figure 5.18. Among both top and bottom face crack patterns, the previously observed vertical cracks were not present after removing the slab edge. This was expected as the cracks form perpendicular to compressive stresses and stresses were no longer being transferred to the left and right slab edges.

a) Top face, analysis BC1-E

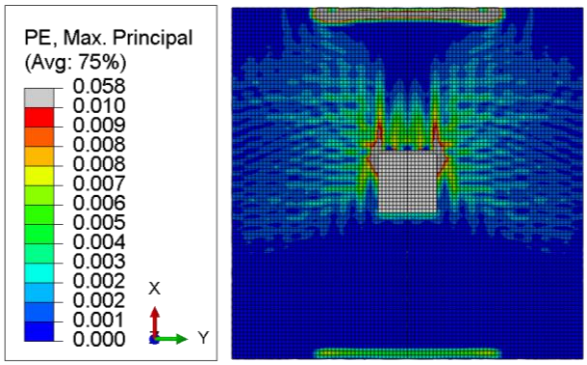

b) Bottom face, analysis BC1-E

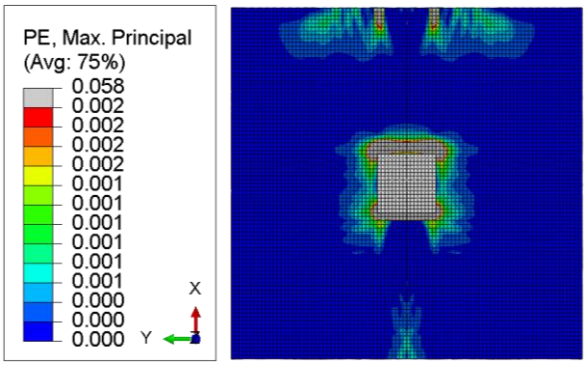

c) Top face, analysis BC2-E

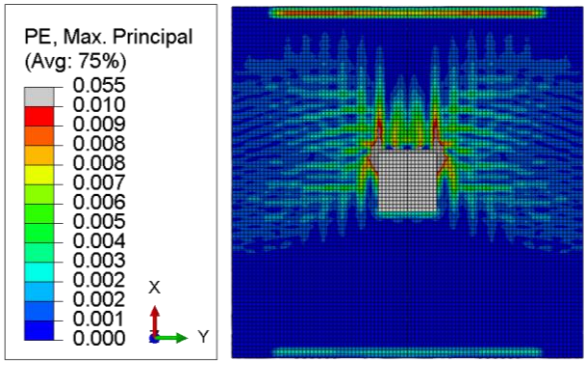

d) Bottom face, analysis BC2-E

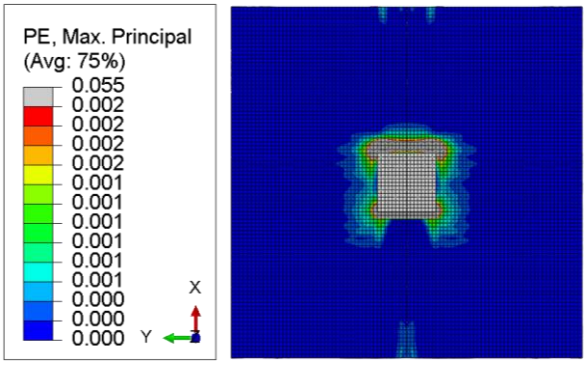

e) Top face, analysis BC3-E

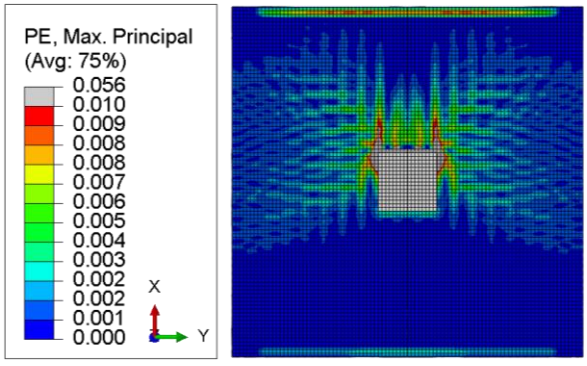

f) Bottom face, analysis BC3-E

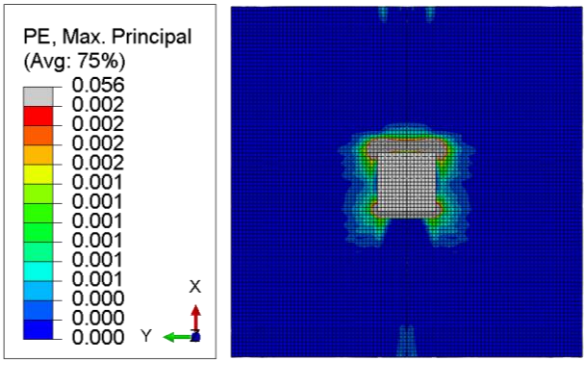

g) Top face, analysis BC4-E

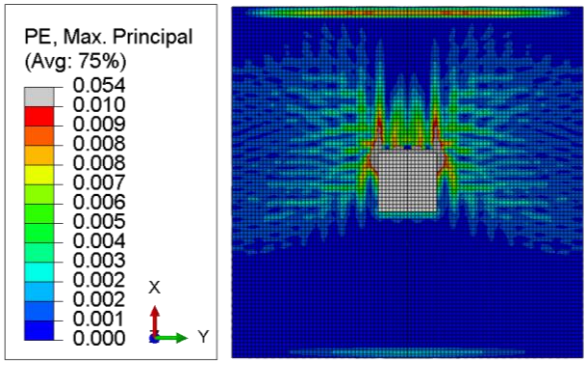

h) Bottom face, analysis BC4-E

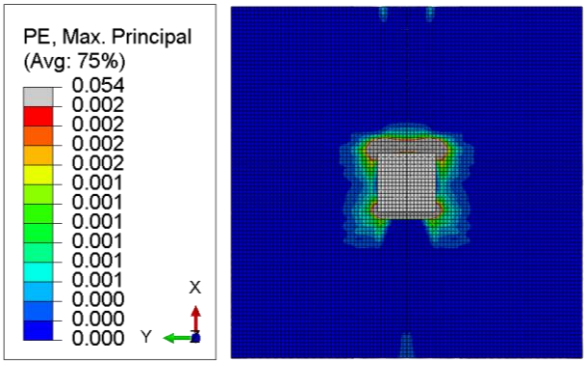

Figure 5.18: Specimen SM 1.0 analyses crack patterns for boundary condition analyses BC1-E through BC4-E

5.2.3 Results of specimen SM 1.5 analyses

5.2.3.1 Results of analyses BC1 through BC4

The moment-rotation and displacement-rotation data for specimen 1.5 analyses BC1 through BC4 are presented in Figure 5.19. A summary of this data is provided in Table 5.9.

Analyses BC2 through BC4 produced identical moment-rotation and displacement-rotation data. Analysis BC1 behaved differently due to tensile failures among its lifting edge support elements.

The effects of the failure were visible from 5 mrad until ultimate failure. For rotations greater than 5 mrad, the lifting edge support elements became inactive and additional stresses were being transferred to the support elements along the edge orthogonal to the failing slab edge. The failure of these elements caused the slab edge to lift and therefore, cause the column to move upwards. The upward movement caused by the support failure added to the downward displacement caused by the vertical load created a net displacement of zero. Furthermore, the lifting of the failing slab edge caused some rigid body motion of the slab.

Unlike the BC1 analyses of specimens SM 0.5 and SM 1.0, specimen SM 1.5 did not have a lower ultimate moment than analyses BC2 through BC4. The additional reinforcement in specimen SM 1.5 prevented the formation of the plastic hinge observed with specimens SM 0.5 and SM 1.0. As such, the slab underwent rigid body motion through the failure of the support elements and did not reduce the moment capacity.

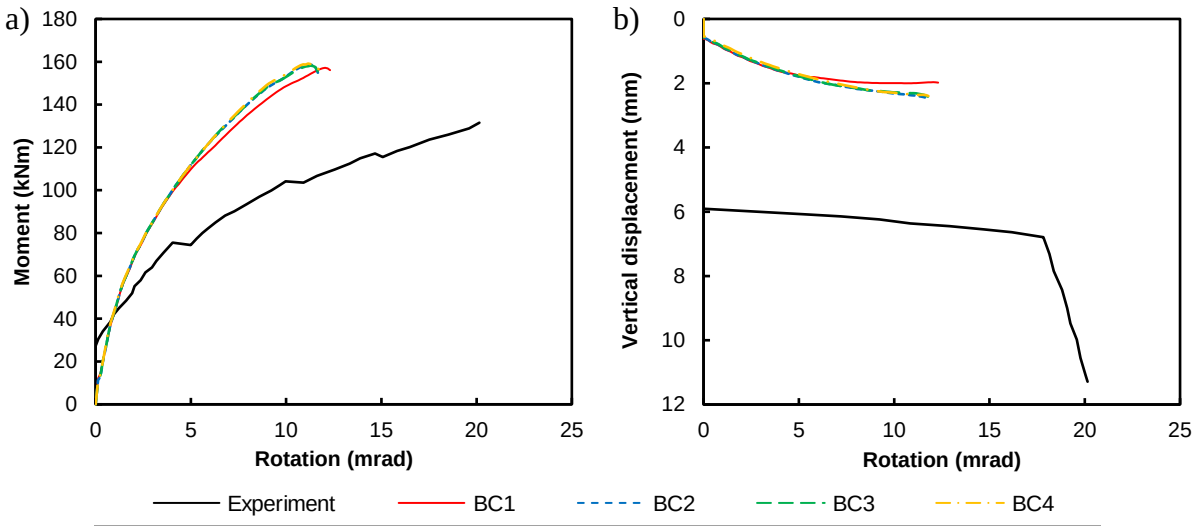

Figure 5.19: Specimen SM 1.5 a) moment-rotation and b) displacement-rotation data for analyses BC1 through BC4

Table 5.9: Specimen SM 1.5 results for analyses BC1 through BC4

	Ultimate moment (kNm)	Displacement (mm) at ultimate moment	Rotation (mrad) at ultimate moment
Analyses			
BC1	157.2	2.0	12.1
BC2	158.7	2.4	11.3
BC3	158.2	2.3	11.3
BC4	159.2	2.4	11.4
Experiment	131.5	11.3	20.1

The top face crack patterns of the experiment and analyses BC1 through BC4 for specimen SM 1.5 are shown in Figure 5.20. As with the other specimens, increasing the support length resulted in increased angles between the diagonal cracks which form between the column and slab edges.

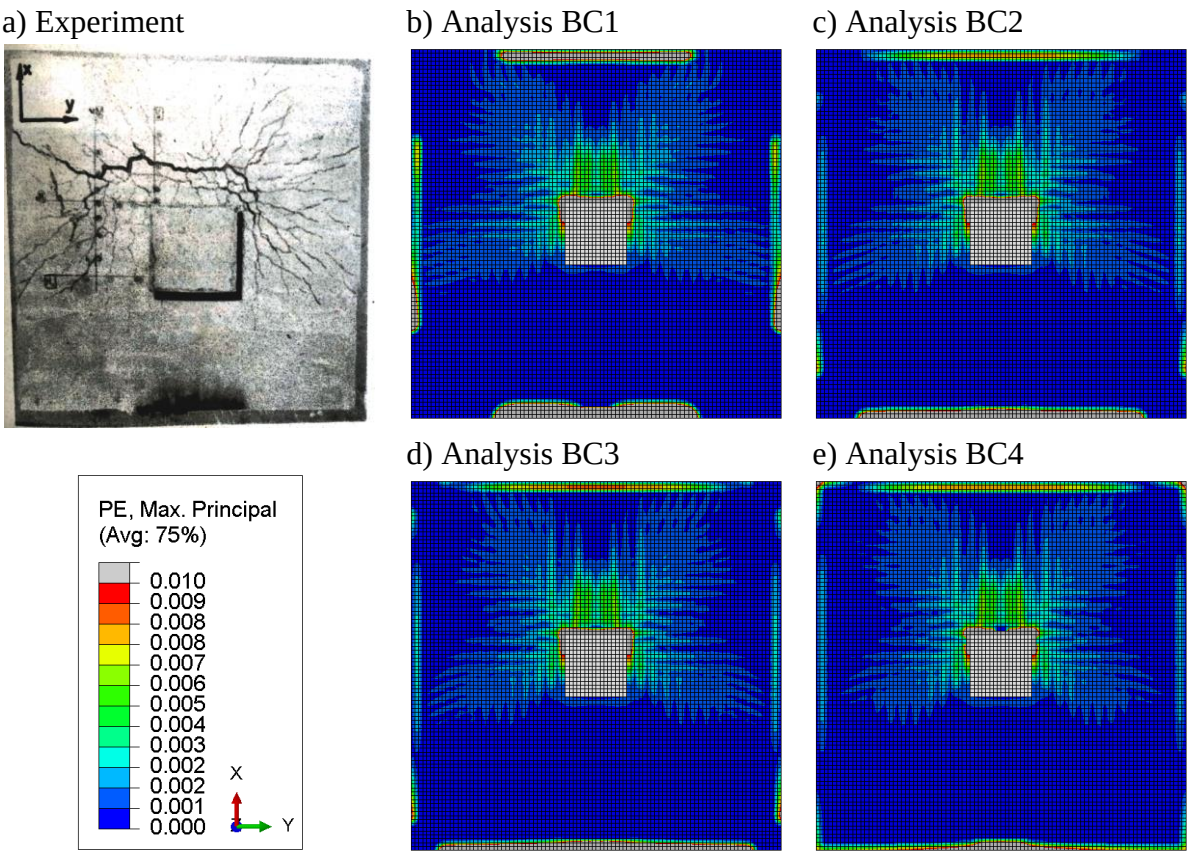

Figure 5.20: Specimen SM 1.5 top face experiment (Ghali et al., 1976) and analyses crack patterns for boundary condition analyses BC1 through BC4. Authorized reprint of experiment photograph from ACI Journal, Volume 73, Issue 10, October 1976.

The bottom face crack patterns of the experiment and analyses BC1 through BC4 for specimen SM 1.5 are shown in Figure 5.21. The two vertical cracks visible in analysis BC1 became diagonal as the support length was increased in analysis BC2. The angle between these cracks increased with subsequent support length increases in analyses BC3 and BC4.

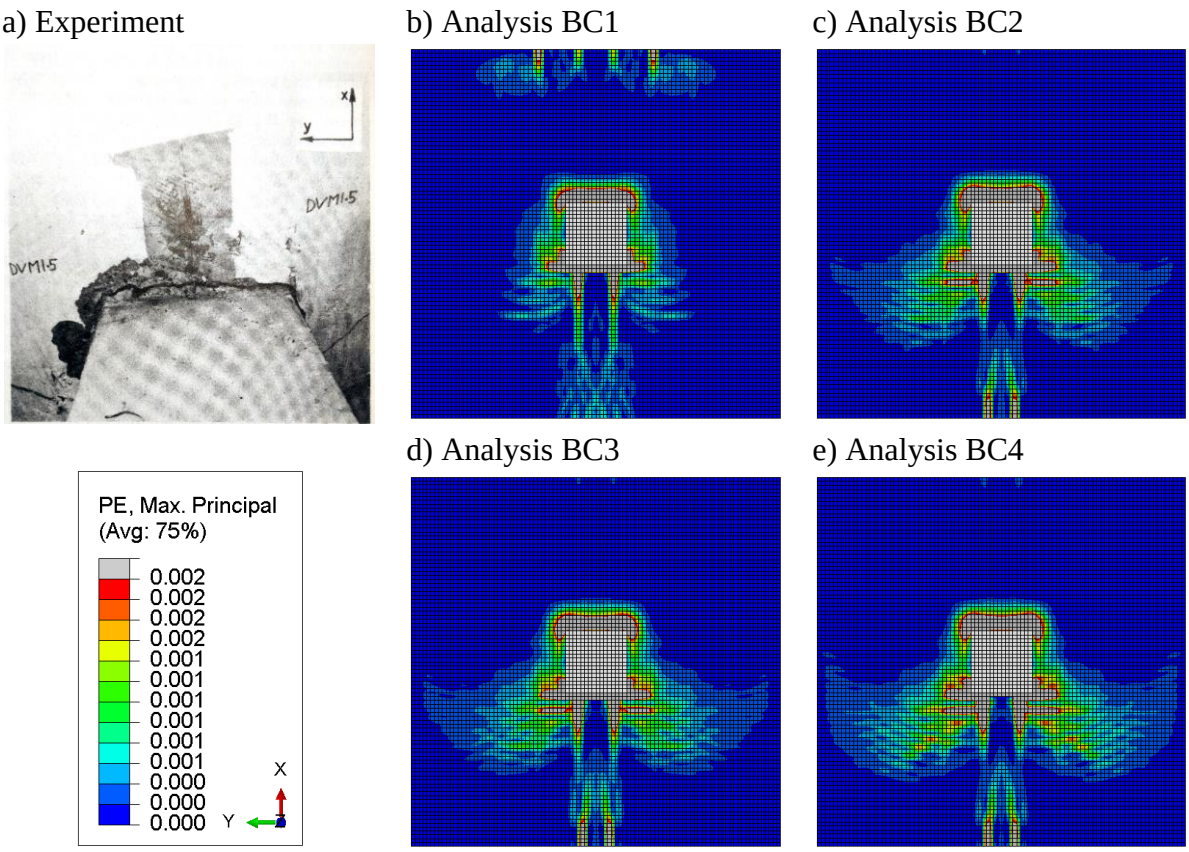

Figure 5.21: Specimen SM 1.5 bottom face experiment (Ghali et al., 1976) and analyses crack patterns for boundary condition analyses BC1 through BC4. Authorized reprint of experiment photograph from ACI Journal, Volume 73, Issue 10, October 1976.

5.2.3.2 Results of analyses BC1-E through BC4-E

The moment-rotation and displacement-rotation data for specimen 1.5 analyses BC1-E through BC4-E are presented in Figure 5.22. A summary of this data is provided in Table 5.10.

Analyses BC1-E through BC4-E produced similar moment-rotation and displacement-rotation results to one another. Compared to analyses BC1 through BC4, analyses BC1-E through BC4-E showed similar moment-rotation behaviour until failure. However, the ultimate moments of each "E" analysis were regularly 5 kNm less than its respective non-"E" analysis. This was consistent with the behaviour observed among the analyses for specimen SM 1.0. The displacement-rotation data of all analyses were nearly identical. The initial displacement values were higher than those of the non-"E" analyses as the removal of the slab edge restraint decreased vertical stiffness. This decreased vertical stiffness was evident by the steeper displacement-rotation data as larger moments were applied on the column.

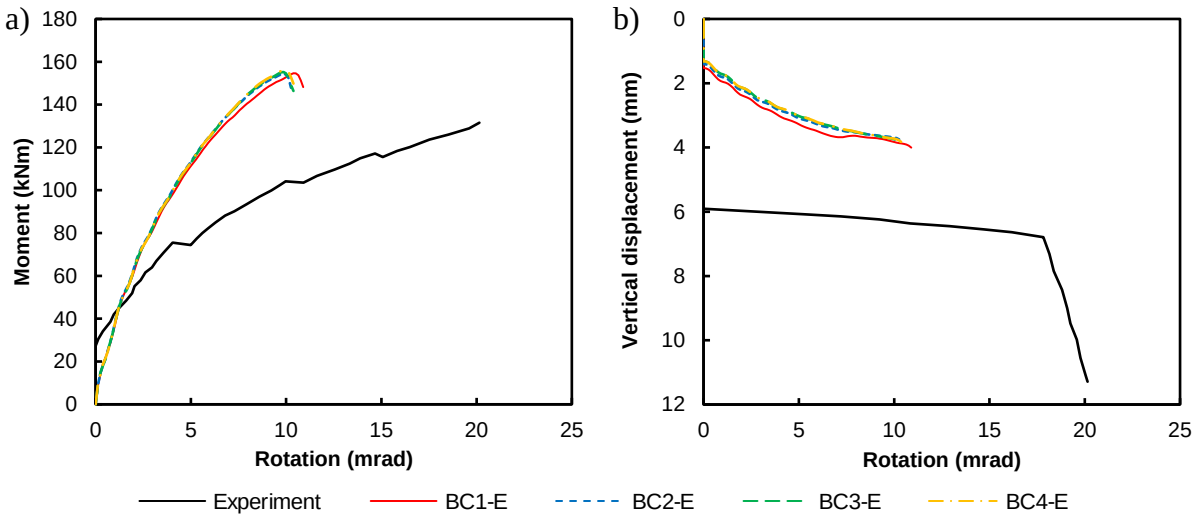

Figure 5.22: Specimen SM 1.5 a) moment-rotation and b) displacement-rotation data for analyses BC1-E through BC4-E

Table 5.10: Specimen SM 1.5 results for analyses BC1-E through BC4-E

	Ultimate moment (kNm)	Displacement (mm) at ultimate moment	Rotation (mrad) at ultimate moment
Analyses			
BC1-E	154.6	3.9	10.4
BC2-E	154.5	3.7	9.9
BC3-E	155.2	3.7	9.9
BC4-E	156.3	3.7	9.9
Experiment	131.5	11.3	20.1

The top face crack patterns of the experiment and analyses BC1-E through BC4-E for specimen SM 1.5 are shown in Figure 5.23. The support length had little influence on the crack patterns. Compared to analyses BC1 through BC4, analyses BC1-E through BC4-E showed similar horizontal cracks but no longer developed vertical cracks. This is consistent with the trends observed for specimens SM 0.5 and SM 1.0.

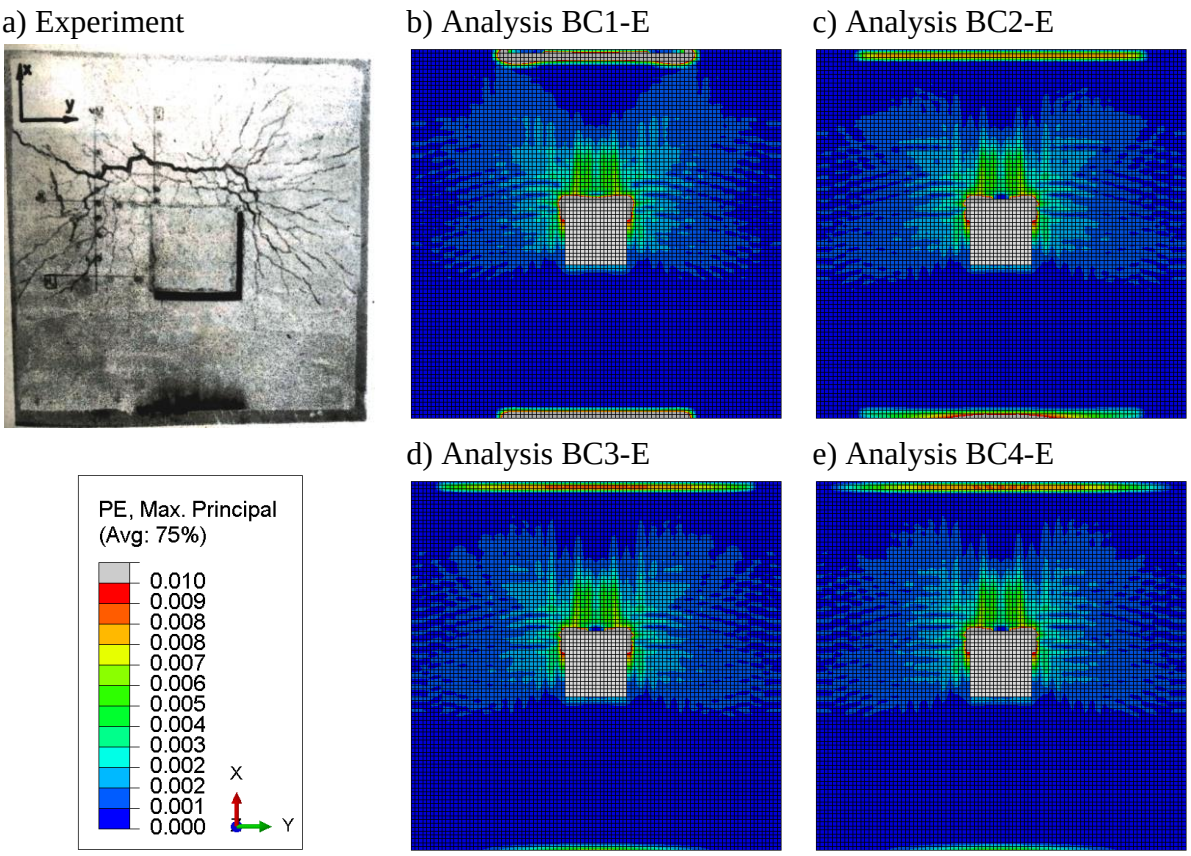

Figure 5.23: Specimen SM 1.5 top face experiment (Ghali et al., 1976) and analyses crack patterns for boundary condition analyses BC1-E through BC4-E. Authorized reprint of experiment photograph from ACI Journal, Volume 73, Issue 10, October 1976.

The bottom face crack patterns of the experiment and analyses BC1-E through BC4-E for specimen SM 1.5 are shown in Figure 5.24. All analyses produced similar crack patterns to one another. Unlike analyses BC1 through BC4, these analyses did not have as much diagonal cracking from the bottom column faces toward the slab corners. Furthermore, unlike BC1 through BC4, any diagonal cracking did not change as the support length was increased.

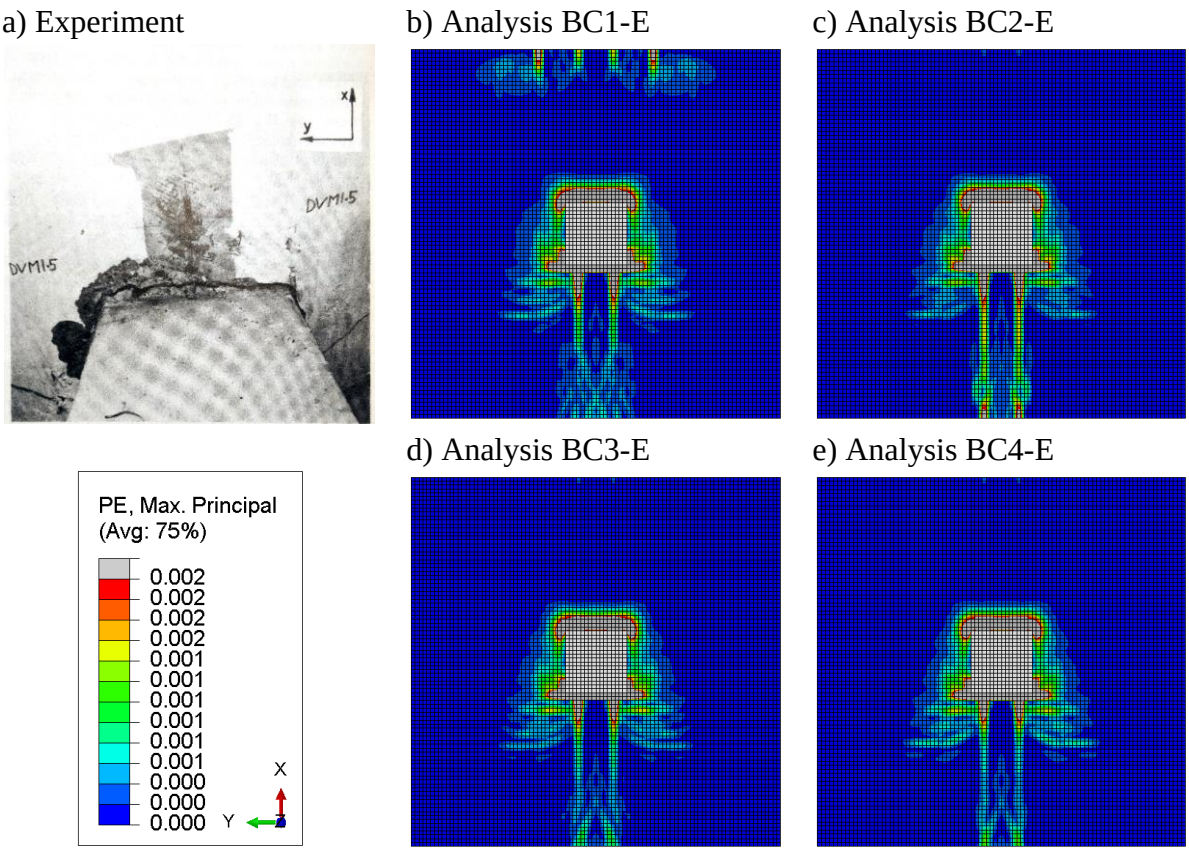

Figure 5.24: Specimen SM 1.5 bottom face experiment (Ghali et al., 1976) and analyses crack patterns for boundary condition analyses BC1-E through BC4-E. Authorized reprint of experiment photograph from ACI Journal, Volume 73, Issue 10, October 1976.

5.2.4 Conclusions and recommendations

Changing the support length had no influence on the moment-rotation nor displacement-rotation responses of the finite element models. As the slabs were restrained along the bottom of their sides, any slab edge lifting resulted in tensile strains among the restrained elements. Due to concrete's low tensile strength, these elements failed under low applied moments and did not have any effect on the rotational stiffness of the models. However, the cracking of these elements contributed to the overall crack patterns. The overall crack patterns were used to determine which support length produced crack patterns most similar to those observed during laboratory testing.

Removing the restraints from the slab edge orthogonal to the axis of the applied moment influenced the displacement-rotation responses but did not influence moment-rotation responses. The removal of these restraints made it such that only one directional reinforcement mat was active. The increased stresses within these reinforcement elements resulted in strain

softening and therefore, larger column displacements. The moment-rotation stiffness was not affected; however, the added stresses resulted in flexural failures occurring prior to slab punching failure.

A support length of 915 mm (i.e. half of the slab length) was used in subsequent calibration analyses. This support length produced crack patterns most similar to the experiment crack patterns. However, using this support length resulted in lifting edge support failures for all specimens. This was because the reaction forces were too large for the few restrained elements to carry without failing. These element failures caused the slab edge to lift. In most cases, this caused the reinforcement within the slab-column connection to fail before punching failure could occur. In all cases, support failure resulted in specimen behaviour that was unrepresentative of the test behaviour.

In subsequent studies, three different options for preventing support failure were examined. Option A was to restraint the top edges along sides of the slab parallel to the moment axis. These restraints were in addition to the restraints along the bottom edges of the slab. Option B was to use a linear-elastic material for the elements along the lifting side of the slab. Finally, option C was to simultaneously add a restraint along the top of the lifting slab edge and remove the restraint along the bottom of the lifting slab edge. This would be done between the vertical loading step and the moment loading step.

5.3 Preventing support failure

5.3.1 Option A: restraining top of failing slab edge

This section examines the accuracy and viability of option A in preventing support failure. Option A requires restraining the top edges along sides of the slab parallel to the moment axis. These top edge restraints were implemented in addition to the restraints along the bottom edges of the slab. The analysis in which only the bottom edges of the slab were restrained is referred to as the base case. The added restraints in option A would provide element confinement and reduce tensile stresses within the elements susceptible to tensile failure. The boundary conditions for option A are presented in Figure 5.25.

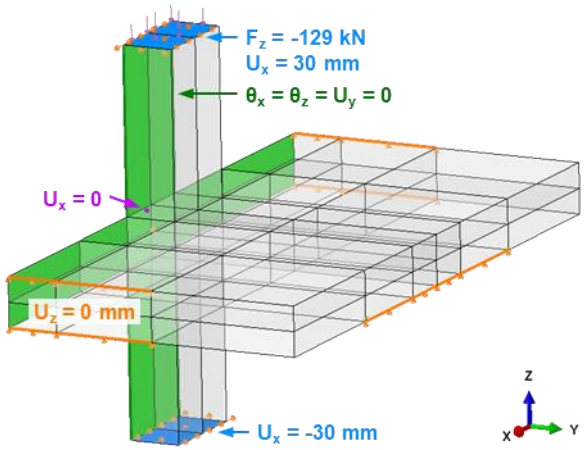

Figure 5.25: Boundary conditions used for option A study of preventing support failure study

The analyses results after implementing option A are shown in Section 5.3.1.1, Section 5.3.1.2, and Section 5.3.1.3 for specimens SM 0.5, SM 1.0, and SM 1.5, respectively. Each section shows comparisons between the option A analysis and the base case analysis. Comparisons are shown between moment-rotation, displacement-rotation, and crack patterns of the analyses and recommendations are made based on the accuracies of the analyses.

5.3.1.1 Results of specimen SM 0.5 analyses

The moment-rotation and displacement-rotation data for option A and base case analyses of specimen 0.5 are presented in Figure 5.26. A summary of this data is provided in Table 5.11.

The addition of the top edge restraints on the slab edges parallel to the moment axis successfully prevented support failure. The moment-rotation data of option A showed an increased stiffness past 5 mrad. Past 10 mrad, option A showed moment-rotation results that were almost parallel to the experimental results. The moment-rotation data of both analyses plateaued as they approached their respective ultimate moments suggesting that they both failed in flexure. This is consistent with the experimental results. The ultimate moment increased from 85 kNm to 92 kNm when restraining the top slab edges in addition to the bottom edges. This meant that the percentage difference between the analysis and the experiment decreased from 15-percent to 8-percent. However, the rotation at ultimate moment decreased.

The displacement-rotation data was identical between both analyses. This meant that the added restraints did not prevent element rotations or displacements.

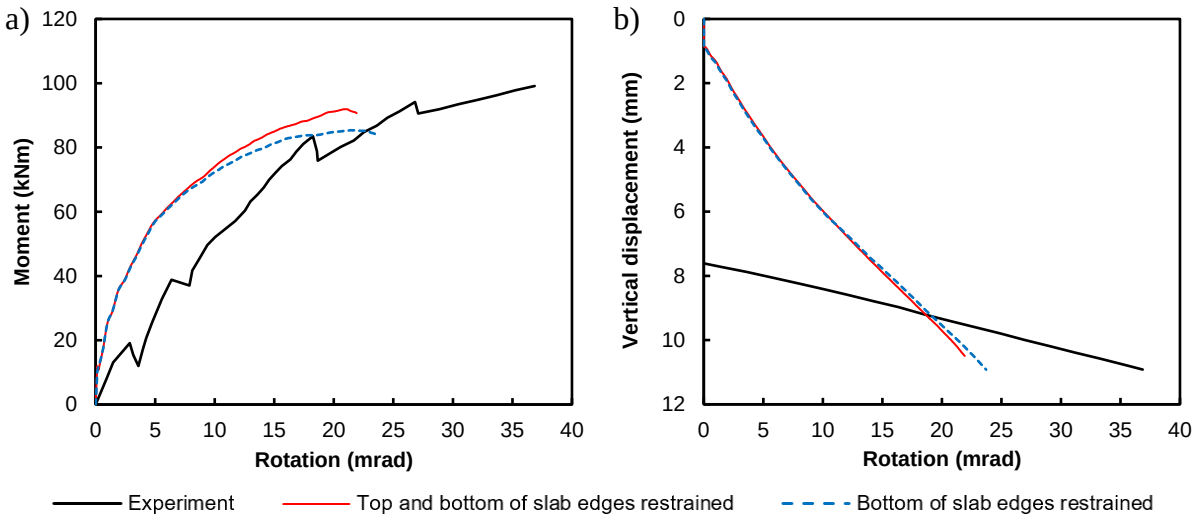

Figure 5.26: Specimen SM 0.5 a) moment-rotation and b) displacement-rotation data for top and bottom of slab edges restrained analysis versus bottom of slab edges restrained analysis

Table 5.11: Specimen SM 0.5 analyses results for top of failing slab edge restrained versus top and bottom of failing slab edges restrained analyses

	Ultimate moment (kNm)	Displacement (mm) at ultimate moment	Rotation (mrad) at ultimate moment
Analyses			
Top and bottom of slab edges restrained	91.9	10.1	21.0
Bottom of slab edges restrained	85.4	10.0	21.4
Experiment	99.1	10.9	36.9

The experiment and analyses crack patterns for option A and base case analyses for specimen SM 0.5 are shown in Figure 5.27. There were few differences in crack patterns between the two analyses. Option A showed much lower strains along the top and bottom supports of the slab compared to the base case. Both analyses were in good agreement with the experimental crack patterns.

a) Top face, experiment

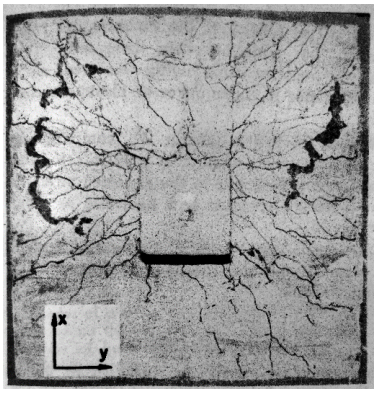

b) Bottom face, experiment

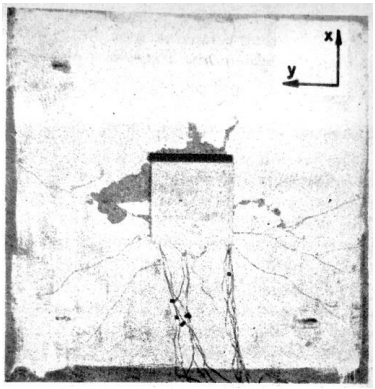

c) Top face, option A

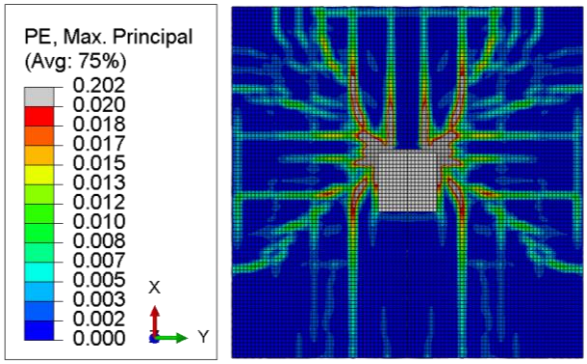

d) Bottom face, option A

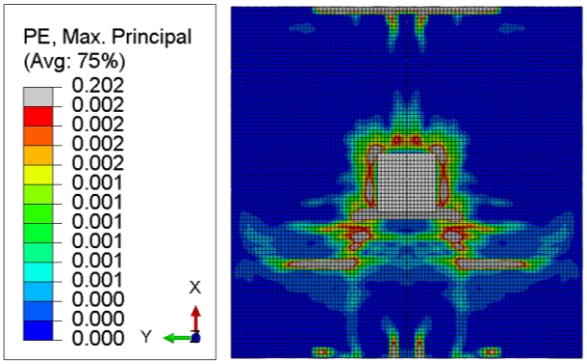

e) Top face, base case

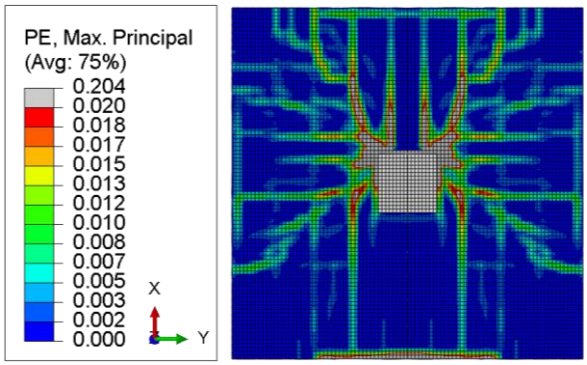

f) Bottom face, base case

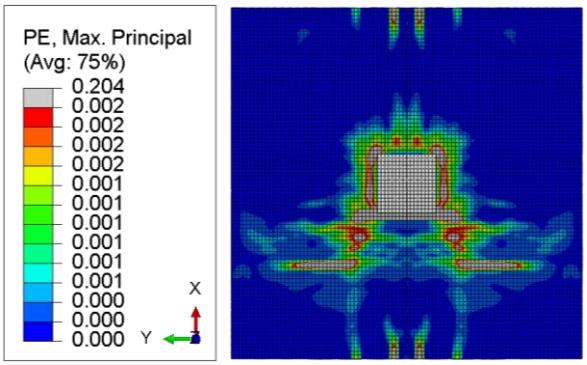

Figure 5.27: Specimen SM 0.5 experiment (Ghali et al., 1976) and analyses crack patterns for option A and base case analyses. Authorized reprint of experiment photographs from ACI Journal, Volume 73, Issue 10, October 1976.

5.3.1.2 Results of specimen SM 1.0 analyses

The moment-rotation and displacement-rotation data for option A and base case analyses of specimen 1.0 are presented in Figure 5.28. A summary of this data is provided in Table 5.12.

The moment-rotation differences between option A and the base case were evident past 6.5 mrad but were negligible. However, option A increased the ultimate moment to 121 kNm from 118

kNm of the base case analysis. The decreased the ultimate moment percentage difference between the analyses and the experiment from 8-percent to 5-percent. With regards to the displacement-rotation data, option A maintained a consistent slope throughout the analysis. The decrease in slope due to support failure did not happen with the option A analysis.

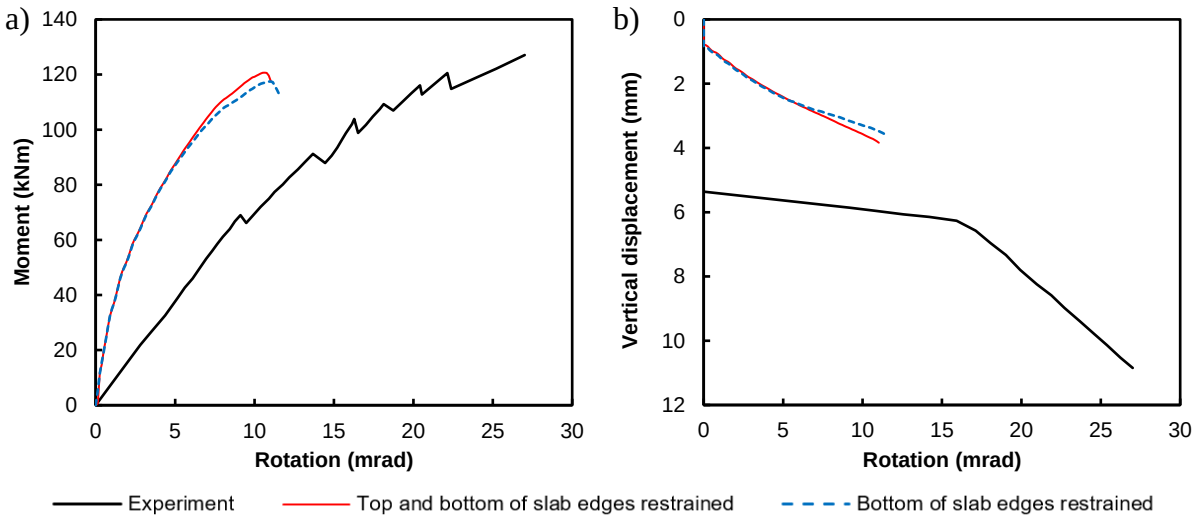

Figure 5.28: Specimen SM 1.0 a) moment-rotation and b) displacement-rotation data for top and bottom of slab edges restrained analysis versus bottom of slab edges restrained analysis

Table 5.12: Specimen SM 1.0 analyses results for top of failing slab edge restrained versus top and bottom of failing slab edges restrained analyses

	Ultimate moment (kNm)	Displacement (mm) at ultimate moment	Rotation (mrad) at ultimate moment
Analyses			
Top and bottom of failing slab edge restrained	120.7	3.7	10.6
Bottom of failing slab edge restrained	117.5	3.5	11.0
Experiment	127.1	10.8	27.0

The analyses crack patterns for option A and base case analyses for specimen SM 1.0 are shown in Figure 5.29. Among the top face crack patterns, option A had significantly lower plastic strains along the top and bottom support edges compared to the base case. This indicated that the lifting-edge supports were no longer failing. The bottom face crack patterns showed wider and longer cracks from the bottom column face toward the bottom slab edge and corners. This was because the support failure in the base case increased the load eccentricity. Therefore,

stresses were being concentrated within the slab-column connection elements by the top column face.

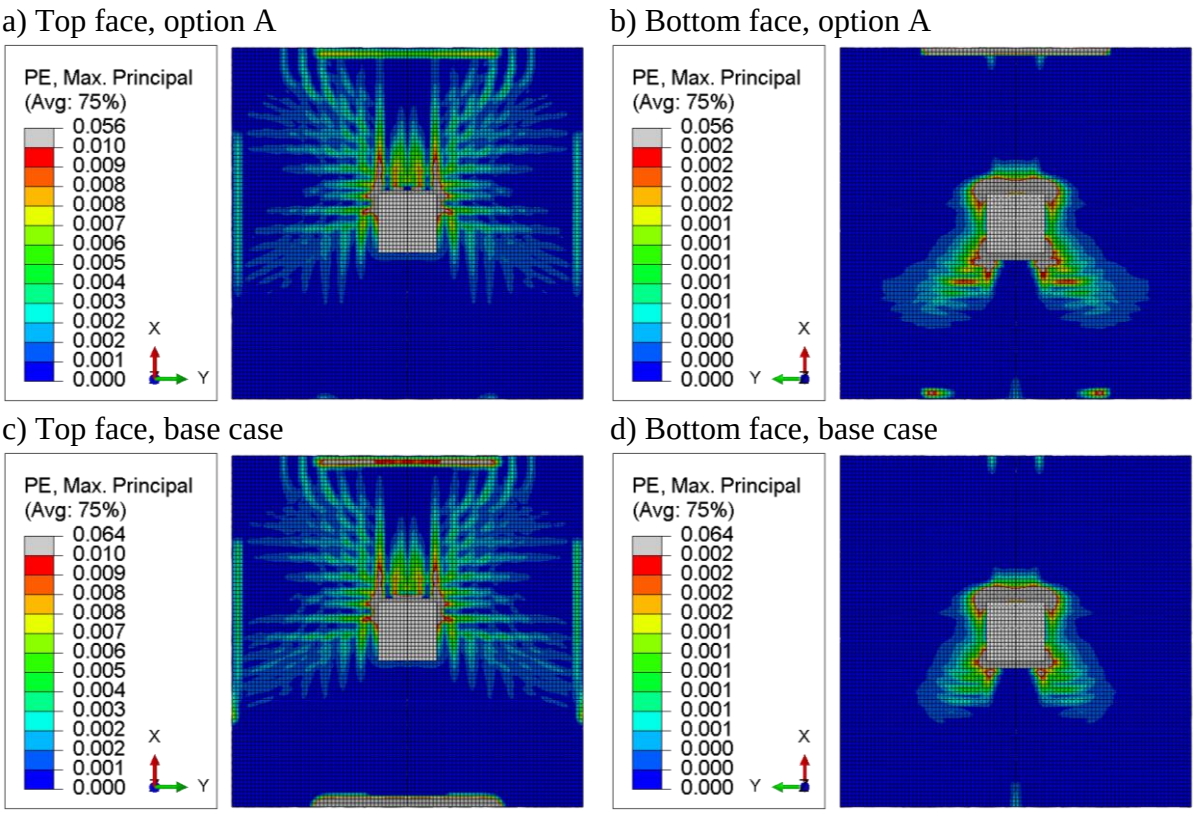

Figure 5.29: Specimen SM 1.0 analyses crack patterns for top and bottom of slab edges restrained analysis versus bottom of slab edges restrained analysis

5.3.1.3 Results of specimen SM 1.5 analyses

The moment-rotation and displacement-rotation data for option A and base case analyses of specimen 1.5 are presented in Figure 5.30. A summary of this data is provided in Table 5.13.

The moment-rotation data of option A showed an increase in stiffness from the base case past 5 mrad. The lower rotational stiffness of the base case was caused by failure of the lift-resisting supports. This failure lead to lifting of the slab edge that contributed to rotations of the column. The increased rotational stiffness of the option A analysis suggested that support failure had not occurred. Although option A resolved the support failure problem, the analysis ultimate moment increased from 157 kNm to 161 kNm. By comparison, the ultimate moment of the experiment was 132 kNm. The ultimate moment percentage difference between the analysis and the experiment increased from 18-percent to 20-percent.

In addition to moment-rotation data, analysis option A produced favourable displacement-rotation data. Past 5 mrad, the plateau observed in the base case data was no longer present. As with the moment rotation data, this suggested that the lifting-resisting supports were active and preventing lift of the slab edge and therefore the column.

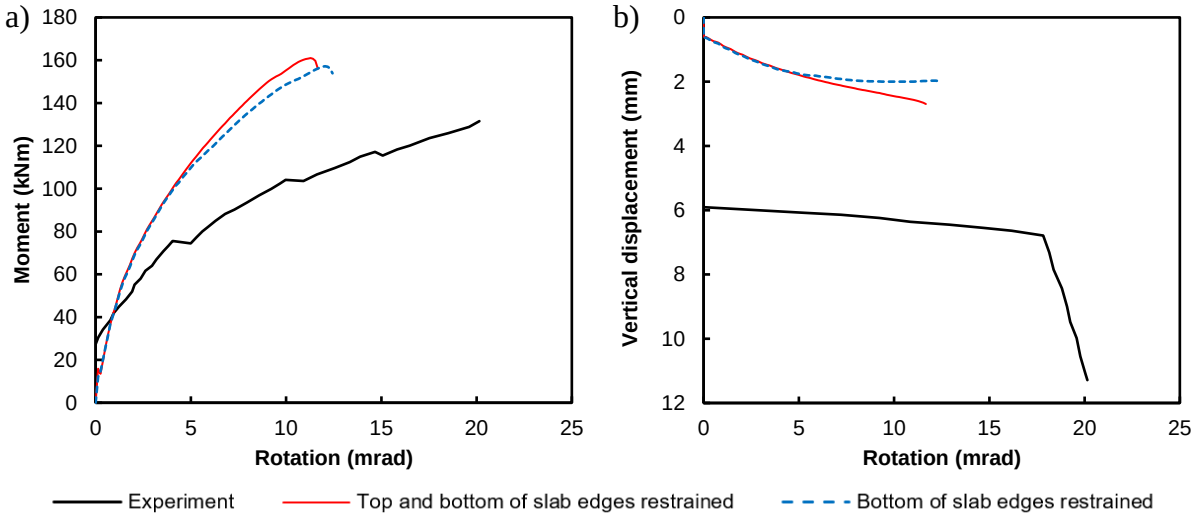

Figure 5.30: Specimen SM 1.5 a) moment-rotation and b) displacement-rotation data for top and bottom of slab edges restrained analysis versus bottom of slab edges restrained analysis

Table 5.13: Specimen SM 1.5 analyses results for top and bottom of slab edges restrained analysis versus bottom of slab edges restrained analysis

	Ultimate moment (kNm)	Displacement (mm) at ultimate moment	Rotation (mrad) at ultimate moment
Analyses			
Top and bottom of failing slab edge restrained	161.0	2.6	11.3
Bottom of failing slab edge restrained	157.2	2.0	12.1
Experiment	131.5	11.3	20.1

The experiment and analyses crack patterns for option A and base case analyses for specimen SM 1.5 are shown in Figure 5.31. As observed with analyses of other specimens, option A reduced strains at the top and bottom support edges of the top face. On the top face, shorter horizontal cracks and longer vertical cracks were observed in the option A results compared to the base case results. The top face crack patterns of option A were in better agreement with the experimental crack patterns compared to the base case. On the bottom face, more cracks were

visible propagating from the bottom column face toward the bottom slab corners. This area was not shown in the photograph of the experiment crack patterns; therefore, it is not possible to say which of the two analyses had more accurate bottom face crack patterns.

a) Top face, experiment

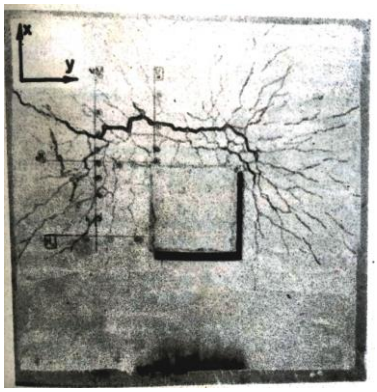

b) Bottom face, experiment

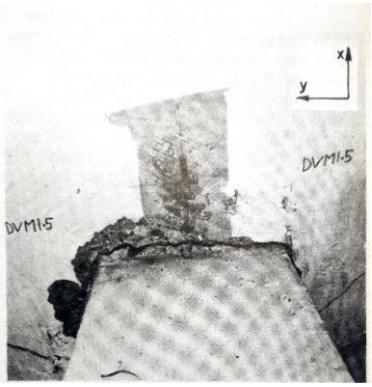

c) Top face, top and bottom of failing slab edges restrained

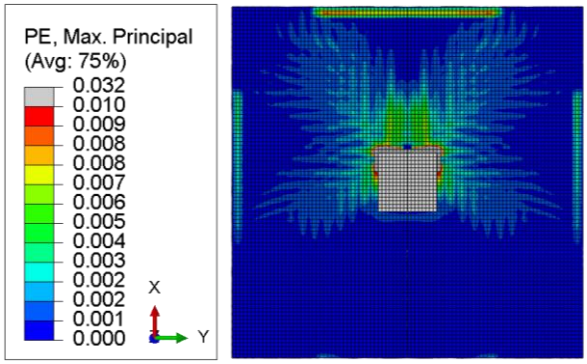

d) Bottom face, top and bottom of failing slab edges restrained

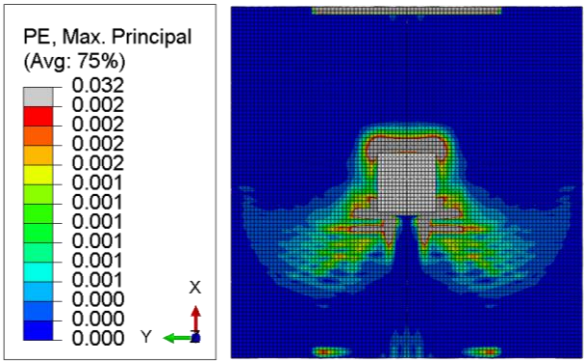

e) Top face, bottom of slab edges restrained

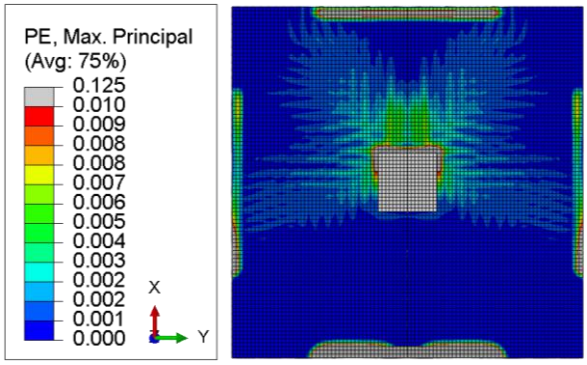

f) Bottom face, bottom of slab edges restrained

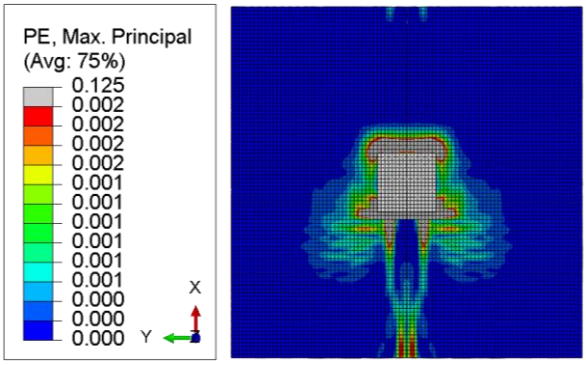

Figure 5.31: Specimen SM 1.5 experiment (Ghali et al., 1976) and analyses crack patterns for top and bottom of slab edges restrained analysis versus bottom of slab edges restrained analysis. Authorized reprint of experiment photographs from ACI Journal, Volume 73, Issue 10, October 1976.

5.3.1.4 Conclusions and Recommendations

Restraining the top and bottom slab edges on the sides parallel to the moment axis effectively prevented support tension failure without adversely affecting moment-rotation, displacement-rotation, and crack pattern results. These restraints provided confinement of support elements which reduced strains and prevented failures.

Among the analyses in which only the bottom slab edges were restrained, the lifting-edge restrained elements commonly failed due to excessive tensile stresses. This caused that side of the slab to lift and created a plastic hinge at the slab-column connection. The lifting increased slab rotation and cause upward displacement of the column. This was observable in both the moment-rotation and displacement-rotation plots. The plastic hinge increased stresses in the slab-column connection which lead to flexural or punching failure (depending on the failure mode of the specimen) occurring under a lower applied moment. This was visible in the moment-rotation plots.

The analyses in which both top and bottom slab edges were restrained no longer showed the aforementioned trends in neither the moment-rotation nor displacement-rotation plots. Furthermore, the maximum principal plastic strains (i.e. crack patterns) no longer showed strain concentrations at the compression and tension slab edges. Although this option prevented support failure, two more options were examined. The option that prevented support failure with the least adverse effects on the results was selected and implemented in subsequent analyses.

5.3.2 Option B: using elastic material at failing slab edge

Option B for preventing lifting-edge support failure was to use an elastic material for the elements along the edge susceptible to failure. This would allow elements to carry unlimited amounts of stresses with no possibility of failing. To define these elements with a different material, additional partitions were made in the concrete and reinforcement mats around the perimeter of the slab. The partitions were made at a distance of 20 mm from the edges of the slab. This distance was the same as the concrete and reinforcement element size as not to affect the element aspect ratio during meshing. The typical material definitions and mesh are shown in Figure 5.32.

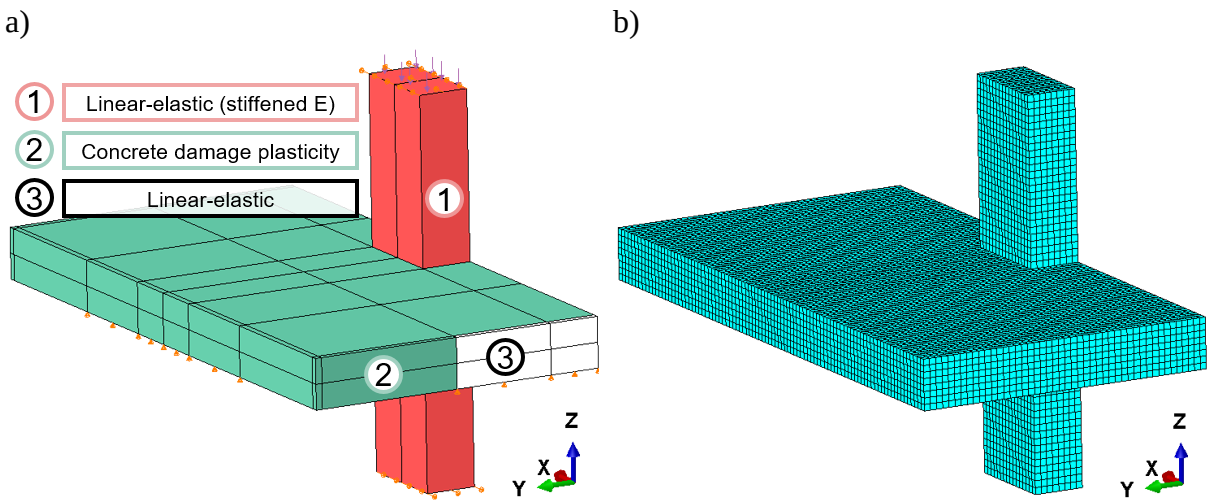

Figure 5.32: Typical a) material properties and b) meshing for option B analyses

5.3.2.1 Results of specimen SM 0.5 analyses

The moment-rotation and displacement-rotation data for option B and base case analyses of specimen 0.5 are presented in Figure 5.33. A summary of this data is provided in Table 5.14.

Option B successfully prevented support failure along the lifting slab edge. Compared to the base case analysis (i.e. plastic material at slab edge), option B showed an increase in rotational stiffness past 10 mrad. As a result, the shape of the option B moment-rotation plot closely resembled the moment-rotation data of the experiment. Furthermore, the ultimate moment was higher for the option B analysis (96 kNm) compared to the base case analysis (85 kNm). Relative to the experiment, the analysis percentage difference decreased from 15-percent to 3-percent when option B was implemented. The rotation at ultimate moment did not change significantly from the base case to option B.

With respect to the displacement-rotation data, both analyses produced near-identical results. The only difference was that option B showed stiffer data past 10 mrad.

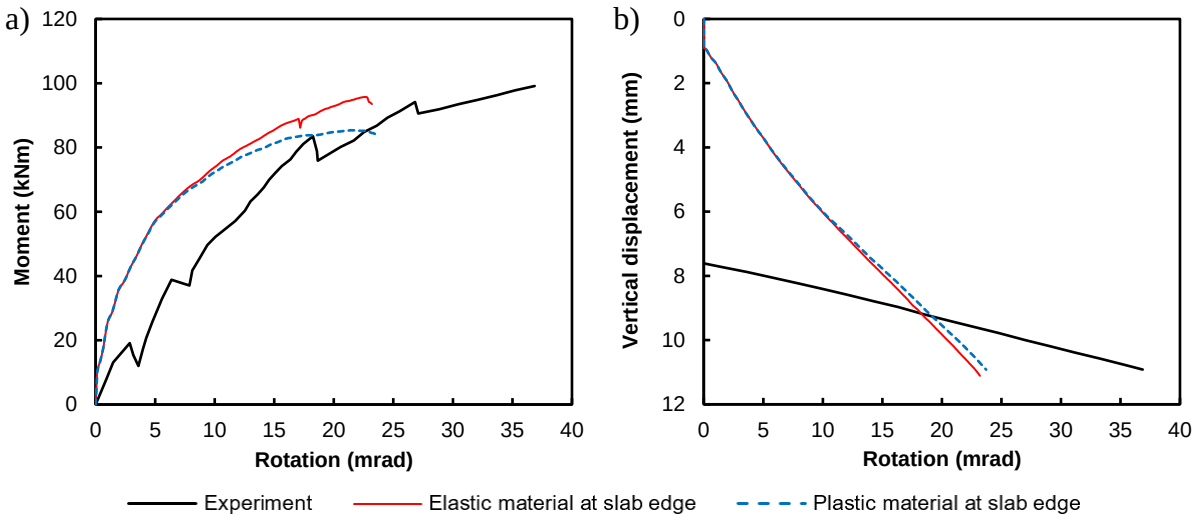

Figure 5.33: Specimen SM 0.5 a) moment-rotation and b) displacement-rotation data for elastic lifting slab edge analysis versus plastic lifting slab edge restrained analysis

Table 5.14: Specimen SM 0.5 analyses results for elastic lifting slab edge analysis versus plastic lifting slab edge restrained analysis

	Ultimate moment (kNm)	Displacement (mm) at ultimate moment	Rotation (mrad) at ultimate moment
Analyses			
Elastic lifting slab edge	95.7	10.9	22.7
Plastic lifting slab edge	85.4	10.0	21.4
Experiment	99.1	10.9	36.9

The experiment and analyses crack patterns for option B and base case analyses for specimen SM 0.5 are shown in Figure 5.34. Among the top face crack patterns, using an elastic lifting slab edge produced more diagonal cracks between the bottom column face and the bottom corners. These were not present in the plastic lifting slab edge analysis but were present in the experiment. Among the bottom face crack patterns, the elastic lifting slab edge analysis showed that diagonal cracks had formed which started halfway between the column and bottom slab edge and continued toward the extents of the bottom edge support. Diagonal cracks were present in the experiment but were not captured using a plastic lifting slab edge.

a) Top face, experiment

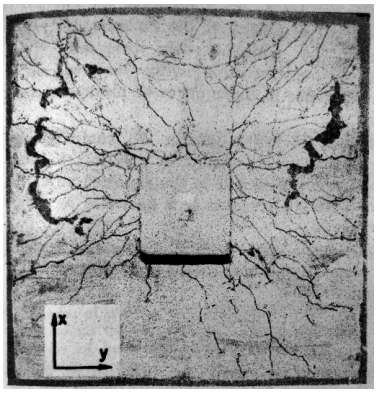

b) Bottom face, experiment

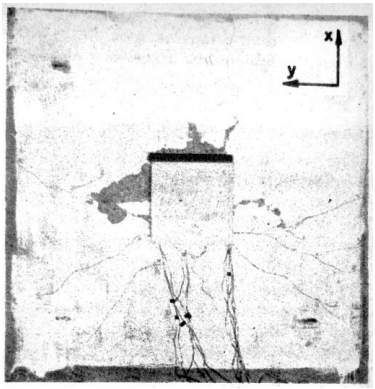

c) Top face, elastic lifting slab edge

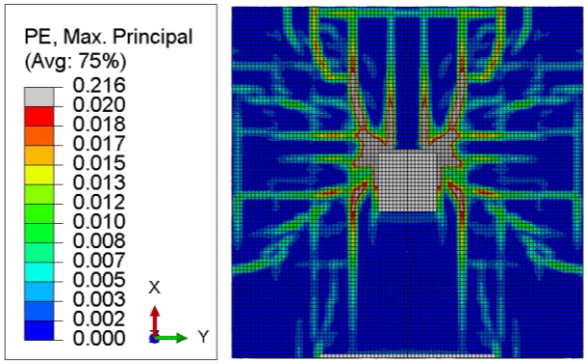

d) Bottom face, elastic lifting slab edge

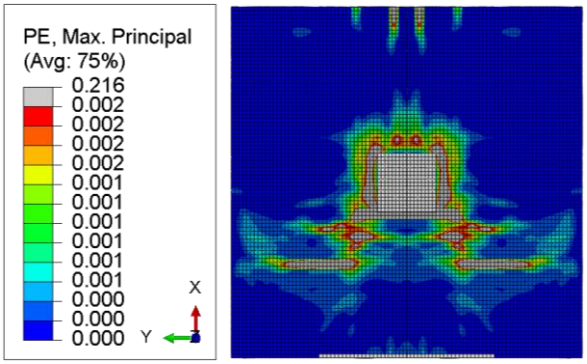

e) Top face, plastic lifting slab edge

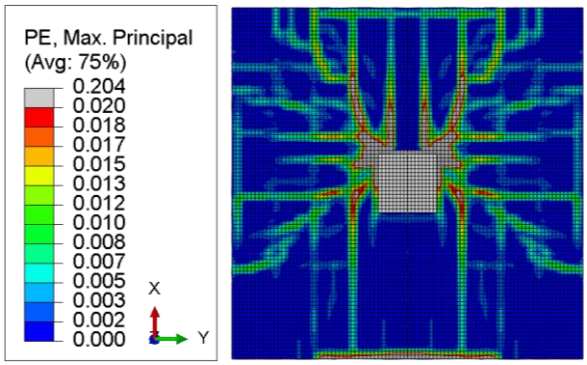

f) Bottom face, plastic lifting slab edge

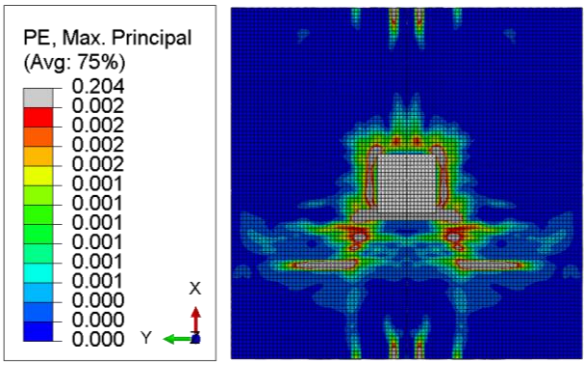

Figure 5.34: Specimen SM 0.5 experiment (Ghali et al., 1976) and analyses crack patterns for elastic lifting slab edge analysis versus plastic lifting slab edge restrained analysis. Authorized reprint of experiment photographs from ACI Journal, Volume 73, Issue 10, October 1976.

5.3.2.2 Results of specimen SM 1.0 analyses

The moment-rotation and displacement-rotation data for option B and base case analyses of specimen 1.0 are presented in Figure 5.35. A summary of this data is provided in Table 5.15.

The differences in moment-rotation data between the two analyses were minimal. Past 5 mrad, the moment-rotation data of the elastic lifting edge analysis were stiffer than the plastic lifting

edge analysis. Using an elastic slab lifting edge resulted in an increase in ultimate moment from 118 kNm to 121 kNm. Relative to the experiment, the percentage difference decreased from 8-percent to 5-percent when an elastic lifting slab edge was used. The displacement-rotation data slope change after 5 mrad which was visible in the plastic lifting slab edge analysis was no longer present in the elastic lifting slab edge analysis. This slope change was caused by the support failure which subsequently resulted in the slab lifting and rotating. The absence of this slope change indicated that support failure did not occur when an elastic material was used for the lifting slab edge.

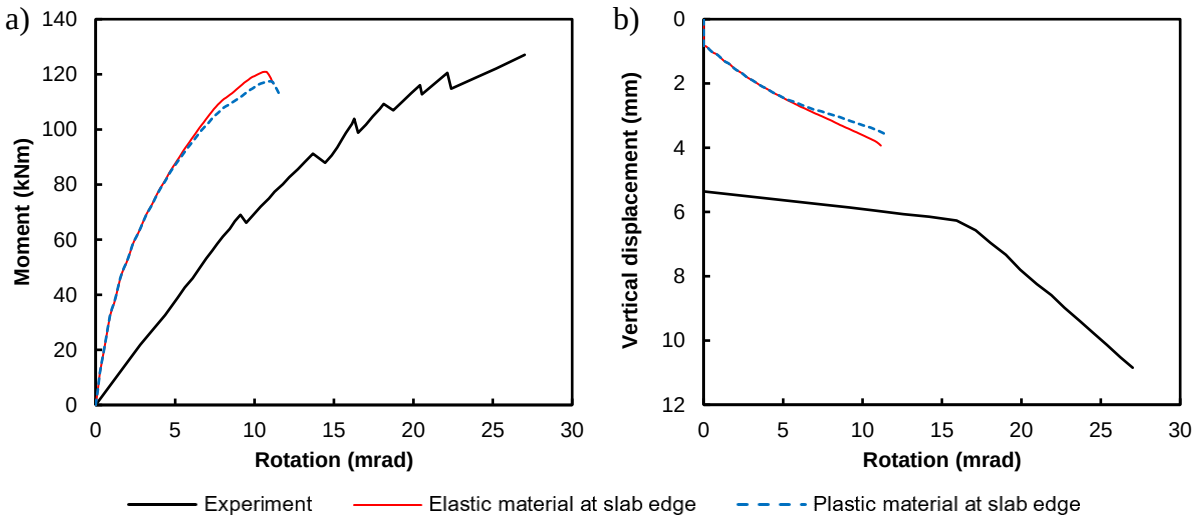

Figure 5.35: Specimen SM 1.0 a) moment-rotation and b) displacement-rotation data for elastic lifting slab edge analysis versus plastic lifting slab edge restrained analysis

Table 5.15: Specimen SM 1.0 analyses results for elastic lifting slab edge analysis versus plastic lifting slab edge restrained analysis

	Ultimate moment (kNm)	Displacement (mm) at ultimate moment	Rotation (mrad) at ultimate moment
Analyses			
Elastic lifting slab edge	120.9	3.8	10.6
Plastic lifting slab edge	117.5	3.5	11.0
Experiment	127.1	10.8	27.0

The analyses crack patterns for option B and base case analyses for specimen SM 1.0 are shown in Figure 5.36. Using an elastic lifting slab edge did not affect the crack patterns on the top face of the slab. Compared to using a plastic lifting slab edge, using an elastic lifting slab edge

resulted in a greater angle between the diagonal cracks from the bottom column face toward the corners.

a) Top face, elastic lifting slab edge

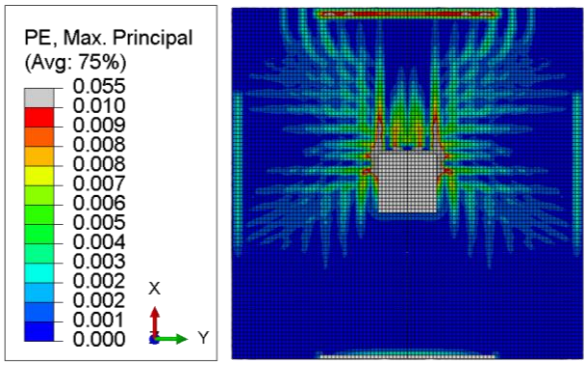

b) Bottom face, elastic lifting slab edge

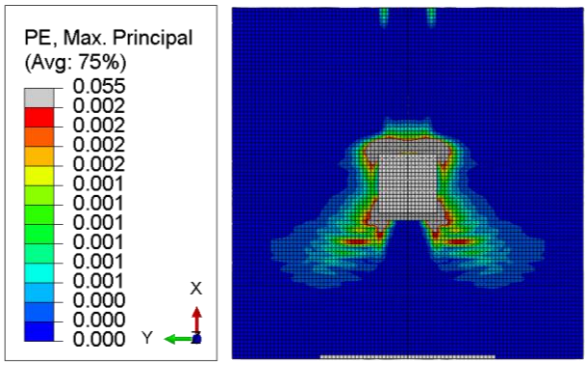

c) Top face, plastic lifting slab edge

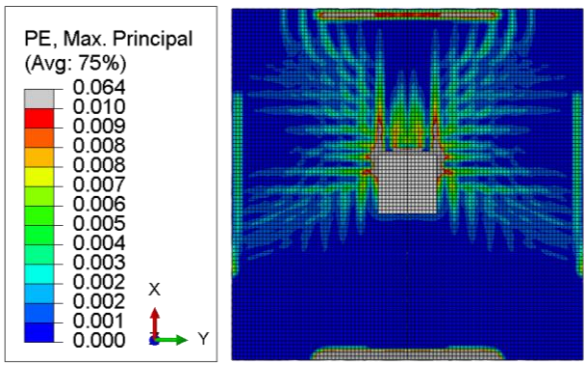

d) Bottom face, plastic lifting slab edge

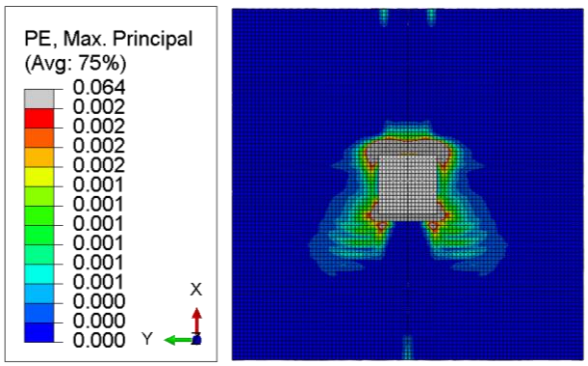

Figure 5.36: Specimen SM 1.0 analyses crack patterns for elastic lifting slab edge analysis versus plastic lifting slab edge restrained analysis

5.3.2.3 Results of specimen SM 1.5 analyses

The moment-rotation and displacement-rotation data for option B and base case analyses of specimen 1.5 are presented in Figure 5.37. A summary of this data is provided in Table 5.16.

The option B analysis had a higher rotational stiffness past 5 mrad compared to the base case analysis. The ultimate moment increased from 157 kNm to 161 kNm when changing the lifting slab edge from a plastic to an elastic material. This meant a percentage difference increase from 18-percent to 20-percent relative to the ultimate moment of the experiment.

The displacement-rotation plateau past 5 mrad observed in the base case analysis was no longer present in the option B analysis. This suggested that support failure did not occur.

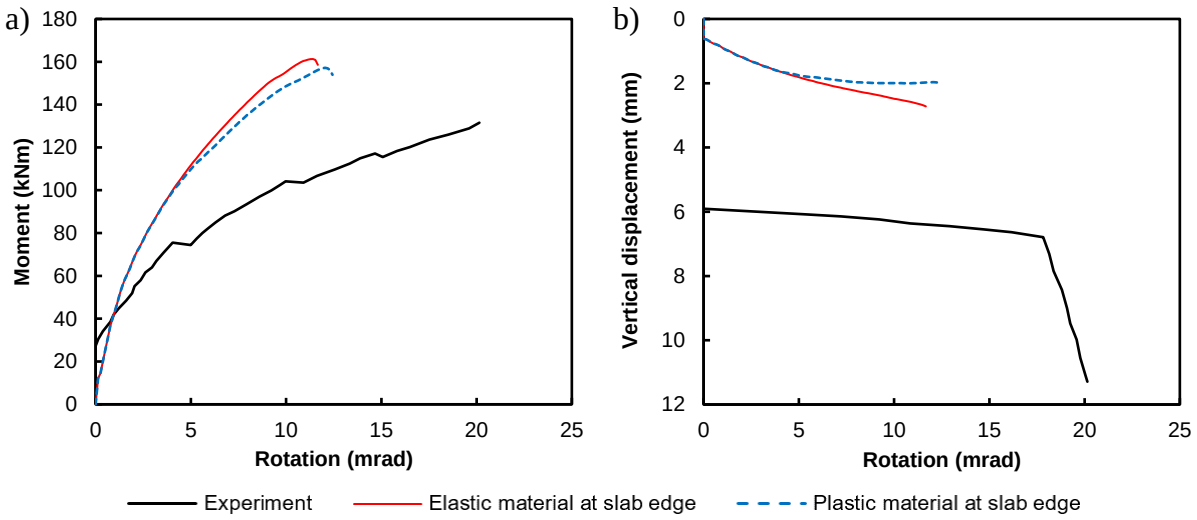

Figure 5.37: Specimen SM 1.5 a) moment-rotation and b) displacement-rotation data for elastic lifting slab edge analysis versus plastic lifting slab edge restrained analysis

Table 5.16: Specimen SM 1.5 analyses results for elastic lifting slab edge analysis versus plastic lifting slab edge restrained analysis

	Ultimate moment (kNm)	Displacement (mm) at ultimate moment	Rotation (mrad) at ultimate moment
Analyses			
Elastic lifting slab edge	161.3	2.7	11.4
Plastic lifting slab edge	157.2	2.0	12.1
Experiment	131.5	11.3	20.1

The experiment and analyses crack patterns for option B and base case analyses for specimen SM 1.5 are shown in Figure 5.38. There were no discernible differences in the top face crack patterns between the option B and base case analyses. The bottom face crack patterns showed a wider angle between diagonal cracks in the option B analysis compared to the base case analysis. Furthermore, the option B analysis did not have as much vertical cracking from the column toward the bottom slab edge as the base case analysis did.

a) Top face, experiment

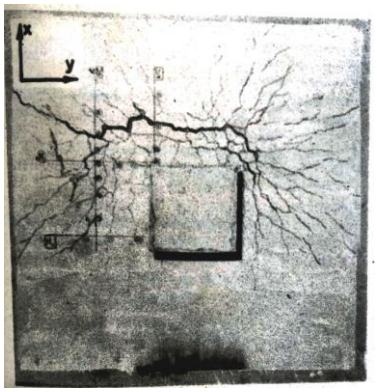

b) Bottom face, experiment

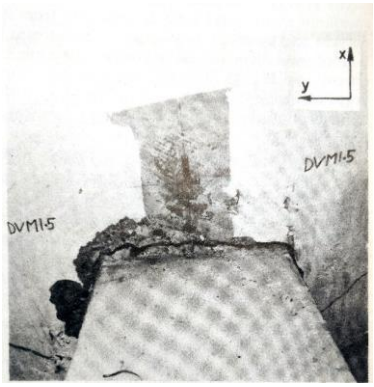

c) Top face, elastic lifting slab edge

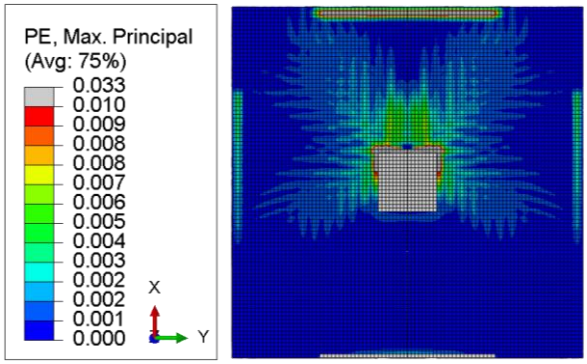

d) Bottom face, elastic lifting slab edge

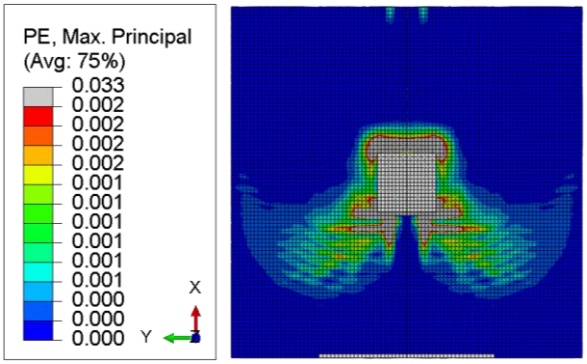

e) Top face, plastic lifting slab edge

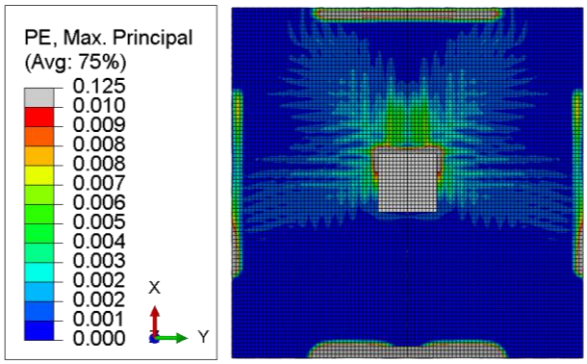

f) Bottom face, plastic lifting slab edge

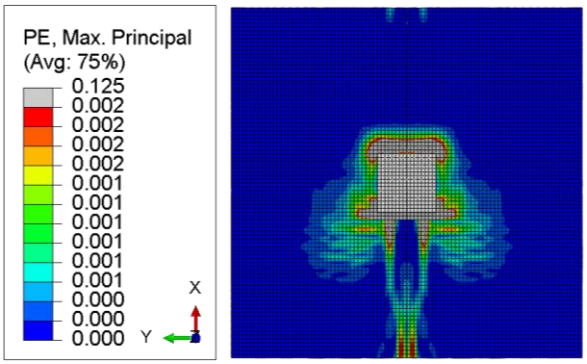

Figure 5.38: Specimen SM 1.5 experiment (Ghali et al., 1976) and analyses crack patterns for elastic lifting slab edge analysis versus plastic lifting slab edge restrained analysis. Authorized reprint of experiment photographs from ACI Journal, Volume 73, Issue 10, October 1976.

5.3.2.4 Conclusions and Recommendations

Using an elastic material (option B) in place of a plastic material (base case) for the lifting slab edge prevented support failure. Among moment-rotation plots, implementing option B resulted in higher ultimate moments. This reduced the difference between the analysis and experiment ultimate moments for specimens SM 0.5 and SM 1.0 but increased the difference for specimen SM 1.5. All displacement-rotation plots no longer decreased in slope mid-analysis. This meant

that implementing option B produced displacement-rotation data that better resembled that of the laboratory-tested specimens. In all cases, the option B analyses produced additional cracks that were present in the experiment. The base case did not produce these same cracks.

5.3.3 Option C: changing support boundary conditions between loads

Option C for preventing support failure was to change support boundary conditions between loads. Recall that the support failure was due to excessive tensile stresses acting on the concrete support elements, which have low tensile strength. Furthermore, the finite element analyses are separated into three steps: the vertical load step, rest step, and moment step. In the vertical load step, the 129 kN vertical load is ramped onto the top column stub. In the rest step, no changes are made to loads or boundary conditions. In the moment step, displacements are ramped equally and in opposite lateral directions at the top and bottom ends of the column.

The intention behind option C was to change tensile stresses into compressive stresses by changing the lifting-edge boundary conditions mid-analysis. In the base case analysis, the side of the slab that lifts during moment application was restrained along its bottom edge throughout the entire analysis. Option C involved removing and replacing this restraint during the rest step with a restraint along the top edge of the same side. The two sets of boundary conditions for the vertical load and rest steps, and the moment step are shown in Figure 5.39. Changing the boundary conditions was done to move the reaction forces from the bottom to the top edge of the slab. This meant that tensile stresses acting on the elements would become compressive stresses. Since concrete performs well in compression, support failure was unlikely to occur.

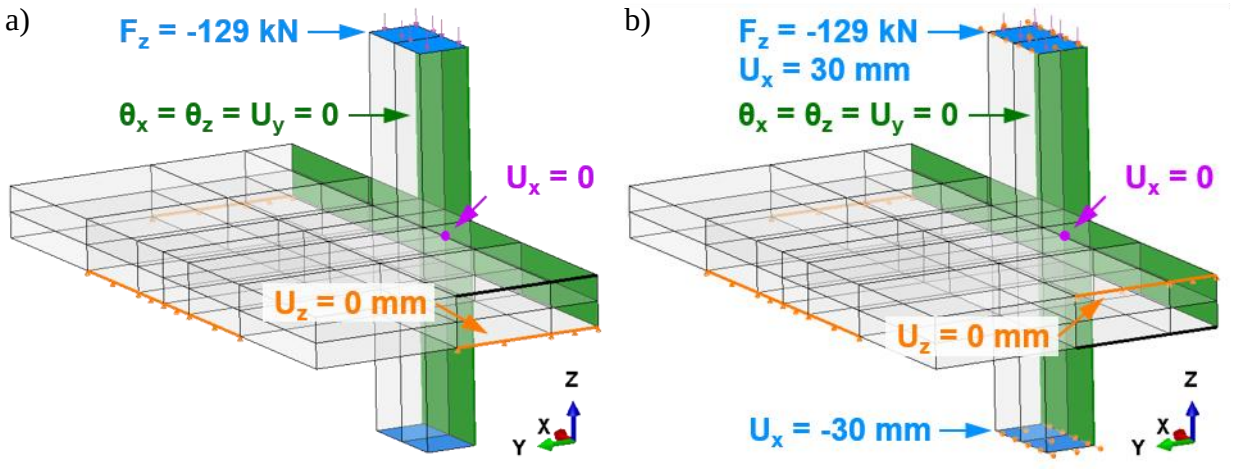

Figure 5.39: Typical boundary conditions for option C analyses in the a) apply vertical load and rest steps and b) apply moment step

5.3.3.1 Results of specimen SM 0.5 analyses

The moment-rotation and displacement-rotation data for option C and base case analyses of specimen 0.5 are presented in Figure 5.40. A summary of this data is provided in Table 5.17.

The option C moment-rotation data starts at (-2 mrad, 0 kNm) rather than (0 mrad, 0 kNm). This was because the reaction forces under the vertical load resulted in tensile stresses among the lifting-edge restrained elements. Due to concrete's low tensile strength, some of these elements became inactive and few active elements remained to resist deformation. As a result, the lifting-edge displaced downwards causing the entire slab and column to rotate with it.

When 2 mrad was added to each datum of the moment-rotation plot, the plot started at the origin and showed similarities to the option A analysis data. However, the downward displacement on one edge of the slab and not the other was not characteristic of what was observed during testing.

One solution to the negative rotation problem would be to change the number of analysis steps from three to five and change the boundary conditions in the fourth step rather than the second step. Option C had three steps: apply vertical load, rest, and apply moment. The boundary conditions were changed in the rest step. The moment applied in the apply moment step was displacement-based. The possible solution would be to use five steps: apply vertical load, first rest, apply partial moment, second rest, and apply remaining moment. In the apply partial moment step, 28 kNm would be applied. This is the moment at which the moment-rotation data intersects the y-axis. In the second rest step, the boundary conditions would be changed. In the apply remaining moment step, displacement-based moment would be applied until failure.

The problem with the five-step analysis was that the three-step analysis would need to be run first to determine how much moment to apply in the apply partial moment step. The moment at which the three-step analysis moment-rotation data intersects the y-axis would be applied in the five-step analysis apply partial moment step. This solution is not favourable because completing two analyses would take more computational time than completing one analysis.

The moment-rotation data of the option C analysis was nearly parallel to the base case analysis. The ultimate moment increased from 85 kNm to 90 kNm. Relative to the experiment, the ultimate moment decreased from 15-percent to 10-percent. The vertical displacement at 0 kNm was 2.6 mm for option C compared to 1.2 mm for the base case analysis. The experiment 0 kNm

displacement was 7.7 mm. The vertical displacement at ultimate moment did not change in the option C analysis compared to the base case analysis. The displacement-rotation data slope of the option C analysis was similar to the base case analysis.

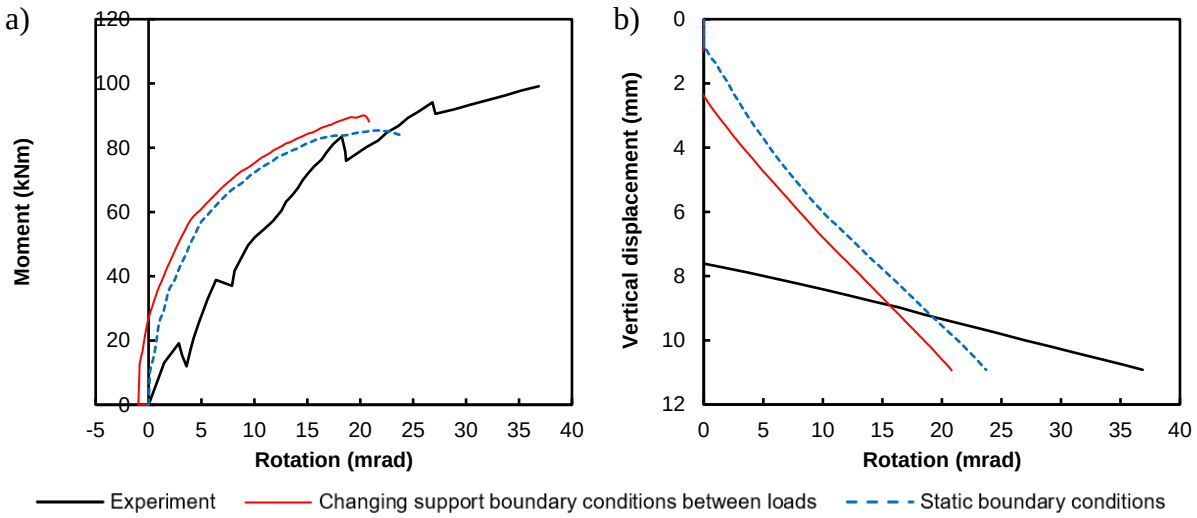

Figure 5.40: Specimen SM 0.5 a) moment-rotation and b) displacement-rotation data for changing support boundary conditions between loads analysis versus static boundary conditions analysis

Table 5.17: Specimen SM 0.5 analyses results for changing support boundary conditions between loads analysis versus static boundary conditions analysis

	Ultimate moment (kNm)	Displacement (mm) at ultimate moment	Rotation (mrad) at ultimate moment
Analyses			
Changing support boundary conditions between loads	90.1	10.7	20.3
Static boundary conditions	85.4	10.0	21.4
Experiment	99.1	10.9	36.9

The moment-rotation and displacement-rotation data for option C and base case analyses of specimen 0.5 are presented in Figure 5.41. A summary of this data is provided in Table 5.18. Among the top face crack patterns, both analyses produced very similar cracks to one another and to the experiment. Subtle cracks were in the option C analysis results that were also visible in the experiment crack patterns. The diagonal crack between the bottom column face and bottom extents of the side slab supports were more straight in the option C analysis compared to the base case analysis. The cracks between the bottom column face and the bottom slab edge

were angled in the option C analysis whereas these cracks were vertical in the base case analysis. Among the bottom face crack patterns, the option C analysis showed higher strain concentrations along the bottom edge compared to the base case analysis. Apart from this, no differences in crack patterns were evident between the two analyses.

a) Top face, experiment

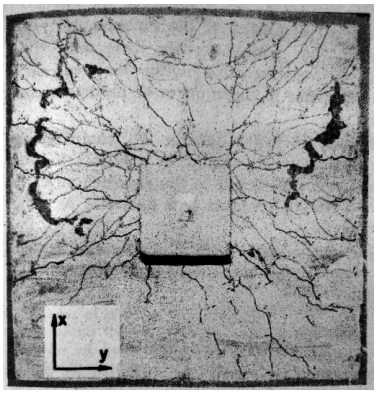

b) Bottom face, experiment

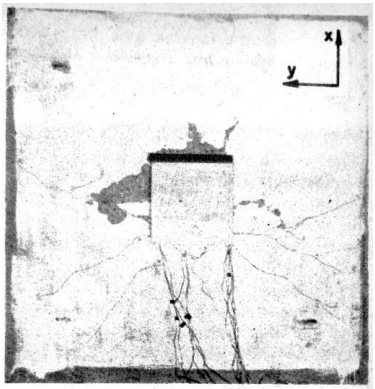

c) Top face, changing boundary conditions between loads

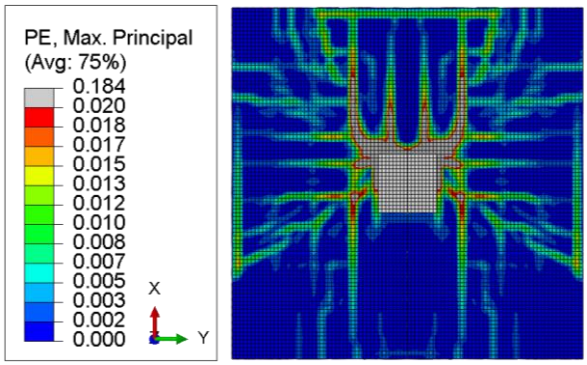

d) Bottom face, changing boundary conditions between loads

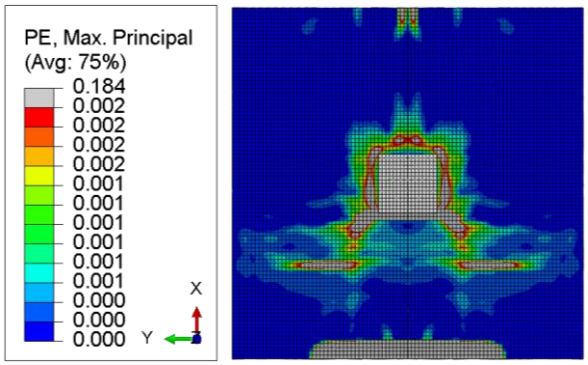

e) Top face, static boundary conditions

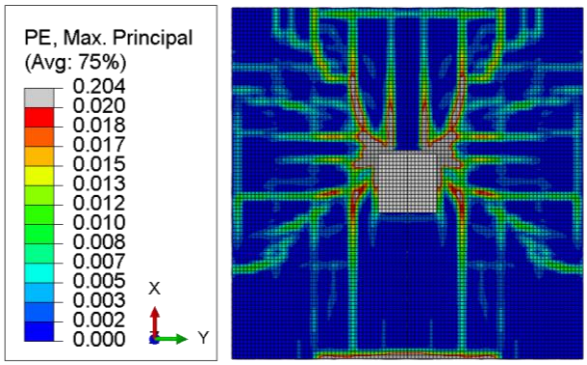

f) Bottom face, static boundary conditions

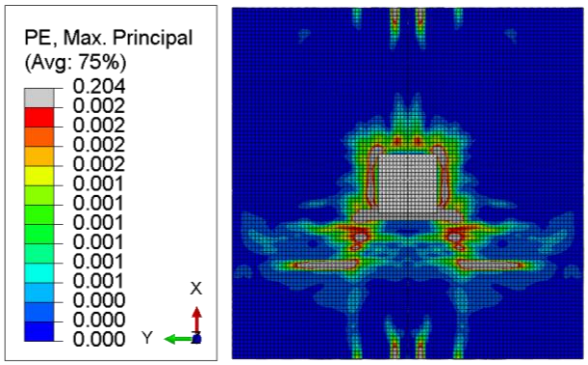

Figure 5.41: Specimen SM 0.5 experiment (Ghali et al., 1976) and analyses crack patterns for changing support boundary conditions between loads analysis versus static boundary conditions analysis. Authorized reprint of experiment photographs from ACI Journal, Volume 73, Issue 10, October 1976.

5.3.3.2 Results of specimen SM 1.0 analyses

The moment-rotation and displacement-rotation data for option C and base case analyses of specimen 1.0 are presented in Figure 5.42. A summary of this data is provided in Table 5.18.

As observed with specimen SM 0.5, the moment-rotation data did not start at the origin. Similarly, the data of the option C analysis was parallel to the base case analysis. The ultimate moment increased from 118 kNm in the base case analysis to 121 kNm in the option C analysis. Relative to the experiment, this was a percentage difference change from 8-percent to 5-percent. The displacement-rotation data of option C was parallel to that of the base case. The displacement before the moment was applied was higher for the option C analysis (1.9 mm) compared to the base case analysis (0.8 mm). The displacement at the ultimate moment was higher for option C (4.0 mm) compared to the base case (3.5 mm).

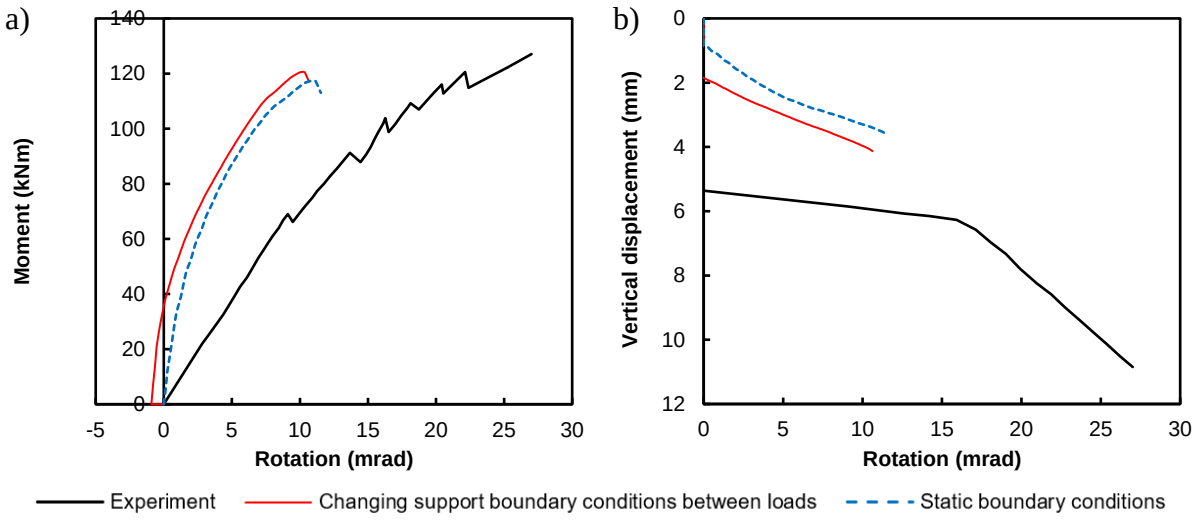

Figure 5.42: Specimen SM 1.0 a) moment-rotation and b) displacement-rotation data for changing support boundary conditions between loads analysis versus static boundary conditions analysis

Table 5.18: Specimen SM 1.0 analyses results for changing support boundary conditions between loads analysis versus static boundary conditions analysis

	Ultimate moment (kNm)	Displacement (mm) at ultimate moment	Rotation (mrad) at ultimate moment
Analyses			
Changing support boundary conditions between loads	120.7	4.0	10.2
Static boundary conditions	117.5	3.5	11.0
Experiment	127.1	10.8	27.0

The analyses crack patterns for option C and base case analyses for specimen SM 1.0 are shown in Figure 5.43. Both analyses produced almost identical crack patterns. The location change of the lifting-edge restraint from the bottom edge to the top edge similarly resulted in a strain concentration change from the bottom face to the top.

a) Top face, changing boundary conditions between loads

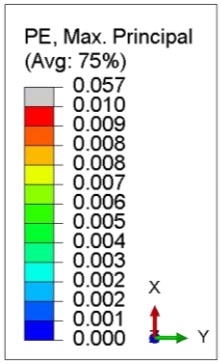

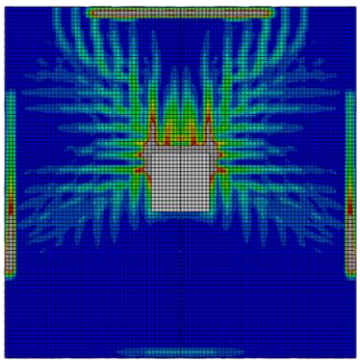

b) Bottom face, changing boundary conditions between loads

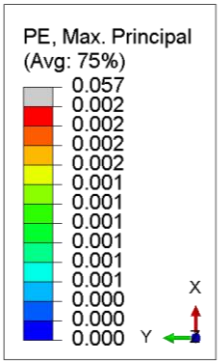

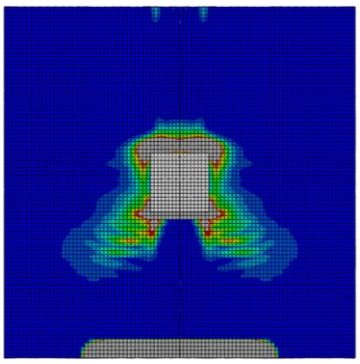

c) Top face, static boundary conditions

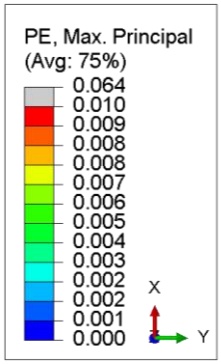

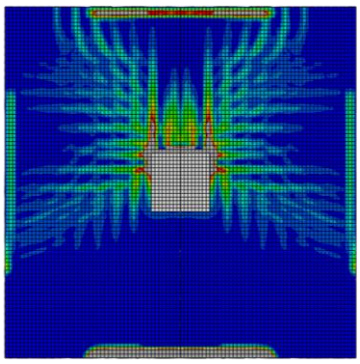

d) Bottom face, static boundary conditions

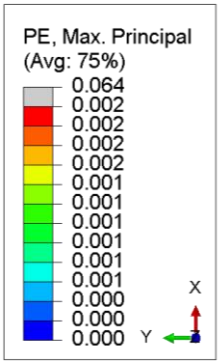

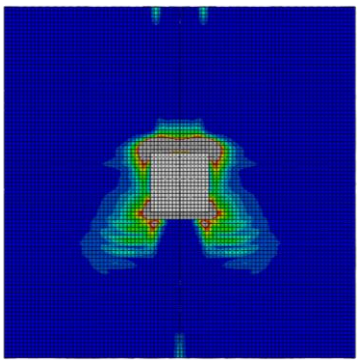

Figure 5.43: Specimen SM 1.0 analyses crack patterns for changing support boundary conditions between loads analysis versus static boundary conditions analysis

5.3.3.3 Results of specimen SM 1.5 analyses

The moment-rotation and displacement-rotation data for option C and base case analyses of specimen 1.5 are presented in Figure 5.44. A summary of this data is provided in Table 5.19.

The same trends were observed for specimen SM 1.5 as for specimens SM 0.5 and SM 1.0. The moment-rotation data: did not start at the origin, was parallel to the base case analysis, and the ultimate moment was higher for option C compared to the base case. The ultimate moment increased from 157 kNm to 161 kNm which was a percentage difference increase from 18-percent to 20-percent relative to the experiment. Similar trends were also observed for the displacement-rotation data: the displacement-rotation data for the option C analysis was parallel to the base case analysis, the displacement under no moment was higher for the option C analysis (1.4 mm compared to 0.7 mm), and the displacement at ultimate moment was higher for the option C analysis (2.7 mm versus 2.0 mm).

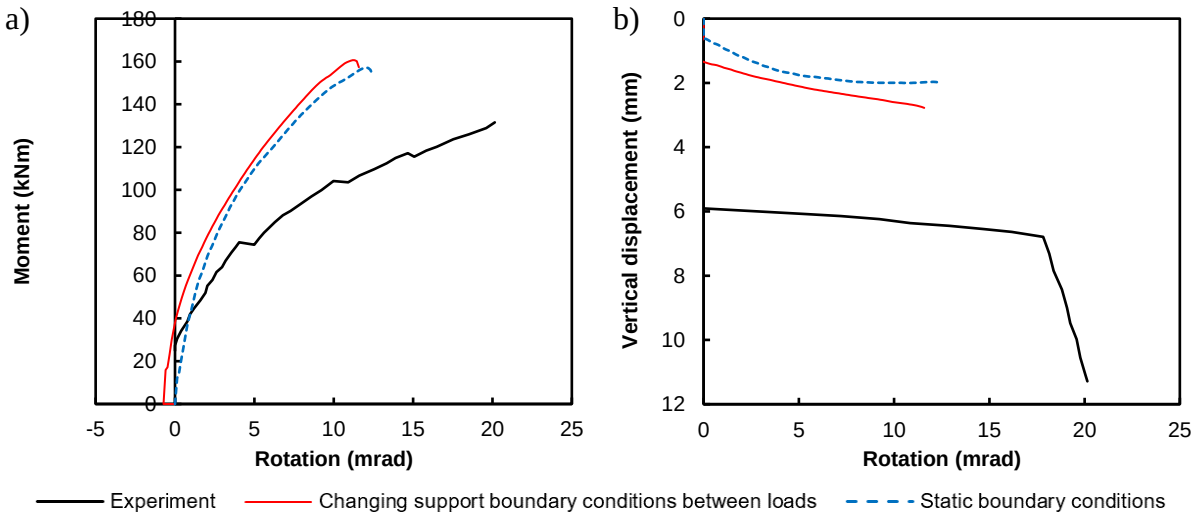

Figure 5.44: Specimen SM 1.5 a) moment-rotation and b) displacement-rotation data for changing support boundary conditions between loads analysis versus static boundary conditions analysis

Table 5.19: Specimen SM 1.5 analyses results for changing support boundary conditions between loads analysis versus static boundary conditions analysis

	Ultimate moment (kNm)	Displacement (mm) at ultimate moment	Rotation (mrad) at ultimate moment
Analyses			
Changing support boundary conditions between loads	160.6	2.7	11.2
Static boundary conditions	157.2	2.0	12.1
Experiment	131.5	11.3	20.1

The experiment and analyses crack patterns for option B and base case analyses for specimen SM 1.5 are shown in Figure 5.45. The top crack patterns of both analyses were the same. The bottom crack patterns of the option C analysis had a wider angle between the diagonal cracks compared to the base case analysis. Furthermore, the vertical cracks visible in the base case analysis were not as prevalent in the option C analysis.

a) Top face, experiment

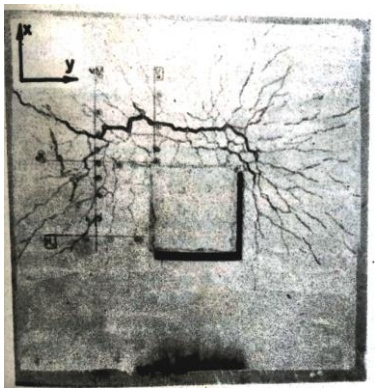

b) Bottom face, experiment

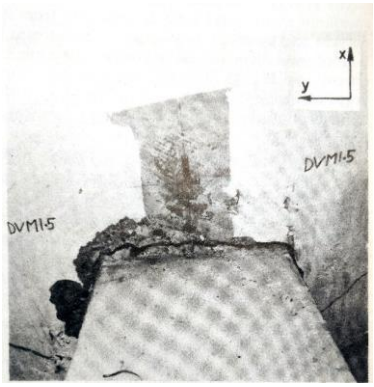

c) Top face, changing boundary conditions between loads

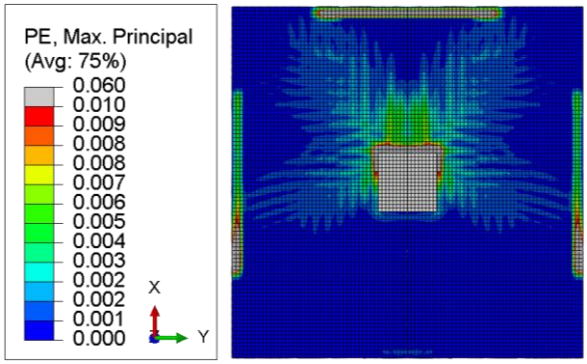

d) Bottom face, changing boundary conditions between loads

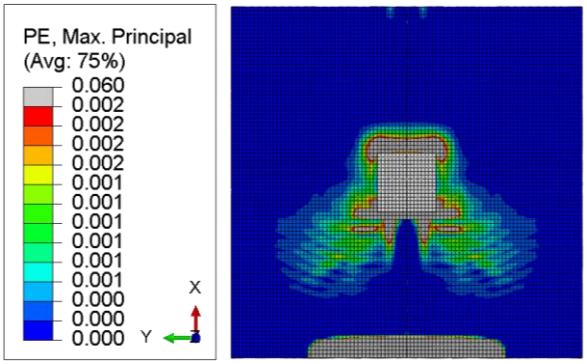

e) Top face, static boundary conditions

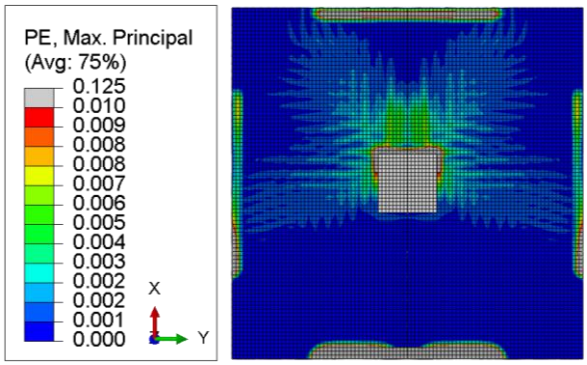

f) Bottom face, static boundary conditions

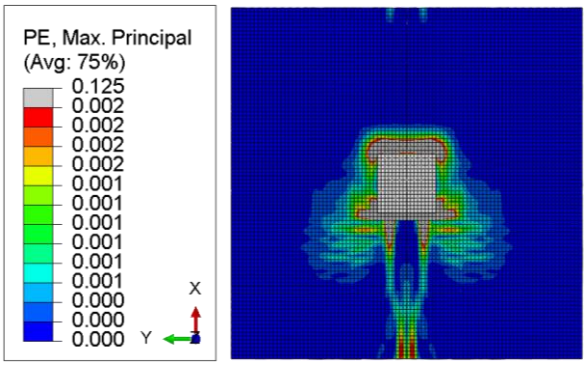

Figure 5.45: Specimen SM 1.5 experiment (Ghali et al., 1976) and analyses crack patterns for changing support boundary conditions between loads analysis versus static boundary conditions analysis. Authorized reprint of experiment photographs from ACI Journal, Volume 73, Issue 10, October 1976.

5.3.3.4 Conclusions and Recommendations

Option C, which was to change the boundary conditions between loads, prevented support failure of the lifting slab edge. The option C analyses of all specimens produced moment-rotation data parallel to their respective base case analyses. All option C analyses had higher

ultimate moments than their respective base case analyses. Lastly, all option C analyses showed negative column rotation prior to the application of moment. The negative rotation was caused by tensile stresses in the top edge slab restraint. This caused the slab edge to displace downward and the entire slab and column to rotate. A solution was proposed in which a five step analysis would be completed after the three step analysis. The five step analysis steps were: apply vertical load, first rest, apply partial moment, second rest, and apply remaining moment. The moment at 0 mrad of the three step analysis would be applied in the apply partial moment step. The support boundary conditions would be changed in the second rest step. The rotation caused by applying the partial moment plus the rotation from changing the support boundary conditions would result in a net zero rotation prior to applying to remaining moment. However, this solution would be computationally intensive and was not investigated.

5.3.4 Comparison of options

The differences in moment-rotation and displacement-rotation data between the options were consistent between the three specimens. As the data trends are common to all specimens, only specimen SM 0.5 is shown as a typical case to present these trends. The specimen SM 0.5 moment-rotation and displacement-rotation data for the three analysis options, base case analysis, and the experiment are shown in Figure 5.46.

Up to 5 mrad, options A and B produced moment-rotation data identical to the base case. Past 5 mrad, options A and B moment-rotation data were similar to one another but stiffer than the base case analysis. The option C analysis had a negative rotation prior to the application of moment due to tensile stresses on its lifting-edge support. These tensile stresses resulted in downward displacement of the support edge which caused negative column rotation. Toward the end of the analysis, option C had similar moment-displacement stiffness and capacity as options A and B. All option analysis reduced the percentage difference in ultimate moment relative to the experiment.

The displacement-rotation data for options A and B resembled that of the experiment. Option C had a larger vertical displacement compared to options A and B and the experiment. As with the negative rotation, this was caused by the downward displacement of the lifting slab edge.

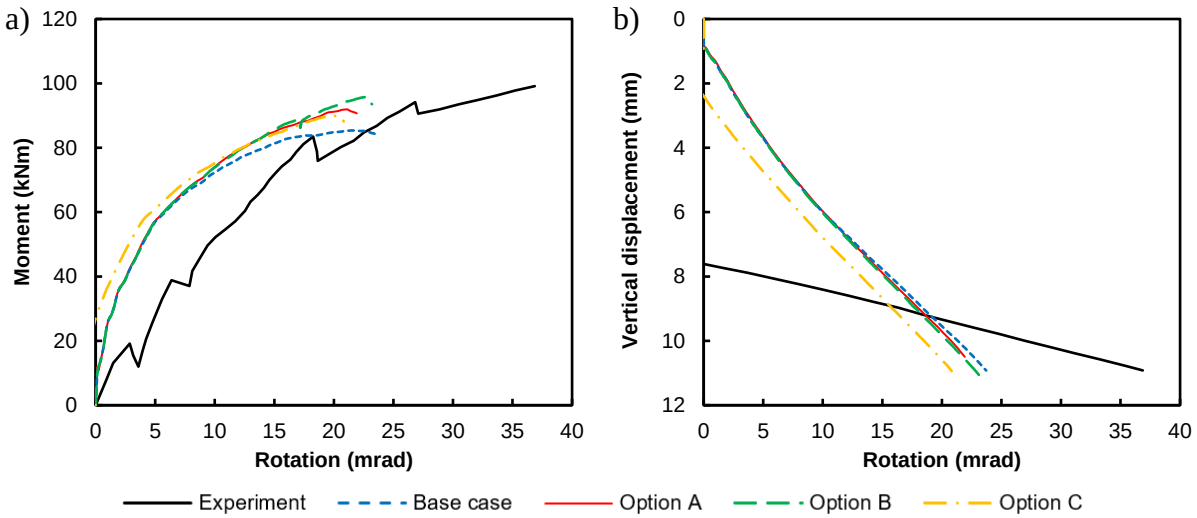

Figure 5.46: Specimen SM 0.5 a) moment-rotation and b) displacement-rotation data for the three options to prevent support failure and base case

For comparison purposes, only the analysis top and bottom face crack patterns of specimen SM 0.5 are presented. The crack patterns of the specimen SM 1.0 analyses are not presented because it is not possible to comment on their accuracy without having the experiment crack patterns for comparison. The crack patterns of the specimen SM 1.5 analyses are not presented because the top face crack patterns were similar to one another for the three options. The specimen SM 1.5 bottom face experiment crack pattern was focused on the area around the column. Therefore, it was not possible to comment on the analyses accuracy without being able to see the rest of the slab.

The specimen SM 0.5 top face crack patterns for the three analysis options, base case analysis, and the experiment are shown in Figure 5.47. Both options B and C captured the diagonal cracking from the bottom column face toward the extents of the bottom edge restrained elements. Both options B and C showed more cracks in the top corners of the slab. These cracks were not captured by option A but were visible in the experiment crack patterns. Option C showed straighter diagonal cracks from the bottom column corners toward the vertical slab edges which were present in the experiment.

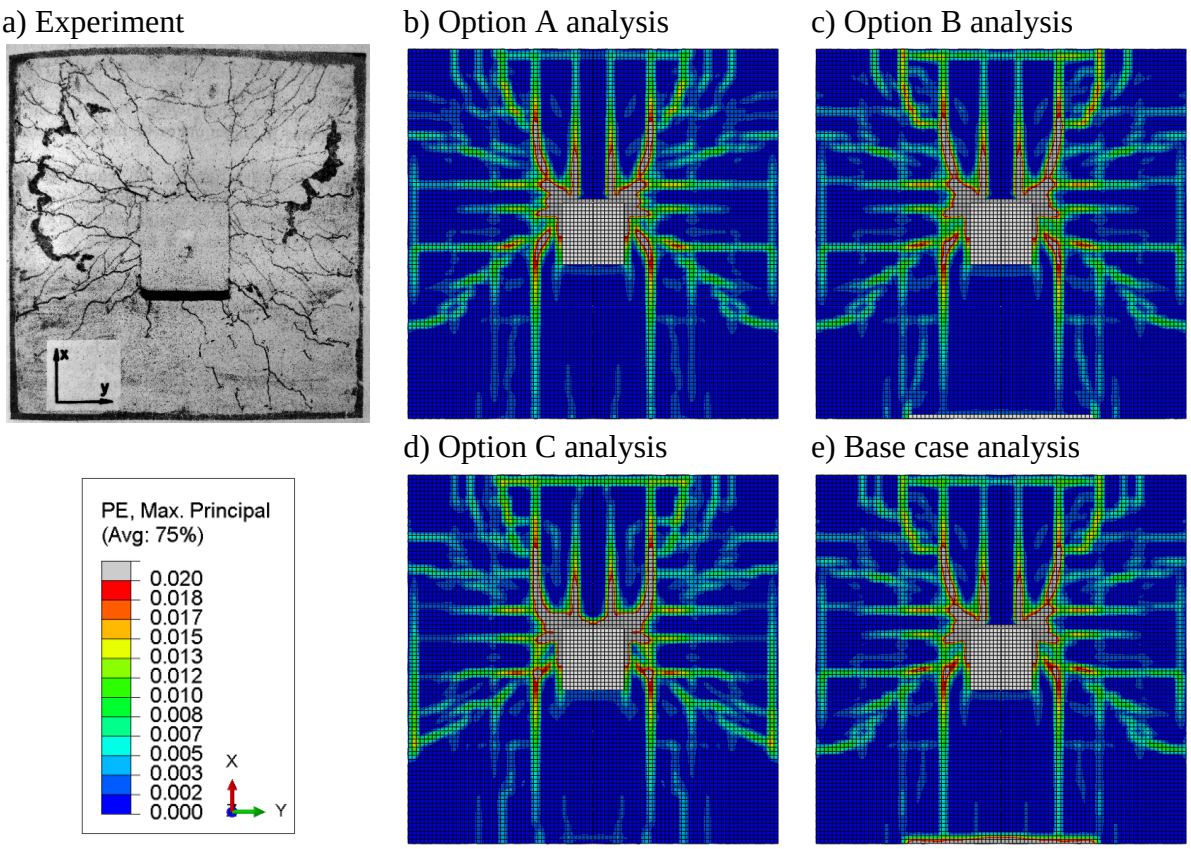

Figure 5.47: Specimen SM 0.5 top face experiment (Ghali et al., 1976) and analyses crack patterns for the support failure prevention options and base case. Authorized reprint of experiment photograph from ACI Journal, Volume 73, Issue 10, October 1976.

The specimen SM 0.5 bottom face crack patterns for the three analysis options, base case analysis, and the experiment are shown in Figure 5.48. All crack patterns were similar to one another. Options B and C produced diagonal cracks below the column which were visible in the experiment. Option A produced more vertical cracking below the column compared to the other analyses. This vertical cracking was visible in the experiment.

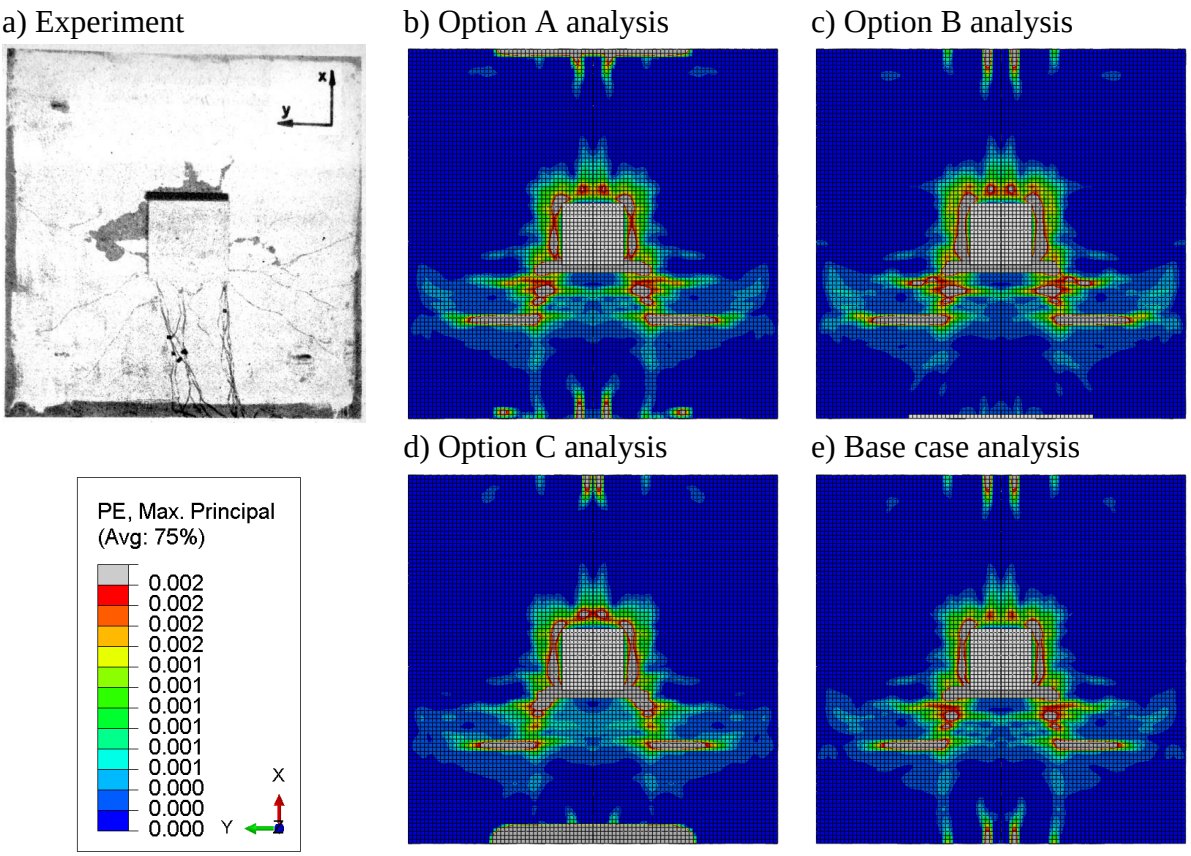

Figure 5.48: Specimen SM 0.5 bottom face experiment (Ghali et al., 1976) and analyses crack patterns for the support failure prevention options and base case. Authorized reprint of experiment photograph from ACI Journal, Volume 73, Issue 10, October 1976.

5.3.5 Conclusions and recommendations

All three options prevented support failure. Option B, using an elastic material along the lifting slab edge, was selected and used in subsequent analyses. Of the three options, option C was quickly eliminated from consideration. Although option C produced accurate crack patterns and showed a larger initial vertical displacement, the excessive strains on the lifting-edge resulted in downward displacement of that slab edge. This was uncharacteristic of the behaviour observed during testing. Option A produced near-identical moment-rotation and displacement-rotation data to option B. However, option B produced crack patterns that closer resembled those of the experiment for specimen SM 0.5. The top face crack patterns for specimen SM 1.5 were the alike for option A and B; however, the bottom face crack patterns were not. As the experiment bottom face crack patterns only showed the area around the column, it was not possible to comment on which of the two options was more accurate.

5.4 Study of fracture energy models

Previously completed SM specimen analyses used concrete fracture energies calculated using the model provided by Model Code 2010 (federation internationale du béton (fib), 2013). In this study, the models were reanalysed using the Model Code 1990 fracture energy model (Comité Euro-International du Béton, 1993). For each specimen, the Model Code 1990 and Model Code 2010 analyses results were compared to the experiment results to determine which fracture energy model produced the most accurate results.

Model Code 2010 provides the following equation for calculating fracture energy G_f:

$$G_f = 73(f_{cm})^{0.18} \qquad \text{(SI units: N, mm) (5.1)}$$

where f_{cm} is the mean value of the concrete compressive strength. This parameter is defined by

$$f_{cm} = f_{ck} + \Delta f \qquad \text{(SI units: N, mm) (5.2)}$$

where f_{ck} is the characteristic compressive strength and Δf is equal to $8\,MPa$. Reineck et al. (2003) proposed that the characteristic compressive strength f_{ck} is related to the concrete cylinder strength f_c' by the equation

$$f_{ck} = f_c' - 1.6 \text{ MPa} . \qquad \text{(SI units: N, mm) (5.3)}$$

Model Code 1990 provides the following model for calculating fracture energy G_f:

$$G_f = G_{fo}\left(\frac{f_{cm}}{f_{cmo}}\right)^{0.7} \qquad \text{(SI units: N, mm) (5.4)}$$

where G_{fo} is the base value of fracture energy obtained by linearly interpolating between data from Table 5.20, and f_{cmo} is equal to 10 MPa.

Table 5.20: Base values of fracture energy G_{Fo} (Comité Euro-International du Béton, 1993)

Maximum aggregate size d_{max} (mm)	G_{fo} (Nmm/mm^2)
8	0.025
16	0.030
32	0.058

The fracture energy G_f values used in the analyses of the SM specimens, and the parameters used in calculating those values, are presented in Table 5.21. The maximum aggregate size was unknown for any of the SM specimens. As such, an assumed maximum aggregate size of 19 mm was used. This value was chosen to maximize the fracture energy calculated using MC 1990 to fracture energy calculated using MC 2010. Since the concrete cover for all specimens was 19 mm, the largest possible maximum aggregate size used was 19 mm.

Table 5.21: Fracture energy G_f values used in analyses of SM specimens

				MC 1990			MC 2010
Specimen	f_c' (MPa)	f_{ck} (MPa)	f_{cm} (MPa)	d_{max} (mm)	G_{fo} (N/mm)	G_f (N/mm)	G_f (N/mm)
SM 0.5	36.77	35.17	43.17	19	0.035	0.098	0.139
SM 1.0	33.36	31.76	39.76			0.093	0.136
SM 1.5	39.98	38.38	46.38			0.103	0.141

5.4.1 Results of specimen SM 0.5 analyses

The moment-rotation and displacement-rotation data using MC 1990 and MC 2010 fracture energy analyses and experimental results for specimen SM 0.5 are presented in Figure 5.49. A summary of this data is provided in Table 5.22.

The moment-rotation data of the MC 1990 fracture energy analysis was closer in slope to the experiment compared to the MC 2010 fracture energy analysis. Of the two fracture energy models, the MC 2010 fracture energy analysis produced an ultimate moment closer to that of the experiment. This higher ultimate moment was expected from the MC 2010 analysis as its higher fracture energy meant that more energy was required to form a crack over a unit area of concrete.

The displacement-rotation data showed that the MC 2010 analysis showed a stiffer response compared to the MC 1990 analysis. The MC 2010 analysis produced a displacement at ultimate moment that was identical to that of the experiment. The MC 1990 analysis produced a displacement at ultimate moment with a percentage difference of 10-percent relative to the experiment value.

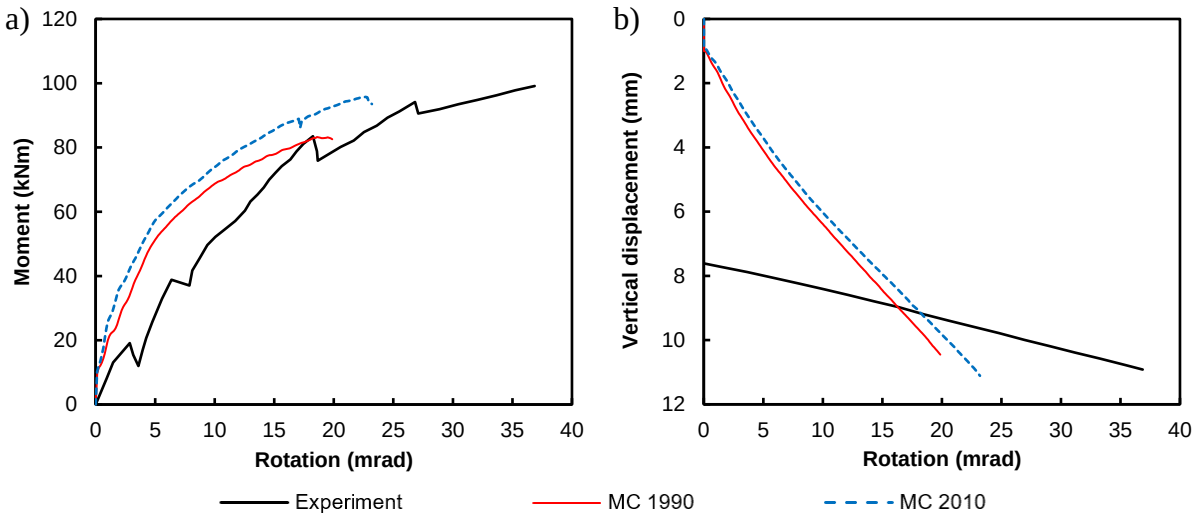

Figure 5.49: Specimen SM 0.5 a) moment-rotation and b) displacement-rotation data using MC 1990 versus MC 2010 fracture energy models

Table 5.22: Specimen SM 0.5 analyses results using MC 1990 versus MC 2010 fracture energy models

	Ultimate moment (kNm)	Displacement (mm) at ultimate moment	Rotation (mrad) at ultimate moment
Analyses			
MC 1990	83.3	9.9	18.6
MC 2010	95.7	10.9	22.7
Experiment	99.1	10.9	36.9

The crack patterns of the experiment as well as the MC 1990 and MC 2010 fracture energy analyses for specimen SM 0.5 are presented in Figure 5.50. Both analyses produced similar crack patterns to one another with varying maximum principal plastic strain magnitudes. The variance in strain magnitudes was because the MC 1990 analysis crack patterns were produced at a lower ultimate moment compared to the MC 2010 analysis crack patterns.

a) Top face, experiment

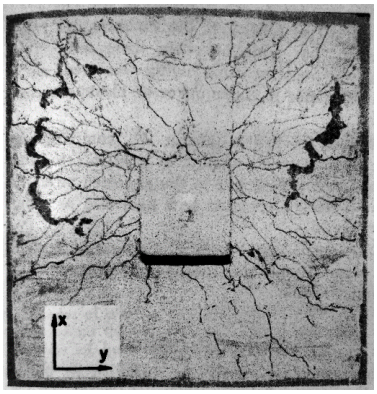

b) Bottom face, experiment

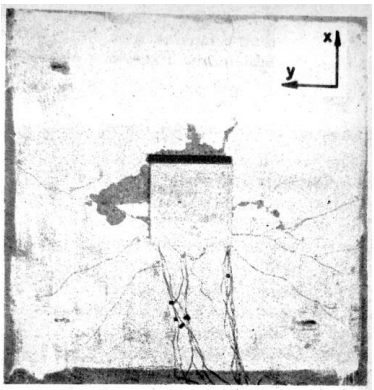

c) Top face, MC 1990

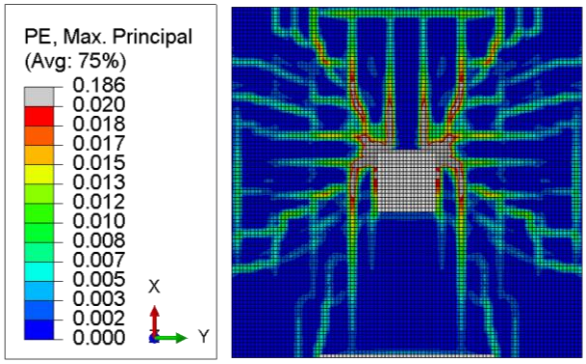

d) Bottom face, MC 1990

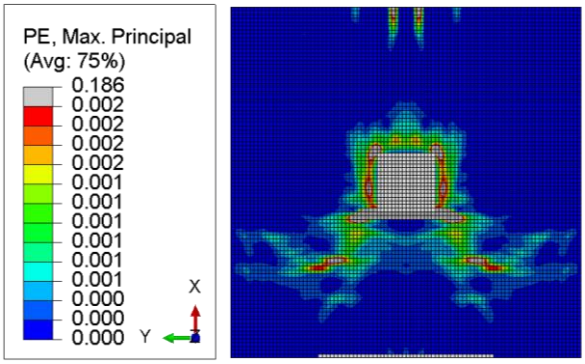

e) Top face, MC 2010

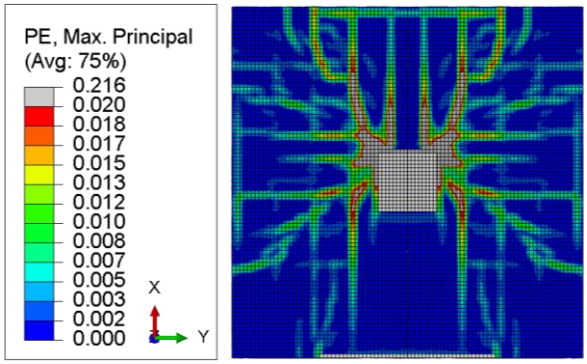

f) Bottom face, MC 2010

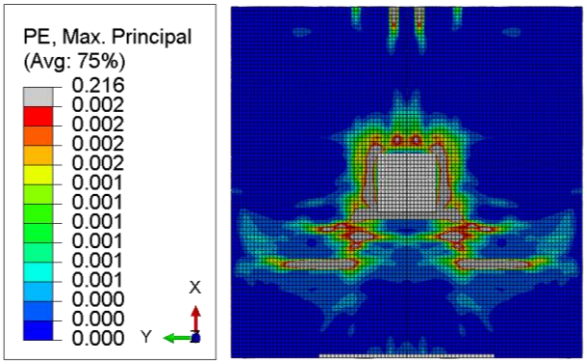

Figure 5.50: Specimen SM 0.5 experiment (Ghali et al., 1976) and analyses crack patterns using MC 1990 versus MC 2010 fracture energy models. Authorized reprint of experiment photographs from ACI Journal, Volume 73, Issue 10, October 1976.

5.4.2 Results of specimen SM 1.0 analyses

The moment-rotation and displacement-rotation data using MC 1990 and MC 2010 fracture energy analyses and experimental results for specimen SM 1.0 are presented in Figure 5.51. A summary of this data is provided in Table 5.23.

As was the case with the specimen SM 0.5 analyses, The softer moment-rotation data produced by the MC 1990 analysis was closer in stiffness to the experiment data than the moment-rotation data produced by the MC 2010 analysis. Of the two analyses, the ultimate moment of the MC 2010 analysis was higher than that of the MC 1990 analysis. Furthermore, the ultimate moment of the MC 2010 analysis was closer to the experiment ultimate moment.

Both analyses produced similar moment-rotation data to one another. The MC 2010 analysis produced negligibly stiffer displacement-rotation data compared to the data produced by the MC 1990 analysis. Both analyses produced a similar displacement at ultimate moment. However, both analyses underestimated the experiment displacement at ultimate moment by a percentage difference of 88-percent.

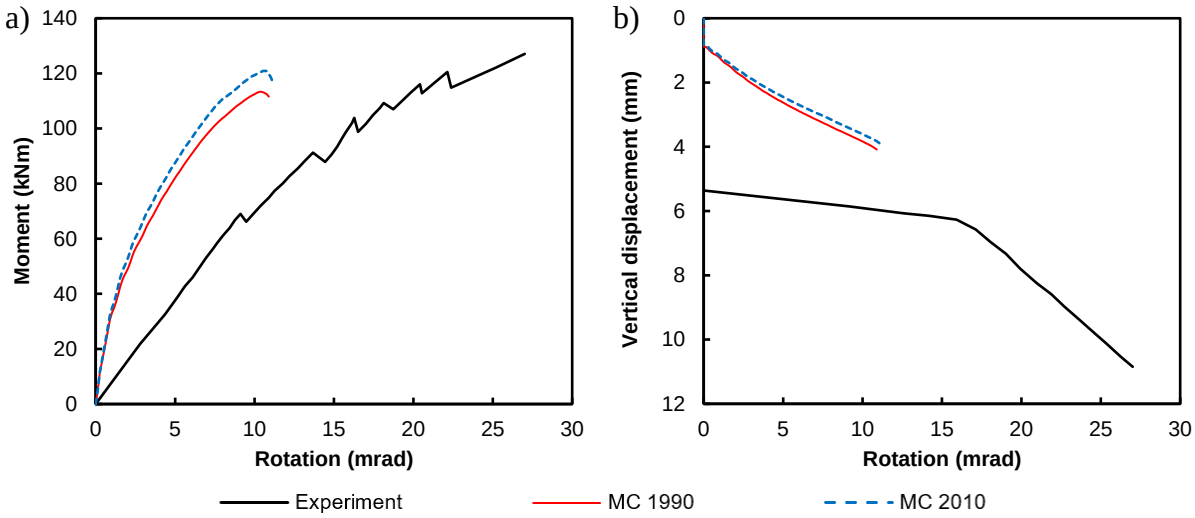

Figure 5.51: Specimen SM 1.0 a) moment-rotation and b) displacement-rotation data using MC 1990 versus MC 2010 fracture energy models

Table 5.23: Specimen SM 1.0 analyses results using MC 1990 versus MC 2010 fracture energy models

	Ultimate moment (kNm)	Displacement (mm) at ultimate moment	Rotation (mrad) at ultimate moment
Analyses			
MC 1990	113.4	3.9	10.4
MC 2010	120.9	3.8	10.6
Experiment	127.1	10.8	27.0

The crack patterns of the MC 1990 and MC 2010 fracture energy analyses for specimen SM 1.0 are presented in Figure 5.52. As observed with the specimen SM 0.5 analyses, both specimen

SM 1.0 analyses produced similar crack patterns to one another with varying maximum principal plastic strain magnitudes.

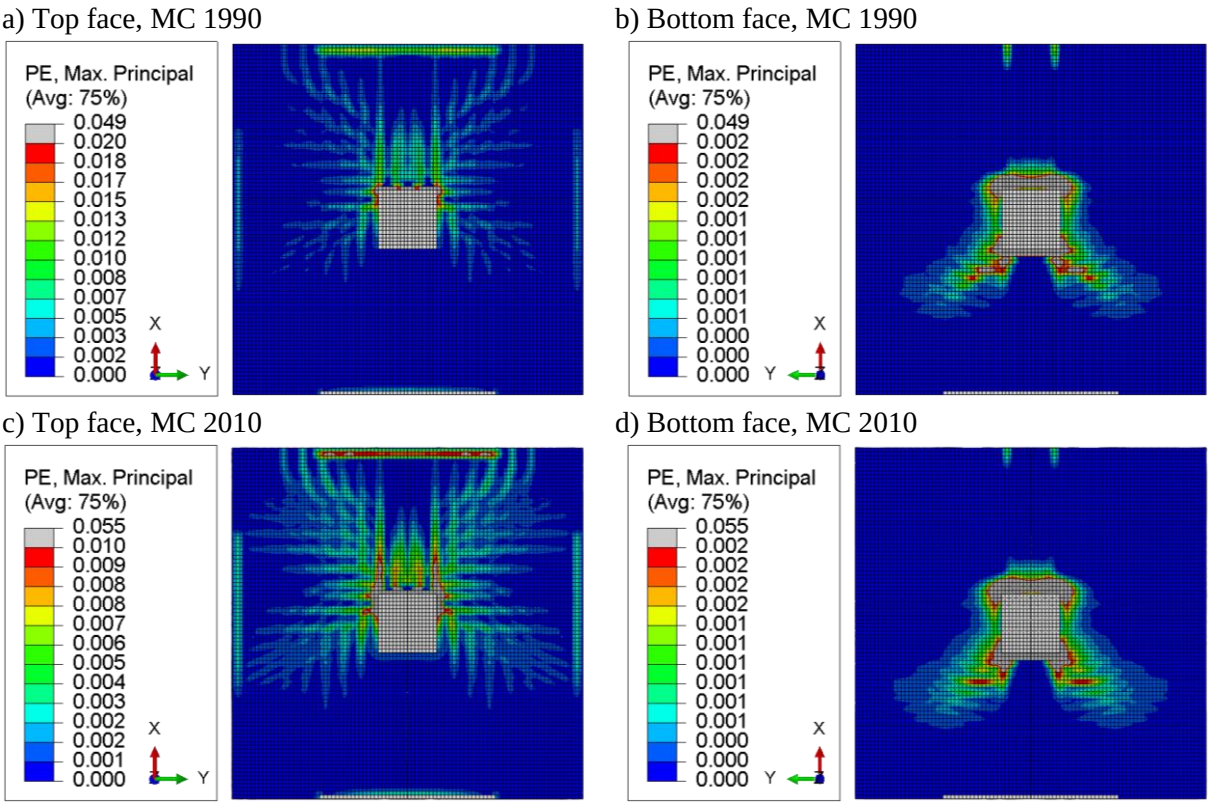

Figure 5.52: Specimen SM 1.0 analyses crack patterns using MC 1990 versus MC 2010 fracture energy models

5.4.3 Results of specimen SM 1.5 analyses

The moment-rotation and displacement-rotation data using MC 1990 and MC 2010 fracture energy analyses and experimental results for specimen SM 1.5 are presented in Figure 5.53. A summary of this data is provided in Table 5.24.

As was the case with the other two SM specimens, the MC 2010 analysis produced stiffer moment-rotation data with a greater ultimate moment compared to the MC 1990 analysis. The increased ultimate moment of the MC 2010 analysis meant an increased percentage difference between the analysis and the experiment. The percentage difference in ultimate moment between the analysis and the experiment was 13.3-percent and 20.4-percent for the MC 1990 and MC 2010 analyses, respectively.

The displacement-rotation data produced by both analyses were similar to one another. Both underestimated the displacement at ultimate moment of the experiment by a percentage difference of 122.9-percent.

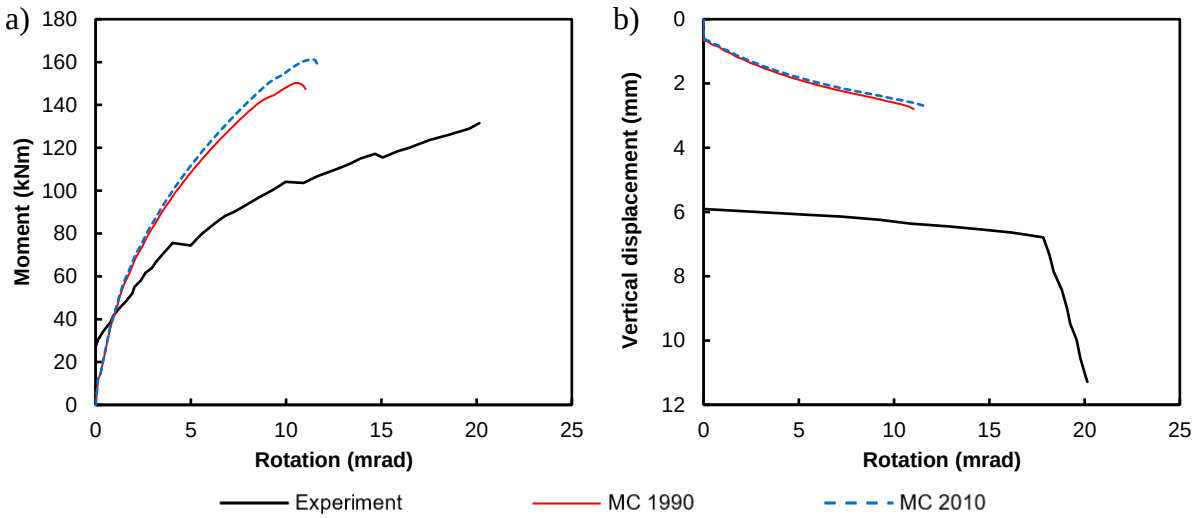

Figure 5.53: Specimen SM 1.5 a) moment-rotation and b) displacement-rotation data using MC 1990 versus MC 2010 fracture energy models

Table 5.24: Specimen SM 1.5 analyses results using MC 1990 versus MC 2010 fracture energy models

	Ultimate moment (kNm)	Displacement (mm) at ultimate moment	Rotation (mrad) at ultimate moment
Analyses			
MC 1990	150.2	2.7	10.5
MC 2010	161.3	2.7	11.4
Experiment	131.5	11.3	20.1

The crack patterns of the experiment as well as the MC 1990 and MC 2010 fracture energy analyses for specimen SM 1.5 are presented in Figure 5.54. As observed with the analyses for specimens SM 0.5 and SM 1.0, both analyses for specimen SM 1.5 produced similar crack patterns to one another with varying plastic strain magnitudes.

a) Top face, experiment

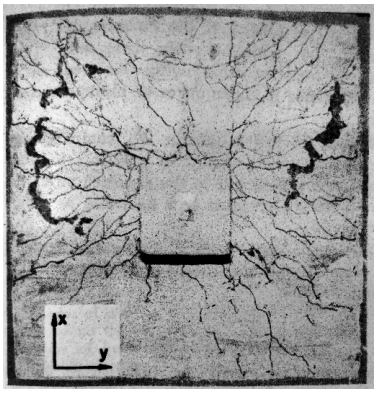

b) Bottom face, experiment

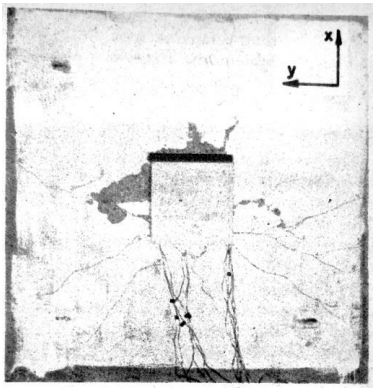

c) Top face, MC 1990

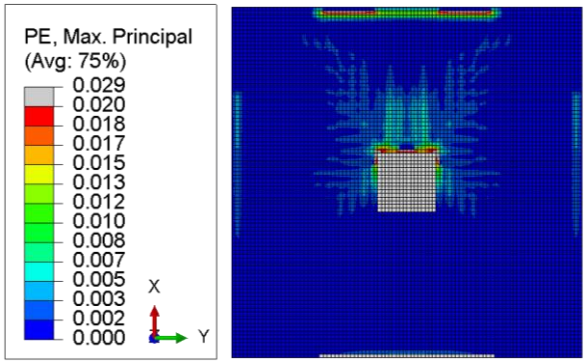

d) Bottom face, MC 1990

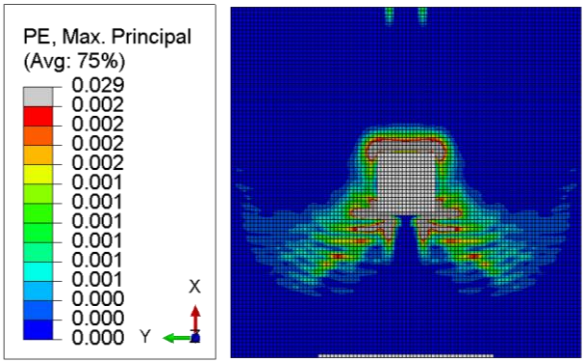

e) Top face, MC 2010

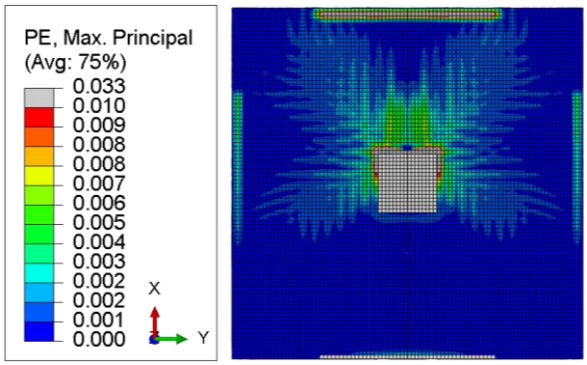

f) Bottom face, MC 2010

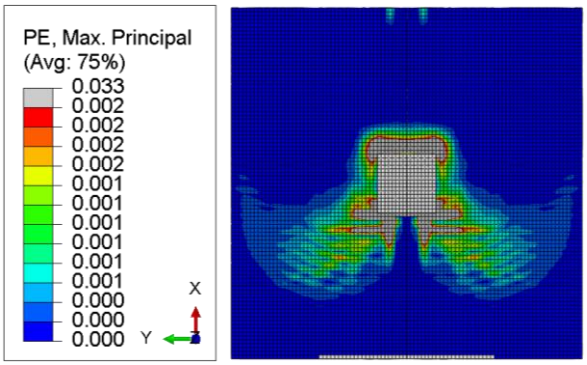

Figure 5.54: Specimen SM 1.5 experiment (Ghali et al., 1976) and analyses crack patterns using MC 1990 versus MC 2010 fracture energy models. Authorized reprint of experiment photographs from ACI Journal, Volume 73, Issue 10, October 1976.

5.4.4 Conclusions and recommendations

Analyses that used the Model Code 2010 fracture energy model produced stiffer moment-rotation data with greater ultimate moments compared to analyses that used the Model Code 1990 fracture energy model. This was expected because the Model Code 2010 fracture energy model produced higher fracture energy values for all specimens compared to the Model Code 1990 fracture energy model. A higher fracture energy meant that more tensile energy was

required to fracture a unit area of concrete. Using the MC 2010 model reduced the difference in ultimate moment between the analysis and the experiment for specimens SM 0.5 and SM 1.0 but increased the difference for specimen SM 1.5. For each specimen, both fracture energy models produced similar displacement-rotation data and crack patterns. The MC 2010 fracture energy model was used in subsequent analyses because it improved the accuracy of the analyses ultimate moments.

5.5 Equivalent versus as-tested reinforcement layout

In this section, the finite element models were modified to use an equivalent reinforcement layout then analysed. In this context, equivalent meant using different mat depths and spacings without affecting the moment resistance of either direction. Their results were compared to the results of the as-tested reinforcement layout models. Among the equivalent reinforcement layout models, the depths and spacings of the inner compression and tension mats were changed to match the depths and spacings of the outer compression and tension mats, respectively. While it was not realistic to have overlapping reinforcement bars, this was done as an exercise to observe if changing element connectivity influenced either the moment-rotation data, displacement-rotation data, or crack patterns.

5.5.1 Results of specimen SM 0.5 analyses

The moment-rotation and displacement-rotation data for the equivalent and as-tested reinforcement layout analyses and experimental results for specimen SM 0.5 are presented in Figure 5.55. A summary of this data is provided in Table 5.25.

Using an equivalent reinforcement layout did not significantly affect the results. When using the equivalent reinforcement layout, the slopes of both sets of data decreased by about 8-percent after 5 mrad (e.g. the displacement-rotation slope decreased from 0.39 mm/mrad to 0.36 mm/mrad). The percentage differences between the equivalent and the as-tested reinforcement layout analyses were 1.67-percent for the ultimate moment, 11.65-percent for the displacement at ultimate moment, and 6.36-percent for the rotation at ultimate moment. The as-tested reinforcement layout produced an ultimate moment closer to the experimental results, while the equivalent reinforcement layout produced displacement and rotation at ultimate moment values that were closer to the experimental results.

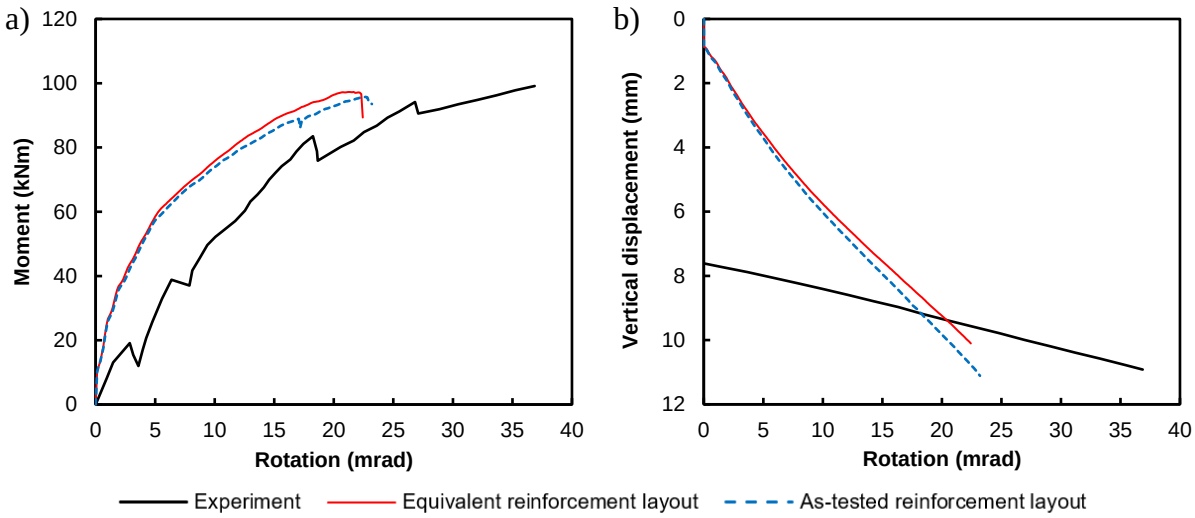

Figure 5.55: Specimen SM 0.5 a) moment-rotation and b) displacement-rotation data using equivalent versus as-tested reinforcement layouts

Table 5.25: Specimen SM 0.5 analyses results using equivalent versus as-tested reinforcement layouts

	Ultimate moment (kNm)	Displacement (mm) at ultimate moment	Rotation (mrad) at ultimate moment
Analyses			
Equivalent reinforcement layout	97.3	9.7	21.3
As-tested reinforcement layout	95.7	10.9	22.7
Experiment	99.1	10.9	36.9

The crack patterns of the experiment as well as the equivalent and as-tested reinforcement layout analyses for specimen SM 0.5 are presented in Figure 5.56. Both analyses produced crack patterns similar to one another. However, the equivalent reinforcement layout analysis did not produce some of the diagonal cracks observed in both the as-tested reinforcement layout analysis and the experiment. The first set of diagonal cracks missing were along the top face from the top column face toward the top left and right slab corners. The second set of diagonal cracks missing were along the bottom face from the bottom column face toward the left and right extents of the bottom edge restraints.

a) Top face, experiment

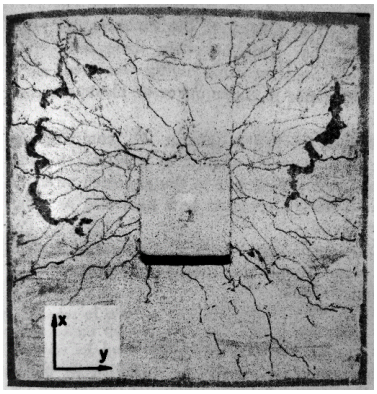

b) Bottom face, experiment

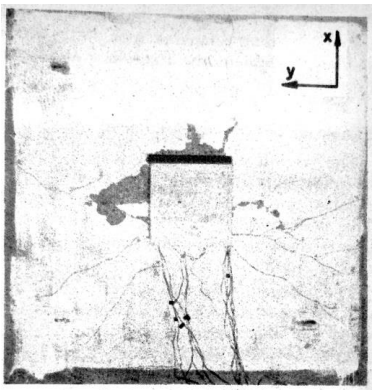

c) Top face, equivalent reinforcement layout

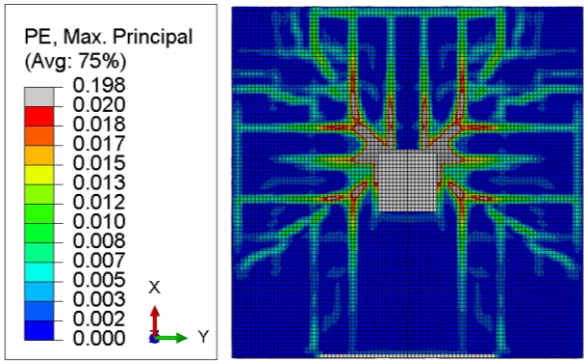

d) Bottom face, equivalent reinforcement layout

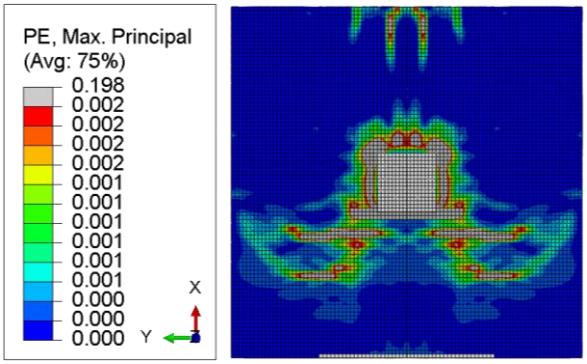

e) Top face, as-tested reinforcement layout

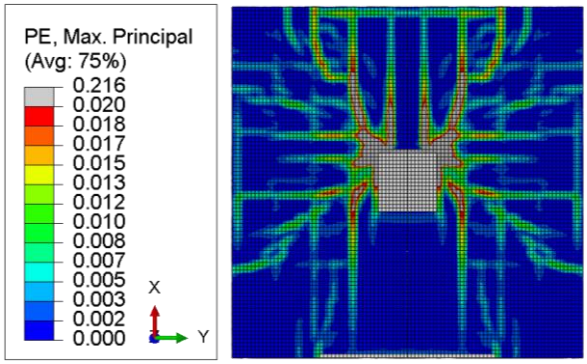

f) Bottom face, as-tested reinforcement layout

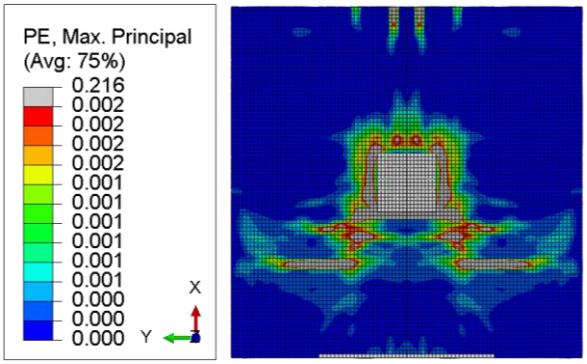

Figure 5.56: Specimen SM 0.5 experiment (Ghali et al., 1976) and analyses crack patterns using equivalent versus as-tested reinforcement layouts. Authorized reprint of experiment photographs from ACI Journal, Volume 73, Issue 10, October 1976.

5.5.2 Results of specimen SM 1.0 analyses

The moment-rotation and displacement-rotation data for the equivalent and as-tested reinforcement layout analyses and experimental results for specimen SM 1.0 are presented in Figure 5.57. A summary of this data is provided in Table 5.26. Both analyses produced identical moment-rotation and displacement-rotation results to one another. The ultimate moments of the two analyses were close to the ultimate moment of the experiment; there was a percentage

difference in ultimate moment of 4-percent and 5-percent relative to the experiment compared to the equivalent and as-tested reinforcement layout analyses, respectively. However, the rotation and vertical displacement at ultimate moment for each analysis were on average 37-percent lower and 33-percent lower than those experimental values.

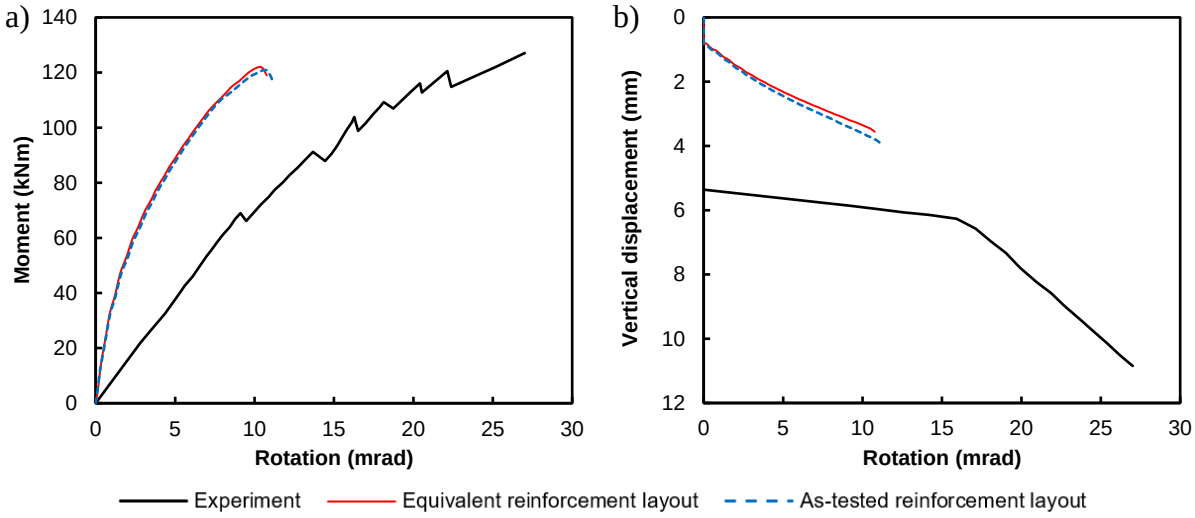

Figure 5.57: Specimen SM 1.0 a) moment-rotation and b) displacement-rotation data using equivalent versus as-tested reinforcement layouts

Table 5.26: Specimen SM 1.0 analyses results using equivalent versus as-tested reinforcement layouts

	Ultimate moment (kNm)	Displacement (mm) at ultimate moment	Rotation (mrad) at ultimate moment
Analyses			
Equivalent reinforcement layout	122.1	3.4	10.4
As-tested reinforcement layout	120.9	3.8	10.6
Experiment	127.1	10.8	27.0

The crack patterns of the experiment as well as the equivalent and as-tested reinforcement layout analyses for specimen SM 1.0 are presented in Figure 5.58. Both analyses produced crack patterns similar to one another. However, the equivalent reinforcement layout analysis did not produce some of the diagonal cracks observed in both the as-tested reinforcement layout analysis and the experiment. The first set of diagonal cracks missing were along the top face from the top column face toward the top left and right slab corners. The second set of diagonal

cracks missing were along the bottom face from the bottom column face toward the left and right extents of the bottom edge restraints.

a) Top face, equivalent reinforcement layout

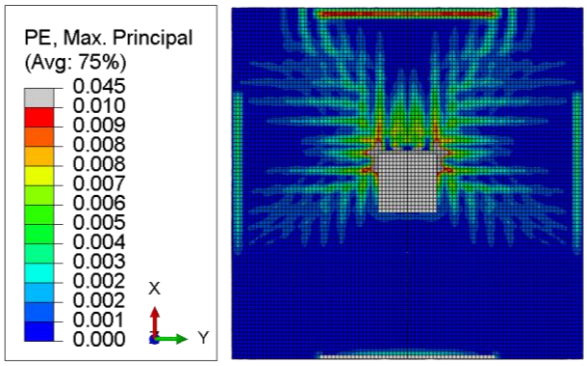

b) Bottom face, equivalent reinforcement layout

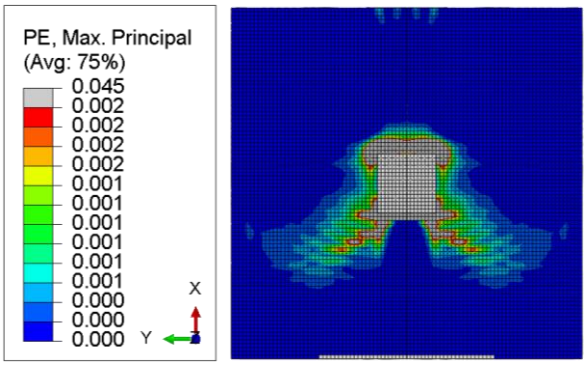

c) Top face, as-tested reinforcement layout

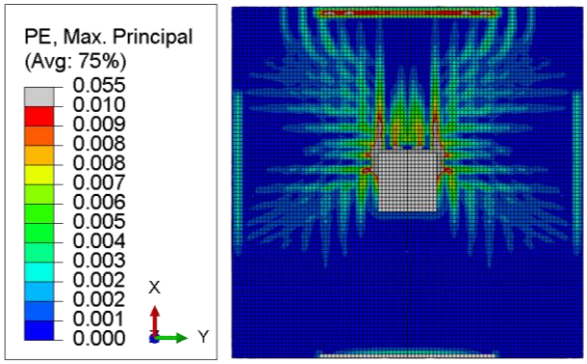

d) Bottom face, as-tested reinforcement layout

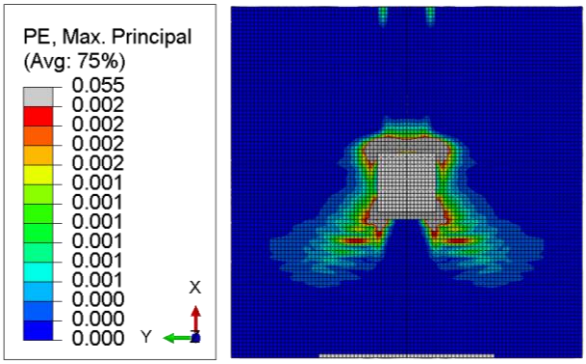

Figure 5.58: Specimen SM 1.0 analyses crack patterns using equivalent versus as-tested reinforcement layouts

5.5.3 Results of specimen SM 1.5 analyses

The moment-rotation and displacement-rotation data for the equivalent and as-tested reinforcement layout analyses and experimental results for specimen SM 1.5 are presented in Figure 5.59. A summary of this data is provided in Table 5.27. Both analyses produced identical moment-rotation and displacement-rotation results to one another.

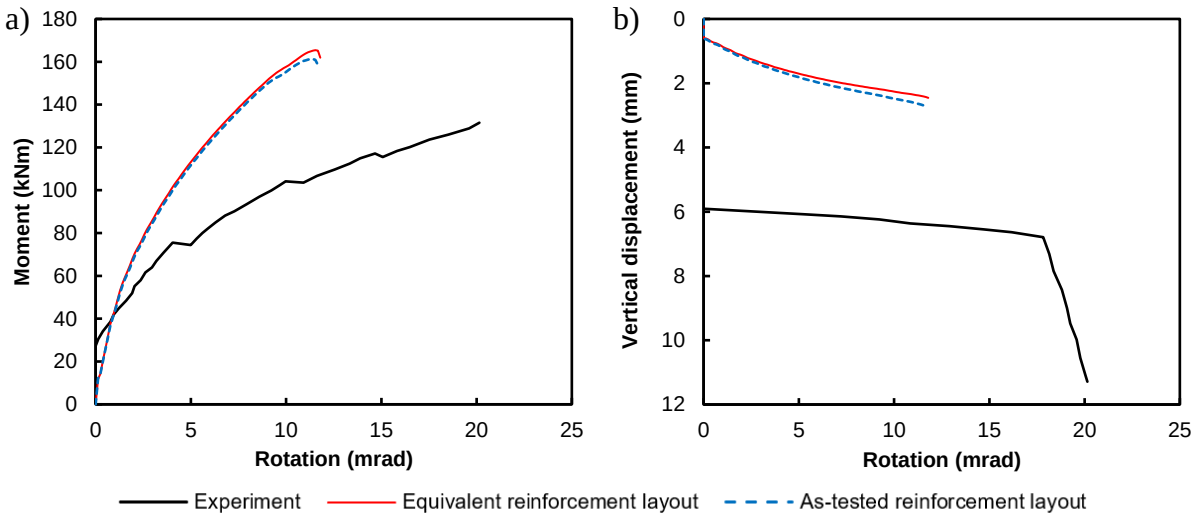

Figure 5.59: Specimen SM 1.5 a) moment-rotation and b) displacement-rotation data using equivalent versus as-tested reinforcement layouts

Table 5.27: Specimen SM 1.5 analyses results using equivalent versus as-tested reinforcement layouts

	Ultimate moment (kNm)	Displacement (mm) at ultimate moment	Rotation (mrad) at ultimate moment
Analyses			
Equivalent reinforcement layout	165.4	2.4	11.5
As-tested reinforcement layout	161.3	2.7	11.4
Experiment	131.5	11.3	20.1

The crack patterns of the experiment as well as the equivalent and as-tested reinforcement layout analyses for specimen SM 1.5 are presented in Figure 5.60. There were no differences between the crack patterns of the two analyses.

a) Top face, experiment

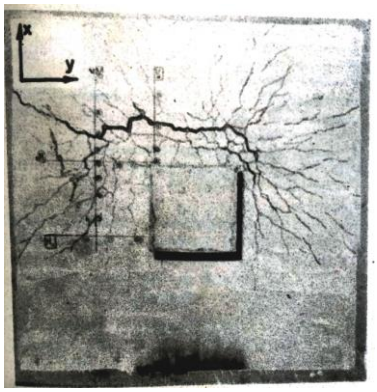

b) Bottom face, experiment

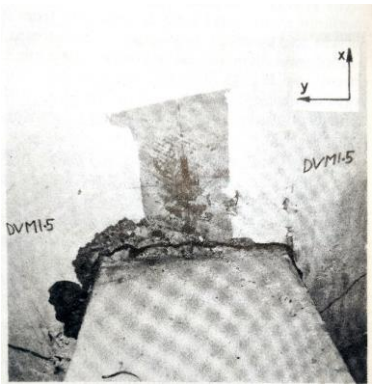

c) Top face, equivalent reinforcement layout

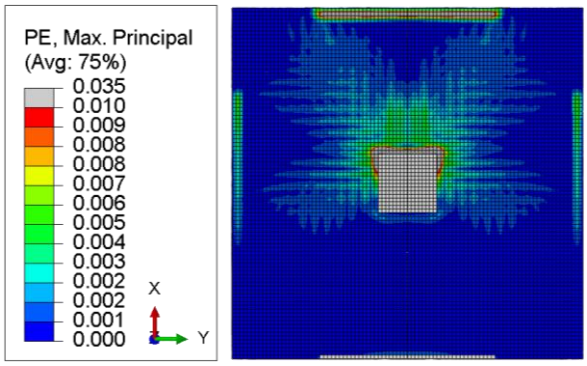

d) Bottom face, equivalent reinforcement layout

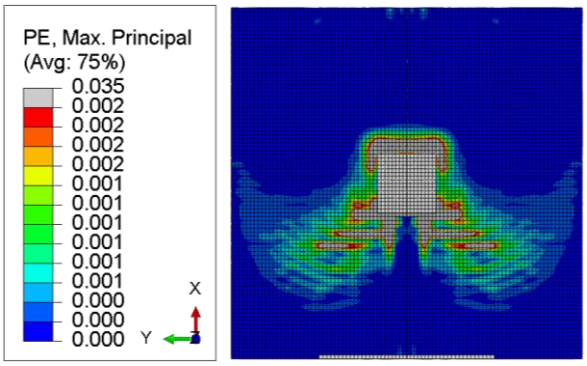

e) Top face, as-tested reinforcement layout

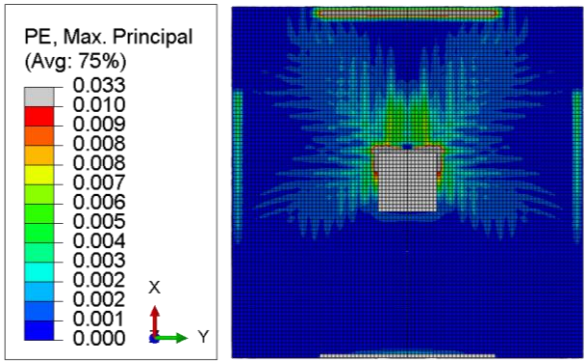

f) Bottom face, as-tested reinforcement layout

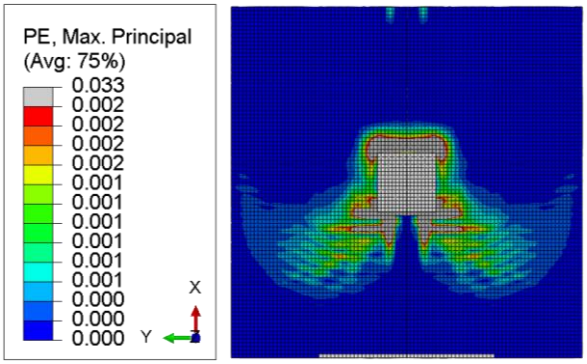

Figure 5.60: Specimen SM 1.5 experiment (Ghali et al., 1976) and analyses crack patterns using equivalent versus as-tested reinforcement layouts. Authorized reprint of experiment photographs from ACI Journal, Volume 73, Issue 10, October 1976.

5.5.4 Conclusions and recommendations

Using equivalent reinforcement layouts (i.e. changing the depths and spacings of the inner reinforcement mats to match the outer reinforcement depths and spacings) produced near identical results to those produced when using the as-tested reinforcement layouts. Fewer diagonal cracks were observed for specimen SM 0.5 when using the equivalent reinforcement layout; however, these cracks were present in both the as-tested reinforcement layout analysis

and during laboratory testing. Based on these results, the as-tested reinforcement layouts continued to be used in subsequent analyses.

5.6 Comparison of concrete mesh sizes

In this section, the effects of using varying concrete mesh sizes were studied. Previous analyses were completed using a concrete mesh size of 20 mm for the three specimens. For this study, previous analyses were modified and reanalysed using concrete mesh sizes of 15 mm, 25 mm, and 30 mm. For each specimen, the moment-rotation data, displacement-rotation data, and crack patterns were compared to one another and to the experiment. The concrete mesh size that produced analysis results that best resembled the experimental results was selected and used in subsequent analyses.

5.6.1 Results of specimen SM 0.5 analyses

The moment-rotation and displacement-rotation data for the analyses of varying concrete mesh sizes and experimental results for specimen SM 0.5 are presented in Figure 5.61. A summary of this data is provided in Table 5.28.

Based on the moment-rotation data, all analyses had slopes parallel to one another as they approached their respective ultimate moments. However, each analysis reached this slope at a different rate. The first analyses to reach this slope were the 25 mm and 30 mm concrete mesh size analyses. Following those analyses, the 20 mm mesh size analysis reached this slope followed by the 15 mm mesh size analysis. Based on these findings, increasing the concrete mesh size resulted in concrete cracking under lower applied moments.

All analyses produced similar displacement-rotation data. The only difference was that each displacement-rotation plot ended at a different rotation and displacement along the same curve. The ultimate rotation and ultimate displacement of each analysis was proportionate to the moment capacity of the analysis.

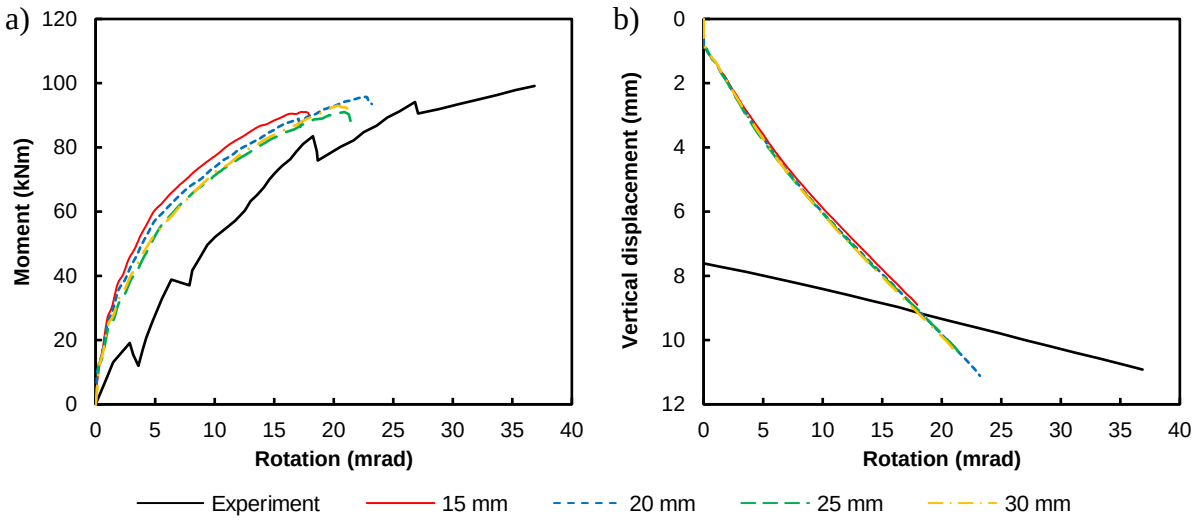

Figure 5.61: Specimen SM 0.5 a) moment-rotation and b) displacement-rotation data using varying concrete mesh sizes

Table 5.28: Specimen SM 0.5 results using varying concrete mesh sizes

	Ultimate moment (kNm)	Displacement (mm) at ultimate moment	Rotation (mrad) at ultimate moment
Analyses			
15 mm	91.1	8.7	17.3
20 mm	95.7	10.9	22.7
25 mm	91.0	10.1	20.9
30 mm	92.9	10.0	20.3
Experiment	99.1	10.9	36.9

Gradually increasing the size of concrete elements eventually resulted in single elements that exceeded the volume of strain concentrations. Since linear elements were used, these strains were distributed across the entire volume of the element. This meant that coarse mesh analyses inaccurately calculated strains in regions that were not strained during laboratory testing. As a result, these added strains reduced the rotational stiffness and ultimate moment of the models.

Contrarily, using too fine of a mesh also resulted in a lower ultimate moment. This was because smaller elements within volumes of high strain would have higher strains compared to larger elements in the same location (since the larger elements would linearly distribute the strains across their volume). The higher element strains for a smaller element would cause element failure to occur at a lower applied moment than it would for a larger element. With fewer elements active, the rotational stiffness and ultimate moment would decrease. This was observed

with the 15 mm concrete mesh size analysis. The moment-rotation data of this analysis showed a slight rotational softening prior to its failure. Furthermore, its ultimate failure occurred at 91.1 kNm, which was lower than the 20 mm concrete mesh size analysis that had an ultimate moment of 95.7 kNm.

As mentioned, using too coarse or too fine of a mesh resulted in lower moment capacities. For best accuracy, element sizes should be the same volume as the regions of strain concentrations.

The top face crack patterns of the experiment as well as the 15 mm, 20 mm, 25 mm, and 30 mm concrete mesh size analyses for specimen SM 0.5 are presented in Figure 5.62. There were no differences between the crack patterns of the four analyses.

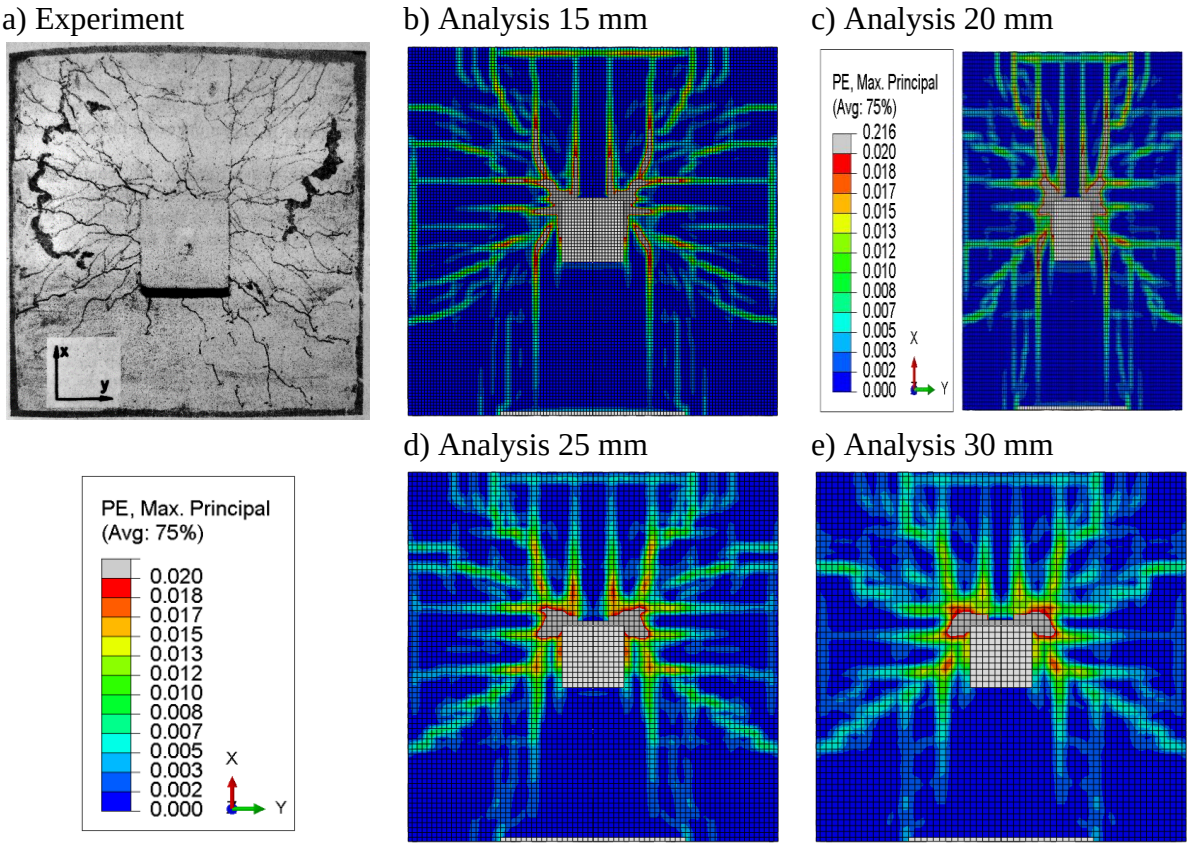

Figure 5.62: Specimen SM 0.5 top face experiment (Ghali et al., 1976) and analyses crack patterns using varying concrete mesh sizes. Authorized reprint of experiment photograph from ACI Journal, Volume 73, Issue 10, October 1976.

The bottom face crack patterns of the experiment as well as the 15 mm, 20 mm, 25 mm, and 30 mm concrete mesh size analyses for specimen SM 0.5 are presented in Figure 5.63. The 15 mm concrete mesh size analysis had higher strains at the top column face compared to the other

analyses. The 25 mm and 30 mm concrete mesh size analyses had strains at the bottom face that propagated further away from the column face compared to the other analyses.

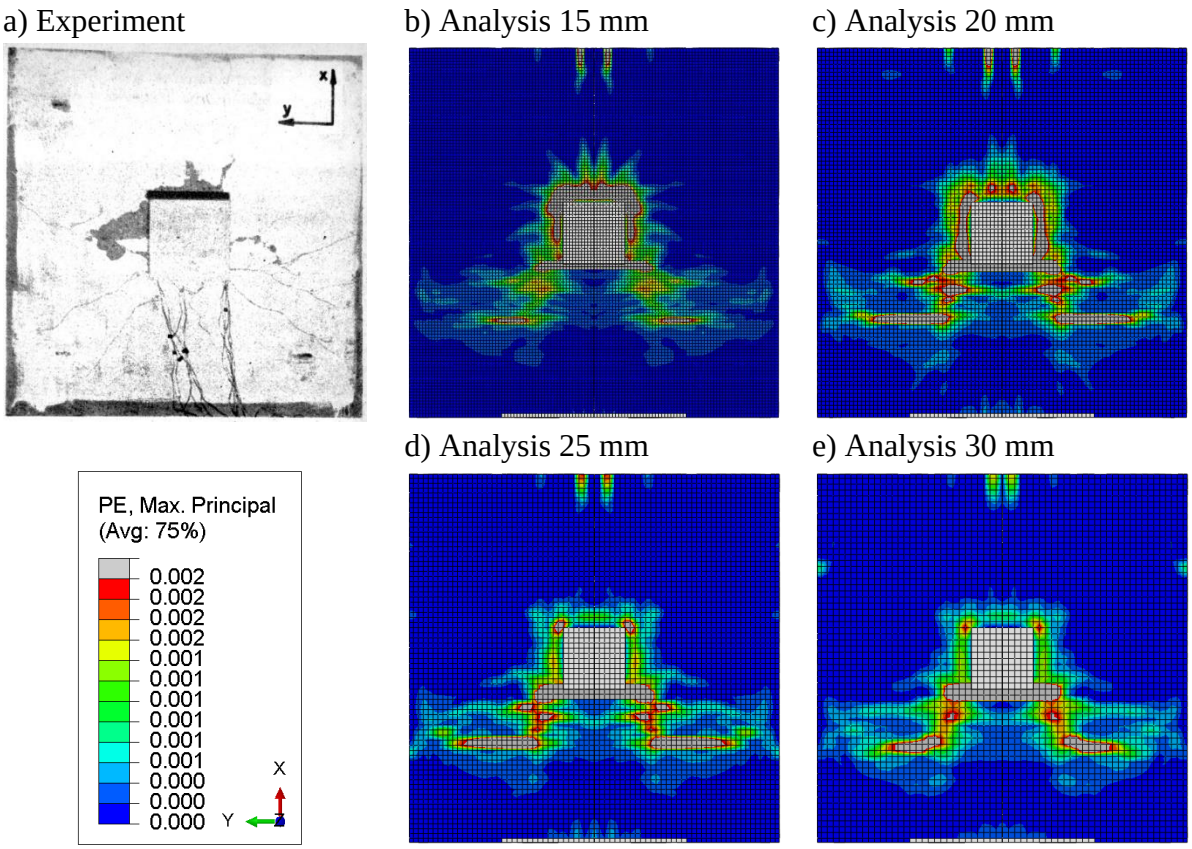

Figure 5.63: Specimen SM 0.5 bottom face experiment (Ghali et al., 1976) and analyses crack patterns using varying concrete mesh sizes. Authorized reprint of experiment photograph from ACI Journal, Volume 73, Issue 10, October 1976.

5.6.2 Results of specimen SM 1.0 analyses

The moment-rotation and displacement-rotation data for the analyses of varying concrete mesh sizes and experimental results for specimen SM 1.0 are presented in Figure 5.64. A summary of this data is provided in Table 5.29.

The same trends were observed among the specimen SM 1.0 analyses as observed among the specimen SM 0.5 analyses. The 25 mm and 30 mm concrete mesh size analyses had smaller ultimate moments compared to the 20 mm concrete mesh size analysis. As with the specimen SM 0.5 analyses, this was due to individual large elements distributing strains to areas where strains were not observed during testing. The 15 mm concrete mesh size analysis had a smaller ultimate moment compared to the 20 mm concrete mesh size analysis. As with the specimen

SM 0.5 analyses, this was because smaller elements within regions of strain concentrations had higher strains compared to when using larger elements. The higher element strains resulted in element failure occurring at lower applied moments. Having fewer active elements meant that the model moment capacity was reduced.

As observed with the displacement-rotation data of the SM 0.5 analyses, the displacement-rotation data of the SM 1.0 analyses overlapped one another. Analyses with larger ultimate moments had proportionately larger ultimate displacements and ultimate moments along the same curve.

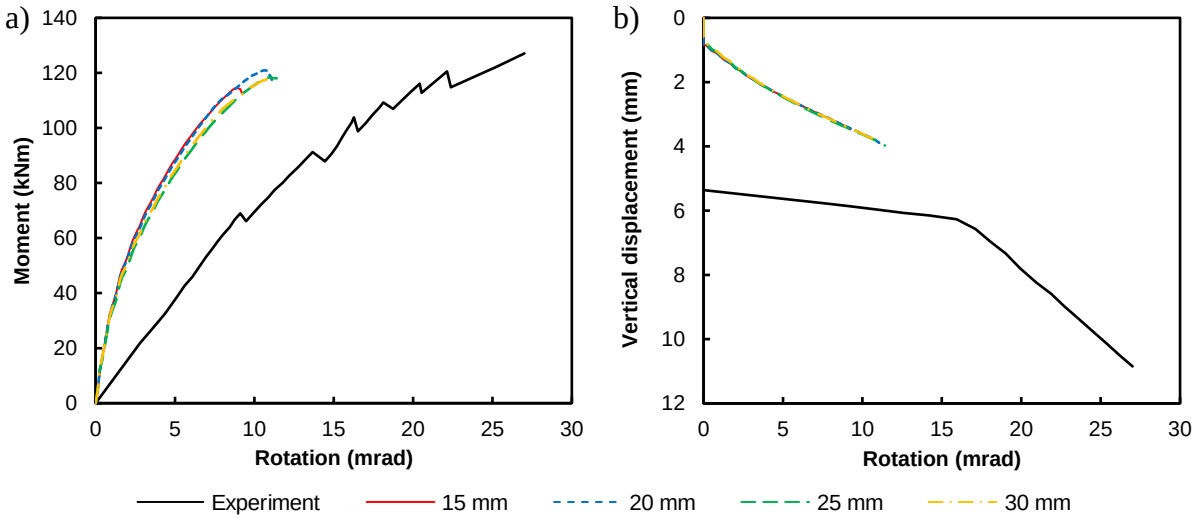

Figure 5.64: Specimen SM 1.0 a) moment-rotation and b) displacement-rotation data using varying concrete mesh sizes

Table 5.29: Specimen SM 1.0 results using varying concrete mesh sizes

	Ultimate moment (kNm)	Displacement (mm) at ultimate moment	Rotation (mrad) at ultimate moment
Analyses			
15 mm	114.6	3.4	8.8
20 mm	120.9	3.8	10.6
25 mm	121.0	4.5	13.6
30 mm	117.7	3.8	10.8
Experiment	127.1	10.8	27.0

The top and bottom crack patterns of the 15 mm, 20 mm, 25 mm, and 30 mm concrete mesh size analyses for specimen SM 1.0 are presented in Figure 5.65. The 15 mm concrete mesh size analysis showed cracks propagating outward from the top column face along its top slab face.

Increasing the concrete mesh size decreased the length of these cracks. Among the bottom face crack patterns, the 15 mm concrete mesh size had the shortest cracks propagating from the bottom face toward the bottom support edge. The length of these cracks increased as the concrete mesh size was increased from 15 mm to 20 mm then to 25 mm. However, the lengths of these cracks produced by the 30 mm concrete mesh size analysis resembled those of the 20 mm concrete mesh size analysis.

a) Top face, analysis 15 mm

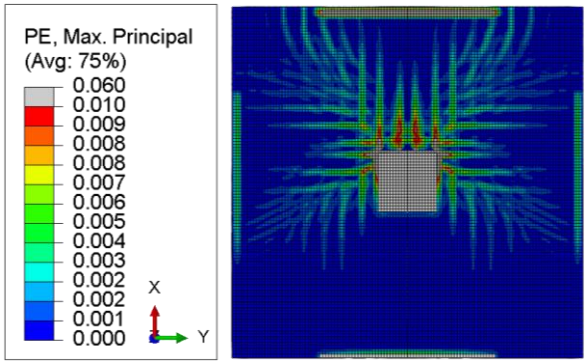

b) Bottom face, analysis 15 mm

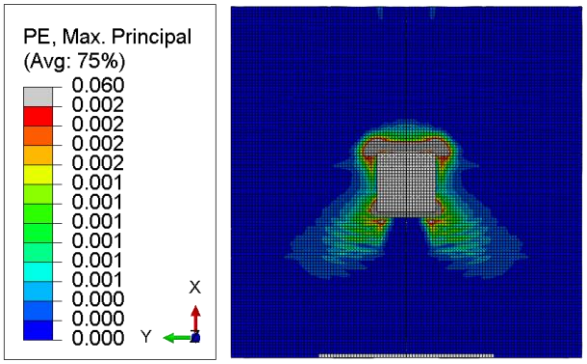

c) Top face, analysis 20 mm

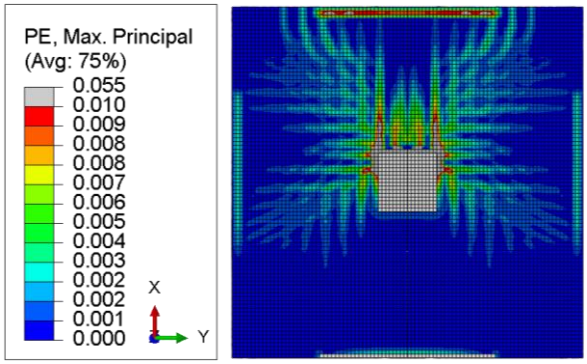

d) Bottom face, analysis 20 mm

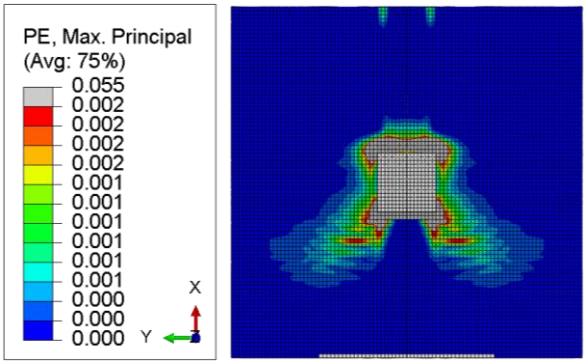

e) Top face, analysis 25 mm

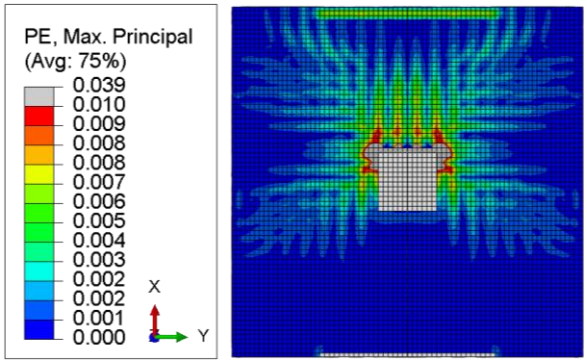

f) Bottom face, analysis 25 mm

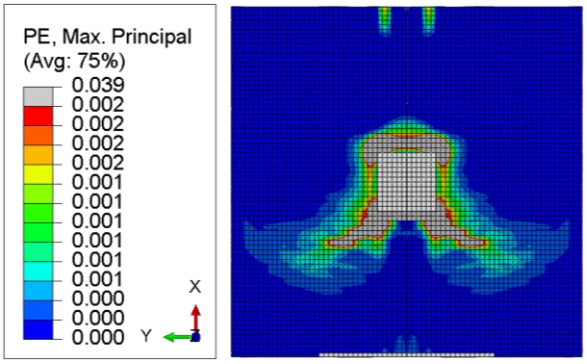

g) Top face, analysis 30 mm

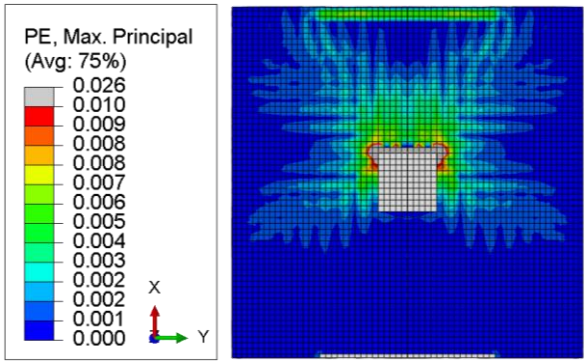

h) Bottom face, analysis 30 mm

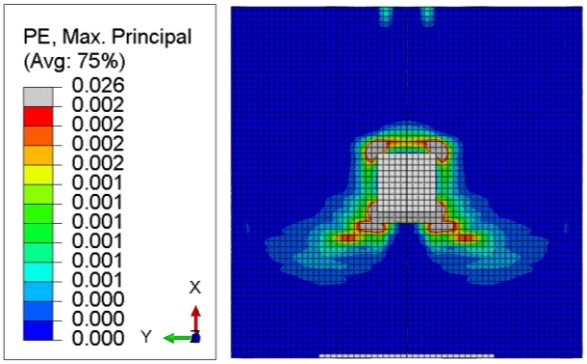

Figure 5.65: Specimen SM 1.0 analyses crack patterns using varying concrete mesh sizes

5.6.3 Results of specimen SM 1.5 analyses

The moment-rotation and displacement-rotation data for the analyses of varying concrete mesh sizes and experimental results for specimen SM 1.5 are presented in Figure 5.66. A summary of this data is provided in Table 5.30.

Both moment-rotation and displacement-rotation data for these analyses produced the same trends as observed with specimens SM 0.5 and SM 1.0. The 25 mm and 30 mm concrete mesh size analyses had the lower ultimate moments compared to the 20 mm concrete mesh size analysis. As with the SM 0.5 and SM 1.0 analyses, this meant these mesh sizes were too large. The 15 mm concrete mesh had the lowest ultimate moment of the four analyses. This meant that this mesh size was too small. The displacement-rotation data for all analyses overlapped one another.

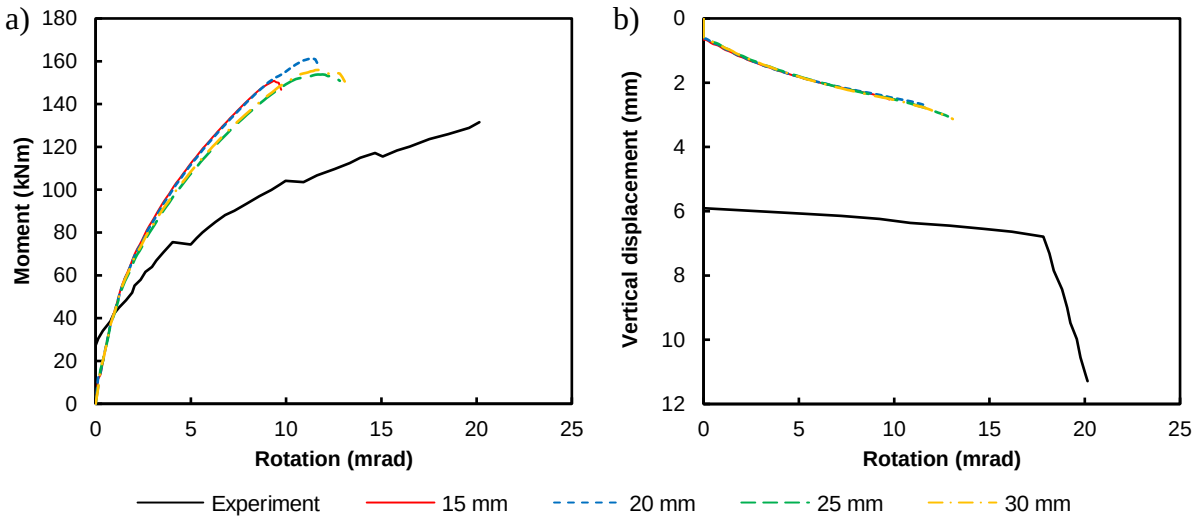

Figure 5.66: Specimen SM 1.5 a) moment-rotation and b) displacement-rotation data using varying concrete mesh sizes

Table 5.30: Specimen SM 1.5 results using varying concrete mesh sizes

	Ultimate moment (kNm)	Displacement (mm) at ultimate moment	Rotation (mrad) at ultimate moment
Analyses			
15 mm	150.9	2.4	9.4
20 mm	161.3	2.7	11.4
25 mm	153.8	2.8	11.7
30 mm	155.9	2.8	11.8
Experiment	131.5	11.3	20.1

The top face crack patterns of the experiment as well as the 15 mm, 20 mm, 25 mm, and 30 mm concrete mesh size analyses for specimen SM 1.5 are presented in Figure 5.67. The 15 mm concrete mesh size analysis produced cracks where it was clear that four main cracks propagated from the column towards the four slab corners. Smaller, orthogonal cracks were visible branching off of the four main cracks. Each subsequent increases in concrete mesh size resulted in lower resolutions of analysis crack patterns. As the elements were linear with one integration point, these larger elements averaged concentrated strains within them over entire element volumes. This made it difficult to discern the difference between the four main cracks and the smaller, branching cracks. Due to its high resolution, the 15 mm concrete mesh size analysis produced top face crack patterns that best resembled the experimental crack patterns.

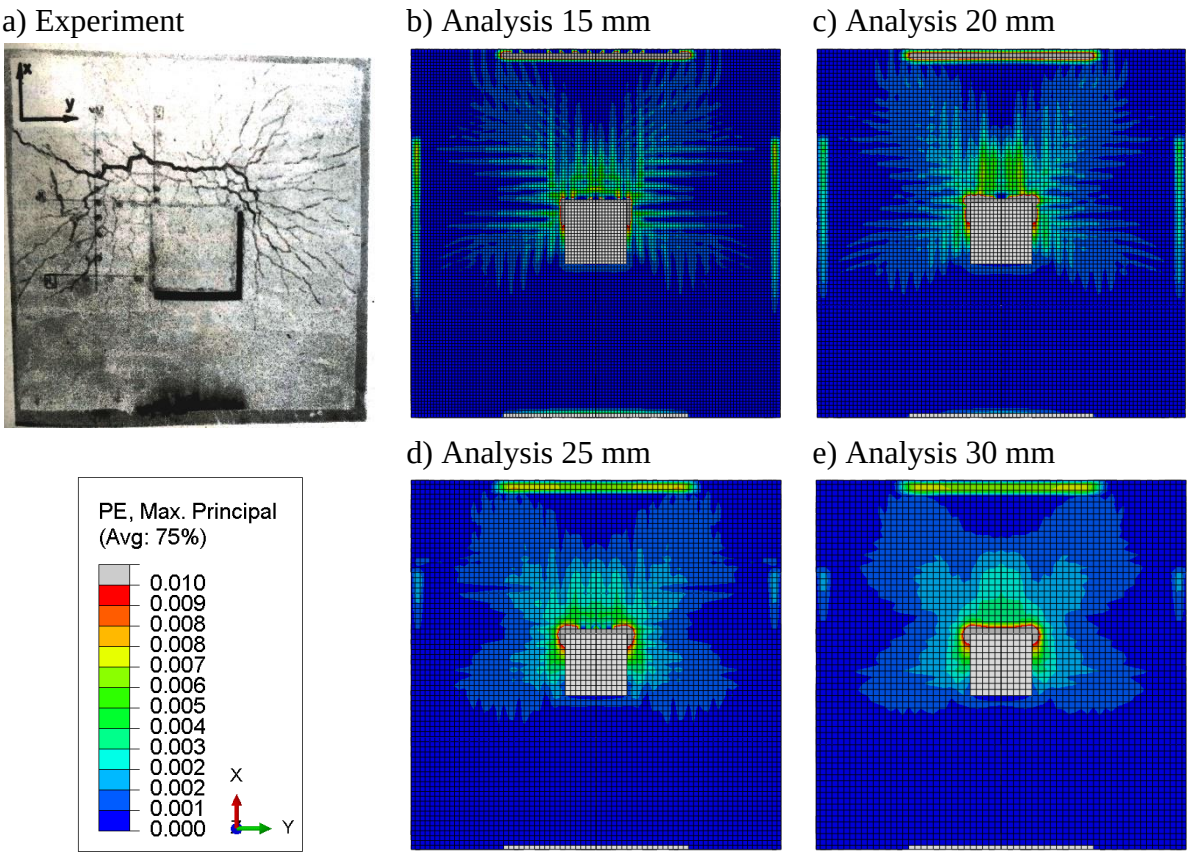

Figure 5.67: Specimen SM 1.5 top face experiment (Ghali et al., 1976) and analyses crack patterns using varying concrete mesh sizes. Authorized reprint of experiment photograph from ACI Journal, Volume 73, Issue 10, October 1976.

The bottom face crack patterns of the experiment as well as the 15 mm, 20 mm, 25 mm, and 30 mm concrete mesh size analyses for specimen SM 1.5 are presented in Figure 5.68. As with the

top face crack patterns, the 15 mm concrete mesh size analysis produced the highest resolution crack patterns and the 30 mm mesh size analysis produced the lowest. Among the analyses, there were two main cracks forming from the bottom column face toward the bottom left and right slab corners. Smaller, orthogonal cracks branched out from those two cracks. Each increase in concrete mesh size made it more difficult to differentiate between the two main cracks and the smaller, branching cracks. As only a close-up photograph of the specimen column was published, it was not possible to comment on the accuracy of the aforementioned cracks. However, the concentration of cracking at the positive-x column face shown in the photograph was also observed in all four analyses.

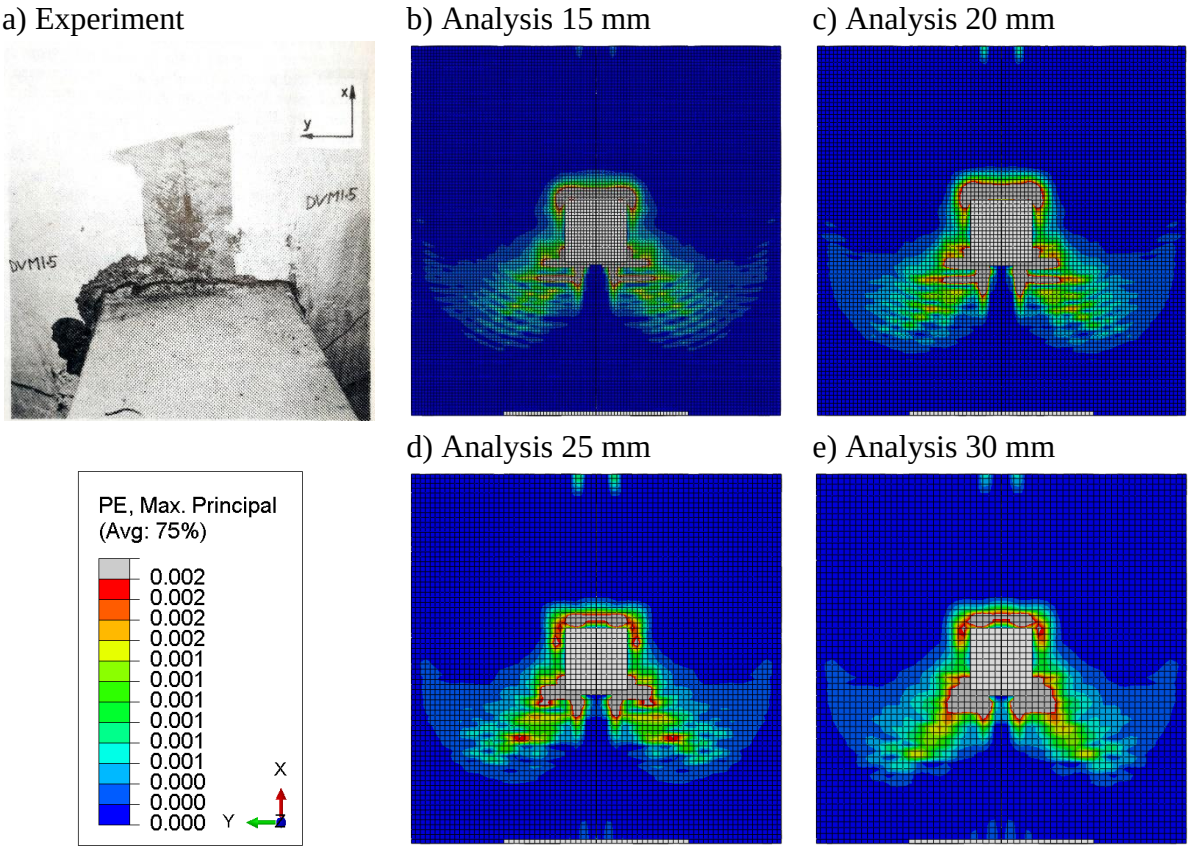

Figure 5.68: Specimen SM 1.5 bottom face experiment (Ghali et al., 1976) and analyses crack patterns using varying concrete mesh sizes. Authorized reprint of experiment photograph from ACI Journal, Volume 73, Issue 10, October 1976.

5.6.4 Conclusions and recommendations

Based on the analyses for the three SM specimens using concrete mesh sizes of 15 mm, 20 mm, 25 mm, and 30 mm, the 20 mm concrete mesh size analyses produced results that most

accurately resembled the results of the experiment. Using a concrete mesh size of 15 mm resulted in high element strains within regions of strain concentrations. This caused elements to fail and become inactive under lower applied moments. With fewer active elements, the effective concrete area was reduced resulting in a lower moment capacity. Contrarily, using large concrete mesh sizes resulted in elements that were partially inside high strain regions and partially inside low/no strain regions. However, as these elements had one integration point and linear shape functions, the analyses produced strains across the entire element. This meant that the analyses produced strains in locations where no strains were observed during testing. As a result, the moment capacities of the models were reduced.

The optimal concrete mesh size for the three specimens was 20 mm. Smaller than 20 mm resulted in high strains within elements leading to element failure. Larger than 20 mm resulted in elements extending beyond regions of strain concentrations. It was important to choose an element size such that when the geometry was meshed and analysed, no element would exist in both high and low strain regions simultaneously. Instead of calibrating the concrete element size, another option was to use higher order elements with multiple integration points. This option was avoided as higher order elements would require much more computational power and time.

With respect to the displacement-rotation data, the analyses for each specimen produced data similar to one another. Furthermore, the crack patterns of all analyses for each specimen showed identical cracks of varying resolution. The 15 mm concrete mesh size analyses showed large cracks propagating from the columns toward the slab corners. Smaller, orthogonal cracks were observed branching off of the larger cracks. As the concrete mesh size was increased, the linear shape functions of the elements would calculate strains in locations where strains were not observed during testing. As a result, it was more difficult to differentiate between the main, large cracks from the branching, smaller cracks. The 15 mm concrete mesh size analyses produced very clear crack patterns that best resembled the cracks observed during testing. However, the 15 mm concrete mesh size analyses produced inaccurate moment-rotation data.

The 20 mm concrete mesh size analyses produced ultimate moments that were close to the experimental values. Furthermore, these analyses produced crack patterns that were clear and

accurate to the experimental crack patterns. For these reasons, a concrete mesh size of 20 mm was used in subsequent analyses.

5.7 Comparison of reinforcement mesh sizes and element types

In this section, the effects of using varying reinforcement mesh sizes and element types were studied. Previous analyses were completed using 20 mm T3D2 truss elements for both the slab and column reinforcement. This element size was selected such that the reinforcement and concrete used the same element size.

For this study, six models of varying reinforcement mesh sizes and element types were analysed and compared. The first three models used T3D2 truss elements with mesh sizes of 20 mm, 50 mm, and 100 mm. The last three models used B31 beam elements with mesh sizes of 20 mm, 50 mm, and 100 mm. The B31 beam element analyses were conducted to determine whether or not the additional degrees of freedom would produce more accurate results compared to the T3D2 truss element analyses. T3D2 truss elements have the three translational degrees of freedom at both ends of the element and only transfer axial stresses. B31 beam elements have three rotational degrees of freedom in additional to the three translational degrees of freedom at both ends. Furthermore, B31 beam elements transfer shear stresses in addition to axial stresses.

For each specimen, the moment-rotation data, displacement-rotation data, and crack patterns were compared to one another and to the experiment. The reinforcement mesh size and element type that produced analysis results that best resembled the experimental results were selected and used in subsequent analyses.

5.7.1 Results of specimen SM 0.5 analyses

The moment-rotation and displacement-rotation data for the analyses of varying reinforcement mesh sizes and element types, in addition to the experimental results, for specimen SM 0.5 are presented in Figure 5.69. A summary of this data is provided in Table 5.31.

All analyses produced moment-rotation data of similar slope and capacity. The moment-rotation slopes of analyses 20 mm T3D2 and 50 mm T3D2 were most similar to the experiment as these analyses approached failure. However, the 50 mm T3D2 analysis had the lowest ultimate moment of 90.8 kNm compared to the other analyses. Analyses 100 mm T3D2 and 100 mm

B31 produced the most accurate ultimate moments compared to the other analyses. Analyses 100 mm T3D2 and 100 mm B31 had a percentage differences of 0.4-percent and 1.5-percent, respectively, relative to the experimental ultimate moment. Also, these analyses had higher rotations at ultimate moments compared to the other analyses.

Based on the displacement-rotation data, all analyses produced data that fit the same curve. Analysis 20 mm T3D2 had a displacement at ultimate moment of 10.9 mm, which matched the experimental value. Analyses 100 mm T3D2 and 100 mm B31 produced displacements similar to that of the experiment (11.1 mm and 11.0 mm, respectively). The displacement at ultimate moment percentage differences relative to the experiment were 1.8-percent and 0.9-percent, respectively. These two analyses also produced the largest rotations of all analyses.

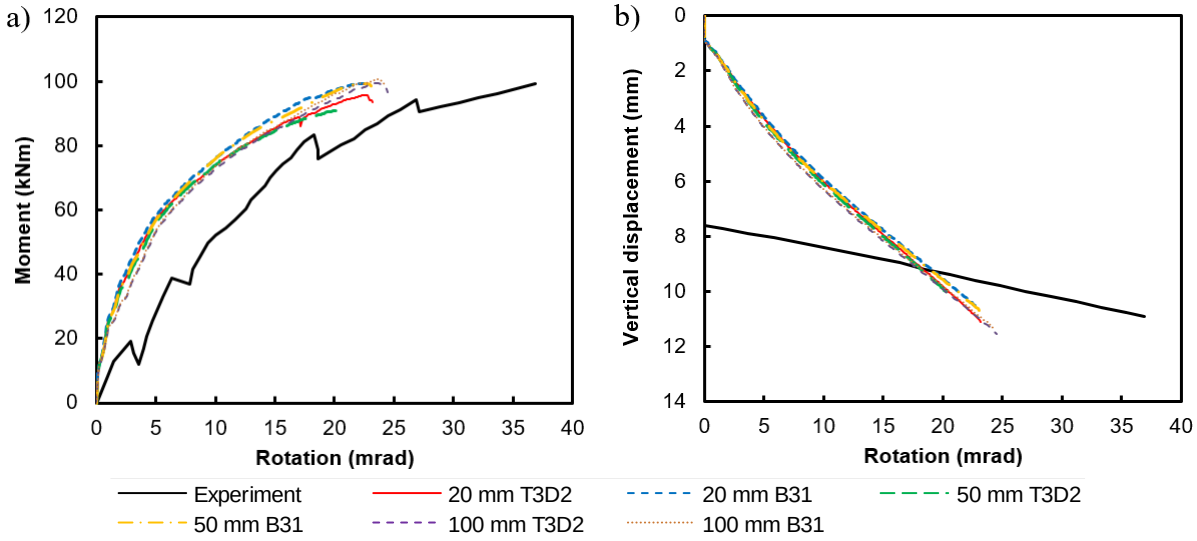

Figure 5.69: Specimen SM 0.5 a) moment-rotation and b) displacement-rotation data using varying reinforcement mesh types and sizes

Table 5.31: Specimen SM 0.5 results using varying reinforcement mesh types and sizes

	Ultimate moment (kNm)	Displacement (mm) at ultimate moment	Rotation (mrad) at ultimate moment
Analyses			
20 mm T3D2	95.7	10.9	22.7
20 mm B31	99.4	10.2	21.9
50 mm T3D2	90.8	9.9	20.0
50 mm B31	99.3	10.5	22.6
100 mm T3D2	99.5	11.1	23.5
100 mm B31	100.6	11.0	23.5
Experiment	99.1	10.9	36.9

The top face crack patterns of the experiment as well as the varying reinforcement element size and element type analyses for specimen SM 0.5 are presented in Figure 5.70. For each reinforcement element size, the T3D2 analyses and the B31 analyses produced crack patterns that were similar to one another. The 20 mm T3D2, 20 mm B31, 50 mm T3D2, and 50 mm B31 analyses were similar to one another. The main cracks produced by these analyses started at the column and propagated outward toward the slab corners. The 100 mm T3D2 and 100 mm B31 analyses produced the same diagonal cracks. However, these analyses produced additional cracks located at half the distance between the column faces and slab edges. These cracks formed parallel to the column faces. The cracks observed within the photographed experiment crack patterns were primarily diagonal. Therefore, the crack patterns of the 100 mm T3D2 and 100 mm B31 analyses were least representative of the experiment crack patterns.

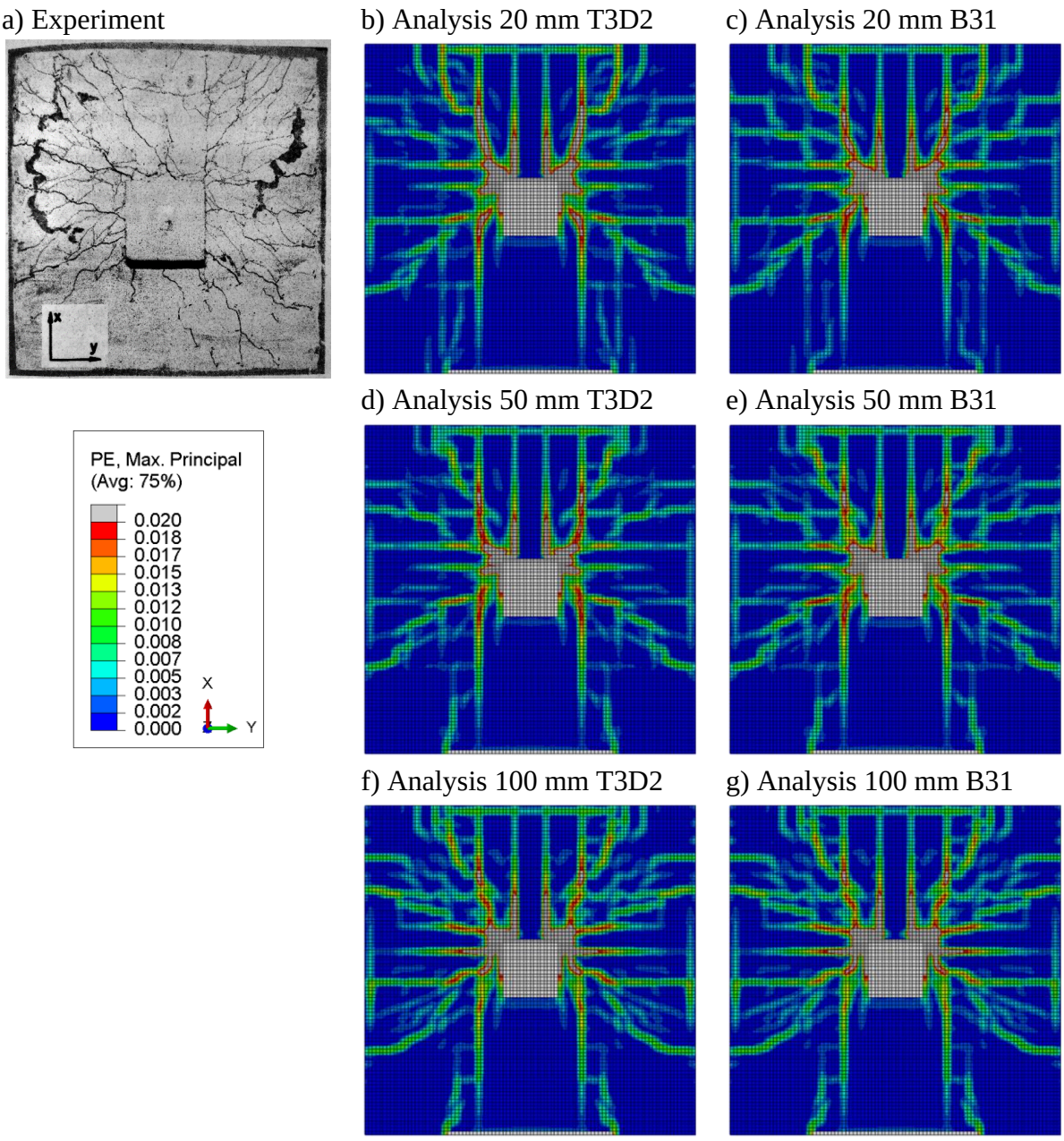

Figure 5.70: Specimen SM 0.5 top face experiment (Ghali et al., 1976) and analyses crack patterns using varying reinforcement mesh types and sizes. Authorized reprint of experiment photograph from ACI Journal, Volume 73, Issue 10, October 1976.

The bottom face crack patterns of the experiment as well as the varying reinforcement element size and element type analyses for specimen SM 0.5 are presented in Figure 5.71. The 20 mm T3D2, 20 mm B31, 50 mm T3D2, and 50 mm B31 analyses were similar to one another. The 100 mm T3D2 and 100 mm B31 analyses produced the same cracks observed among the other analyses. However, these analyses produced additional horizontal cracks starting along the

bottom column face and propagating toward the left and right slab edges. These cracks were not observed among the photographed experiment crack patterns.

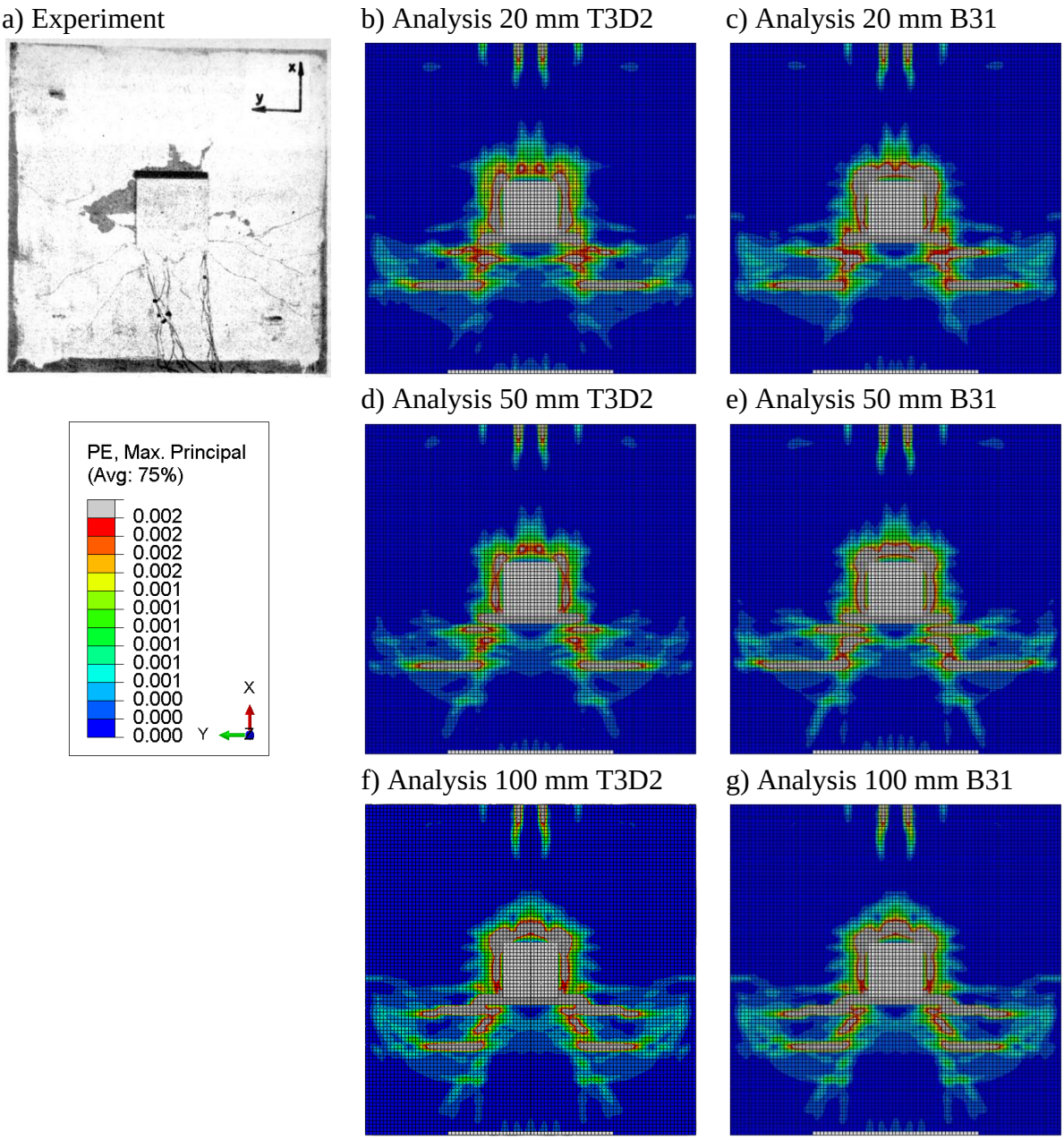

Figure 5.71: Specimen SM 0.5 bottom face experiment (Ghali et al., 1976) and analyses crack patterns using varying reinforcement mesh types and sizes. Authorized reprint of experiment photograph from ACI Journal, Volume 73, Issue 10, October 1976.

5.7.2 Results of specimen SM 1.0 analyses

The moment-rotation and displacement-rotation data for the analyses of varying reinforcement mesh sizes and element types, in addition to the experimental results, for specimen SM 1.0 are presented in Figure 5.72. A summary of this data is provided in Table 5.32.

The 20 mm T3D2, 20 mm B31, 50 mm T3D2, and 50 mm B31 analyses produced near-identical results. The 100 mm T3D2 and 100 mm B31 analyses produced softer moment-rotation data compared to the other analyses. Furthermore, the ultimate moments of these analyses were 116.9 kNm and 117.7 kNm, respectively. The other analyses produced ultimate moments between 120.0 kNm and 122.6 kNm. These analyses were closer to the ultimate moment of the experiment (127.1 kNm).

The displacement-rotation data of all analyses overlapped one another. All analyses except for the 100 mm analyses produced displacements at ultimate moments of approximately 3.8 mm. The 100 mm T3D2 and 100 mm B31 analyses had the same displacement at ultimate moment (4.1 mm). These analyses had displacements at ultimate moments that were closest to the experimental value (10.8 mm).

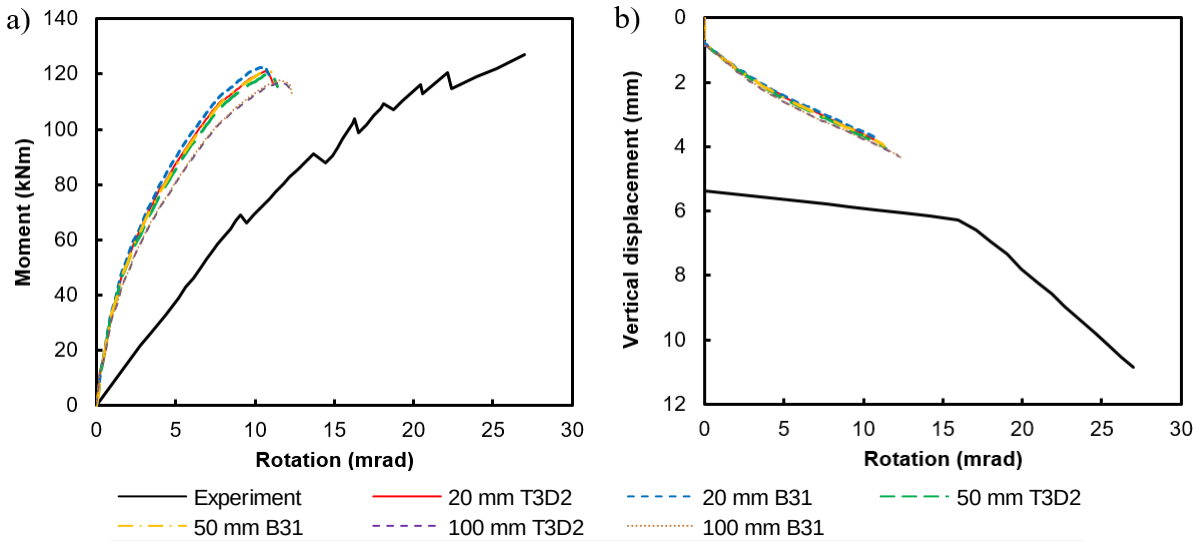

Figure 5.72: Specimen SM 1.0 a) moment-rotation and b) displacement-rotation data using varying reinforcement mesh types and sizes

Table 5.32: Specimen SM 1.0 results using varying reinforcement mesh types and sizes

	Ultimate moment (kNm)	Displacement (mm) at ultimate moment	Rotation (mrad) at ultimate moment
Analyses			
20 mm T3D2	120.9	3.8	10.6
20 mm B31	122.6	3.7	10.5
50 mm T3D2	120.0	3.8	10.8
50 mm B31	121.2	3.8	10.9
100 mm T3D2	116.9	4.1	11.5
100 mm B31	117.7	4.1	11.5
Experiment	127.1	10.8	27.0

The top face crack patterns of the experiment as well as the varying reinforcement element size and element type analyses for specimen SM 1.0 are presented in Figure 5.73. For each reinforcement element size, the T3D2 analyses and the B31 analyses produced crack patterns identical to one another. The main cracks produced by all analyses started at the column and propagated outward toward the slab corners. The 50 mm reinforcement element size analyses had large vertical and horizontal cracks along the reinforcement bars near the column. This was because the long elements linearly distributed large strains from the column faces across the length of the elements. This resulted in crack patterns showing strains where strains were not observed during testing. This is similar to the findings of the concrete mesh size study. The 100 mm reinforcement element size analyses produced even larger vertical and horizontal cracks. This was because the high strains were now being distributed over an even larger element length.

a) Top face, analysis 20 mm T3D2

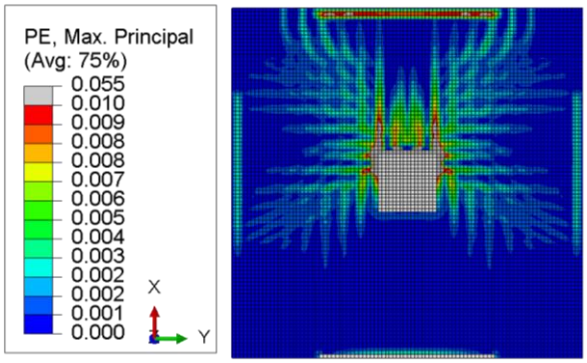

b) Top face, analysis 20 mm B31

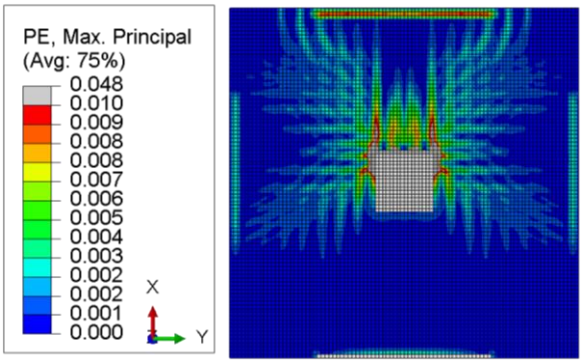

c) Top face, analysis 50 mm T3D2

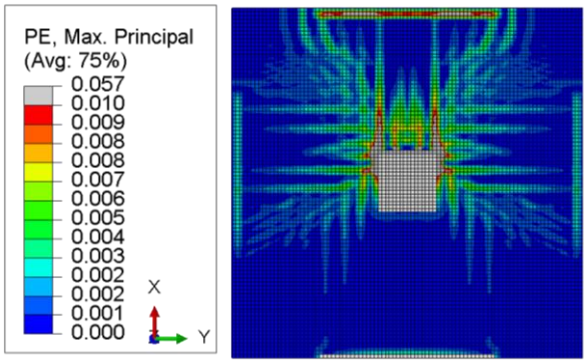

d) Top face, analysis 50 mm B31

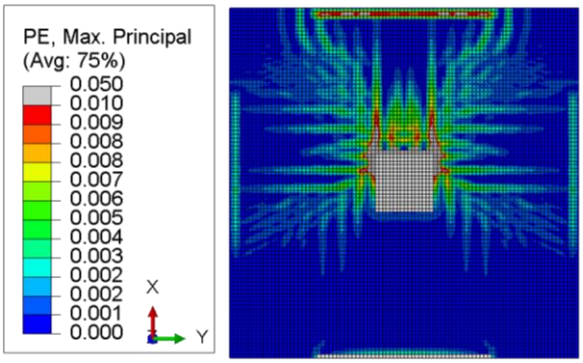

e) Top face, analysis 100 mm T3D2

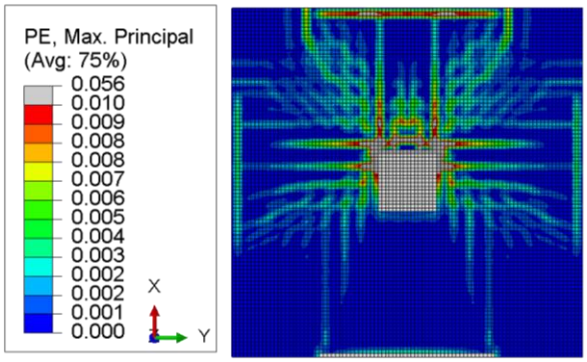

f) Top face, analysis 100 mm B31

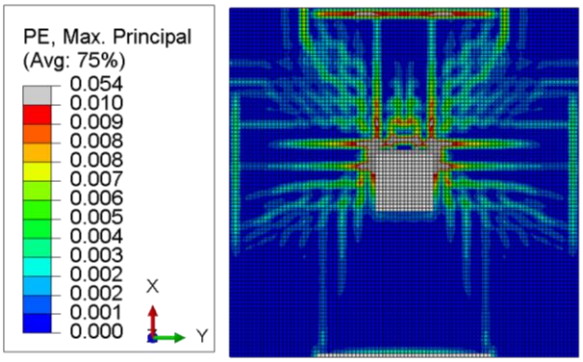

Figure 5.73: Specimen SM 1.0 top face analyses crack patterns using varying reinforcement mesh types and sizes

The bottom face crack patterns of the experiment as well as the varying reinforcement element size and element type analyses for specimen SM 1.0 are presented in Figure 5.74. All analyses cracks were similar to one another. The analyses produced cracks that started from the bottom column face and continued toward the bottom left and bottom right slab corners. However, increasing the reinforcement element size resulted in widening of the aforementioned diagonal cracks.

a) Bottom face, analysis 20 mm T3D2

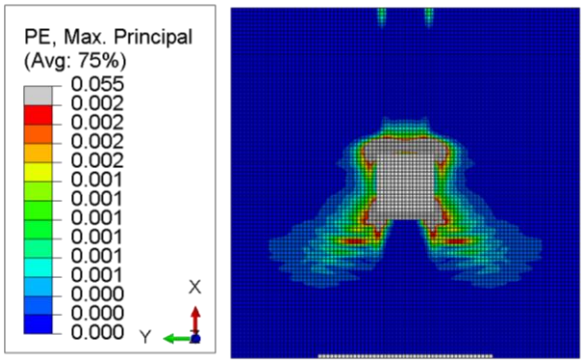

b) Bottom face, analysis 20 mm B31

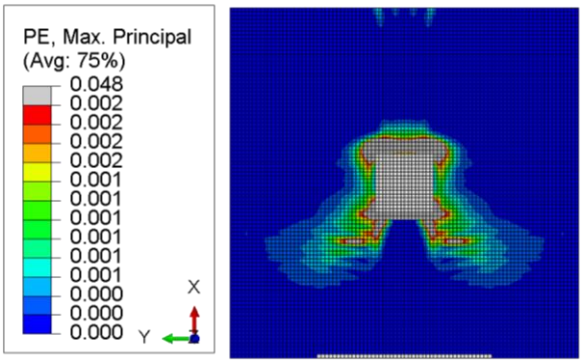

c) Bottom face, analysis 50 mm T3D2

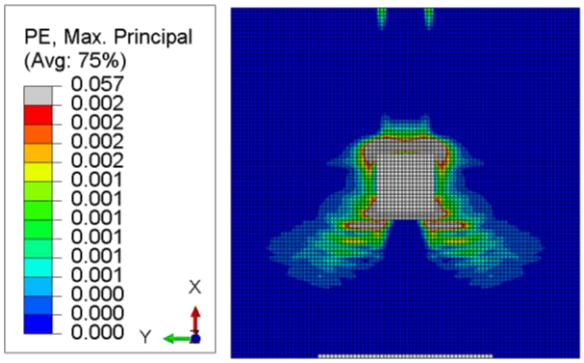

d) Bottom face, analysis 50 mm B31

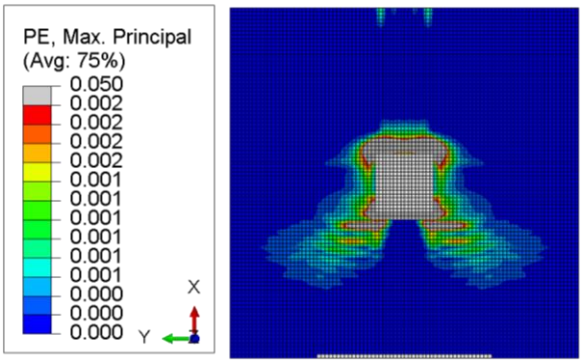

e) Bottom face, analysis 100 mm T3D2

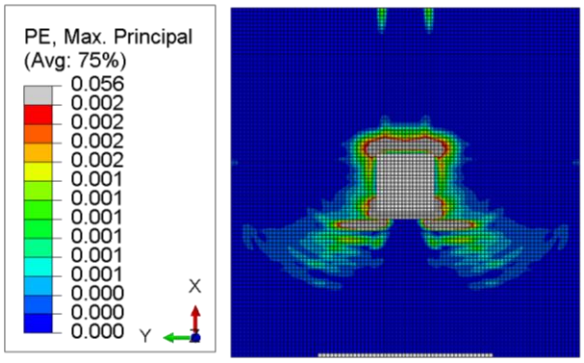

f) Bottom face, analysis 100 mm B31

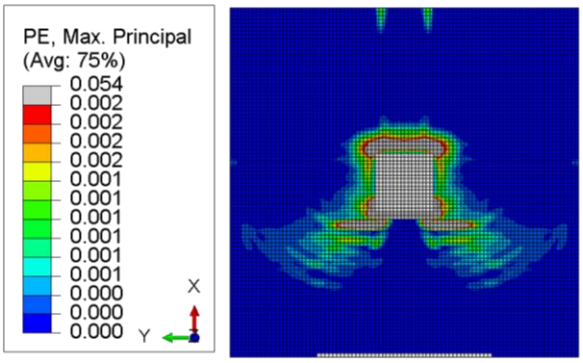

Figure 5.74: Specimen SM 1.0 bottom face analyses crack patterns using varying reinforcement mesh types and sizes

5.7.3 Results of specimen SM 1.5 analyses

The moment-rotation and displacement-rotation data for the analyses of varying reinforcement mesh sizes and element types, in addition to the experimental results, for specimen SM 1.5 are presented in Figure 5.75. A summary of this data is provided in Table 5.33.

The 20 mm T3D2, 20 mm B31, 50 mm T3D2, and 50 mm B31 analyses produced similar moment-rotation data. The 100 mm T3D2 and 100 mm B31 analyses had lower moment-

rotation slopes and capacities compared to the other analyses. These analyses had ultimate moments of 143.5 kNm and 145.4 kNm, respectively. The other analyses had ultimate moments between 159.0 kNm and 164.4 kNm.

All analyses produced similar displacement-rotation data to one another. All analyses had similar rotations at ultimate moments between 10.8 mm and 11.7 mm.

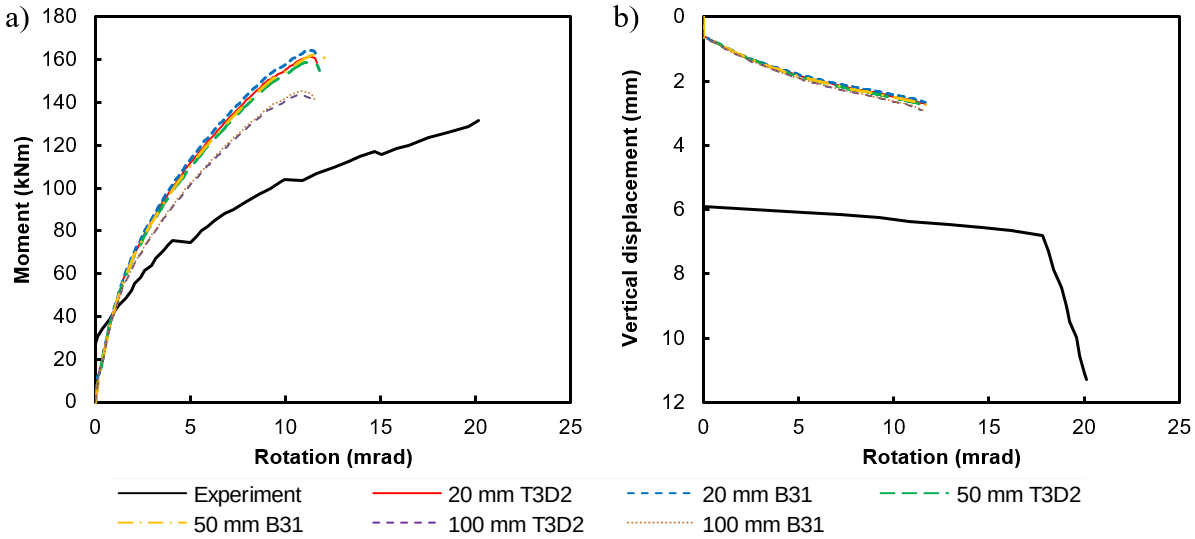

Figure 5.75: Specimen SM 1.5 a) moment-rotation and b) displacement-rotation data using varying reinforcement mesh types and sizes

Table 5.33: Specimen SM 1.5 results using varying reinforcement mesh types and sizes

	Ultimate moment (kNm)	Displacement (mm) at ultimate moment	Rotation (mrad) at ultimate moment
Analyses			
20 mm T3D2	161.3	2.7	11.4
20 mm B31	164.4	2.6	11.4
50 mm T3D2	159.0	2.7	11.4
50 mm B31	162.2	2.7	11.7
100 mm T3D2	143.5	2.7	10.8
100 mm B31	145.4	2.8	10.9
Experiment	131.5	11.3	20.1

The top face crack patterns of the experiment as well as the varying reinforcement element size and element type analyses for specimen SM 1.5 are presented in Figure 5.76. As with the SM 0.5 and SM 1.0 analyses, the T3D2 analyses and the B31 analyses produced crack patterns identical to one another for a given element size. All analyses produced cracks that started at the

column and propagated outward toward the slab corners. As observed with specimen SM 1.0, the 50 mm reinforcement element size analyses had large vertical and horizontal cracks along the reinforcement bars near the column. Recall, this was due to the long elements linearly distributing high strains from the column face to low strain regions away from the column. These strain distributions were not representative of the strain distributions of the experiment. The 100 mm reinforcement element size analyses produced even larger vertical and horizontal cracks as the strains were distributed over an even longer element length.

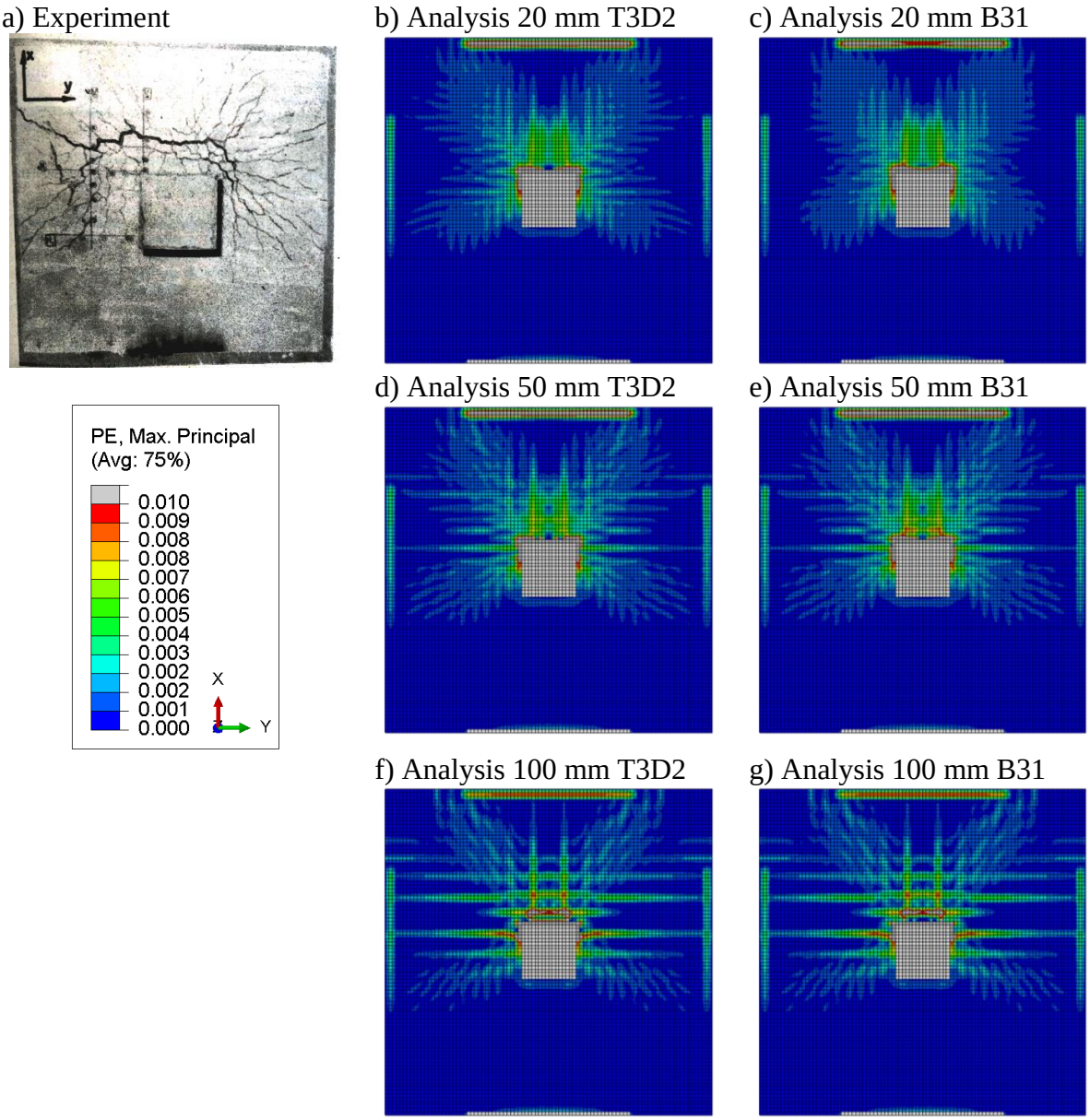

Figure 5.76: Specimen SM 1.5 top face experiment (Ghali et al., 1976) and analyses crack patterns using varying reinforcement mesh types and sizes. Authorized reprint of experiment photograph from ACI Journal, Volume 73, Issue 10, October 1976.

The bottom face crack patterns of the experiment as well as the varying reinforcement element size and element type analyses for specimen SM 1.5 are presented in Figure 5.77. No discernable crack pattern differences were observed among the analyses.

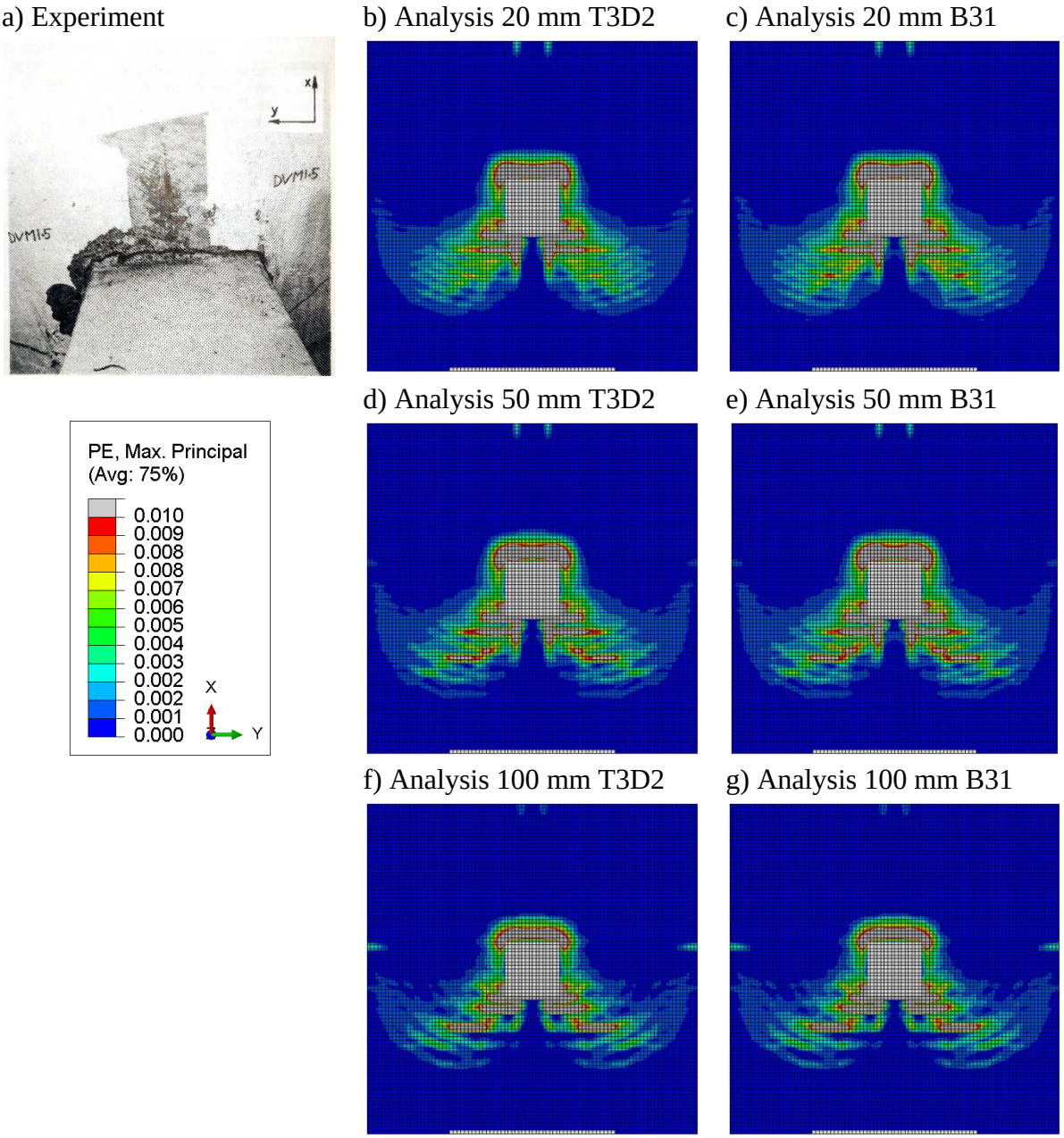

Figure 5.77: Specimen SM 1.5 bottom face experiment (Ghali et al., 1976) and analyses crack patterns using varying reinforcement mesh types and sizes. Authorized reprint of experiment photograph from ACI Journal, Volume 73, Issue 10, October 1976.

5.7.4 Conclusions and recommendations

The analyses within this study showed that the most accurate results for each specimen were produced when using a reinforcement element size of 20 mm and element type of T3D2.

Generally, using B31 elements in place of T3D2 elements did not impact the moment-rotation data, displacement-rotation data, or crack patterns. The 20 mm analyses had the highest ultimate moments, the 50 mm analyses had the next highest ultimate moments, and the 100 mm analyses had the lowest ultimate moments. The exception to this was specimen SM 0.5 in which the 100 mm T3D2 and B31 analyses had ultimate moments of 99.5 kNm and 100.6 kNm, respectively. The 20 mm T3D2 and B31 analyses ultimate moments were 95.7 kNm and 99.4 kNm, respectively. Comparatively, the specimen SM 0.5 experiment ultimate moment was 99.1 kNm.

For each specimen, all six analyses produced displacement-rotation curves that overlapped one another. Analyses with higher ultimate moments showed the full shape of this displacement-rotation curve and analyses with lower ultimate moments showed only a portion of the same curve.

Using reinforcement element sizes of 50 mm and 100 mm resulted in strains in areas where no strains were observed during testing. Elements located near the column would linearly distribute (as both T3D2 and B31 use linear interpolation) high strains at the column across the entire length of the element. This was evident as the 50 mm and 100 mm analyses had long vertical and horizontal cracks near and around their columns. These cracks were not present in the photographed crack patterns of the experiment.

Due to the strain inaccuracies when using larger elements, it was necessary to use 20 mm reinforcement elements in subsequent analyses. The ultimate moments were similar between the T3D2 and B31 analyses. However, T3D2 elements were selected for use in subsequent analyses because these elements are less computationally demanding.

5.8 Comparison of concrete dilation angles

In this section, the effects of using varying concrete dilation angles were studied. Previous analyses were completed using a concrete dilation angle of 40 degrees. For this study, each of the three specimens were analysed using concrete dilation angles of 30, 35, 40, and 45 degrees.

The concrete dilation angle that produced accurate results for all three specimens was selected and used in subsequent analyses.

5.8.1 Results of specimen SM 0.5 analyses

The moment-rotation and displacement-rotation data for the specimen SM 0.5 analyses using varying concrete dilation angles, in addition to the experimental results, are presented in Figure 5.78. A summary of this data is provided in Table 5.34.

Among the analyses, using a 40 degree concrete dilation angle resulted in an ultimate moment closest to that of the experiment. With respect to displacement at ultimate moment, both the 40 and 45 degree concrete dilation angle analyses produced displacements that were similar to the displacement of the experiment.

The moment-displacement curves of the analyses shared similar shapes to one another. Past 5 mrad, analyses with higher dilation angles had steeper slopes compared to analyses with lower dilation angles. The reason for this is that the plastic flow of the Concrete Damaged Plasticity model is defined by the Drucker-Prager hyperbolic function. The dilation angle within this function proportionately affected the angle between the hydrostatic axis and the failure surface. Since using a larger dilation angle resulted in a wider failure surface cone, a higher value for the second invariant of the deviatoric stress tensor was required to meet the Drucker-Prager failure criterion. This was evident by the higher rotational stiffness and capacity of the analyses which used higher dilation angles.

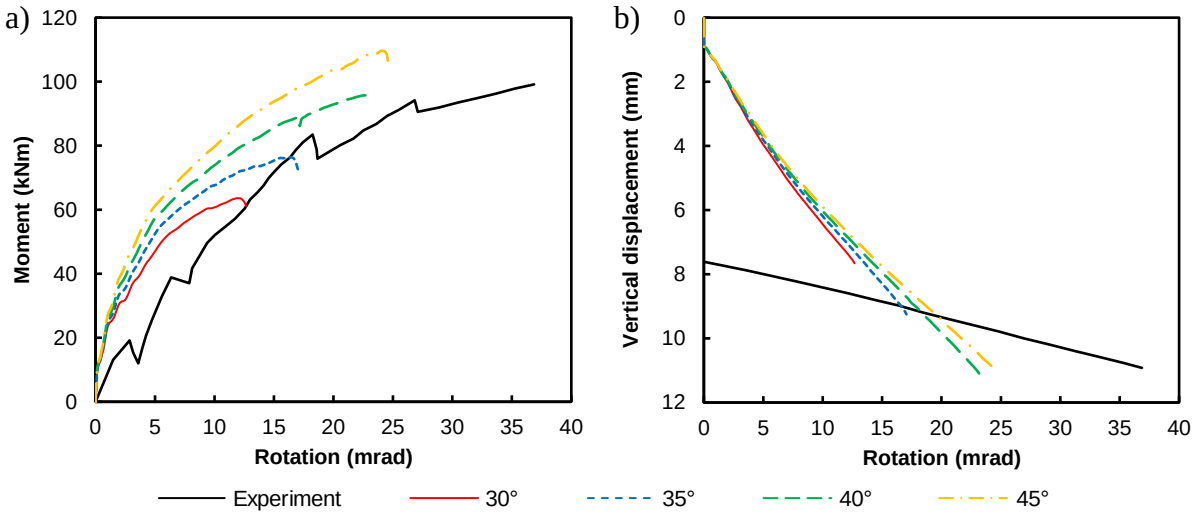

Figure 5.78: Specimen SM 0.5 a) moment-rotation and b) displacement-rotation data using varying concrete dilation angles

Table 5.34: Specimen SM 0.5 results using varying concrete dilation angles

	Ultimate moment (kNm)	Displacement (mm) at ultimate moment	Rotation (mrad) at ultimate moment
Analyses			
30°	63.6	7.3	11.9
35°	76.4	8.9	16.4
40°	95.7	10.9	22.7
45°	109.7	10.8	24.1
Experiment	99.1	10.9	36.9

Linear interpolation could be done to determine the dilation angle required to reproduce the ultimate moment of the experiment. The ultimate moment versus dilation angle and displacement versus dilation angle data for specimen SM 0.5 are shown in Figure 5.79. On the ultimate moment versus dilation angle plot, a line was fitted through the four data points. The equation of this line was rearranged such that the dilation angle was a function of ultimate moment. This function was used to determine the dilation angle required to produce an analysis with an ultimate moment identical to the ultimate moment of the experiment. To produce an ultimate moment of 99.1 kNm, a dilation angle of 41.5 degrees needed to be used. This datum was plotted on the ultimate moment versus dilation angle graph as a red triangle. A vertical displacement of 10.9 mm was predicted by linearly interpolating between the 40 and 45 degree data points using the dilation angle of 41.5 degrees. This datum was plotted on the vertical displacement versus dilation angle graph as a red triangle.

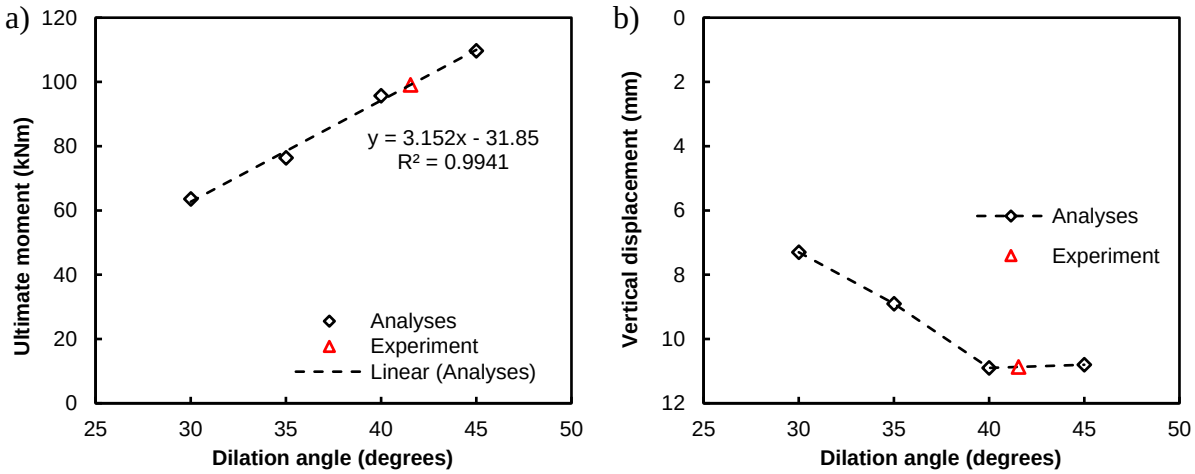

Figure 5.79: Specimen SM 0.5 a) moment versus dilation angle and b) displacement versus dilation angle data using varying concrete dilation angles

The top face crack patterns for the specimen SM 0.5 analyses using varying concrete dilation angles, in addition to the experimental results, are presented in Figure 5.80. All analyses produced identical crack patterns to one another. However, each subsequent increase in dilation angle resulted in increased strains at the top column face and within the diagonal cracks that formed from the bottom column face toward the extents of the bottom support elements. Since it was not possible to compare the experiment strain magnitudes to those of the analyses, strain magnitudes were not used as a criterion for determining analysis accuracy.

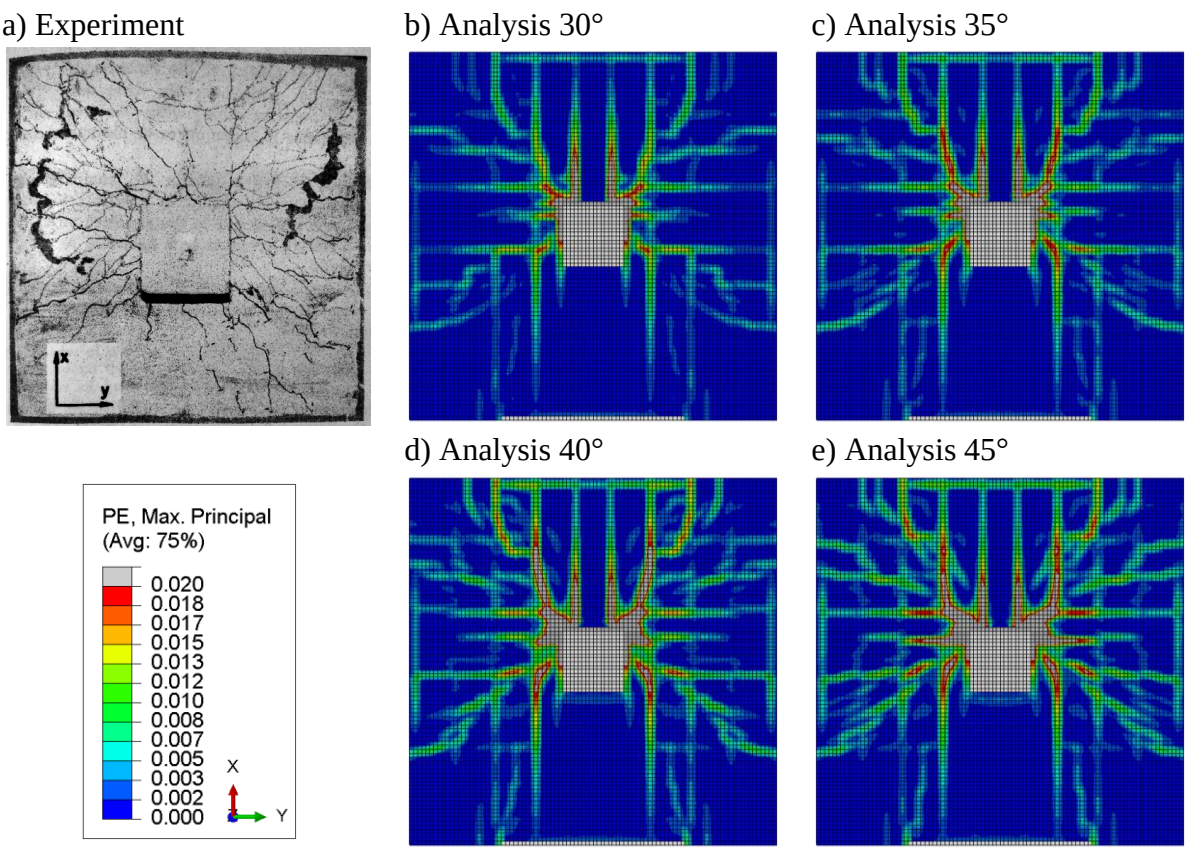

Figure 5.80: Specimen SM 0.5 top face experiment (Ghali et al., 1976) and analyses crack patterns using varying concrete dilation angles. Authorized reprint of experiment photograph from ACI Journal, Volume 73, Issue 10, October 1976.

The bottom face crack patterns for the specimen SM 0.5 analyses using varying concrete dilation angles, in addition to the experimental results, are presented in Figure 5.81. As with the top crack patterns, all analyses produced crack patterns with similar shapes to one another but with varying strain magnitudes. Decreasing the upper limit of the maximum principal plastic strain for the 30 and 35 degree analyses would show the same cracks observed for the 40 and 45 degree analyses. As such, all dilation angles produced accurate crack patterns.

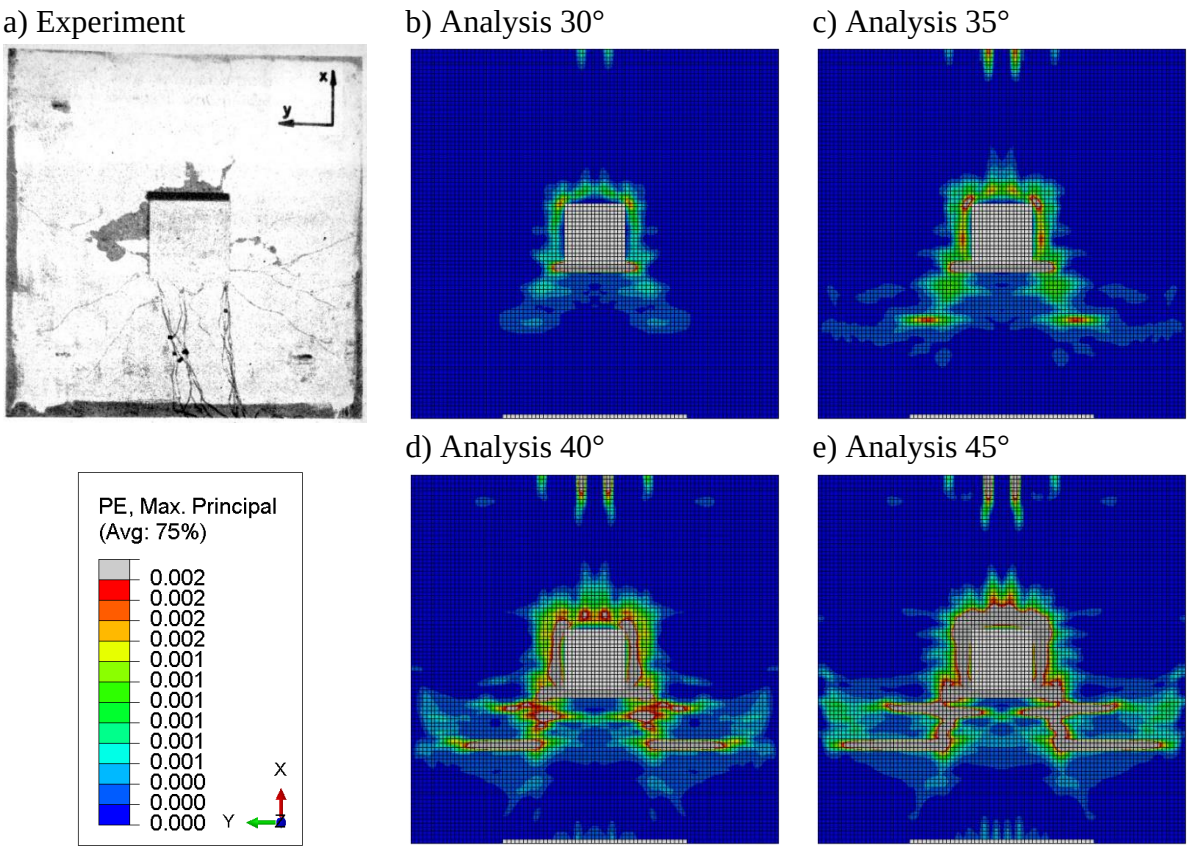

Figure 5.81: Specimen SM 0.5 bottom face experiment (Ghali et al., 1976) and analyses crack patterns using varying concrete dilation angles. Authorized reprint of experiment photograph from ACI Journal, Volume 73, Issue 10, October 1976.

5.8.2 Results of specimen SM 1.0 analyses

The moment-rotation and displacement-rotation data for the specimen SM 1.0 analyses using varying concrete dilation angles, in addition to the experimental results, are presented in Figure 5.82. A summary of this data is provided in Table 5.35.

As observed with the specimen SM 0.5 analyses, increasing the dilation angle resulted in an increase in rotational stiffness and ultimate moment. The 45 degree dilation angle analysis had an ultimate moment (129.3 kNm) closest to the ultimate moment of the experiment (127.1 kNm). The analysis with the next closest ultimate moment was the 40 degree dilation angle analysis which had an ultimate moment of 120.9 kNm.

The displacements at ultimate moments were the same for all analyses. However, the rotations at ultimate moments increased as the dilation angle was increased.

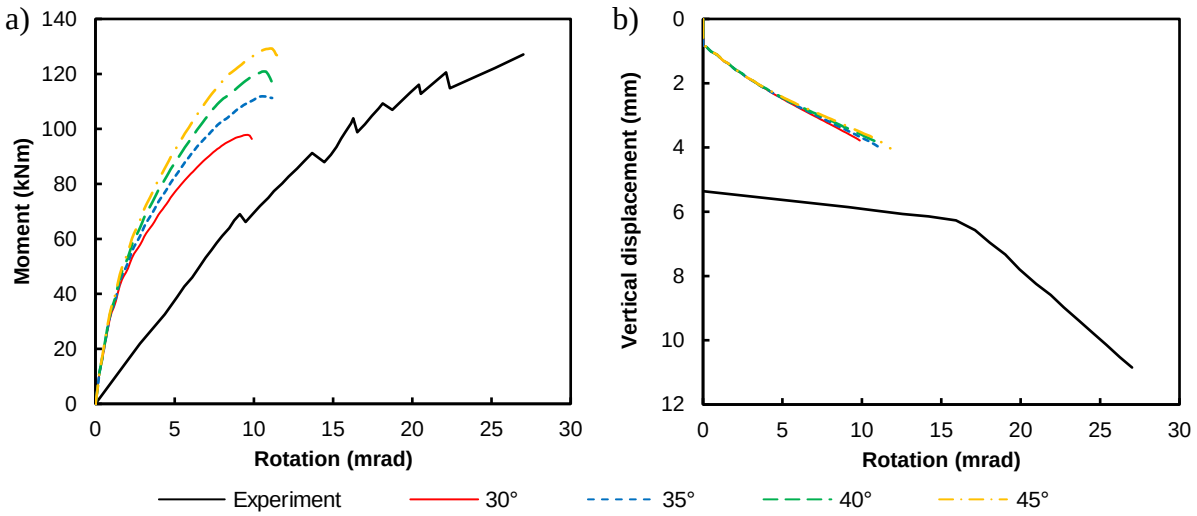

Figure 5.82: Specimen SM 1.0 a) moment-rotation and b) displacement-rotation data using varying concrete dilation angles

Table 5.35: Specimen SM 1.0 results using varying concrete dilation angles

	Ultimate moment (kNm)	Displacement (mm) at ultimate moment	Rotation (mrad) at ultimate moment
Analyses			
30°	97.8	3.7	9.6
35°	111.9	3.8	10.5
40°	120.9	3.8	10.6
45°	129.3	3.8	11.0
Experiment	127.1	10.8	27.0

Linear interpolation was done to determine the dilation angle required to reproduce the ultimate moment of the experiment. The ultimate moment versus dilation angle and displacement versus dilation angle data for specimen SM 1.0 are shown in Figure 5.83. On the ultimate moment versus dilation angle plot, a line was fitted through the four data points. Using this linear regression, a dilation angle of 44.6 degrees was required to produce an ultimate moment of 127.1 kNm. This datum was plotted on the ultimate moment versus dilation angle graph as a red triangle. A vertical displacement of 3.8 mm was predicted by linearly interpolating between the 40 and 45 degree data points using a dilation angle of 44.6 degrees. This datum was plotted on the vertical displacement versus dilation angle graph as a red triangle.

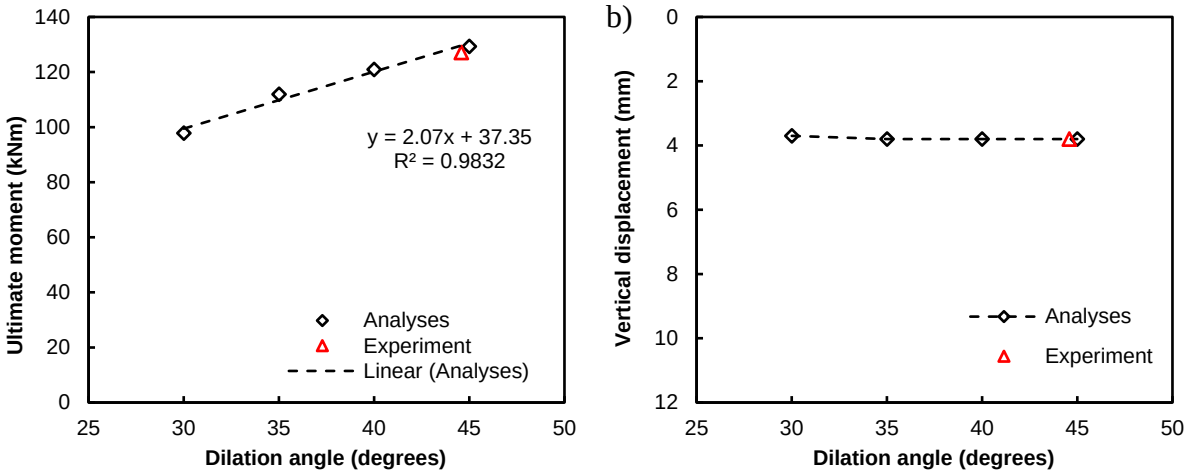

Figure 5.83: Specimen SM 1.0 a) moment versus dilation angle and b) displacement versus dilation angle data using varying concrete dilation angles

The top face and bottom face crack patterns for the specimen SM 1.0 analyses using varying concrete dilation angles are presented in Figure 5.84. As with the specimen SM 0.5 analyses, the strain magnitudes among the specimen SM 1.0 analyses differed from one another but the overall crack patterns were the same.

a) Top face, analysis 30°

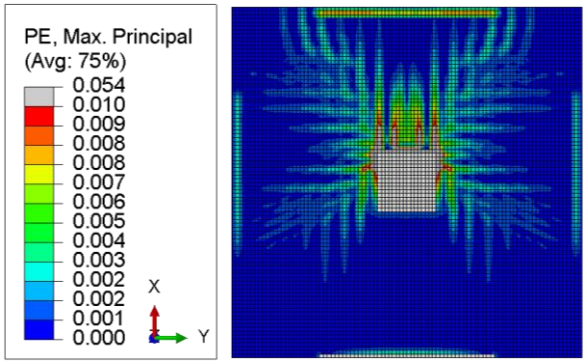

b) Bottom face, analysis 30°

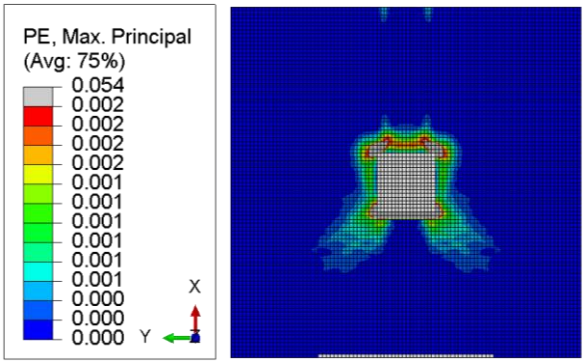

c) Top face, analysis 35°

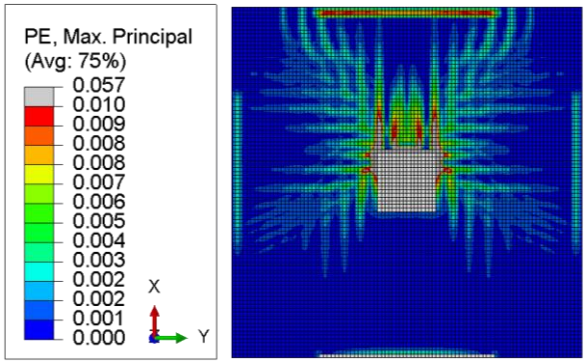

d) Bottom face, analysis 35°

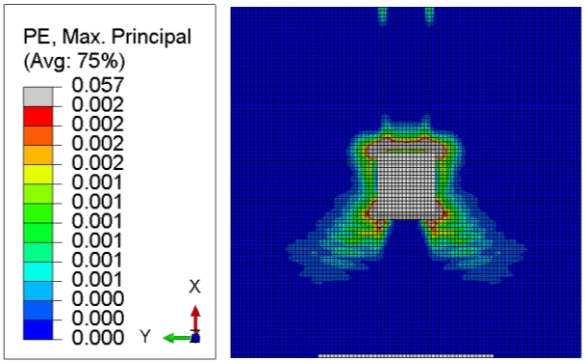

e) Top face, analysis 40°

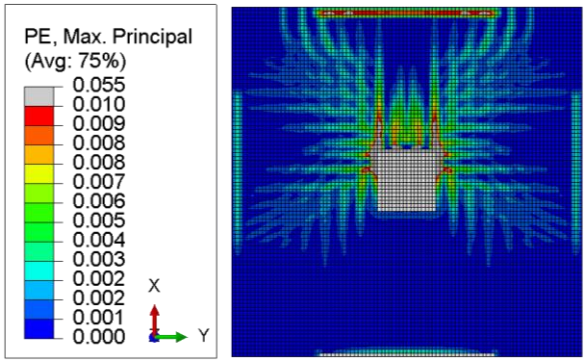

f) Bottom face, analysis 40°

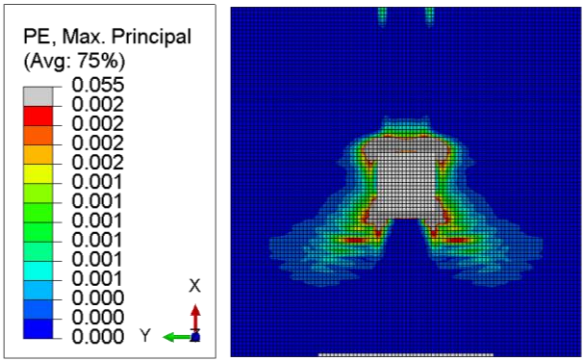

g) Top face, analysis 45°

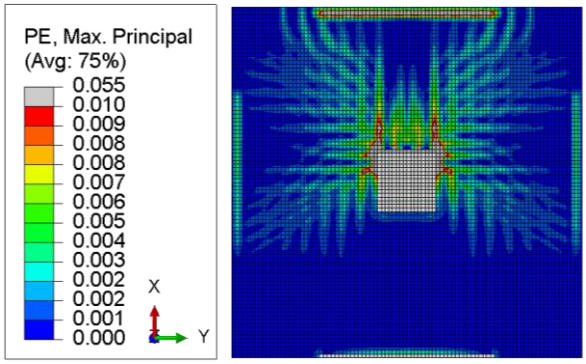

h) Bottom face, analysis 45°

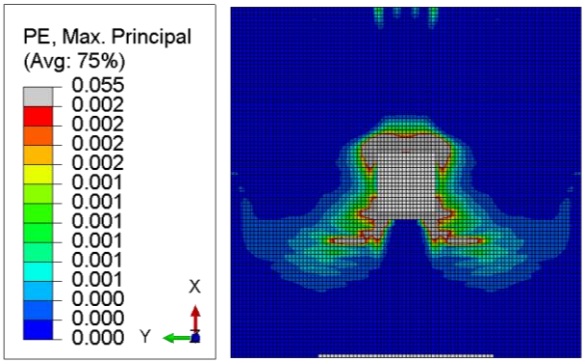

Figure 5.84: Specimen SM 1.0 analyses crack patterns using varying concrete dilation angles

5.8.3 Results of specimen SM 1.5 analyses

The moment-rotation and displacement-rotation data for the specimen SM 1.5 analyses using varying concrete dilation angles, in addition to the experimental results, are presented in Figure 5.85. A summary of this data is provided in Table 5.36.

As observed with the dilation angle analyses for specimens SM 0.5 and SM 1.0, increasing the dilation angle resulted in an increase in rotational stiffness and ultimate moment. The 35 degree dilation angle analysis had an ultimate moment (138.6 kNm) closest to the ultimate moment of the experiment (131.5 kNm). The analysis with the next closest ultimate moment was the 30 degree dilation angle analysis which had an ultimate moment of 120.6 kNm.

The displacements at ultimate moments were the same for all analyses but the rotations at ultimate moments increased with increases in dilation angle.

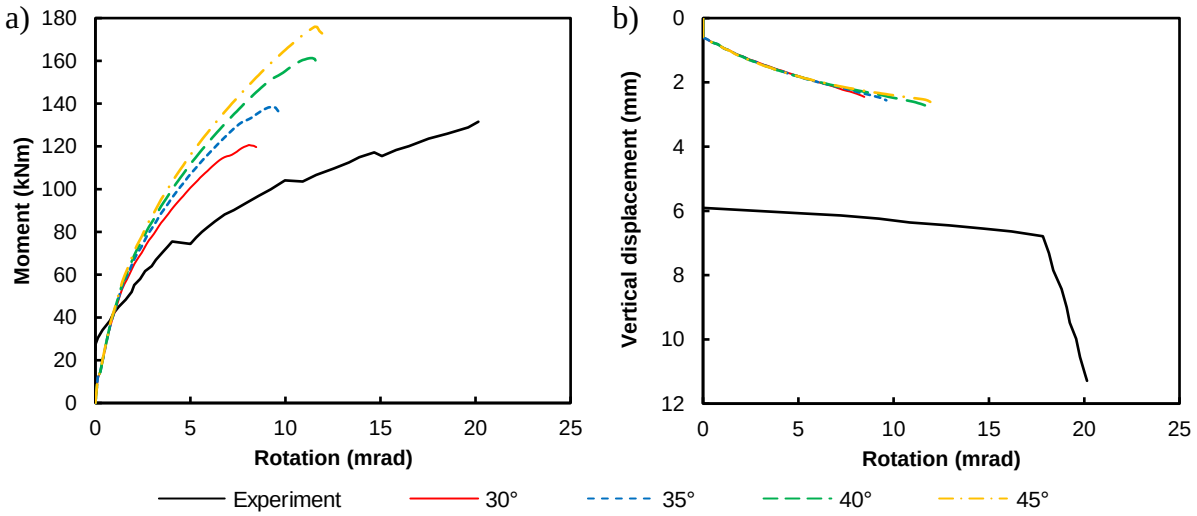

Figure 5.85: Specimen SM 1.5 a) moment-rotation and b) displacement-rotation data using varying concrete dilation angles

Table 5.36: Specimen SM 1.5 results using varying concrete dilation angles

	Ultimate moment (kNm)	Displacement (mm) at ultimate moment	Rotation (mrad) at ultimate moment
Analyses			
30°	120.6	2.4	8.1
35°	138.6	2.5	9.4
40°	161.3	2.7	11.4
45°	176.0	2.5	11.5
Experiment	131.5	11.3	20.1

Linear interpolation was done to determine the dilation angle required to reproduce the ultimate moment of the experiment. The ultimate moment versus dilation angle and displacement versus dilation angle data for specimen SM 1.5 are shown in Figure 5.86. On the ultimate moment versus dilation angle plot, a line was fitted through the four data points. Using the equation of this line, a dilation angle of 32.8 degrees was required to produce an ultimate moment of 131.5 kNm. This datum was plotted on the ultimate moment versus dilation angle graph as a red triangle. A vertical displacement of 2.5 mm was predicted by linearly interpolating between the 30 and 35 degree data points using the dilation angle of 32.8 degrees. This datum was plotted on the vertical displacement versus dilation angle graph as a red triangle.

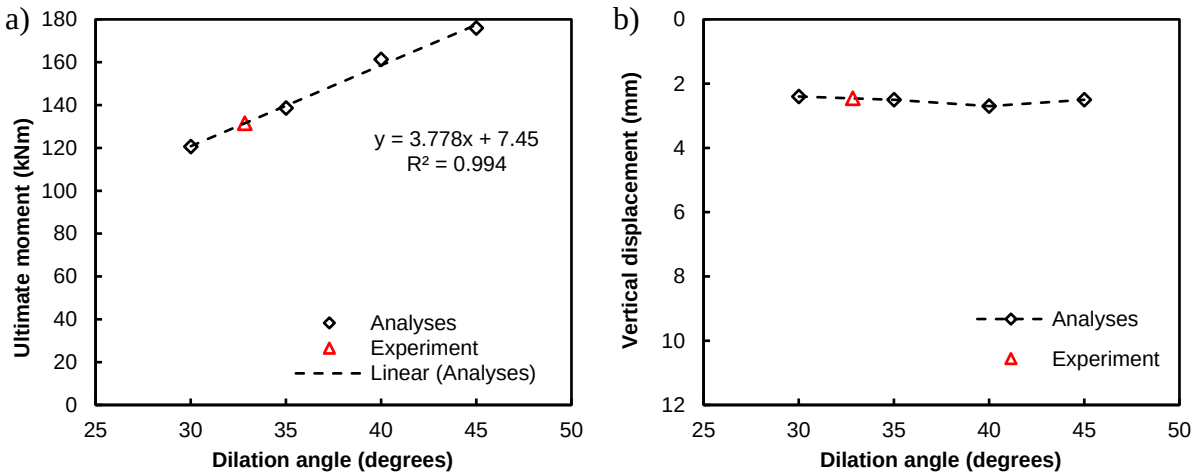

Figure 5.86: Specimen SM 1.5 a) moment versus dilation angle and b) displacement versus dilation angle data using varying concrete dilation angles

The top face crack patterns for the specimen SM 1.5 analyses using varying concrete dilation angles, in addition to the experimental results, are presented in Figure 5.87. As with the specimen SM 0.5 and SM 1.0 analyses, all specimen SM 1.5 analyses produced identical top face crack patterns to one another. The only differences between the analyses crack patterns were with respect to strain magnitudes. As previously discussed, strain magnitudes were not a criterion for analysis accuracy as the strain magnitudes of the experiment were unknown.

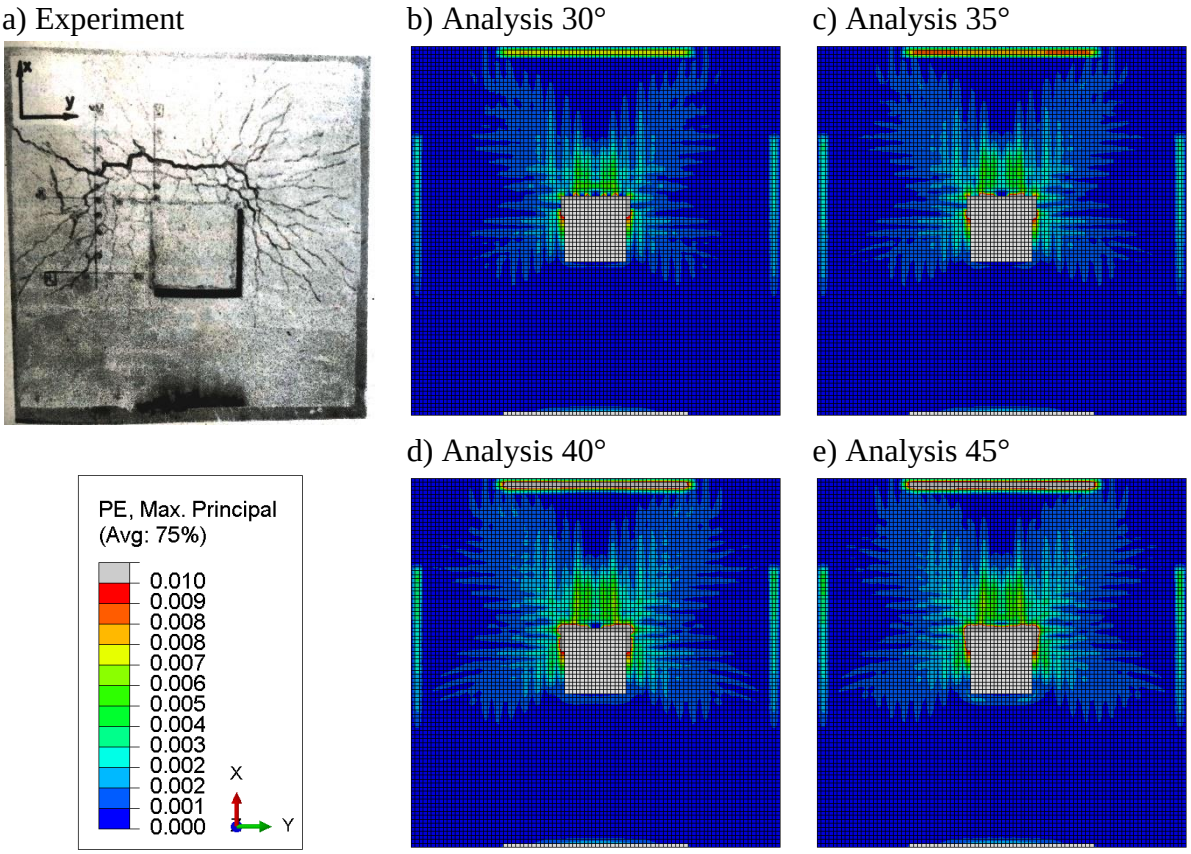

Figure 5.87: Specimen SM 1.5 top face experiment (Ghali et al., 1976) and analyses crack patterns using varying concrete dilation angles. Authorized reprint of experiment photograph from ACI Journal, Volume 73, Issue 10, October 1976.

The bottom face crack patterns for the specimen SM 1.5 analyses using varying concrete dilation angles, in addition to the experimental results, are presented in Figure 5.88. All specimen SM 1.5 analyses produced identical bottom face crack patterns to one another. There were differences between the maximum principal plastic strain magnitudes. If the upper contour limits of the 30 and 35 degree analyses were reduced, the contour plots produced would be identical to the contour plots of the 40 and 45 degree analyses.

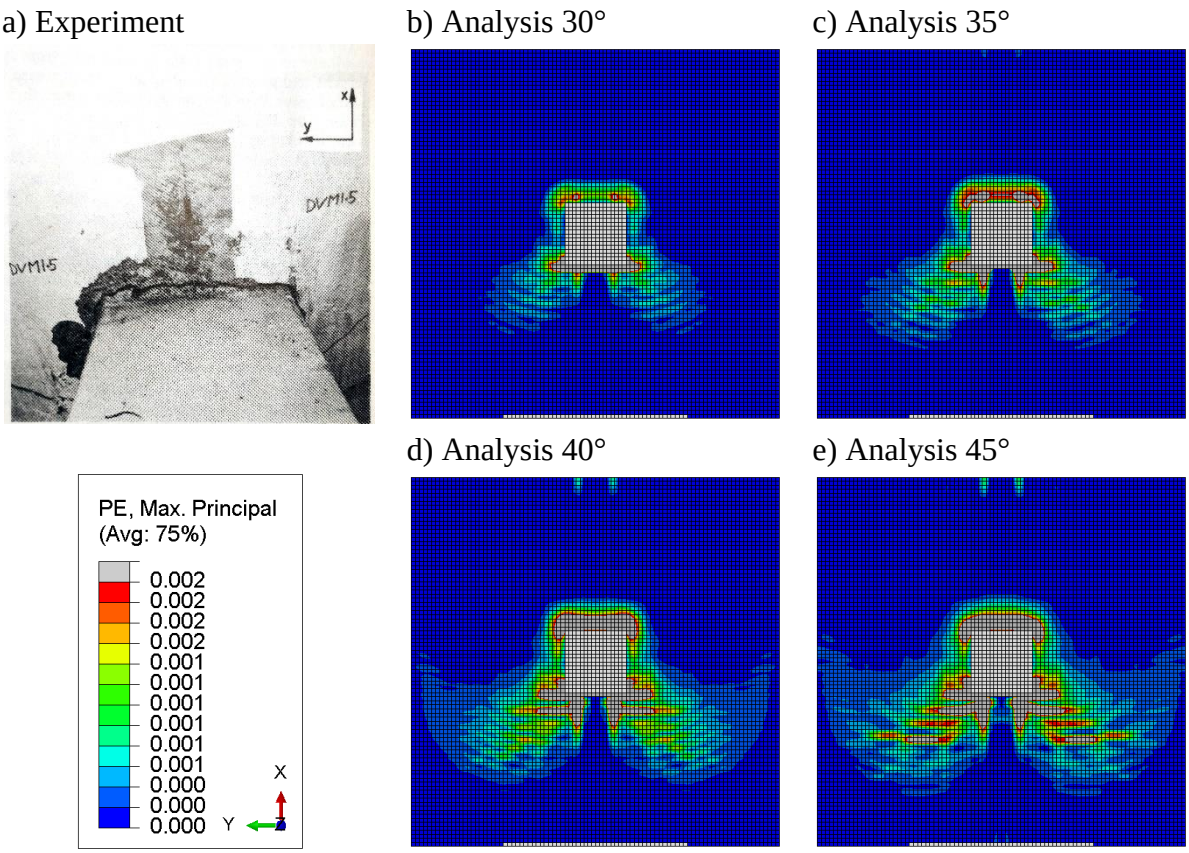

Figure 5.88: Specimen SM 1.5 bottom face experiment (Ghali et al., 1976) and analyses crack patterns using varying concrete dilation angles. Authorized reprint of experiment photograph from ACI Journal, Volume 73, Issue 10, October 1976.

5.8.4 Comparison of specimen results

The experiment ultimate moments increased from 127.1 kNm to 131.5 kNm when the reinforcement ratio was increased from 1.0-percent to 1.5-percent. This was a 3-percent increase in ultimate moment for a 33-percent increase in steel reinforcement. Using a concrete dilation angle of 40 degrees, the finite element analyses showed a 32-percent increase in ultimate moment for the same increase in steel reinforcement. For this reason, it was believed that the specimen SM 1.5 experiment would produce a higher ultimate moment had the experiment been repeated. Therefore, the specimen SM 1.5 analyses were not considered when calculating the concrete dilation angle to use. Had they been considered, the overall concrete dilation angle would be lower and the error would increase for specimens SM 0.5 and SM 1.0.

In previous sections, linear equations relating ultimate moments to concrete dilation angles were obtained for the three specimens. These ultimate moment versus concrete dilation angle

equations were modified by subtracting their respective experiment ultimate moments from the equations. The modified equations, in addition to the average of the modified equations, were plotted in Figure 5.89. The average of the modified equations provided the average difference in ultimate moment between the analyses and their respective experiments. The x-intercept of this average provided the concrete dilation angle required to minimize the overall ultimate moment error between the analyses and the experiments.

Figure 5.89a shows all three specimen equations in addition to the average of the three equations. As aforementioned, specimen SM 1.5 was treated as an outlier and including specimen SM 1.5 results would lower the overall concrete dilation angle. Based on Figure 5.89a, the concrete dilation angle that would result in the lowest overall error was 38.3 degrees.

Figure 5.89b shows the equations for specimens SM 0.5 and SM 1.0 in addition to the average of these two specimen equations. Based on this figure, the concrete dilation angle that would result in the lowest overall error was 42.3 degrees.

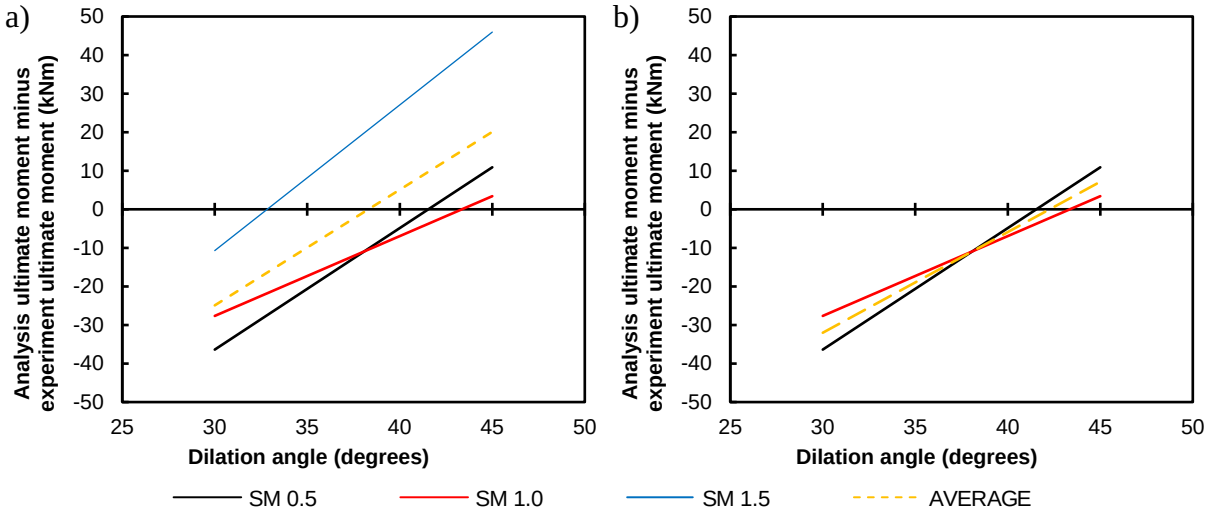

Figure 5.89: Analysis ultimate moments minus experiment ultimate moments versus dilation angles for specimens a) SM 0.5, SM 1.0, and SM 1.5; and b) SM 0.5 and SM 1.0

5.8.5 Conclusions and recommendations

In this section, the three SM specimens were analysed using concrete dilation angles of 30, 35, 40, and 45 degrees. For each specimen, linear relationships were observed between the ultimate moments and the concrete dilation angles used. These linear relationships were used to

determine the optimal concrete dilation angle that would produce the least ultimate moment error among the three specimen analyses. The optimal concrete dilation angle was 42.3 degrees.

As mentioned, the ultimate moment increased proportionately when the concrete dilation angle was increased. The vertical displacements at ultimate moments increased when the dilation angle was increased for specimen SM 0.5. However, these vertical displacements did not change when the concrete dilation angle was increased for specimens SM 1.0 and SM 1.5. Lastly, the crack patterns remained the same when the concrete dilation angle was changed.

Based on these findings, the optimal concrete dilation angle to use for subsequent analyses was 42 degrees. Due to user error, a dilation angle of 40 degrees was used instead. However, as the differences in results when using a 42 degree dilation angle versus a 40 degree dilation angle were minimal, the models were not reanalysed.

5.9 Study of effects of self-weight

In this section, analyses were completed in which self-weight forces were included. Previously completed analyses neglected self-weight forces based on the assumption that these forces were negligible. This study was completed to determine whether or not this assumption was correct.

Ghali et al. (1976) stated that the SM specimens were rotated 90 degrees relative to their positions within actual structures. This meant that the specimens were positioned such that their columns were parallel to the ground. Figure 5.90 shows the test orientation of SM specimens including the vertical force *V*, force couple *P*, and gravity force *G*. The coordinate system shown matches the coordinate system used in Abaqus analyses.

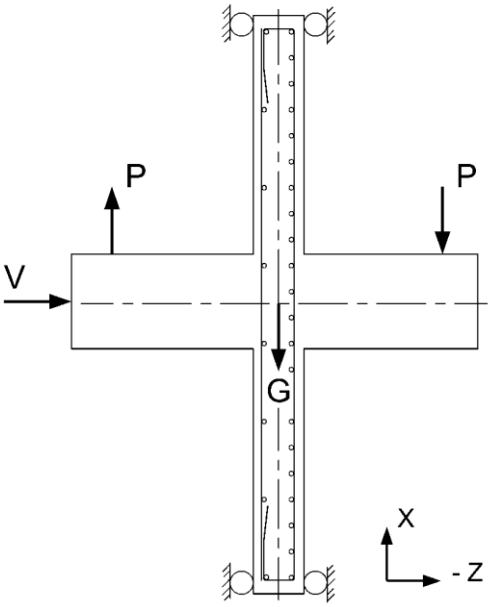

Figure 5.90: Test orientation of SM specimens including vertical force *V*, force couple *P*, and gravity force *G*

Gravity loads were applied on the analyses specimens through the load module of Abaqus. An acceleration of -9,810 mm/s^2 was defined in the x-direction. The resultant loads were calculated by Abaqus using the acceleration, part volumes, and material densities.

5.9.1 Results of specimen SM 0.5 analyses

The moment-rotation and displacement-rotation data for the specimen SM 0.5 analyses including and excluding self-weight, in addition to the experimental results, are presented in Figure 5.91. A summary of this data is provided in Table 5.37.

Both the self-weight included and self-weight excluded produced identical moment-rotation and displacement-rotation results to one another. Therefore, the self-weight of specimen SM 0.5 was not enough to affect the ultimate moment nor the displacement or rotation at the ultimate moment.

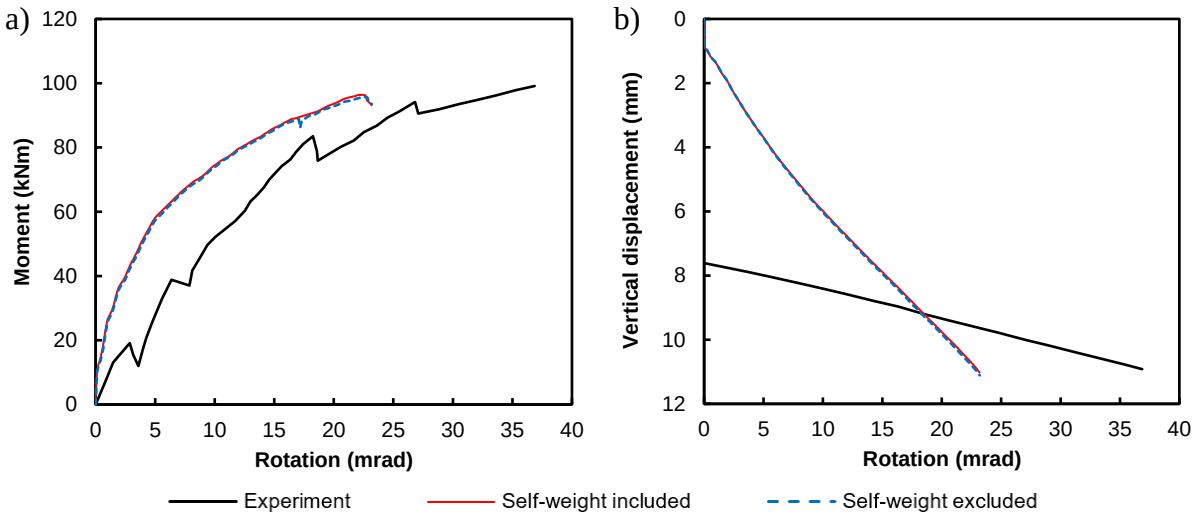

Figure 5.91: Specimen SM 0.5 a) moment-rotation and b) displacement-rotation data when including versus excluding self-weight

Table 5.37: Specimen SM 0.5 analyses results when including versus excluding self-weight

	Ultimate moment (kNm)	Displacement (mm) at ultimate moment	Rotation (mrad) at ultimate moment
Analyses			
Self-weight included	96.4	10.7	22.4
Self-weight excluded	95.7	10.9	22.7
Experiment	99.1	10.9	36.9

The crack patterns for the specimen SM 0.5 analyses including and excluding self-weight, in addition to the experimental crack patterns, are presented in Figure 5.92. Both analyses produced identical crack patterns to one another.

a) Top face, experiment

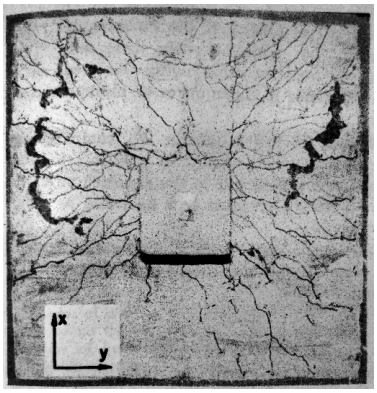

b) Bottom face, experiment

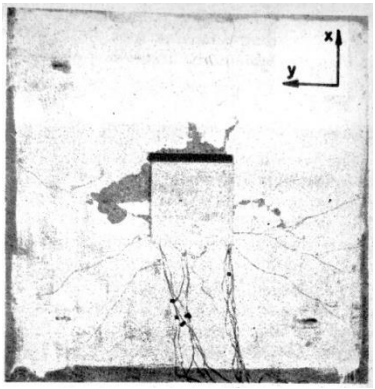

c) Top face, self-weight included

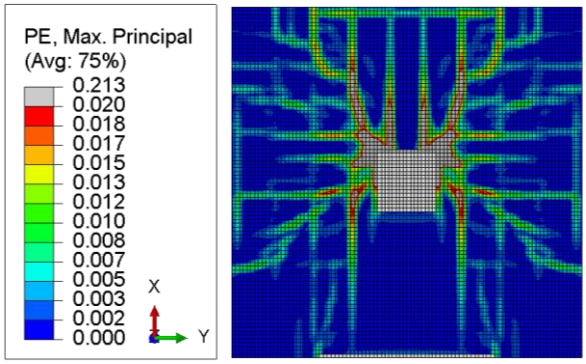

d) Bottom face, self-weight included

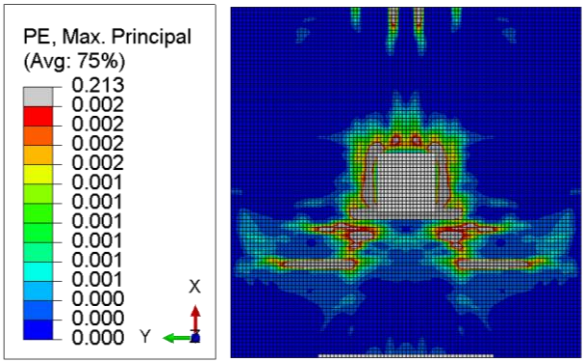

e) Top face, self-weight excluded

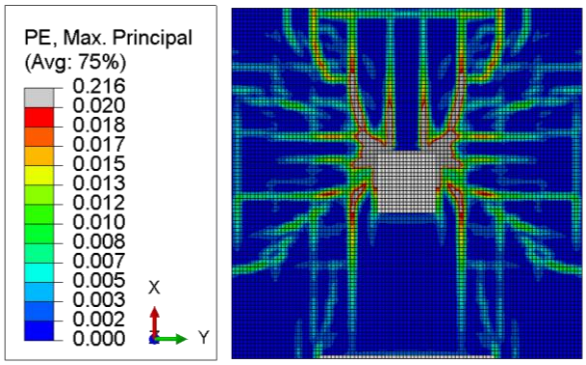

f) Bottom face, self-weight excluded

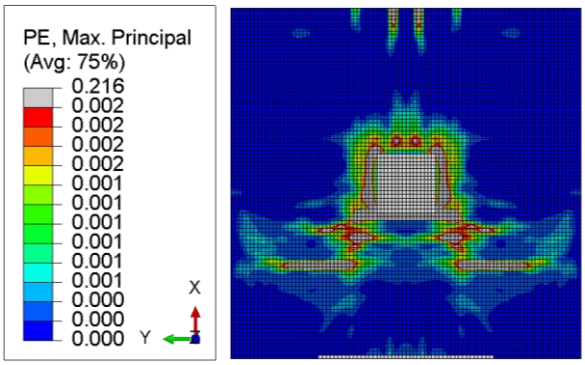

Figure 5.92: Specimen SM 0.5 experiment (Ghali et al., 1976) and analyses crack patterns when including versus excluding self-weight. Authorized reprint of experiment photographs from ACI Journal, Volume 73, Issue 10, October 1976.

5.9.2 Results of specimen SM 1.0 analyses

The moment-rotation and displacement-rotation data for the specimen SM 1.0 analyses including and excluding self-weight, in addition to the experimental results, are presented in Figure 5.93. A summary of this data is provided in Table 5.38.

Both the self-weight included and self-weight excluded produced identical moment-rotation and displacement-rotation results to one another. As with specimen SM 0.5, the self-weight of specimen SM 1.0 was not enough to affect the results.

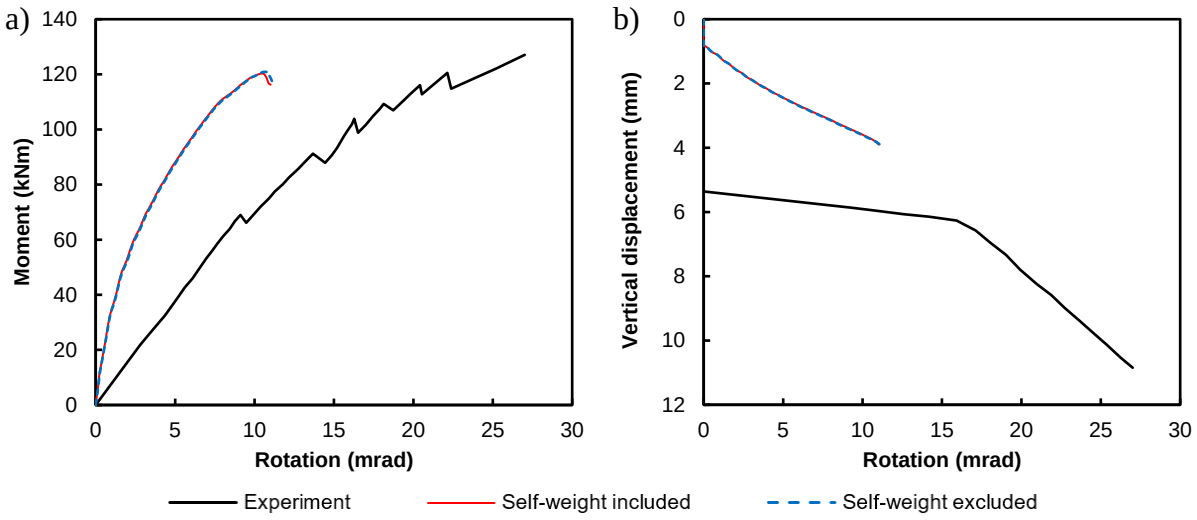

Figure 5.93: Specimen SM 1.0 a) moment-rotation and b) displacement-rotation data when including versus excluding self-weight

Table 5.38: Specimen SM 1.0 analyses results when including versus excluding self-weight

	Ultimate moment (kNm)	Displacement (mm) at ultimate moment	Rotation (mrad) at ultimate moment
Analyses			
Self-weight included	120.3	3.7	10.5
Self-weight excluded	120.9	3.8	10.6
Experiment	127.1	10.8	27.0

The crack patterns for the specimen SM 1.0 analyses including and excluding self-weight are presented in Figure 5.94. Both analyses produced identical crack patterns to one another.

a) Top face, self-weight included

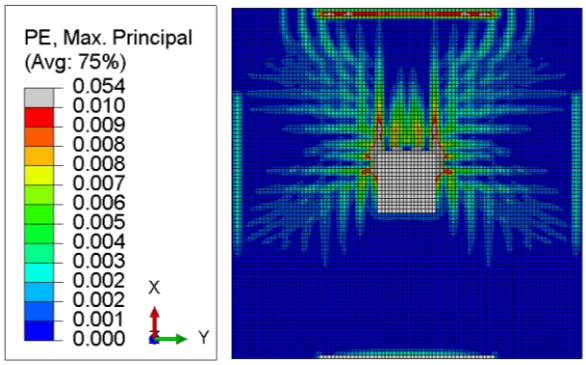

b) Bottom face, self-weight included

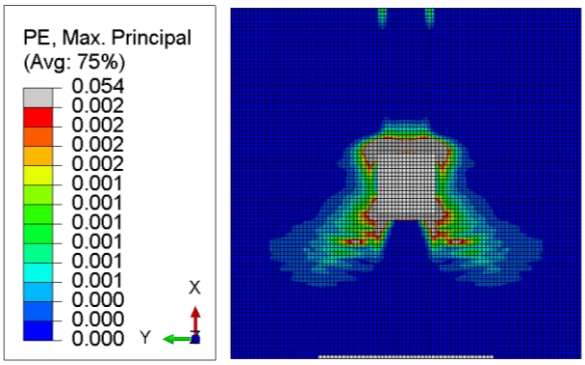

c) Top face, self-weight excluded

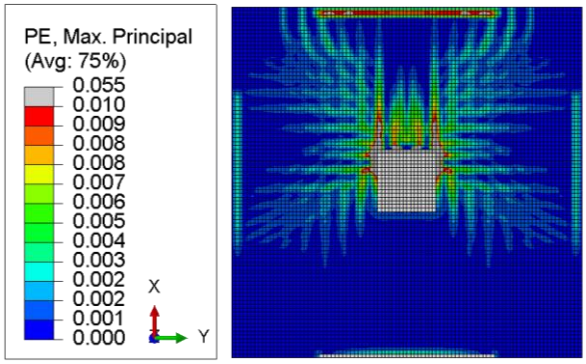

d) Bottom face, self-weight excluded

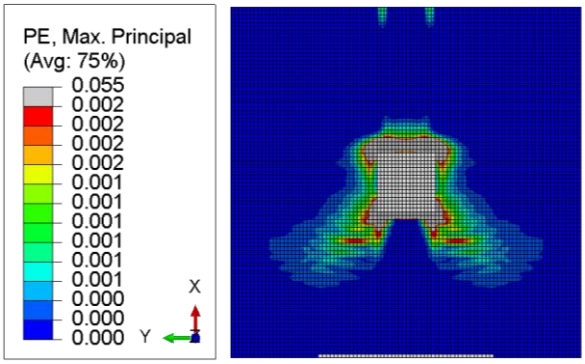

Figure 5.94: Specimen SM 1.0 analyses crack patterns when including versus excluding self-weight

5.9.3 Results of specimen SM 1.5 analyses

The moment-rotation and displacement-rotation data for the specimen SM 1.5 analyses including and excluding self-weight, in addition to the experimental results, are presented in Figure 5.95. A summary of this data is provided in Table 5.39.

Both the self-weight included and self-weight excluded produced identical moment-rotation and displacement-rotation results to one another. As with specimens SM 0.5 and SM 1.0, the self-weight of specimen SM 1.5 was not large enough to affect the results.

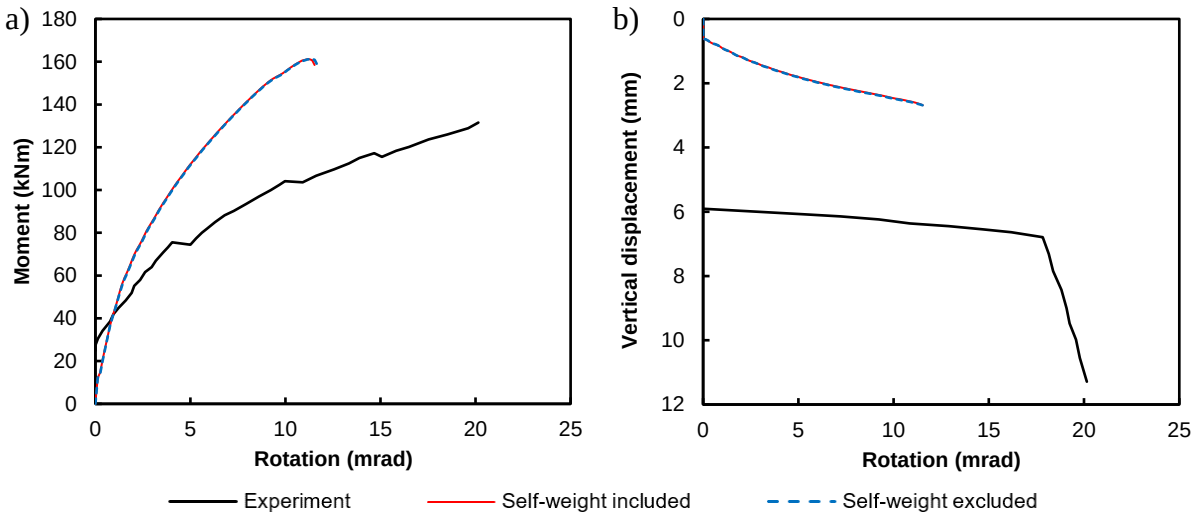

Figure 5.95: Specimen SM 1.5 a) moment-rotation and b) displacement-rotation data when including versus excluding self-weight

Table 5.39: Specimen SM 1.5 analyses results when including versus excluding self-weight

	Ultimate moment (kNm)	Displacement (mm) at ultimate moment	Rotation (mrad) at ultimate moment
Analyses			
Self-weight included	161.2	2.6	11.1
Self-weight excluded	161.3	2.7	11.4
Experiment	131.5	11.3	20.1

The crack patterns for the specimen SM 1.5 analyses including and excluding self-weight, in addition to the experimental crack patterns, are presented in Figure 5.96. Both analyses produced identical crack patterns to one another.

a) Top face, experiment

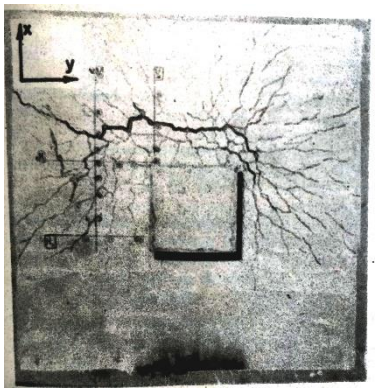

b) Bottom face, experiment

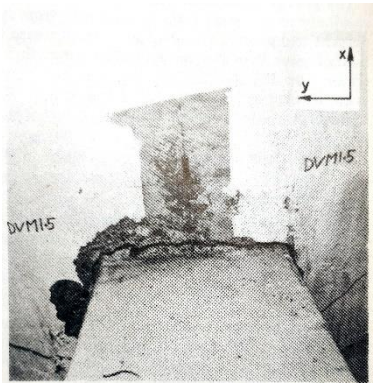

c) Top face, self-weight included

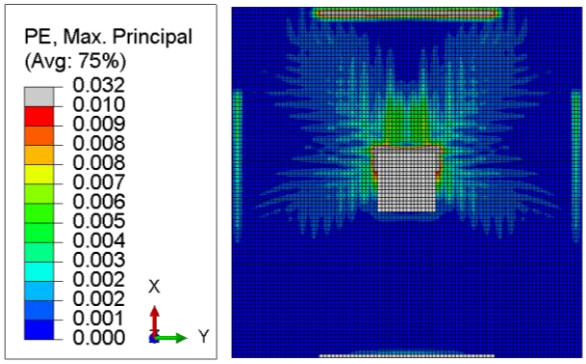

d) Bottom face, self-weight included

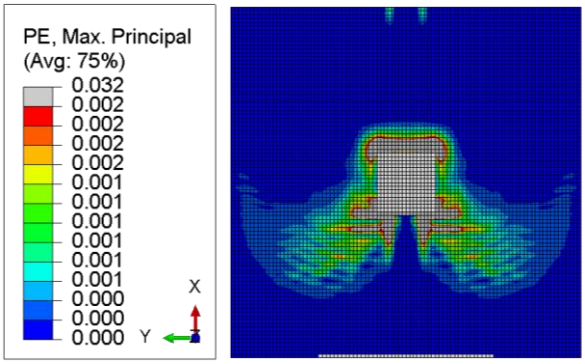

e) Top face, self-weight excluded

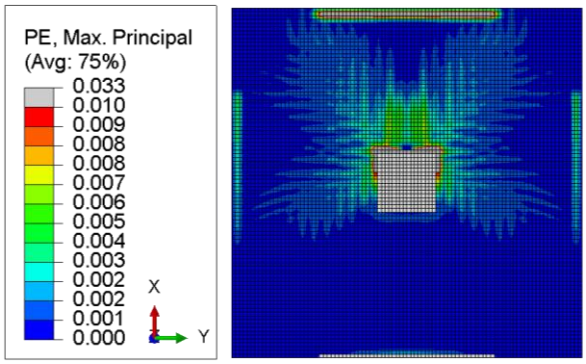

f) Bottom face, self-weight excluded

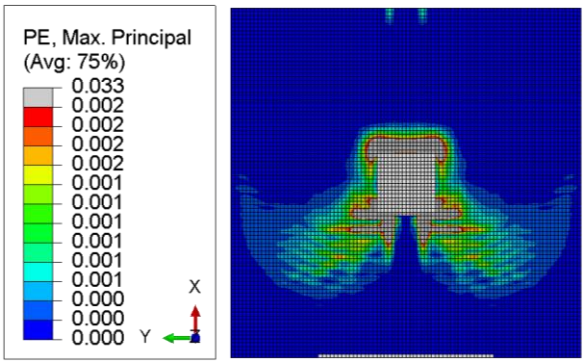

Figure 5.96: Specimen SM 1.5 experiment (Ghali et al., 1976) and analyses crack patterns when including versus excluding self-weight. Authorized reprint of experiment photographs from ACI Journal, Volume 73, Issue 10, October 1976.

5.9.4 Conclusions and recommendations

In this section, the three SM specimens were analysed with and without self-weight forces. The moment-rotation data, displacement-rotation data, and crack patterns of analyses with self-weight included were identical to the aforementioned results for analyses without self-weight. For subsequent analyses, gravity loads continued being excluded as they increased computational resources but did not influence the results.

5.10 Study of concrete modulus of elasticity

In this study, the concrete uniaxial compression stress-strain data was horizontally stretched by reducing the tangent modulus of elasticity E_t. More information about the Hognestad parabola used to define the stress-strain data is presented in Section 3.1.2. The motivation for this study came from compression cylinder test data produced by El-Salakawy (1998). In previous analyses, the Hognestad parabola stress-strain data was defined using E_t equal to $5500\sqrt{f_c'}$. When this E_t and the Hognestad parabola to predict stress-strain data for El-Salakawy's cylinder tests, the predicted strains at peak stresses were on average 57-percent smaller than the tested strains at peak stresses.

In Section 5.10.1, an equation for E_t is presented that produces strains at peak stresses (when used with the Hognestad parabola) closer to the strains at peak stresses obtained from compression cylinder testing by El-Salakawy. In Sections 5.10.2 through 5.10.4, the SM specimens were reanalysed using E_t equal to $3150\sqrt{f_c'}$ to define the Hognestad parabola. The analyses using E_t with equal to $5500\sqrt{f_c'}$ and $3150\sqrt{f_c'}$ were compared to the experimental data to determine which of the E_t equations produced more accurate results.

It was expected that reducing the modulus of elasticity would reduce the large differences in rotations and displacements at ultimate moments between the experiments and their respective analyses. Additionally, it was predicted that using the reduced tangent modulus of elasticity would provide increased punching shear capacity due to the increased area under the Hognestad parabola. Since the area under the parabola is equal to the energy required to crush the concrete, specimens would be able to withstand higher moments before failure.

5.10.1 Calculation of tangent modulus of elasticity

The compressive strengths, tested strains at peak stresses, and Hognestad strains at peak stresses for each specimen are presented in Table 5.40. As previously mentioned, the tested strains at peak stresses were on average 57-percent smaller than strains at peak stresses predicted using the Hognestad parabola with a tangent modulus of elasticity E_t equal to $5500\sqrt{f_c'}$.

Table 5.40: Concrete properties of specimens tested by El-Salakawy (1998)

Specimen	Compressive strength f_c' (MPa)	Tested strain at peak stress ε_o	Hognestad strain at peak stress ε_o
CF0	30.5	0.0035	0.0020
CF0-R	32.0	0.0036	0.0021
HSE0	36.5	0.0040	0.0022
HSF0	36.0	0.0038	0.0022
HXXX	36.5	0.0038	0.0022
HXXX-R	33.5	0.0042	0.0021
SE0	32.5	0.0035	0.0021
SE0-R	31.5	0.0035	0.0020
SF0	31.5	0.0034	0.0020
SF0-R	32.5	0.0036	0.0021
SF1	33.0	0.0036	0.0021
SF2	30.0	0.0035	0.0020
XXX	33.0	0.0036	0.0021
XXX-R	32.0	0.0036	0.0021

El-Salakawy provided a typical stress-strain curve using the average of the data from Table 5.40. The typical stress-strain curve (El-Salakawy, 1998) and the Hognestad parabolas with E_t equal to $5500\sqrt{f_c'}$ for specimens XXX and HXXX are presented in Figure 5.97. Figure 5.97 shows that the Hognestad parabola predictions with E_t equal to $5500\sqrt{f_c'}$ were too stiff for El-Salakawy's specimens.

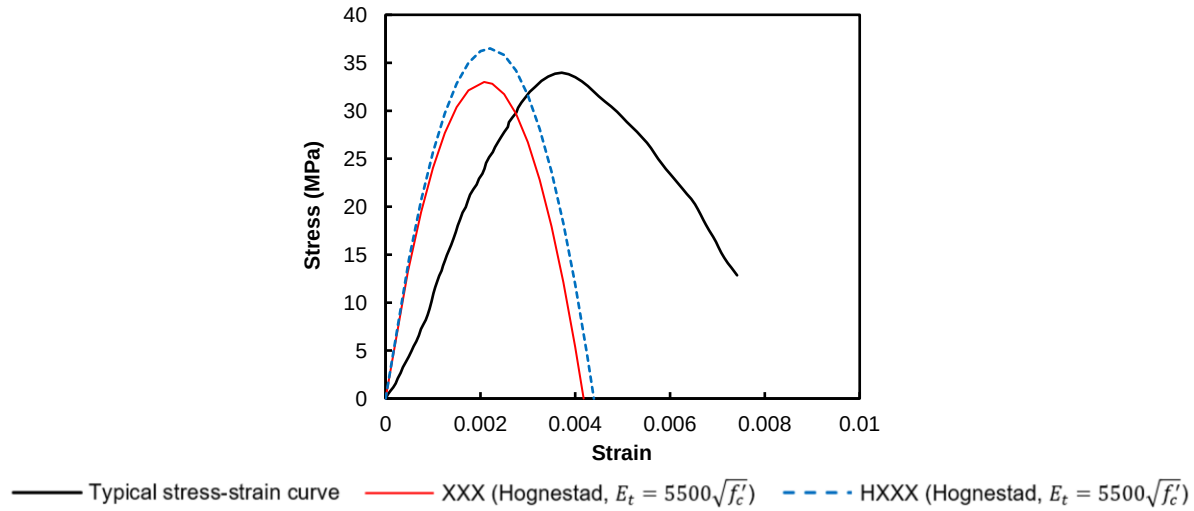

Figure 5.97: Typical stress-strain curve (El-Salakawy, 1998) and Hognestad parabolas with E_t equal to $5500\sqrt{f_c'}$ for specimens XXX and HXXX

To horizontally stretch the stress-strain data, the tangent modulus of elasticity was reduced. The 5500 coefficient within the tangent modulus of elasticity equation (previously shown in Equation 3.4) was replaced with a variable x:

$$E_t(x) = x\sqrt{f_c'} \ . \tag{5.5}$$

Next, Equation 5.5 was substituted into Equation 3.3 and rearranged to solve for x:

$$x = 2\frac{\sqrt{f_c'}}{\varepsilon_{ot}} \tag{5.6}$$

where the ε_{ot} is the strain at peak stress from El-Salakawy's tests.

Table 5.41 shows the required E_t coefficient for each of El-Salakawy's specimens such that the Hognestad parabola predicts a strain at peak stress equal to the tested strain at peak stress. The required coefficients varied between specimens but were typically between 3100 and 3200. As such, a tangent modulus of elasticity coefficient of 3150 was selected for use in FE analyses of specimens SM 0.5, SM 1.0, and SM 1.5.

Figure 5.98 shows strains at peak stresses versus compressive strengths from El-Salakawy's tests as well as calculated values using the Hognestad parabola with tangent modulus of elasticity equations equal to $5500\sqrt{f_c'}$ and $3150\sqrt{f_c'}$. Based on this figure, the Hognestad parabola using a tangent modulus of elasticity equal to $3150\sqrt{f_c'}$ produced data that was in good agreement with the tested values.

Table 5.41: Required tangent modulus of elasticity coefficients for El-Salakawy's specimens

Specimen	Compressive strength f_c' (MPa)	Tested strain at peak stress ε_o	Tangent modulus of elasticity coefficient
SF2	30.0	0.0035	3130
CF0	30.5	0.0035	3156
SE0-R	31.5	0.0035	3207
SF0	31.5	0.0034	3301
CF0-R	32.0	0.0036	3143
XXX-R	32.0	0.0036	3143
SE0	32.5	0.0035	3258
SF0-R	32.5	0.0036	3167
SF1	33.0	0.0036	3191
XXX	33.0	0.0036	3191
HXXX-R	33.5	0.0042	2756
HSF0	36.0	0.0038	3158
HSE0	36.5	0.0040	3021
HXXX	36.5	0.0038	3180

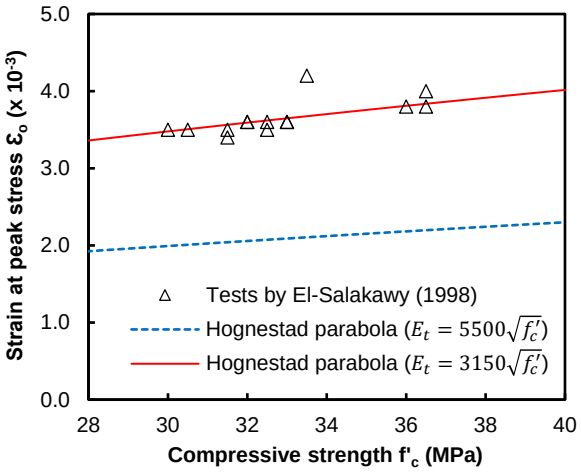

Figure 5.98: Strain at peak stress versus compressive strength for tested and Hognestad values

The reduced elastic modulus of elasticity was obtained by finding the slope of the secant between the origin and the Hognestad parabola datum at $0.4f_c'$ calculated using the reduced tangent modulus of elasticity (since the stress-strain data is assumed linear-elastic up to $0.4f_c'$):

$$E_c = 2795\sqrt{f_c'} \quad . \qquad \text{(SI units: N, mm)} \quad (5.7)$$

As discussed, the reduced tangent modulus of elasticity is

$$E_t = 3150\sqrt{f_c'} \quad . \qquad \text{(SI units: N, mm)} \quad (5.8)$$

The typical stress-strain curve (El-Salakawy, 1998) and the Hognestad parabolas (using E_t equal to $3150\sqrt{f_c'}$) for specimens XXX and HXXX are presented in Figure 5.99. The stretched Hognestad parabolas for specimens XXX and HXXX better represented the typical stress-strain curve compared to the classical Hognestad parabolas for these same specimens.

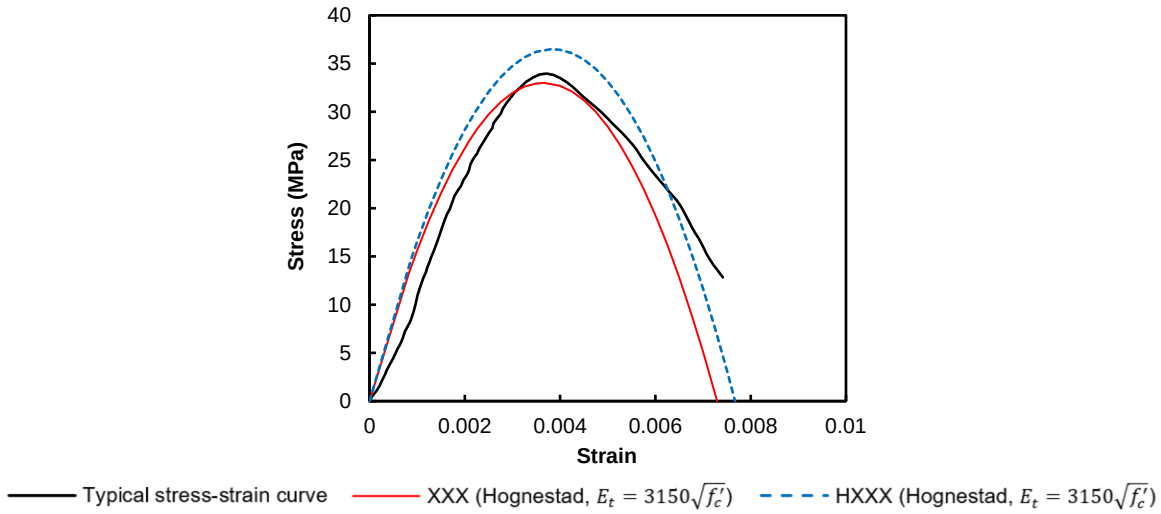

Figure 5.99: Typical stress-strain curve (El-Salakawy, 1998) and Hognestad parabolas with E_t equal to $3150\sqrt{f_c'}$ for specimens XXX and HXXX

5.10.2 Results of specimen SM 0.5 analyses

The moment-rotation and displacement-rotation data for the specimen SM 0.5 analyses using the Hognestad parabola with E_t equal to $3150\sqrt{f_c'}$ and $5500\sqrt{f_c'}$, in addition to the experimental results, are presented in Figure 5.100. A summary of this data is provided in Table 5.42.

Of the two analyses, the analysis in which E_t was equal to $3150\sqrt{f_c'}$ produced softer moment-rotation data. The analysis in which E_t was equal to $5500\sqrt{f_c'}$ produced moment-rotation data with a slope closer to that of the experiment. The ultimate moment percentage difference between the analysis and the experiment was 3.5-percent and 8.1-percent when E_t was equal to $5500\sqrt{f_c'}$ and $3150\sqrt{f_c'}$, respectively. The rotation at ultimate moment percentage difference

between the analysis and the experiment decreased from 47.6-percent to 32.1-percent when E_t was reduced from $5500\sqrt{f_c'}$ to $3150\sqrt{f_c'}$.

Using E_t equal to $3150\sqrt{f_c'}$ reduced the ultimate moment and increased the rotation at ultimate moment for specimen SM 0.5. Since specimen SM 0.5 failed in flexure, the analysis did not benefit from the increased crushing energy of the stretched Hognestad parabola. Instead, the lower modulus of elasticity values meant that higher column rotations occurred under lower applied moments. This meant that the flexural reinforcement yielded under a lower applied moment compared to the analysis that used E_t equal to $5500\sqrt{f_c'}$.

The displacement-rotation data showed that the initial vertical displacement was higher for the analysis in which E_t was equal to $3150\sqrt{f_c'}$ (1.5 mm versus 0.7 mm). For comparison, the specimen SM 0.5 experiment initial vertical displacement was 7.7 mm. The slopes of the two analyses were similar to one another. The displacement at ultimate moment percentage difference increased from 0.4-percent to 15.2-percent when E_t was reduced from $5500\sqrt{f_c'}$ to $3150\sqrt{f_c'}$.

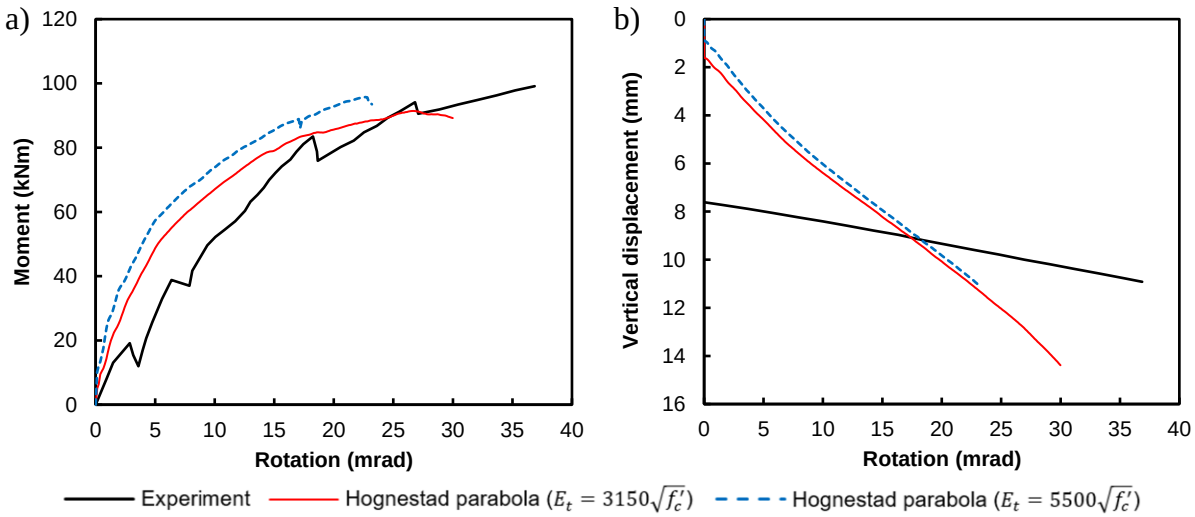

Figure 5.100: Specimen SM 0.5 a) moment-rotation and b) displacement-rotation data using the Hognestad parabola with E_t equal to $3150\sqrt{f_c'}$ and $5500\sqrt{f_c'}$

Table 5.42: Specimen SM 0.5 analyses results using the Hognestad parabola with E_t equal to $3150\sqrt{f_c'}$ and $5500\sqrt{f_c'}$

	Ultimate moment (kNm)	Displacement (mm) at ultimate moment	Rotation (mrad) at ultimate moment
Analyses			
Hognestad parabola, $E_t = 3150\sqrt{f_c'}$	91.4	12.7	26.7
Hognestad parabola, $E_t = 5500\sqrt{f_c'}$	95.7	10.9	22.7
Experiment	99.1	10.9	36.9

The crack patterns for the specimen SM 0.5 analyses using the Hognestad parabola with E_t equal to $3150\sqrt{f_c'}$ and $5500\sqrt{f_c'}$, in addition to the experimental crack patterns, are presented in Figure 5.101. Both analyses produced similar crack patterns to one another.

a) Top face, experiment

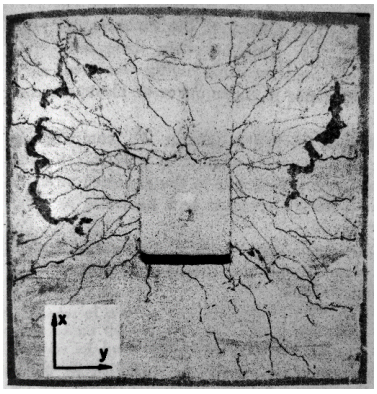

b) Bottom face, experiment

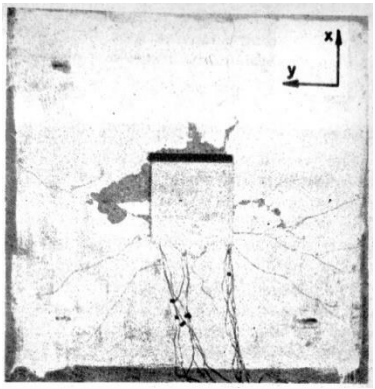

c) Top face, $E_t = 3150\sqrt{f_c'}$

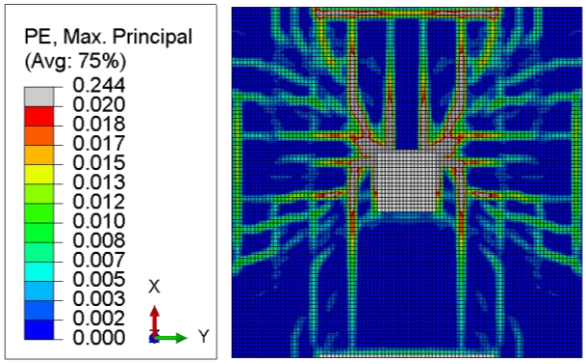

d) Bottom face, $E_t = 3150\sqrt{f_c'}$

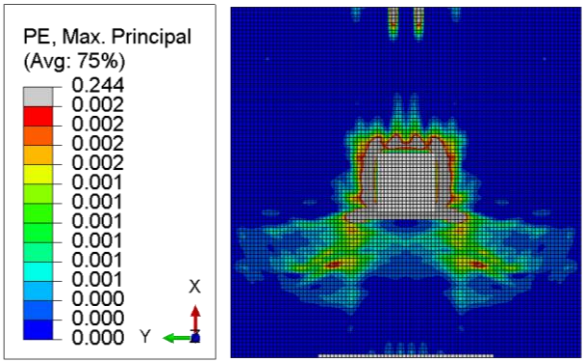

e) Top face, $E_t = 5500\sqrt{f_c'}$

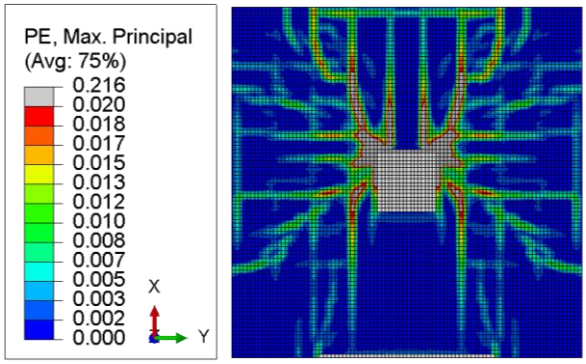

f) Bottom face, $E_t = 5500\sqrt{f_c'}$

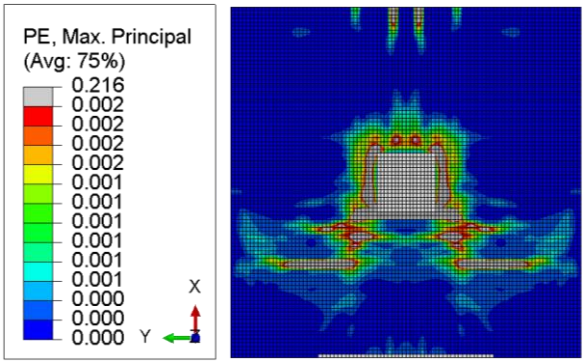

Figure 5.101: Specimen SM 0.5 experiment (Ghali et al., 1976) and analyses crack patterns using the Hognestad parabola with E_t equal to $3150\sqrt{f_c'}$ and $5500\sqrt{f_c'}$. Authorized reprint of experiment photographs from ACI Journal, Volume 73, Issue 10, October 1976.

5.10.3 Results of specimen SM 1.0 analyses

The moment-rotation and displacement-rotation data for the specimen SM 1.0 analyses using the Hognestad parabola with E_t equal to $3150\sqrt{f_c'}$ and $5500\sqrt{f_c'}$, in addition to the experimental results, are presented in Figure 5.102. A summary of this data is provided in Table 5.43.

Of the two analyses, the analysis in which E_t was equal to $3150\sqrt{f_c'}$ produced softer moment-rotation data. Furthermore, the slope of this analysis was closer to that of the experiment past 10 mrad. The reduced E_t analysis produced a larger ultimate moment and ultimate rotation compared to the larger E_t analysis. The larger ultimate moment was due to the greater concrete crushing energy of the stretched Hognestad parabola and the larger ultimate rotation was a result of the stretched parabolas lower modulus of elasticity. The increased column rotation was not enough to yield the flexural reinforcement and the specimen still failed in punching.

The moment-rotation results of the reduced E_t analysis produced results closer to the experiment compared to the larger E_t analysis. The ultimate moment percentage difference between the analyses and the experiment was 3.2-percent and 5.0-percent when E_t was equal to $3150\sqrt{f_c'}$ and $5500\sqrt{f_c'}$, respectively. The rotation at ultimate moment percentage difference between the analyses and the experiment was 47.4-percent and 87.0-percent when E_t was equal to $3150\sqrt{f_c'}$ and $5500\sqrt{f_c'}$, respectively.

The displacement-rotation data showed that the reduced E_t analysis had a higher initial vertical displacement of 1.2 mm compared to the original E_t analysis which had an initial vertical displacement of 0.7 mm. The experiment had an initial vertical displacement of 5.8 mm. Relative to the experiment, the initial displacement percentage differences were 131.4-percent and 156.9-percent for the reduced and original E_t analyses, respectively. The displacement-rotation data produced by both analyses had similar slopes to one another until failure. The reduced E_t analysis had a larger displacement at ultimate moment of 5.2 mm compared to the original E_t analysis which had a displacement of 3.8 mm. Relative to the experiment, the displacement at ultimate moment percentage differences were 70.2-percent and 97.1-percent for the reduced and original E_t analyses, respectively.

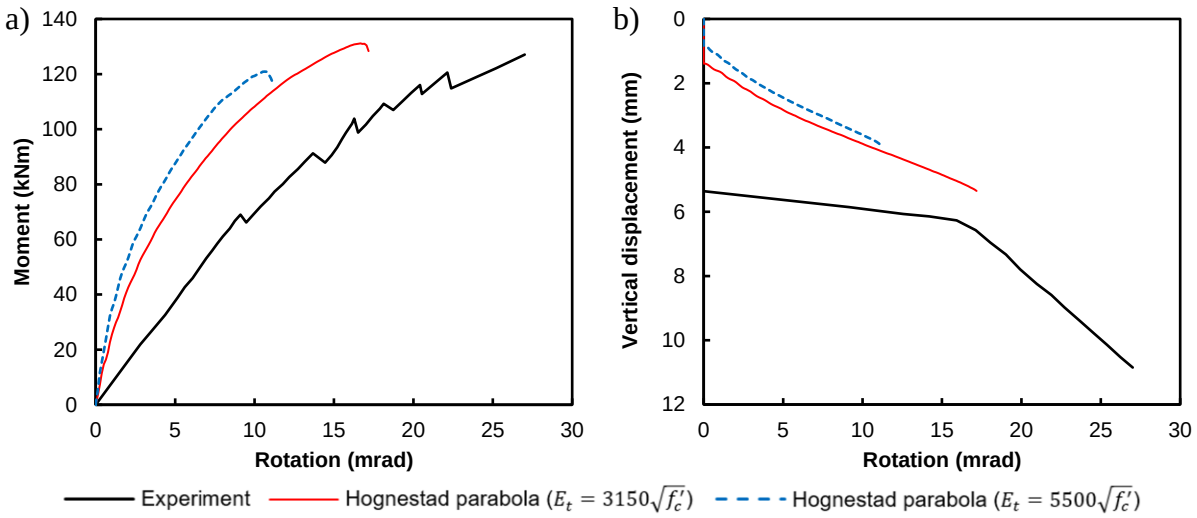

Figure 5.102: Specimen SM 1.0 a) moment-rotation and b) displacement-rotation data using the Hognestad parabola with E_t equal to $3150\sqrt{f_c'}$ and $5500\sqrt{f_c'}$

Table 5.43: Specimen SM 1.0 analyses results using the Hognestad parabola with E_t equal to $3150\sqrt{f_c'}$ and $5500\sqrt{f_c'}$

	Ultimate moment (kNm)	Displacement (mm) at ultimate moment	Rotation (mrad) at ultimate moment
Analyses			
Hognestad parabola, $E_t = 3150\sqrt{f_c'}$	131.1	5.2	16.7
Hognestad parabola, $E_t = 5500\sqrt{f_c'}$	120.9	3.8	10.6
Experiment	127.1	10.8	27.0

The crack patterns for the specimen SM 1.0 analyses using the Hognestad parabola with E_t equal to $3150\sqrt{f_c'}$ and $5500\sqrt{f_c'}$ are presented in Figure 5.103. Both analyses produced similar crack patterns to one another.

a) Top face, $E_t = 3150\sqrt{f_c'}$ b) Bottom face, $E_t = 3150\sqrt{f_c'}$

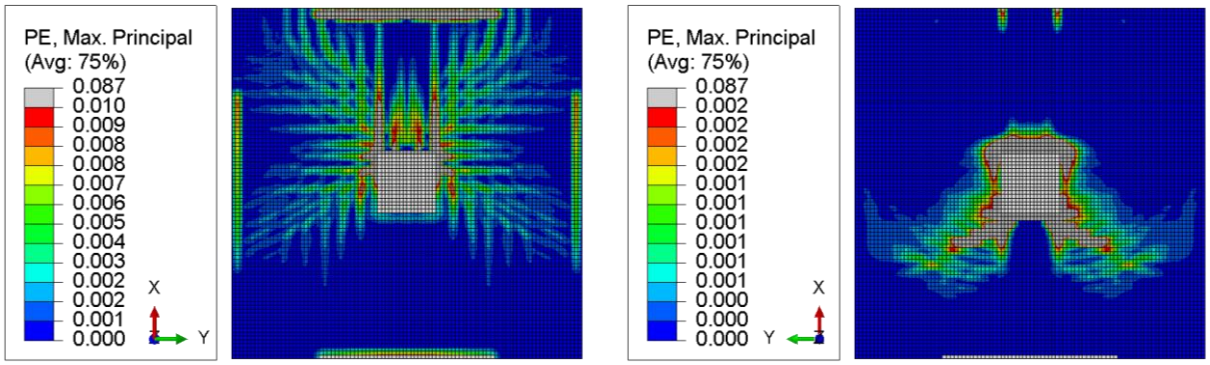

c) Top face, $E_t = 5500\sqrt{f_c'}$ d) Bottom face, $E_t = 5500\sqrt{f_c'}$

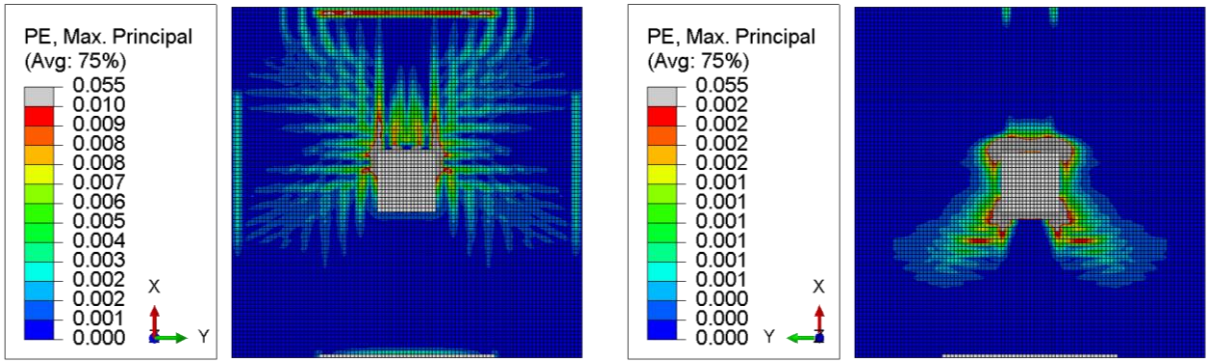

Figure 5.103: Specimen SM 1.0 analyses crack patterns using the Hognestad parabola with E_t equal to $3150\sqrt{f_c'}$ and $5500\sqrt{f_c'}$

5.10.4 Results of specimen SM 1.5 analyses

The moment-rotation and displacement-rotation data for the specimen SM 1.5 analyses using the Hognestad parabola with E_t equal to $3150\sqrt{f_c'}$ and $5500\sqrt{f_c'}$, in addition to the experimental results, are presented in Figure 5.104. A summary of this data is provided in Table 5.44.

As with the other SM specimens, the reduced E_t analysis produced softer moment-rotation data compared to the original E_t analysis. Of the two analyses, the moment-rotation slope of the reduced E_t analysis that was closer to that of the experiment. As with specimen SM 1.0, specimen SM 1.5 had a larger ultimate moment and rotation at ultimate moment when using the lower E_t value. Similarly, the larger ultimate moment was caused by the greater concrete crushing energy of the stretched Hognestad parabola and the larger rotation at ultimate moment was a result of the stretched Hognestad parabolas lower modulus of elasticity.

The ultimate moment percentage difference between the analyses and the experiment was 23.6-percent and 20.3-percent for the reduced and original E_t parabola analyses, respectively. The

rotation at ultimate moment percentage difference between the analyses and the experiment was 21.2-percent and 55.4-percent for the reduced and original E_t analyses, respectively.

As with the other specimen analyses, the reduced E_t analysis had a higher initial displacement (1.2 mm compared to 0.5 mm). By comparison, the experiment had an initial vertical displacement of 6.1 mm. The slope of the displacement-rotation data for the two analyses and the experiment were similar to one another. The analysis displacement at ultimate moment was closer to that of the experiment for the reduced E_t analysis compared to the original E_t analysis. The displacement at ultimate moment percentage difference was 108.9-percent and 123.6-percent for the reduced and original E_t analyses, respectively.

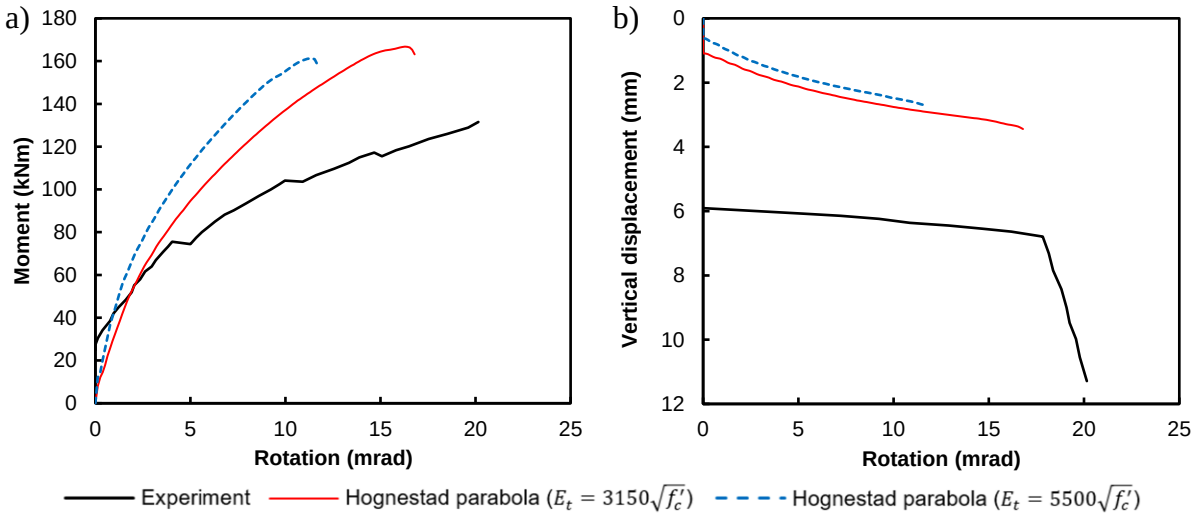

Figure 5.104: Specimen SM 1.5 a) moment-rotation and b) displacement-rotation data using the Hognestad parabola with E_t equal to $3150\sqrt{f_c'}$ and $5500\sqrt{f_c'}$

Table 5.44: Specimen SM 1.5 analyses results using the Hognestad parabola with E_t equal to $3150\sqrt{f_c'}$ and $5500\sqrt{f_c'}$

	Ultimate moment (kNm)	Displacement (mm) at ultimate moment	Rotation (mrad) at ultimate moment
Analyses			
Hognestad parabola, $E_t = 3150\sqrt{f_c'}$	166.8	3.3	16.3
Hognestad parabola, $E_t = 5500\sqrt{f_c'}$	161.3	2.7	11.4
Experiment	131.5	11.3	20.1

The crack patterns for the specimen SM 1.5 analyses using the Hognestad parabola with E_t equal to $3150\sqrt{f_c'}$ and $5500\sqrt{f_c'}$, in addition to the experimental crack patterns, are presented in Figure 5.105. Both analyses produced similar crack patterns to one another.

a) Top face, experiment

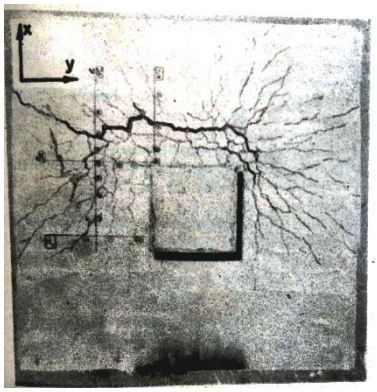

b) Bottom face, experiment

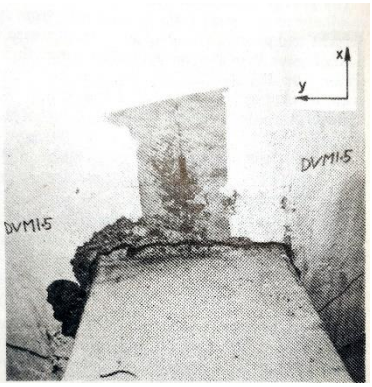

c) Top face, $E_t = 3150\sqrt{f_c'}$

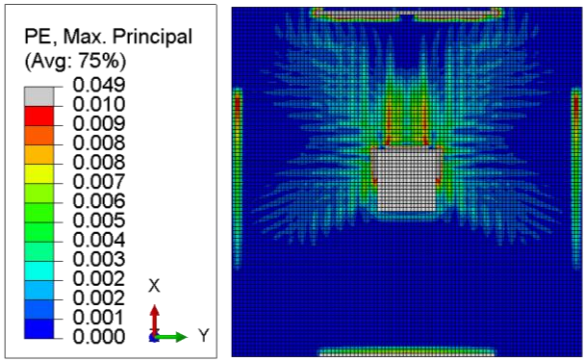

d) Bottom face, $E_t = 3150\sqrt{f_c'}$

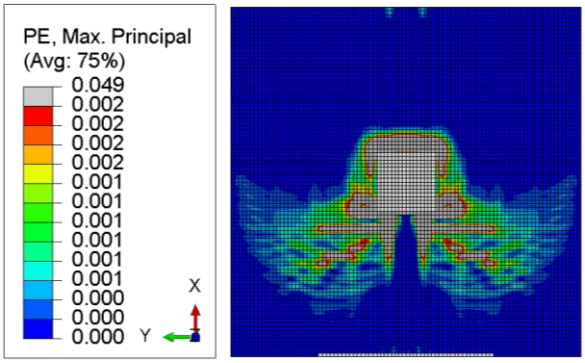

e) Top face, $E_t = 5500\sqrt{f_c'}$

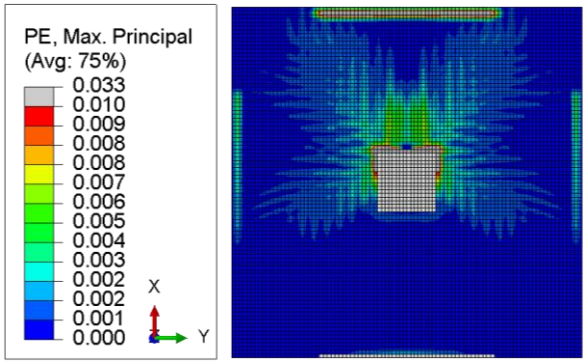

f) Bottom face, $E_t = 5500\sqrt{f_c'}$

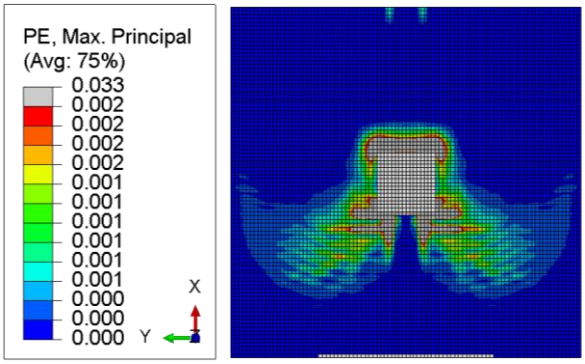

Figure 5.105: Specimen SM 1.5 experiment (Ghali et al., 1976) and analyses crack patterns using the Hognestad parabola with E_t equal to $3150\sqrt{f_c'}$ and $5500\sqrt{f_c'}$. Authorized reprint of experiment photographs from ACI Journal, Volume 73, Issue 10, October 1976.

5.10.5 Conclusions and recommendations

In this study, each of the three SM specimens were analysed using a reduced tangent modulus of elasticity E_t equation to define uniaxial compression stress-strain data with the Hognestad parabola. In previous analyses, E_t was equal to $5500\sqrt{f_c'}$ but was reduced to $3150\sqrt{f_c'}$ for analyses in this study. Using a reduced E_t coefficient of 3150 produced larger strains at peak

stress, which produced a better correlation between the stress-strain data predicted by the Hognestad parabola and by El-Salakawy's (1998) test stress-strain data obtained through compression cylinder testing. It was expected that using a lower modulus of elasticity would increase rotations and displacements at ultimate moments for the three specimens.

When using the reduced E_t equation versus the original E_t equation (i.e. from previous analyses), specimen SM 0.5 had a larger rotation at ultimate moment but a lower ultimate moment. The larger rotation was a direct result of using a smaller modulus of elasticity. The ultimate moment was lower because the larger rotations under the same applied moments resulted in higher strains within the flexural reinforcement. As a result, the flexural reinforcement reached its yield strain at a lower applied moment compared to the original E_t equation analyses. The slope of the moment-rotation data was closer to the slope of the experiment data when using the Hognestad parabola with reduced E_t equation compared to the original E_t equation.

Specimens SM 1.0 and SM 1.5 had larger rotations at ultimate moments and larger ultimate moments. As with specimen SM 0.5, each of the specimens had a reduced rotational stiffness which meant increased rotations at ultimate moments. Specimens SM 1.0 and SM 1.5 had higher ultimate moments as a result of the increased area under the Hognestad parabola when using a reduced E_t equation. The increased area under the Hognestad parabola meant that the concrete could withstand more energy from greater applied moments before crushing. For both specimen SM 1.0 and specimen SM 1.5, the slopes of the moment-rotation data sets were closer to the slopes of the experiments when using the reduced E_t equation versus the original E_t equation.

The displacement-rotation differences when using the reduced E_t versus the original E_t were consistent between all specimen analyses. When a reduced E_t was used, all specimens saw a higher initial vertical displacement. The reduced E_t analyses produced higher displacement at ultimate moments compared to the original E_t analyses. For each specimen, the displacement-rotation slopes were similar to one another regardless the E_t equation.

For all specimens, changing the value of E_t did not affect analyses crack patterns. Using smaller E_t values to define the Hognestad parabola decreased the analysis accuracy for specimen SM 0.5 but improved the analysis accuracy for specimens SM 1.0 and SM 1.5. Since using the

reduced E_t equation improved analysis accuracy for two of three specimens, the reduced E_t equation was used for subsequent analyses.

5.11 Comparison of strain-hardening versus perfectly-plastic reinforcement

Previous analyses used an elastic-perfectly-plastic model to define the uniaxial stress-strain data of the steel reinforcement. In this study, each of the three SM specimen models were reanalysed using elastic-strain-hardening stress-strain data that was obtained from a publication entitled *Dynamic Tests of Large Reinforcing Bar Splices* by Flathau (1971). This stress-strain data was used because both Flathau (1971) and Ghali et al. (1976) used reinforcement that met the requirements of ASTM A615-68 *Standard Specification for Deformed Billet-Steel Bars for Concrete Reinforcement* (1968).

The elastic-strain-hardening analyses results were compared to the elastic-perfectly-plastic analyses results. This was done to determine whether or not strain-hardening significantly affected the analyses results. Since specimen SM 0.5 was the only specimen to fail in flexure, the expectation of this study was that the ultimate moment of the specimen SM 0.5 analysis would increase. Increasing the analysis ultimate moment of specimen SM 0.5 would mean a smaller difference between the ultimate moment of the analysis and the experiment.

5.11.1 Strain-hardening stress-strain data

Ghali et al. (1976) stated that No. 4 steel reinforcement was used and that the reinforcement had a yield stress of 69 ksi (475 MPa). At the time of their publication, ASTM A615-68 outlined the requirements for deformed billet-steel bars produced for use as concrete reinforcement. ASTM A615-68 stated that there were three grades of steel reinforcement: Grade 40, Grade 60, and Grade 75, which had minimum yield stresses of 40 ksi (280 MPa), 60 ksi (420 MPa), and 75 ksi (520 MPa), respectively. The steel used by Ghali et al. exceeded 60 ksi but not 75 ksi. Therefore, Ghali et al. used Grade 60 deformed reinforcing bars for their tests.

Stress-strain data was obtained from a publication entitled *Dynamic Tests of Large Reinforcing Bar Splices* by Flathau (1971). In this publication, Flathau performed a number of tensile tests using No. 11 deformed bars. The tested specimens had varying grades of A615 billet-steel (Grades 60 and 75), different types of splices, and varying rates at which strains were applied (slow, intermediate, and rapid). In addition, Flathau tested as-rolled and machined bars using

the varying grades of A615 billet-steel and strain rates. For each combination of steel grade and strain rate, the spliced bar results were compared to the as-rolled and machined bar results to evaluate the performance of the splicing methods.

The tensile test results obtained by Flathau (1971) in which a No. 11 as-rolled bar with Grade 60 steel (loaded with an intermediate strain rate) was used for this study. The stress-strain data met the ASTM A615-68 requirements for a No. 11 bar; however, it was necessary to check if the data met the requirements for a No. 4 bar. The minimum percent elongation requirement for No. 4 bars was higher compared to the requirement for No. 11 bars (i.e. 9-percent elongation compared to 7-percent elongation). Flathau's stress-strain data had a percent elongation of approximately 12-percent which exceeded the ASTM A615-68 requirements for No. 4 bars.

It was necessary to convert the engineering stress-strain data into true stress-strain data before it could be used to define the steel reinforcement behaviour in Abaqus. The procedure to do this was explained in Section 3.2. The engineering and true stress-strain data are presented in Figure 5.106.

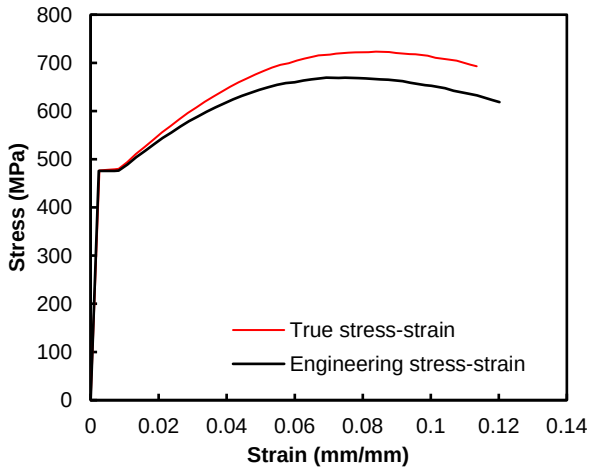

Figure 5.106: True and engineering stress-strain data of steel reinforcement used for SM specimens (Flathau, 1971)

5.11.2 Results of specimen SM 0.5 analyses

The moment-rotation and displacement-rotation data for the specimen SM 0.5 analyses using the strain-hardening and perfectly-plastic reinforcement, in addition to the experimental results, are presented in Figure 5.107. A summary of this data is provided in Table 5.45.

The strain-hardening reinforcement analysis produced more accurate moment-rotation data compared to the perfectly-plastic reinforcement analysis. For the strain-hardening reinforcement analysis, the slope of the moment-rotation data was similar in slope to the experiment data. This was expected as specimen SM 0.5 was the only specimen to fail in flexure. The additional toughness of the strain-hardening uniaxial stress-strain data allowed the reinforcement to carry more energy before fracturing compared to the perfectly-plastic stress-strain data.

Compared to the perfectly-plastic reinforcement analysis, the strain-hardening reinforcement analysis had an ultimate moment closer to that of the experiment. The ultimate moment percentage difference between the analyses and the experiment was 1.4-percent and 8.1-percent for the strain-hardening and perfectly-plastic reinforcement analyses, respectively. Furthermore, the strain-hardening reinforcement analysis had a displacement at ultimate moment closer to that of the experiment compared to the perfectly-plastic reinforcement analysis. The displacement at ultimate moment percentage difference between the analyses and the experiment was 13.0-percent and 15.2-percent for the strain-hardening and perfectly-plastic reinforcement analyses, respectively.

Both analyses produced similar displacement-rotation data to one another. There was a negligible increase in stiffness observed with the strain-hardening reinforcement analysis toward the end of the analysis. Of the two analyses, the strain-hardening reinforcement analysis had a displacement at ultimate moment closer to the experiment value. The percentage difference for the displacement at ultimate moment between the analyses and the experiment was 30.3-percent for the strain-hardening analysis and 32.1-percent for the perfectly-plastic analysis.

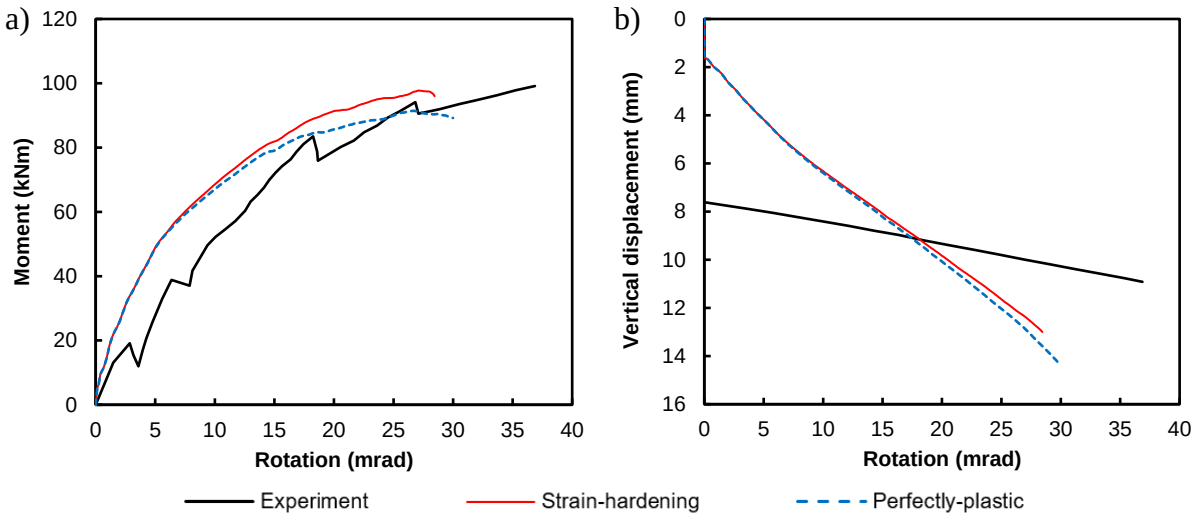

Figure 5.107: Specimen SM 0.5 a) moment-rotation and b) displacement-rotation data using strain-hardening versus perfectly-plastic reinforcement

Table 5.45: Specimen SM 0.5 analyses results using strain-hardening versus perfectly-plastic reinforcement

	Ultimate moment (kNm)	Displacement (mm) at Ultimate moment	Rotation (mrad) at Ultimate moment
Analyses			
Strain-hardening	97.7	12.4	27.2
Perfectly-plastic	91.4	12.7	26.7
Experiment	99.1	10.9	36.9

The crack patterns for the specimen SM 0.5 analyses using strain-hardening versus perfectly-plastic reinforcement, in addition to the experimental crack patterns, are presented in Figure 5.108. The two analyses produced crack patterns that were identical to one another.

a) Top face, experiment

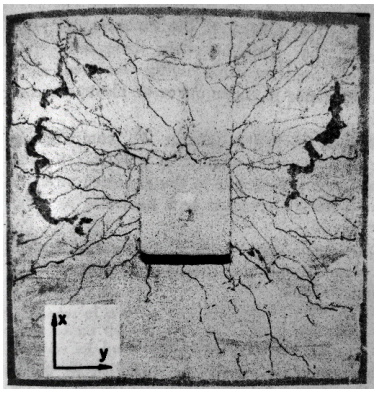

b) Bottom face, experiment

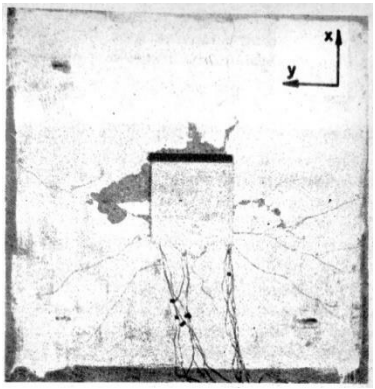

c) Top face, strain-hardening

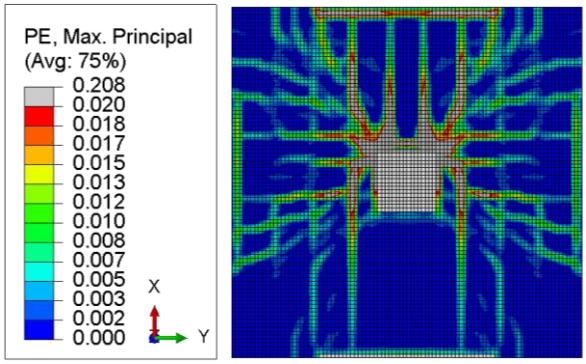

d) Bottom face, strain-hardening

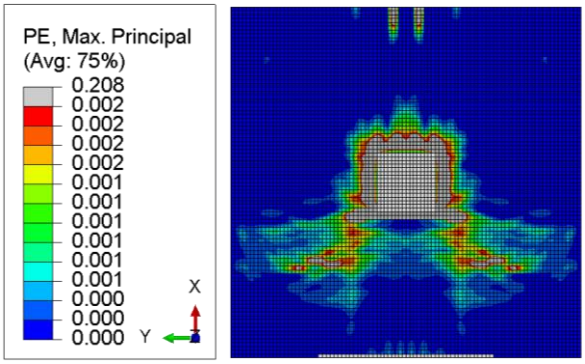

e) Top face, perfectly-plastic

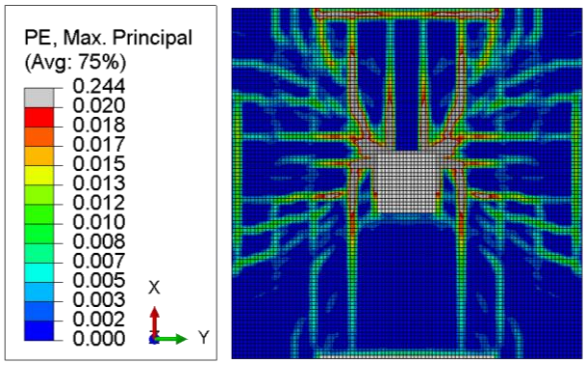

f) Bottom face, perfectly-plastic

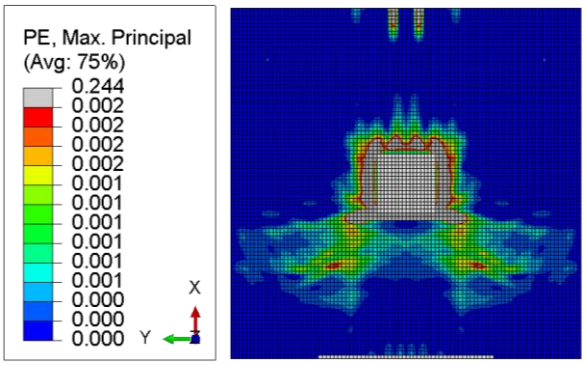

Figure 5.108: Specimen SM 0.5 experiment (Ghali et al., 1976) and analyses crack patterns using strain-hardening versus perfectly-plastic reinforcement. Authorized reprint of experiment photographs from ACI Journal, Volume 73, Issue 10, October 1976.

5.11.3 Results of specimen SM 1.0 analyses

The moment-rotation and displacement-rotation data for the specimen SM 1.0 analyses using the strain-hardening and perfectly-plastic reinforcement, in addition to the experimental results, are presented in Figure 5.109. A summary of this data is provided in Table 5.46.

The moment-rotation and displacement-rotation data produced by the two analyses were identical to one another. Since the reinforcement did not yield for specimen SM 1.0, the plastic portion of the stress-strain data was not important as the reinforcement remained linear elastic until the specimen failed.

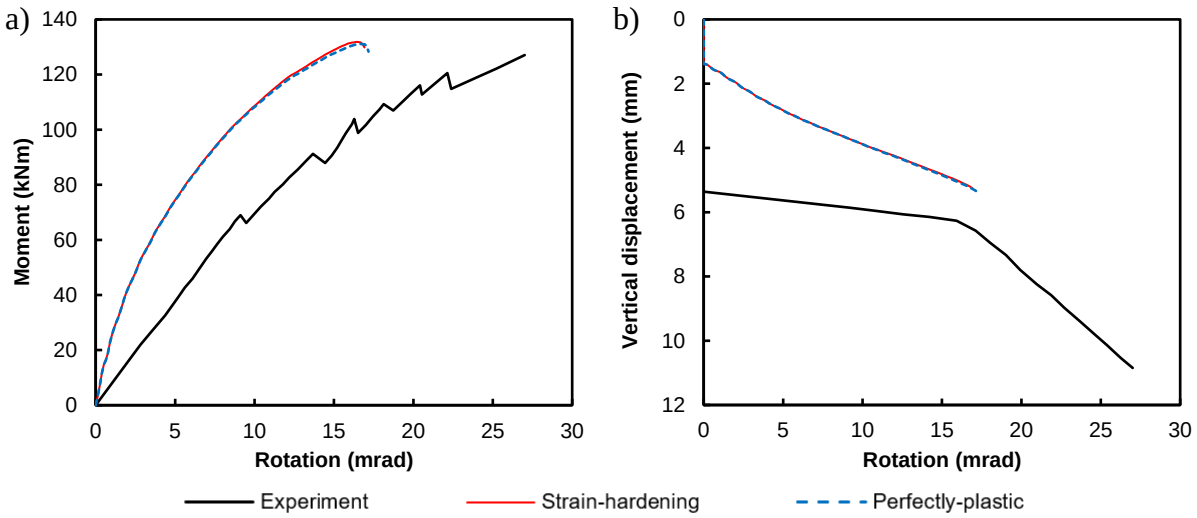

Figure 5.109: Specimen SM 1.0 a) moment-rotation and b) displacement-rotation data using strain-hardening versus perfectly-plastic reinforcement

Table 5.46: Specimen SM 1.0 analyses results using strain-hardening versus perfectly-plastic reinforcement

	Ultimate moment (kNm)	Displacement (mm) at ultimate moment	Rotation (mrad) at ultimate moment
Analyses			
Strain-hardening	131.9	5.1	16.4
Perfectly-plastic	131.1	5.2	16.7
Experiment	127.1	10.8	27.0

The crack patterns for the specimen SM 1.0 analyses using strain-hardening versus perfectly-plastic reinforcement are presented in Figure 5.110. Both analyses produced identical crack patterns to one another.

a) Top face, strain-hardening

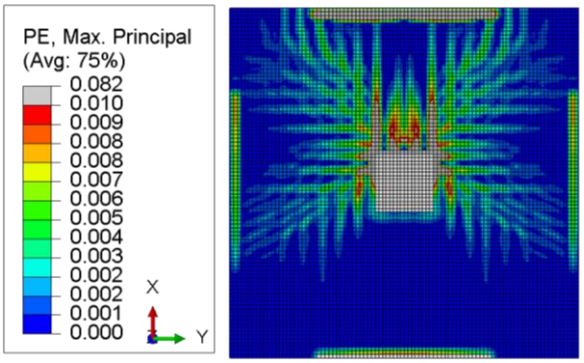

b) Bottom face, strain-hardening

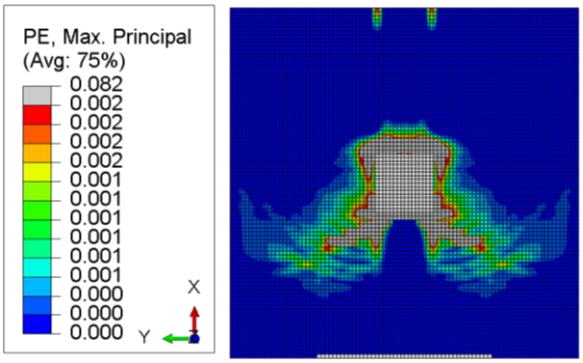

c) Top face, perfectly-plastic

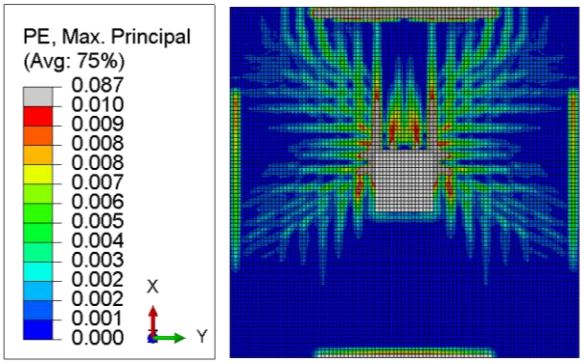

d) Bottom face, perfectly-plastic

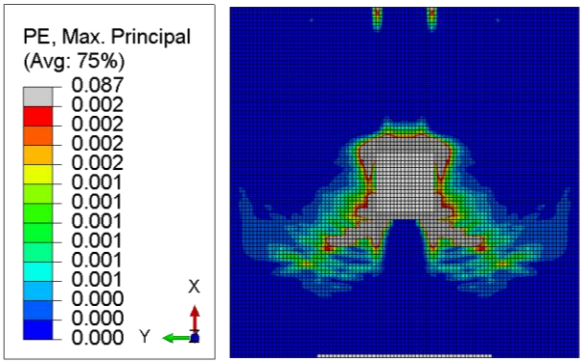

Figure 5.110: Specimen SM 1.0 analyses crack patterns using strain-hardening versus perfectly-plastic reinforcement

5.11.4 Results of specimen SM 1.5 analyses

The moment-rotation and displacement-rotation data for the specimen SM 1.5 analyses using the strain-hardening and perfectly-plastic reinforcement, in addition to the experimental results, are presented in Figure 5.111. A summary of this data is provided in Table 5.47.

Both the moment-rotation and displacement-rotation were identical for both analyses. As was the case with specimen SM 1.0, both analyses produced the same data because the steel reinforcement did not yield.

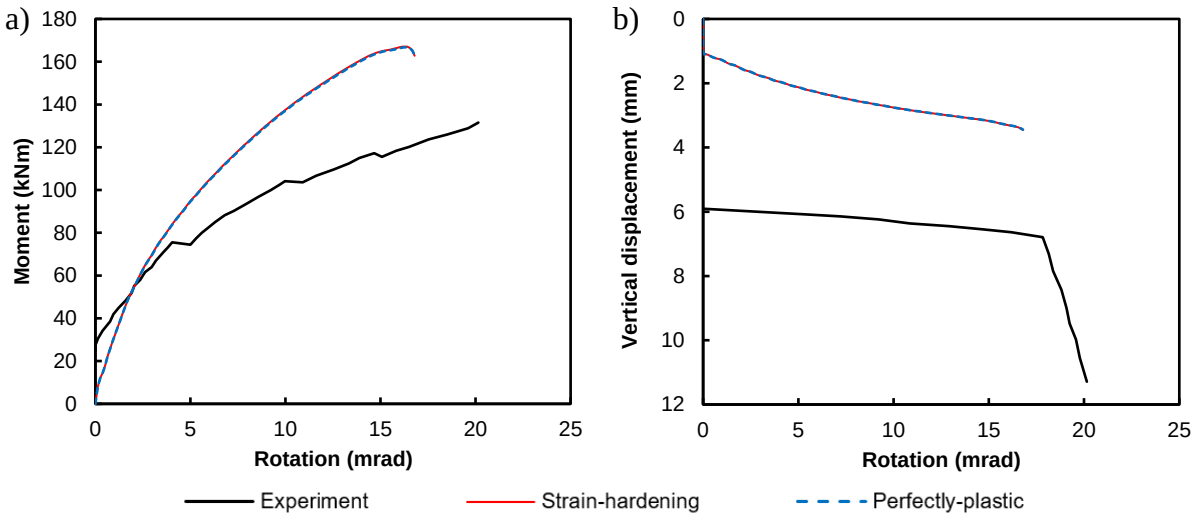

Figure 5.111: Specimen SM 1.5 a) moment-rotation and b) displacement-rotation data using strain-hardening versus perfectly-plastic reinforcement

Table 5.47: Specimen SM 1.5 analyses results using strain-hardening versus perfectly-plastic reinforcement

	Ultimate moment (kNm)	Displacement (mm) at ultimate moment	Rotation (mrad) at ultimate moment
Analyses			
Strain-hardening	167.0	3.3	16.3
Perfectly-plastic	166.8	3.3	16.3
Experiment	131.5	11.3	20.1

The crack patterns for the specimen SM 1.5 analyses using strain-hardening versus perfectly-plastic reinforcement, in addition to the experimental crack patterns, are presented in Figure 5.112. The two analyses produced identical crack patterns to one another.

a) Top face, experiment

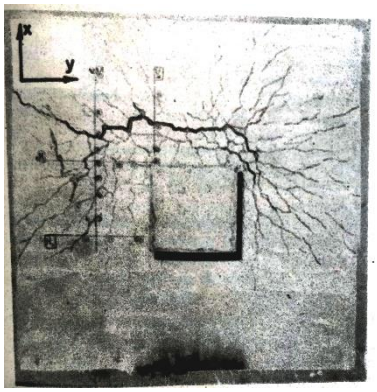

b) Bottom face, experiment

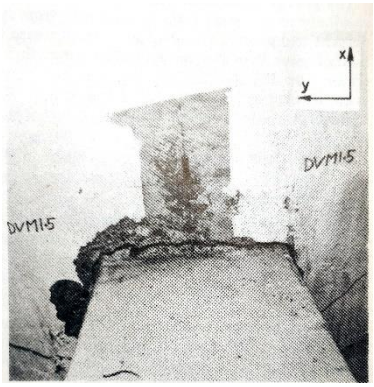

c) Top face, strain-hardening

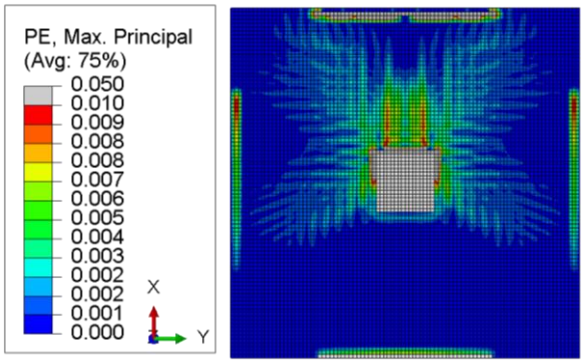

d) Bottom face, strain-hardening

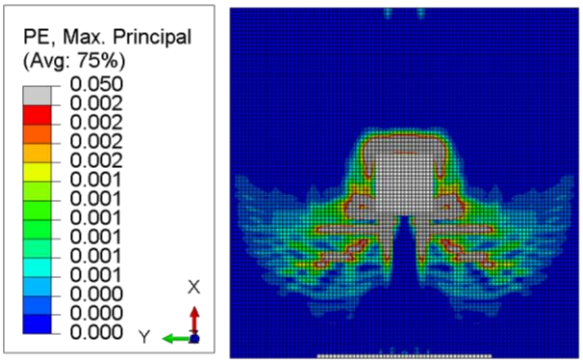

e) Top face, perfectly-plastic

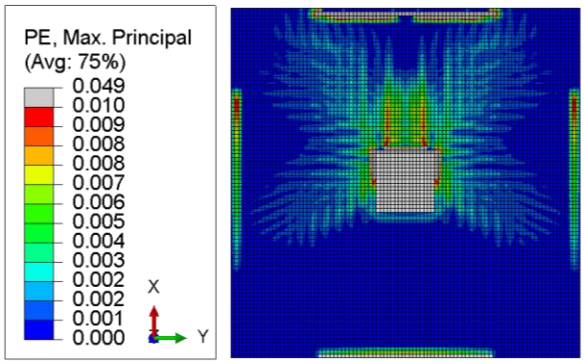

f) Bottom face, perfectly-plastic

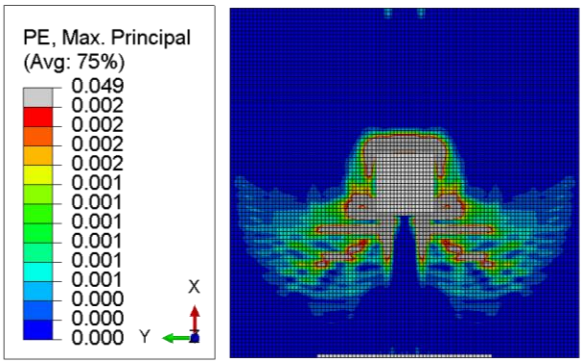

Figure 5.112: Specimen SM 1.5 experiment (Ghali et al., 1976) and analyses crack patterns using strain-hardening versus perfectly-plastic reinforcement. Authorized reprint of experiment photographs from ACI Journal, Volume 73, Issue 10, October 1976.

5.11.5 Conclusions and recommendations

In this study, the three SM specimen models were reanalysed using strain-hardening uniaxial plasticity data whereas previous analyses were completed using perfectly-plastic data. Engineering stress-strain data was obtained from *Dynamic Tests of Large Reinforcing Bar Splices* (Flathau, 1971). After checking that the stress-strain data fulfilled ASTM A615-68

requirements, the engineering stress-strain data was converted into true stress-strain data then used in reanalyses of the specimens.

Specimen SM 0.5 was the only specimen to produce different results when the uniaxial stress-strain data was changed from elastic-perfectly-plastic to elastic-strain-hardening. This was because specimen SM 0.5 failed in flexure rather than punching. The reinforcement strain-hardening provided additional capacity to the reinforcing bars and subsequently increased the moment-rotation slope and the ultimate moment. The resulting moment-rotation slope and ultimate moment was closer to that of the experiment. The differences in displacement-rotation data between the two specimen SM 0.5 analyses were negligible.

The results of specimens SM 1.0 and SM 1.5 did not change when strain-hardening was introduced. This was because both specimens failed in punching and the steel reinforcement within both specimens did not yield. It was predicted that specimens SM 1.0 and SM 1.5 would show a greater sensitivity to reinforcement stress-strain data during parametric studies. This was because these specimens were expected fail in flexural when the applied vertical load was reduced.

For each of the three analyses, introducing strain-hardening did not have any affect on the crack patterns.

Since strain-hardening improved the accuracy of the specimen SM 0.5 analysis and did not affect the results of the other specimen analyses, elastic-strain-hardening uniaxial stress-strain data was used for the steel reinforcement for subsequent analyses.

5.12 Additional possible calibration: neoprene supports

Neoprene supports were shown in another publication describing tests by Langohr, Ghali, and Dilger (1976), which were also tested at the University of Calgary. Neoprene supports could be introduced to decrease the slope of the moment-rotation data under lower moments. Also, using neoprene supports would increase the initial vertical displacement prior to the application of moment. If more information about the neoprene supports was available including their geometry and material properties, it would be possible to model these supports in Abaqus.

Chapter 6: Finite element analyses of laboratory-tested specimens

In this section, the calibrated numerical model parameters were verified through numerical modelling of different specimens. Chapter 5 focused on calibrating numerical model parameters based on specimens SM 0.5, SM 1.0, and SM 1.5 tested by Ghali et al. (1976). The final model parameters and subsequent FEA results for the SM specimens are presented in Section 6.1.

To validate the numerical model parameters, three additional specimens were analysed using numerical modelling and their results were compared to laboratory test results. The first two specimens analysed were specimens XXX and HXXX. These specimens were tested by El-Salakawy (1998) at the University of Waterloo. Specimens XXX and HXXX were edge slab-column sub-assemblages without shear reinforcement with eccentricities of 0.30-meters and 0.66-meters, respectively. More information about these specimens, in addition to analysis and experimental results, are presented in Section 6.2.

The final specimen analysed was specimen SB1 tested by Adetifa (2003) at the University of Waterloo. This specimen was an interior slab-column sub-assemblage without shear reinforcement. Unlike the other specimens, specimen SB1 was subjected to only a linearly ramping concentric load until failure. More information about specimen SB1, as well as its analysis and experimental results, is presented in Section 6.3.

6.1 SM specimens by Ghali, Elmasri, and Dilger (1976)

Information about the geometries, loadings, boundary conditions, and materials for specimens SM 0.5, SM 1.0, and SM 1.5 is provided in Section 4.1.

6.1.1 Boundary conditions

The final boundary conditions used for the FE analyses of all SM specimens did not differ from the preliminary boundary conditions. Information about the boundary conditions used for these analyses is presented in Section 4.3.

6.1.2 Concrete properties

The concrete mesh used for the FE analyses of the SM specimens is shown in Figure 6.1. The concrete slab and column were meshed with C3D8R continuum elements with an element size of 20 mm.

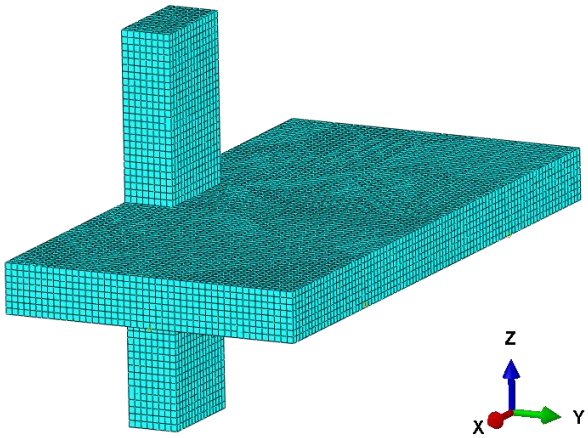

Figure 6.1: Concrete mesh used for FE analyses of SM specimens

The concrete compression and tension stress-strain data are presented in Figure 6.2 and Figure 6.3, respectively. The compression stress-strain data were calculated using the Hognestad parabola with reduced E_c and E_t parameters. More information about these modifications is presented in Section 5.10.

Linear-elastic data

Specimen	E_c (MPa)	ε_{co}	σ_{co} (MPa)
SM 0.5	16,948	0.0009	14.71
SM 1.0	16,144	0.0008	13.34
SM 1.5	17,672	0.0009	15.99

Plastic data

Specimen	E_t (MPa)	ε_o	f_c' (MPa)
SM 0.5	19,101	0.0039	36.77
SM 1.0	18,194	0.0037	33.36
SM 1.5	19,917	0.0040	39.98

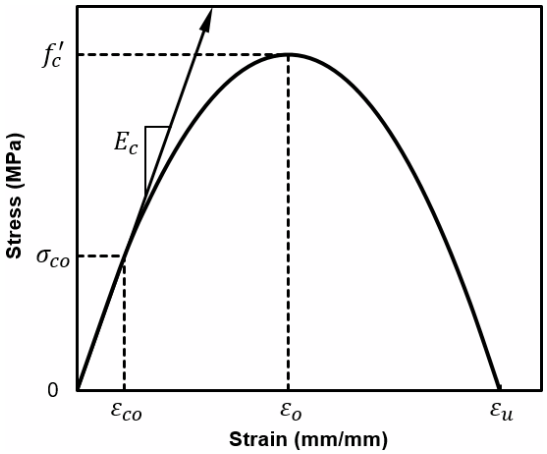

Figure 6.2: Compression stress-strain data used for FE analyses of SM specimens

Linear-elastic data

Specimen	E_c (MPa)	ε_{cr}	f_t' (MPa)
SM 0.5	16,948	0.0001	2.00
SM 1.0	16,144	0.0001	1.91
SM 1.5	17,672	0.0001	2.09

Plastic data

Specimen	G_f (N/mm)	ε_1	ε_u
SM 0.5	0.139	0.0029	0.0128
SM 1.0	0.136	0.0030	0.0132
SM 1.5	0.141	0.0029	0.0124

Note: Element length l_c is equal to 19.70 mm

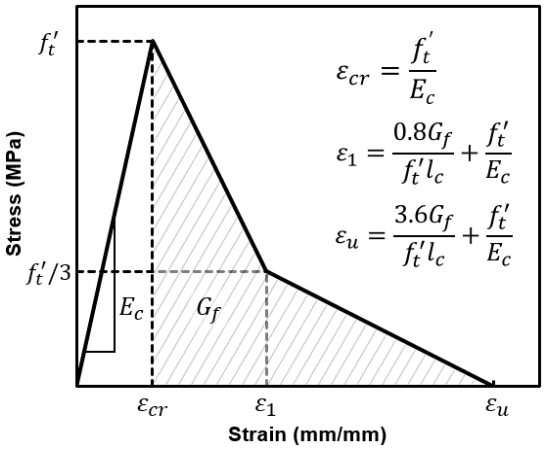

Figure 6.3: Tension stress-strain data used for FE analyses of SM specimens

The concrete material assignments used for all SM specimens are shown in Figure 6.4. Most of the concrete slab elements included the Concrete Damaged Plasticity material model. The edge of the slab used linear-elastic elements to prevent tension failures of the restrained elements. Tension stresses were present within these elements because the slab edge lifted when moments were applied. The concrete column used stiffened linear-elastic elements to reproduce the confinement effects of the stirrups on the concrete. For each specimen, the column E_c values were ten times those presented in Figure 6.2.

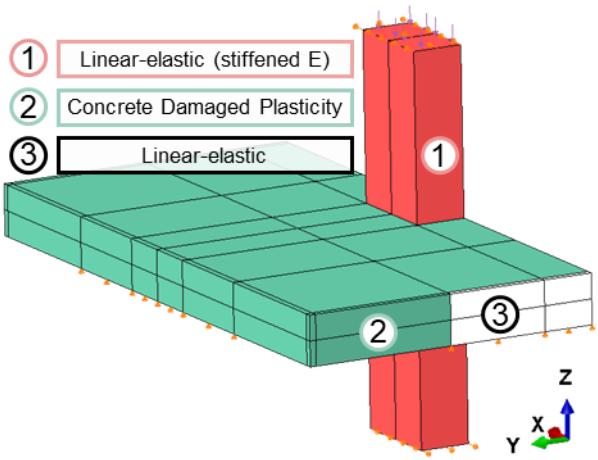

Figure 6.4: Concrete material assignments for FE analyses of SM specimens

6.1.3 Reinforcement properties

All steel reinforcement was meshed using T3D2 truss elements with an element size of 20 mm. The compression and tension reinforcement properties, including reinforcement spacing and areas, are presented in Table 6.1 and Table 6.2, respectively. The column reinforcement was not

modelled using truss elements. Instead, the effects of the column longitudinal reinforcement and stirrups were reproduced using linear-elastic concrete elements with higher modulus of elasticity values (i.e. ten times the modulus of elasticity of the slab concrete).

Table 6.1: Compression reinforcement properties for FE analyses of SM specimens

Specimen	x-direction			y-direction		
	Depth	Spacing	Area	Depth	Spacing	Area
SM 0.5		600 mm			534 mm	
SM 1.0	25 mm	300 mm	127 mm^2	38 mm	264 mm	127 mm^2
SM 1.5		198 mm			171 mm	

Table 6.2: Tension reinforcement properties for FE analyses of SM specimens

Specimen	x-direction			y-direction		
	Depth	Spacing	Area	Depth	Spacing	Area
SM 0.5		200 mm			178 mm	
SM 1.0	127 mm	100 mm	127 mm^2	114 mm	88 mm	127 mm^2
SM 1.5		66 mm			57 mm	

The steel reinforcement true stress-strain data obtained from Flathau (1971) is shown in Figure 6.5.

Linear-elastic data	
Poisson's ratio	Modulus of elasticity
0.3	183,686 MPa

Plastic data		
	Strain (mm/mm)	Stress (MPa)
Yield	0.0026	476
Ultimate	0.0839	723
Rupture	0.1135	693

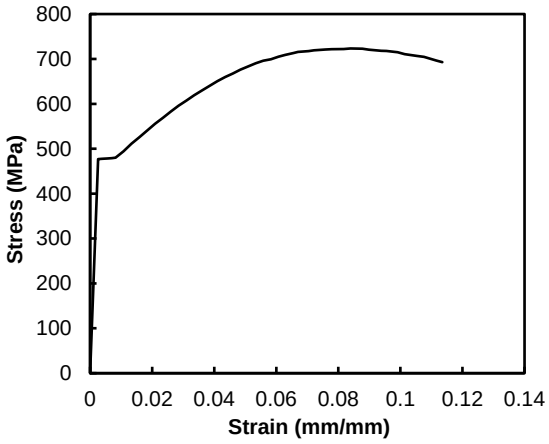

Figure 6.5: Reinforcement stress-strain data used for FE analyses of SM specimens

6.1.4 Moment versus rotation results

The FEA and experiment moment versus rotation results for specimen SM 0.5 are presented in Figure 6.6. The FEA moment-rotation data had similar slopes for all moment values compared to the experiment moment-rotation data. The FEA accurately reproduced the ultimate moment

of the experiment. The ultimate moments of the FEA and the experiment were 97.7 kNm and 99.1 kNm, respectively.

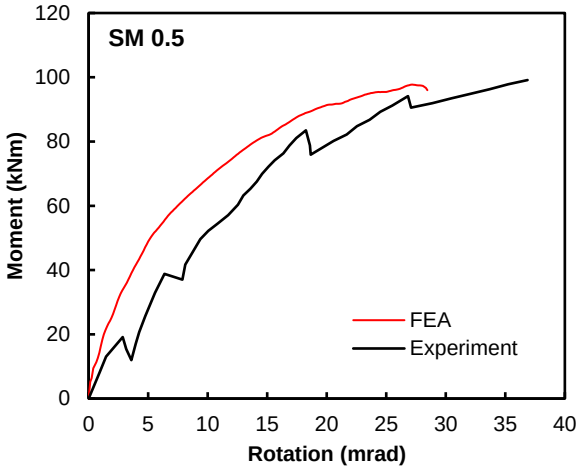

Figure 6.6: Specimen SM 0.5 moment versus rotation results

The moment versus rotation results for specimen SM 1.0 are presented in Figure 6.7. The slope of the FEA data was steeper than that of the experiment until 10 mrad. Past 10 mrad, both the FEA and experiment moment-rotation data had similar slopes. The ultimate moment of the FEA and the experiment were 131.9 kNm and 127.1 kNm, respectively.

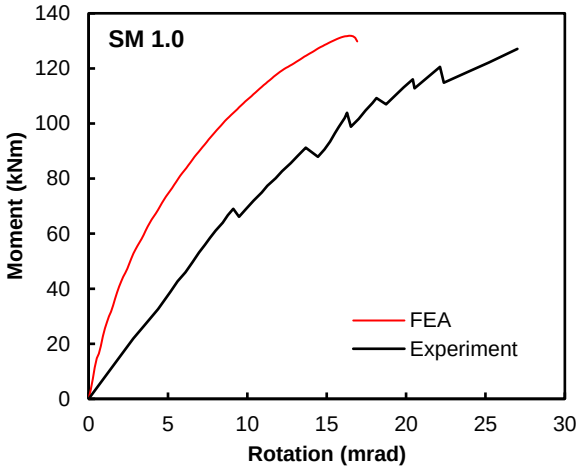

Figure 6.7: Specimen SM 1.0 moment versus rotation results

The moment versus rotation results for specimen SM 1.5 are presented in Figure 6.8. The FEA moment-rotation did not accurately reproduce the experiment moment-rotation data. Despite a 50-percent increase in reinforcement area, the difference in ultimate moment between specimen SM 1.0 and SM 1.5 was minimal. It was expected that the ultimate moment of specimen SM 1.5

would be greater if the specimen was recast and tested. The additional reinforcement was expected to reduce rotations. This would result in smaller crack widths and, therefore, greater punching shear capacity through aggregate interlock. Ghali et al. (1976) tested three specimens named DM 0.5, DM 1.0, and DM 1.5. These specimens were identical to SM 0.5, SM 1.0, and SM 1.5 except they were subjected to dynamic loading instead of static loading. Specimens DM 0.5 and DM 1.0 were loaded to ultimate moments which were 20 kNm greater than the ultimate moments of SM 0.5 and SM 1.0. Specimen DM 1.5 failed when subjected to a moment of 180 kNm. It was expected that SM 1.5 would fail when subjected to an ultimate moment of 160 kNm. An ultimate moment of 160 kNm would be closer to the ultimate moment observed through finite element analysis. The ultimate moment of the FEA and the experiment were 167.0 kNm and 131.5 kNm, respectively.

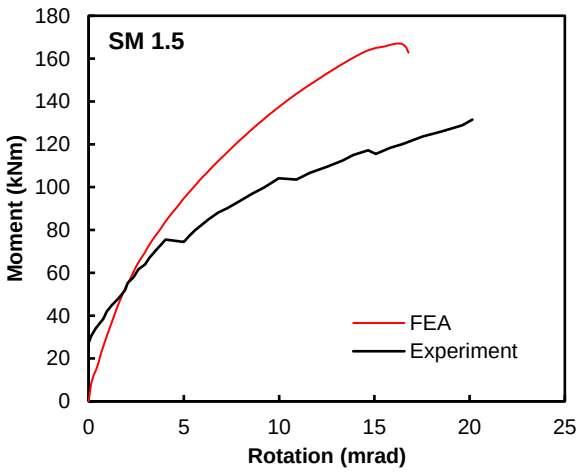

Figure 6.8: Specimen SM 1.5 moment-rotation results

6.1.5 Vertical displacement versus rotation results

The vertical displacement versus rotation results for specimen SM 0.5 are presented in Figure 6.9. The vertical displacement at ultimate moment of the FEA and the experiment were 12.4 mm and 10.9 mm, respectively. The FEA initial vertical displacement was 1.9 mm, while the experiment initial vertical displacement was 7.6 mm. The additional vertical displacement of the experiment is likely to due to the compression of neoprene bearing pads, which were not modelled in the finite element analyses. Also, additional displacements from creep effects during vertical loading were not captured using FEA. The slopes of the two data sets were not similar to one another. The ultimate displacement of the FEA was 13.0 mm and the ultimate displacement of the experiment was 10.9 mm.

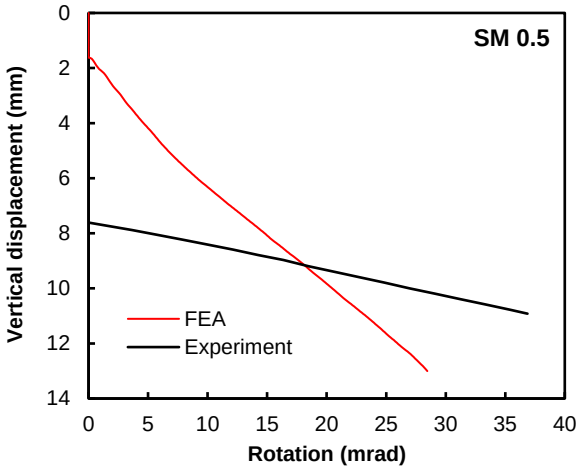

Figure 6.9: Specimen SM 0.5 vertical displacement versus rotation results

The vertical displacement versus rotation results for specimen SM 1.0 are presented in Figure 6.10. The vertical displacement at ultimate moment of the FEA and the experiment were 5.1 mm and 10.8 mm, respectively. The slope of the FEA displacement-rotation data was similar to the slope of the experiment displacement-rotation data as the experiment specimen approached its ultimate moment (i.e. for rotations between 15 mrad and 27 mrad).

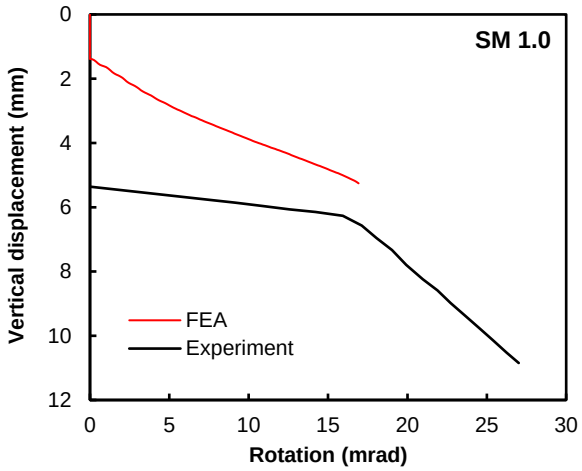

Figure 6.10: Specimen SM 1.0 vertical displacement versus rotation results

The vertical displacement versus rotation results for specimen SM 1.5 are presented in Figure 6.11. The vertical displacement at ultimate moment of the FEA and the experiment were 3.3 mm and 11.3 mm, respectively. The slope of the FEA displacement-rotation data was similar to the slope of the experiment displacement-rotation data for rotations between 0 mrad and 18 mrad.

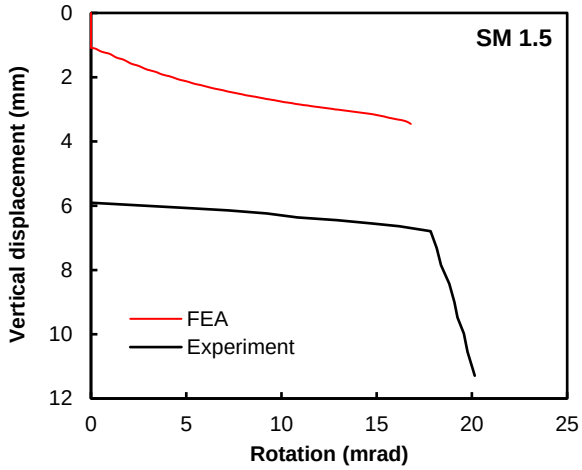

Figure 6.11: Specimen SM 1.5 vertical displacement versus rotation results

6.1.6 Crack patterns

The specimen SM 0.5 experiment and FEA crack patterns are presented in Figure 6.12. The analysis crack patterns were identical to the experiment crack patterns. On the top face, the analysis captured the vertical cracks that formed from the –x column face toward the –x slab edge. On the same face, the FEA reproduced the cracks that formed from the other column faces toward the restrained support elements. Furthermore, the FEA showed a concentration of cracking at the +x column face, which is observed among the experiment crack patterns. On the bottom face, the FEA reproduced the cracks that propagated from the –x column face toward the –x slab edge and slab columns. Similarly, the FEA reproduced the concentration of cracks around the column on the bottom face.

a) Top face, experiment

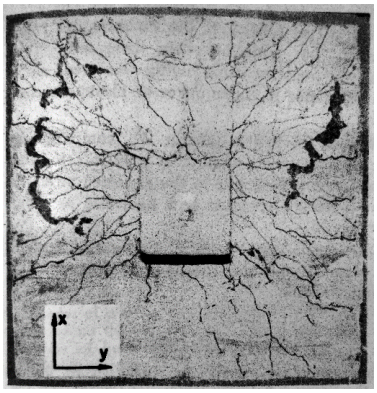

b) Bottom face, experiment

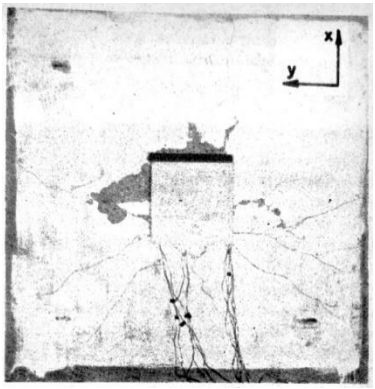

c) Top face, FE analysis

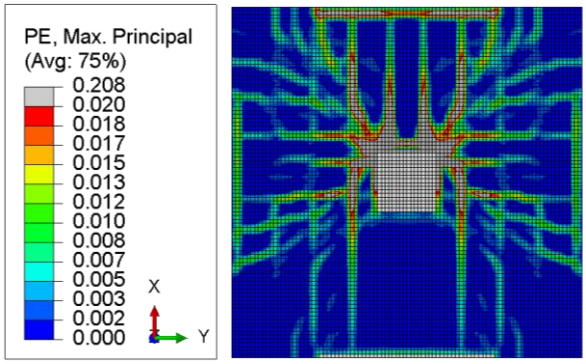

d) Bottom face, FE analysis

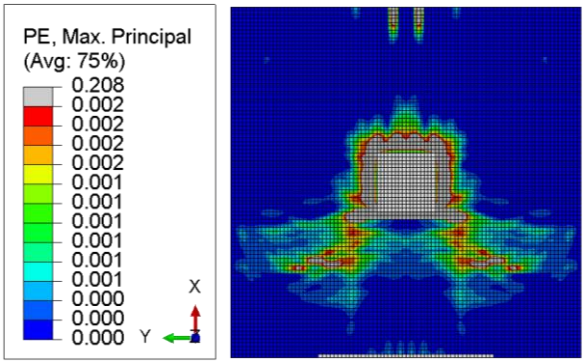

Figure 6.12: Specimen SM 0.5 experiment (Ghali et al., 1976) and analyses crack patterns. Authorized reprint of experiment photographs from ACI Journal, Volume 73, Issue 10, October 1976.

The specimen SM 1.0 FEA crack patterns are presented in Figure 6.13. Experimental crack patterns for specimen SM 1.0 were not published by Ghali et al. (1976). However, the crack patterns of specimen SM 1.5.

a) Top face

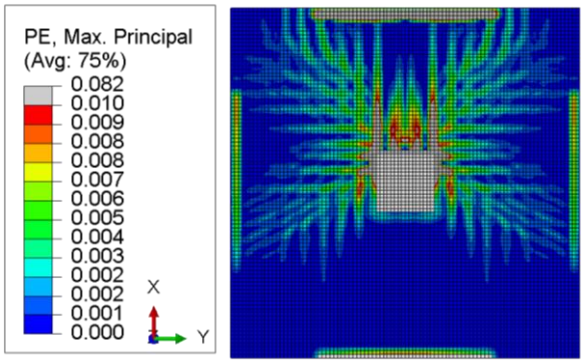

b) Bottom face

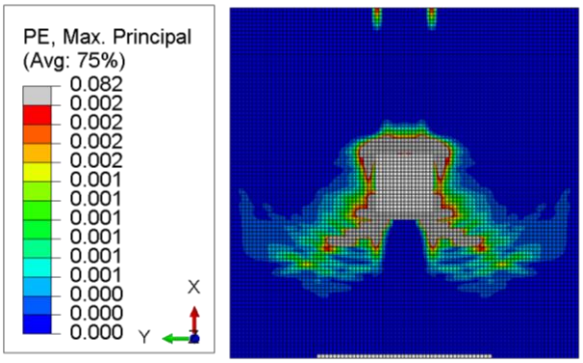

Figure 6.13: Specimen SM 1.0 FE analyses crack patterns

The specimen SM 1.5 experiment and FEA crack patterns are presented in Figure 6.14. On the top face, the tangential cracks around the –y, +x, and +y column faces was reproduced by the finite element analysis. Furthermore, the radial cracks propagating from the column toward the slab supports were reproduced by the FEA. On the bottom face, the FEA reproduced crack concentrations observed during laboratory testing.

a) Top face, experiment

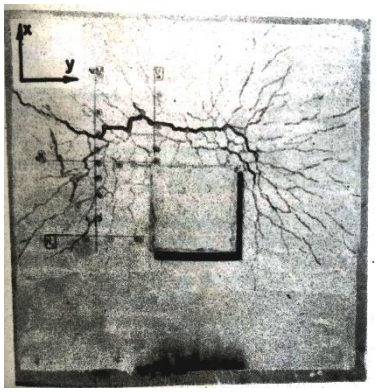

b) Bottom face, experiment

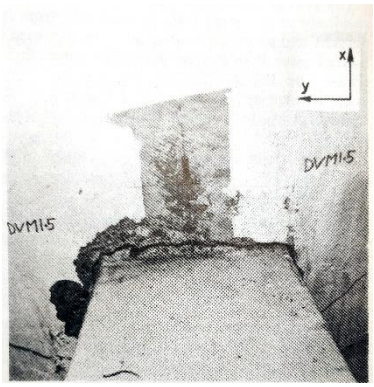

c) Top face, FE analysis

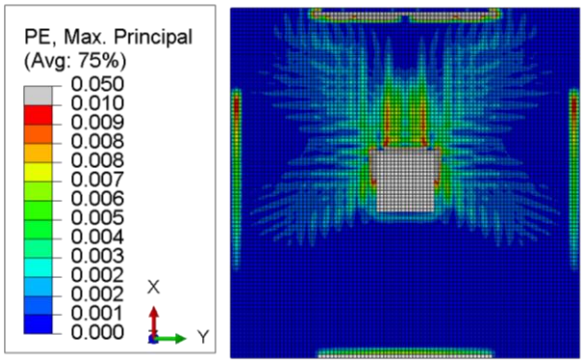

d) Bottom face, FE analysis

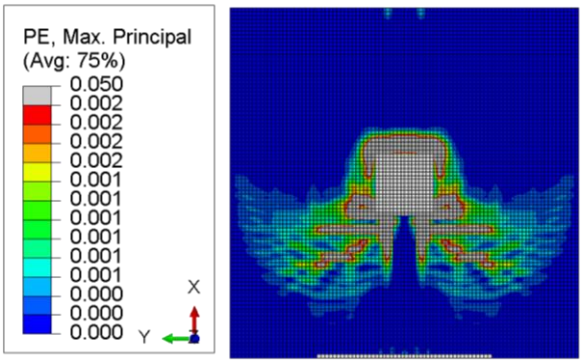

Figure 6.14: Specimen SM 1.5 experiment (Ghali et al., 1976) and FE analyses crack patterns. Authorized reprint of experiment photographs from ACI Journal, Volume 73, Issue 10, October 1976.

6.2 Specimens XXX and HXXX by El-Salakawy (1998)

Specimens XXX and HXXX were edge slab-column sub-assemblages tested by El-Salakawy (1998) at the University of Waterloo. Each specimen was subjected to a vertical load and unbalanced moment applied simultaneously through the column. The moments were applied about the axis parallel to the free edge. Both specimens were identical to one another except for the ratio between the moment and vertical load ($e = M/V$). The moment-to-shear ratio was 0.30-meters and 0.66-meters for specimens XXX and HXXX, respectively. For both specimens,

the vertical loads were applied at a rate of 1.5 kN per minute (kN/min). The lateral loads were applied at a rate of 0.34 kN/min and 0.75 kN/min for specimens XXX and HXXX, respectively.

For both specimens, the slab dimension parallel to the free edge was 1540 mm. The slab dimension orthogonal to the free edge was 1020 mm. The slabs were 120 mm thick with a cover of 20 mm. The tension reinforcement mats were reinforced with 10M deformed bars with a reinforcement ratio of 0.75-percent in both directions. The compression reinforcement mats were reinforced with 5M bars with a reinforcement ratio of 0.45-percent in both directions. The slabs did not contain any transverse reinforcement.

A 250 mm by 250 mm square column was centered at the midpoint of the free edge with its free column face flush with the slab edge. The columns of each specimen were reinforced with 25M longitudinal bars with a gross reinforcement ratio of 4.8-percent. Plain bars with a diameter of 8 mm were used as ties and were placed at a distance of 115 mm center-to-center. The distance between the two column ends was 1320 mm.

Three of the slab edges were simply supported on steel I-beams. Steel bearing pads and neoprene strips were placed between the I-beams and the slabs. The steel bearing pads and neoprene strips were 25 mm and 3 mm thick, respectively, and both were 40 mm wide. The corners of the slab were restrained from lifting using built-up steel sections.

The compressive strengths of XXX and HXXX were 33.0 MPa and 36.5 MPa, respectively. The tensile strengths of XXX and HXXX were 3.38 MPa and 3.36 MPa, respectively. The yield stresses of the 5M and 10M bars were 430 MPa and 476 MPa, respectively.

6.2.1 Boundary conditions

The boundary conditions used for the analyses of specimens XXX and HXXX are presented in Figure 6.15. At the plane of symmetry, rotation about the y and z axes were restrained and displacement in the x-direction was restrained. The center of the concrete at the free edge was restrained from translating in the y-direction to prevent any lateral movement of the concrete. The full length of each slab edge was restrained from translating in the z-direction. A pressure equivalent to force F_z was applied at the top face of the top column stub with a linear ramp. Simultaneously, a force-couple moment $F_y l$ was applied through two equal and opposite forces F_y toward the top and bottom ends of the column stubs with a linear ramp. The lever arm l was

equal to 1320 mm. The magnitudes of forces F_z and F_y were selected arbitrarily while maintaining the $e = F_y l/F_z$ ratios of the experiments.

Magnitude of forces for each specimen

Specimen	F_z	$F_y l$	$F_y l/F_z$
XXX	150 kN	45 kNm	0.30 m
HXXX	150 kN	99 kNm	0.66 m

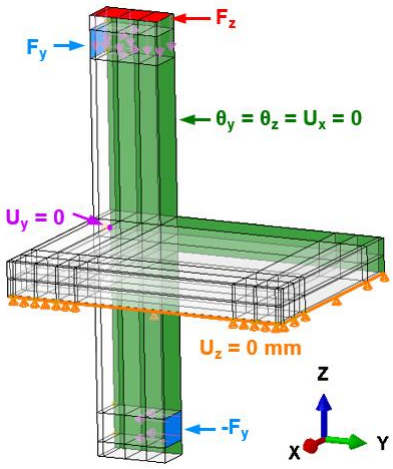

Figure 6.15: Boundary conditions used for FE analyses of specimens XXX and HXXX

6.2.2 Concrete properties

The concrete mesh used for the FE analyses of specimens XXX and HXXX is shown in Figure 6.16. The concrete slab and column were meshed with C3D8R continuum elements with an element size of 20 mm.

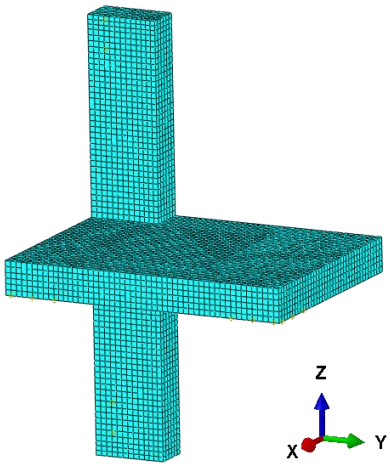

Figure 6.16: Concrete mesh used for FE analyses of specimens XXX and HXXX

The concrete compression and tension stress-strain data are presented in Figure 6.17 and Figure 6.18, respectively.

Linear-elastic data

Specimen	E_c (MPa)	ε_{co}	σ_{co} (MPa)
XXX	16,056	0.0008	13.20
HXXX	16,886	0.0009	14.60

Plastic data

Specimen	E_t (MPa)	ε_o	f_c' (MPa)
XXX	18,095	0.0036	33.00
HXXX	19,031	0.0038	36.50

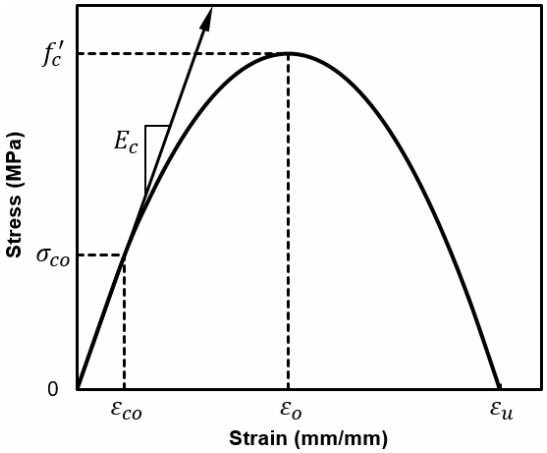

Figure 6.17: Compression stress-strain data used for FEA of specimens XXX and HXXX

Linear-elastic data

Specimen	E_c (MPa)	ε_{cr}	f_t' (MPa)
XXX	16,056	0.0002	3.38
HXXX	16,886	0.0002	3.36

Plastic data

Specimen	G_f (N/mm)	ε_1	ε_u
XXX	0.136	0.0018	0.0074
HXXX	0.138	0.0018	0.0075

Note: Element length l_c is equal to 20.22 mm

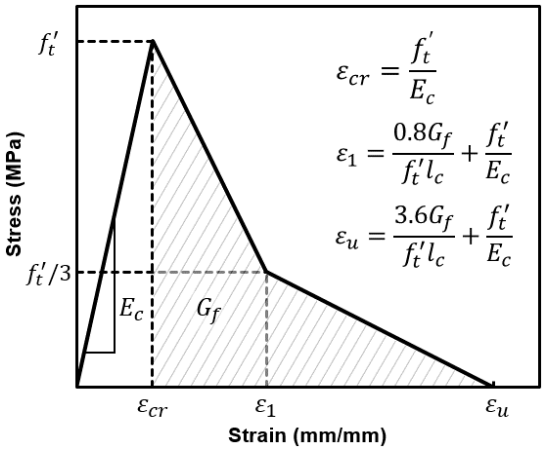

Figure 6.18: Tension stress-strain data used for FEA of specimens XXX and HXXX

The concrete material assignments used for specimens XXX and HXXX are shown in Figure 6.19. For each specimen, the column E_c values were ten times those presented in Figure 6.17.

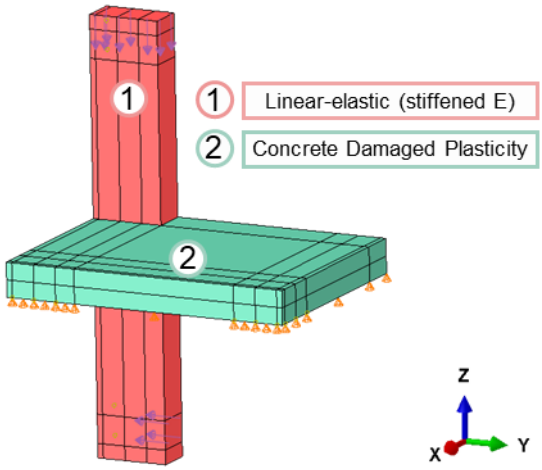

Figure 6.19: Concrete material assignments for FE analyses of specimens XXX and HXXX

6.2.3 Reinforcement properties

All steel reinforcement was meshed using T3D2 truss elements with an element size of 20 mm. The compression and tension reinforcement properties are presented in Table 6.3 and Table 6.4, respectively. The column longitudinal reinforcement properties are presented in Table 6.5. The column stirrups were 8M bars with an area equal to 50 mm^2 spaced at 115 mm center-to-center.

Table 6.3: Compression reinforcement properties for FEA of specimens XXX and HXXX

	x-direction			y-direction		
Specimen	Depth	Spacing (from free edge)	Area	Depth	Spacing (from centerline)	Area
XXX HXXX	31 mm	1-10M at 60 mm, 1-10M at 20 mm, 6-5M at 135 mm	5M: 38 mm^2 10M: 100 mm^2	43 mm	1-10M at 65 mm, 5-5M at 135 mm	5M: 38 mm^2 10M: 100 mm^2

Table 6.4: Tension reinforcement properties for FEA of specimens XXX and HXXX

	x-direction			y-direction		
Specimen	Depth	Spacing (from free edge)	Area	Depth	Spacing (from centerline)	Area
XXX HXXX	91 mm	1-10M at 30 mm, 1-10M at 190 mm, 5-10M at 154 mm	100 mm^2	98 mm	1-10M at 60 mm, 2-10M at 120 mm, 2-10M at 220 mm	100 mm^2

Table 6.5: Column reinforcement properties for FEA of specimens XXX and HXXX

	x-direction		y-direction	
Specimen	Spacing	Area	Spacing	Area (mm^2)
XXX HXXX	3-25M at 105 mm	490 mm^2	2-25M at 210 mm	490 mm^2

The true stress-strain data for the 5M steel reinforcement is shown in Figure 6.20.

Linear-elastic data	
Poisson's ratio	Modulus of elasticity
0.3	180,000 MPa

Plastic data		
	Strain (mm/mm)	Stress (MPa)
Yield	0.0024	430
Rupture	0.1389	724

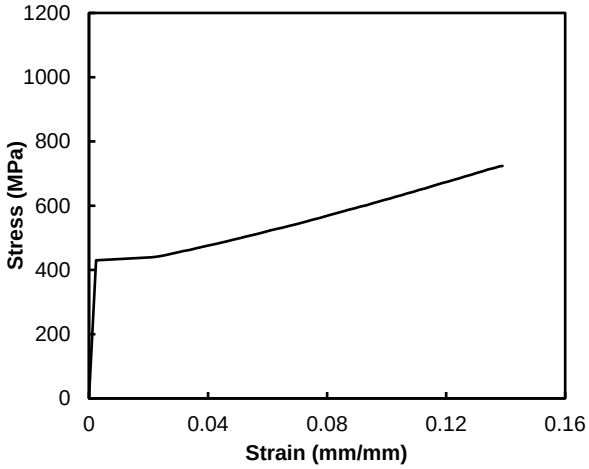

Figure 6.20: 5M reinforcement stress-strain data used for specimens XXX and HXXX FE analyses

The true stress-strain data for the 10M steel reinforcement is shown in Figure 6.21.

Linear-elastic data	
Poisson's ratio	Modulus of elasticity
0.3	195,000 MPa

Plastic data		
	Strain (mm/mm)	Stress (MPa)
Yield	0.0026	476
Rupture	0.0945	989

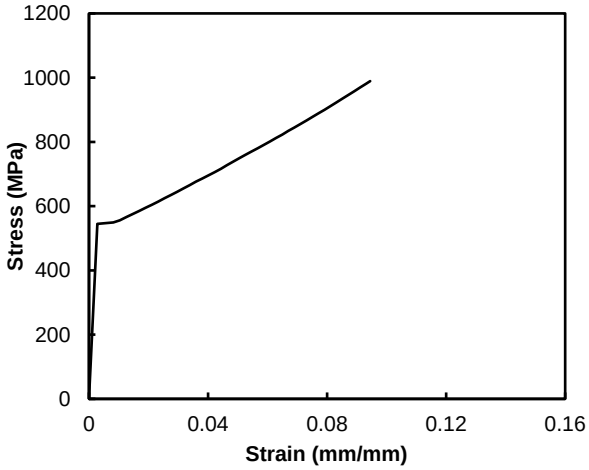

Figure 6.21: 10M reinforcement stress-strain data used for specimens XXX and HXXX FE analyses

6.2.4 Moment versus rotation results

The FEA and experiment moment versus rotation results for specimen XXX and HXXX are presented in Figure 6.22. The FEA accurately reproduced the slope of moment-rotation data for specimens XXX and HXXX for moments up to 21.5 kNm and 18.1 kNm, respectively. For larger applied moments, both analyses predicted moment-rotation data with shallower slopes than respective experimental data. As such, both FE analyses under-predicted the ultimate moments of their respective experiments. For specimen XXX, the ultimate moment of the FEA and the experiment were 31.6 kNm and 38.0 kNm, respectively. For specimen HXXX, the ultimate moment of the FEA and the experiment were 38.4 kNm and 50.7 kNm, respectively.

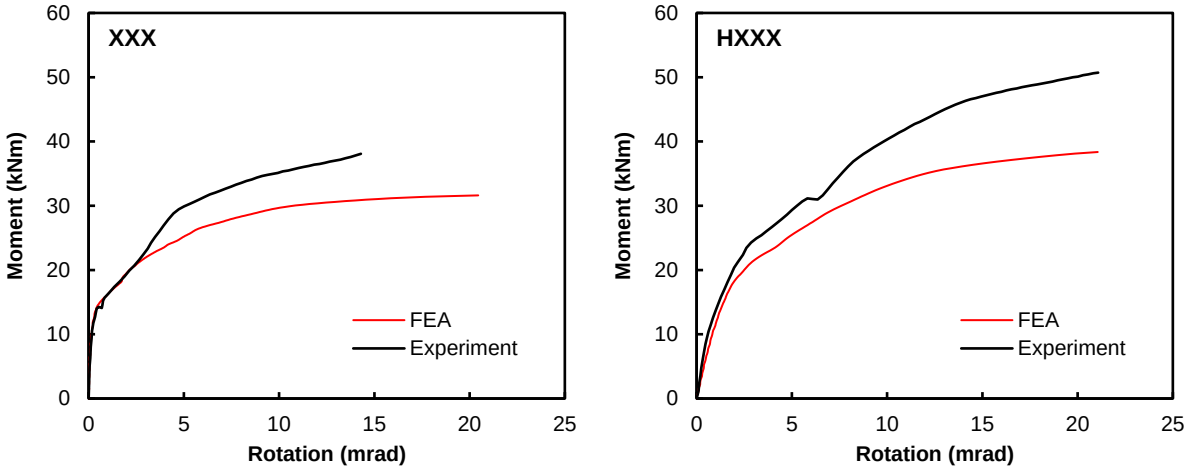

Figure 6.22: Moment versus rotation results for specimens XXX and HXXX

6.2.5 Vertical load versus displacement results

The FEA and experiment vertical load versus vertical load results for specimen XXX and HXXX are presented in Figure 6.23. For specimen XXX, the FEA accurately reproduced the load-displacement data of the experiment with respect to the slope of the data and ultimate vertical displacement. The ultimate moment of the specimen XXX FE analysis and experiment were 103.7 kNm and 125.0 kNm, respectively. For specimen HXXX, the FE analysis accurately reproduced the slope of the load-displacement of the experiment. The ultimate moment of the specimen HXXX FE analysis and experiment were 58.5 kNm and 70.0 kNm, respectively.

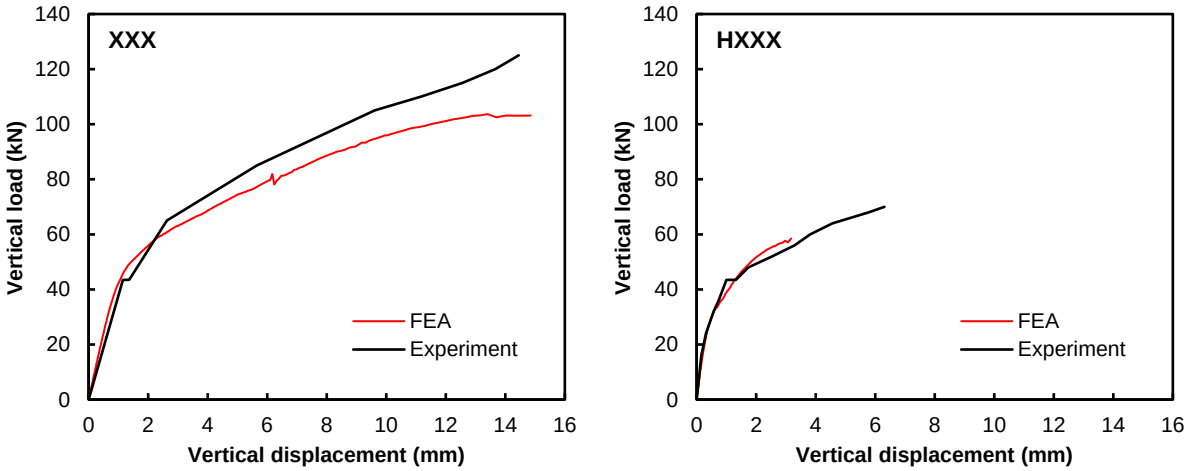

Figure 6.23: Load versus displacement results for specimens XXX and HXXX

6.2.6 Crack patterns

The top view of the specimen XXX crack patterns for the experiment and the FEA are presented in Figure 6.24. The FEA accurately reproduced experiment cracks that formed from the inner column face toward the inner slab corners. Furthermore, the FEA reproduced the cracks which were tangential to the column faces in the vicinity of the column.

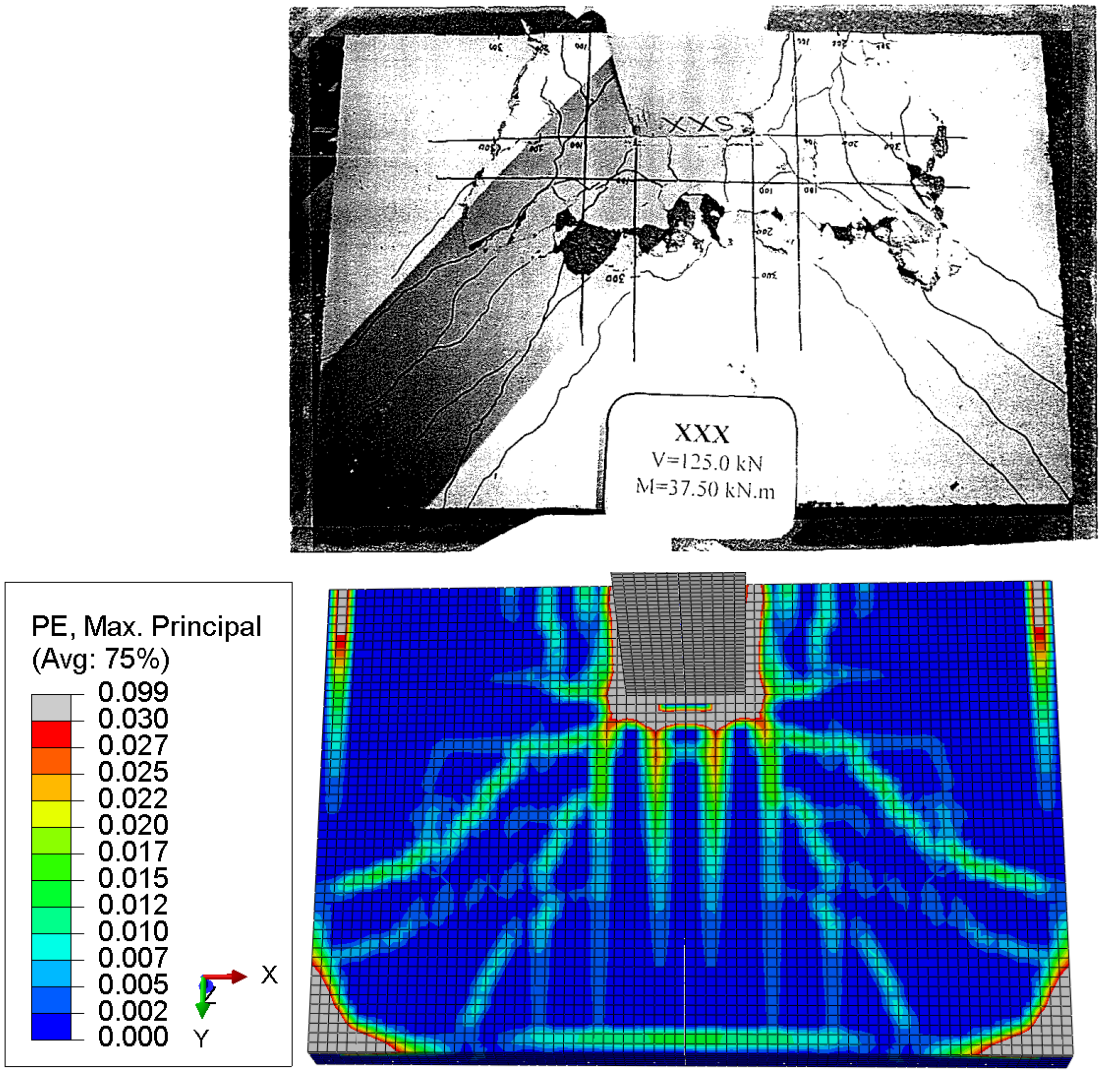

Figure 6.24: Top view of specimen XXX experiment (El-Salakawy, 1998) and FEA crack patterns. Photograph reprinted from *Shear behaviour of reinforced concrete flat slab-column edge connections with openings* (p.115), by E. El-Salakawy, 1998. Reprinted with permission.

The perspective view of specimen XXX crack patterns for the experiment and the FEA are presented in Figure 6.25. Although the quality of the experiment crack patterns photograph is low, the photograph shows diagonal cracking along the compression slab face at the inner slab corners. These cracks were adequately reproduced by the analysis.

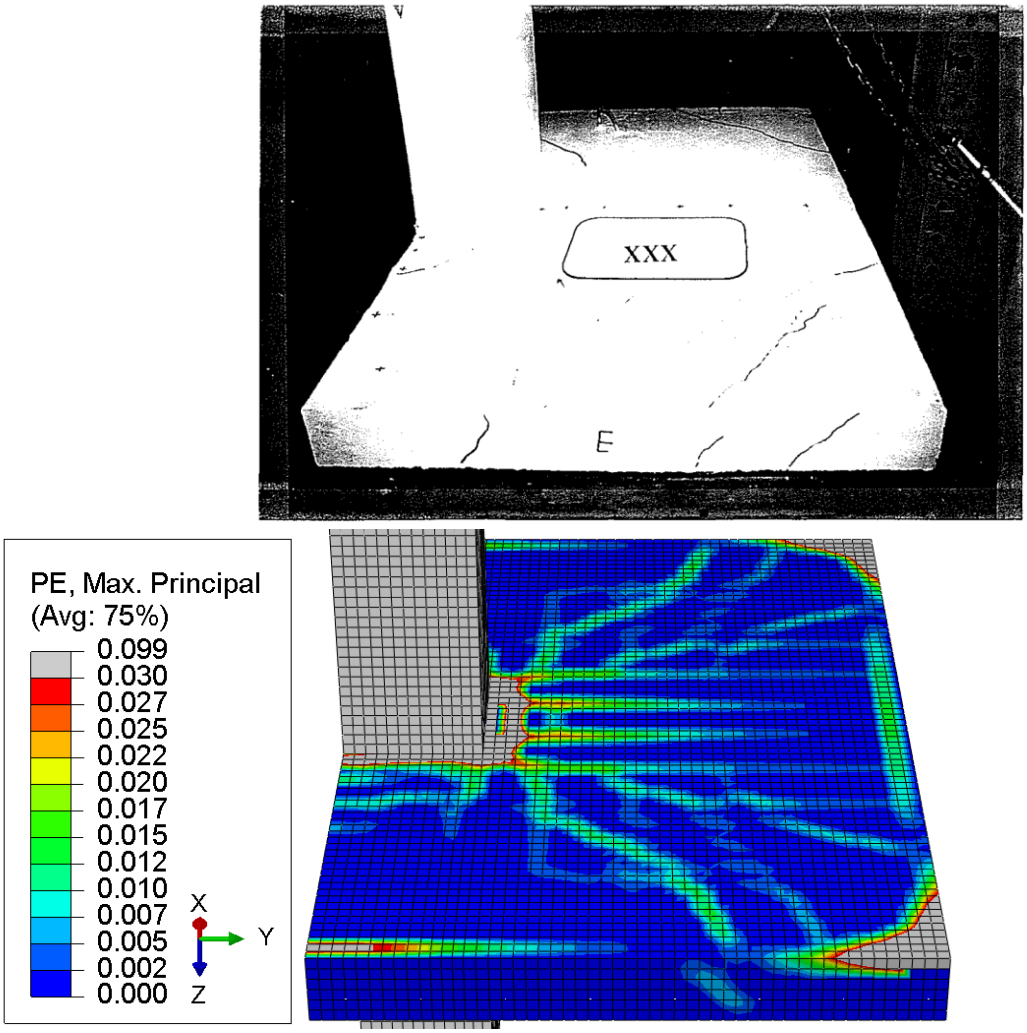

Figure 6.25: Perspective view of specimen XXX experiment (El-Salakawy, 1998) and FEA crack patterns. Photograph reprinted from *Shear behaviour of reinforced concrete flat slab-column edge connections with openings* (p.122), by E. El-Salakawy, 1998. Reprinted with permission.

The perspective view of specimen HXXX crack patterns for the experiment and the FEA are presented in Figure 6.26. The FEA accurately reproduced the tangential cracks near the column that were present in the experiment photograph. Furthermore, the FEA accurately reproduced the cracks from the inner column face toward the inner slab corners as well as the cracks from the inner column face toward the inner slab edge.

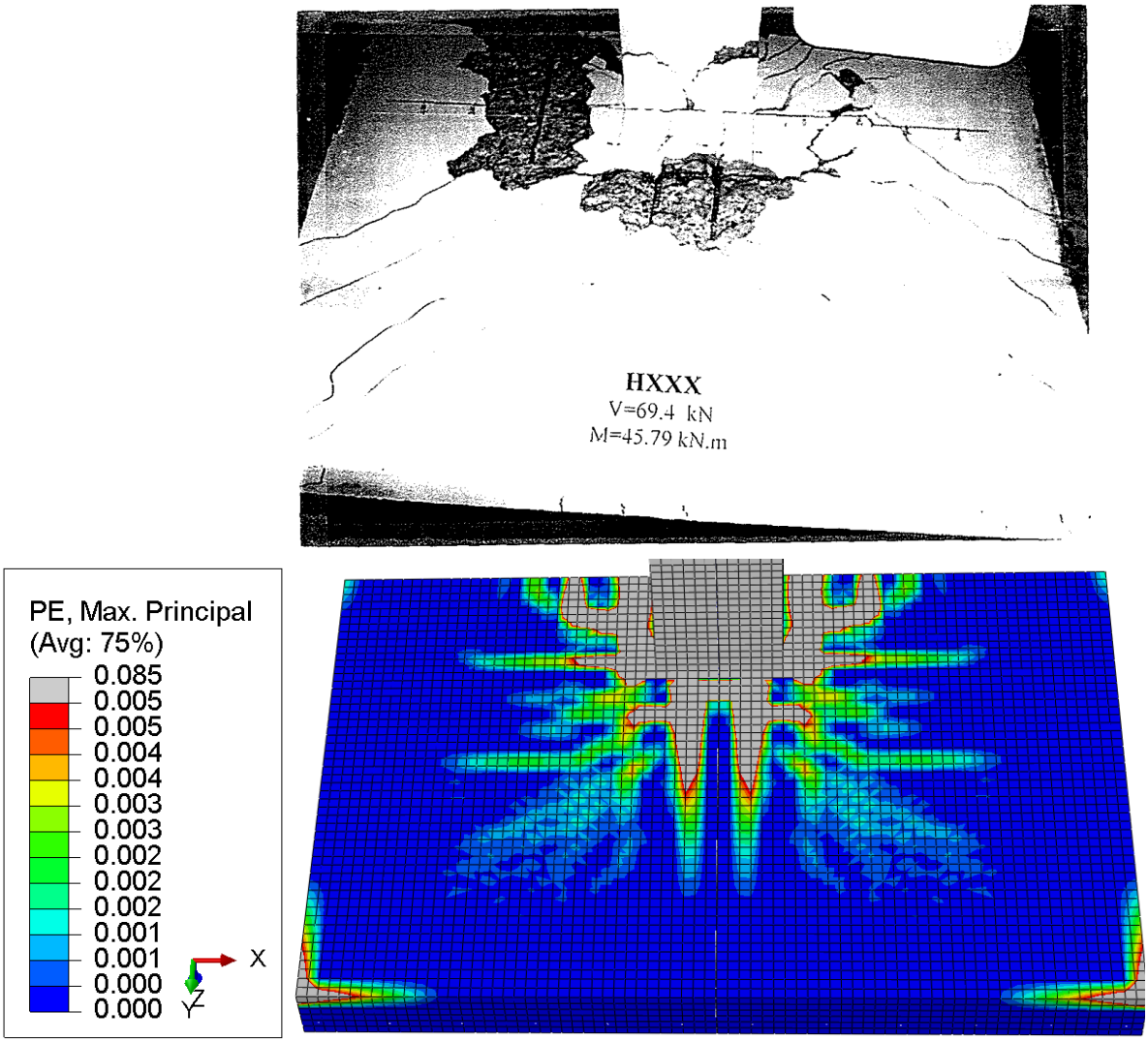

Figure 6.26: Perspective view of specimen HXXX experiment (El-Salakawy, 1998) and FEA crack patterns. Photograph reprinted from *Shear behaviour of reinforced concrete flat slab-column edge connections with openings* (p.143), by E. El-Salakawy, 1998. Reprinted with permission.

The column view of specimen HXXX crack patterns for the experiment and FEA are presented in Figure 6.27. The FEA reproduced the diagonal cracks that started at the slab-column interface of the tension face and continued away from the column toward the compression face.

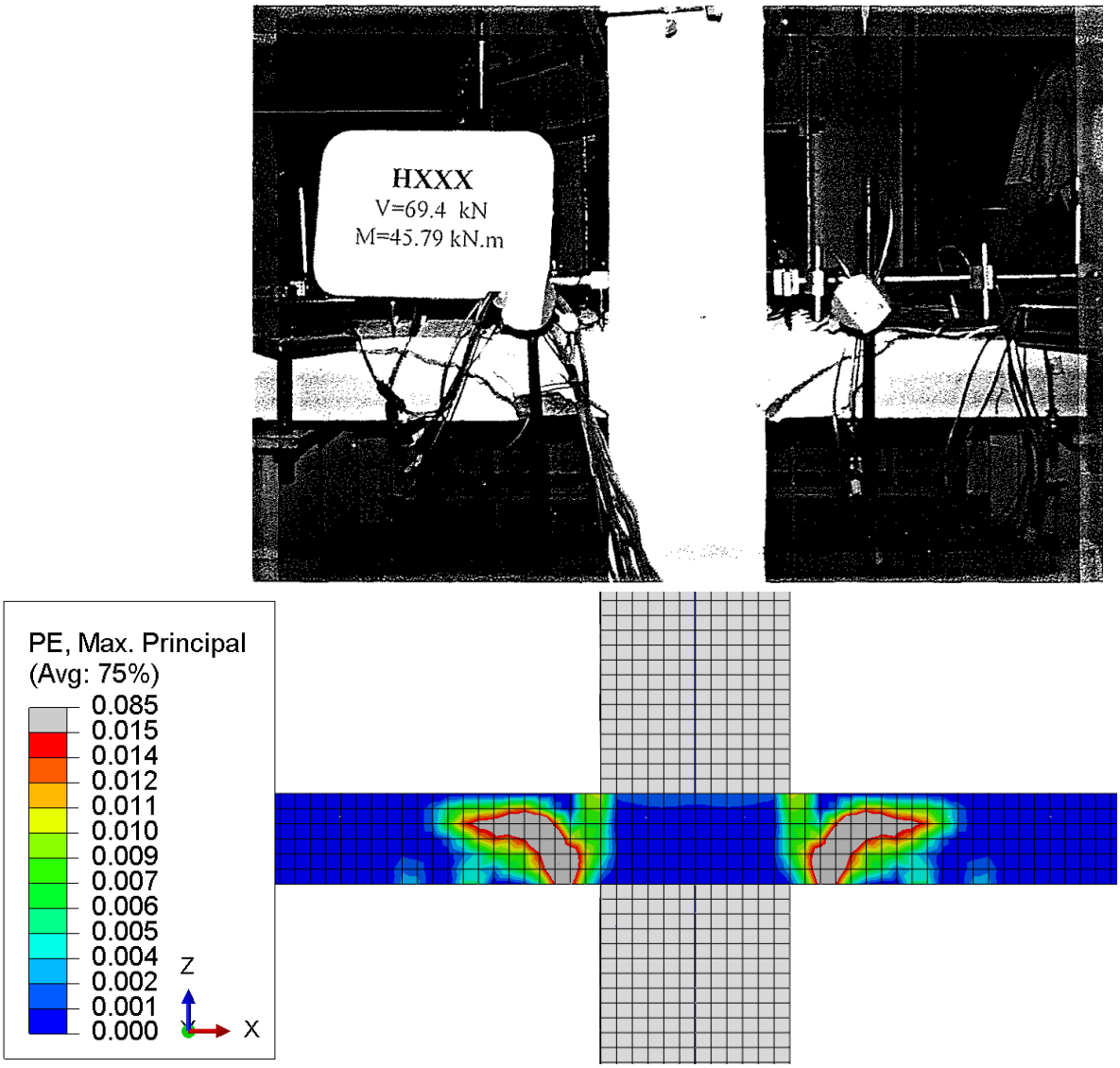

Figure 6.27: Column view of specimen HXXX experiment (El-Salakawy, 1998) and FEA crack patterns. Photograph reprinted from *Shear behaviour of reinforced concrete flat slab-column edge connections with openings* (p.146), by E. El-Salakawy, 1998. Reprinted with permission.

6.3 Specimen SB1 by Adetifa (2003)

Specimen SB1 was a interior slab-column sub-assemblage tested by Adetifa (2003) at the University of Waterloo. A linearly increasing concentric axial load was applied through the specimen column until failure. The rate of loading was 4 kN/min up to 70-percent of the anticipated ultimate load then 2 kN/min until failure.

Specimen SB1 had a square slab with dimensions of 1800 mm by 1800 mm. The slab was 120 mm thick with a cover of 20 mm. The tension reinforcement mats were reinforced with 10M deformed bars with a reinforcement ratio of 1.2-percent in both directions. The compression reinforcement mats were reinforced with 10M bars with a reinforcement ratio of 0.6-percent in both directions. The slab did not contain any transverse reinforcement.

Specimen SB1 had a square column with dimensions of 150 mm by 150 mm. The column was reinforced with four 20M bars with 8 mm ties placed at a distance of 100 mm center-to-center. The distance between the two column ends was 420 mm.

The edges of the slabs represented the lines of contraflexure within a flat plate system when subjected to uniform gravity loading. The slab edges were simply supported on long flat solid bars with a width of 40 mm width and a thickness of 25 mm. These bars formed a 1500 mm by 1500 mm square. This meant that there was a slab overhang of 150 mm on each of the four sides. Neoprene strips were placed between the steel bars and the slab.

The compressive and tension strengths of the slab were 44 MPa and 2.2 MPa, respectively. The yield stress of the flexural reinforcement was 455 MPa.

6.3.1 Boundary conditions

The boundary conditions used for the FE analysis of specimen SB1 is presented in Figure 6.28. At the plane of symmetry, rotation about the y and z axes were restrained and displacement in the x-direction was restrained. The center of the concrete geometry at the free edge was restrained from translating in the y-direction to prevent any lateral movement of the concrete. The full length of each slab edge was restrained from translating in the z-direction. A pressure equivalent to 250 kN was applied at the top face of the top column stub with a linear ramp. The slab dimension was 1500 mm by 1500 mm and the column dimension was 150 mm by 150 mm. The column stub extended 150 mm from each slab face.

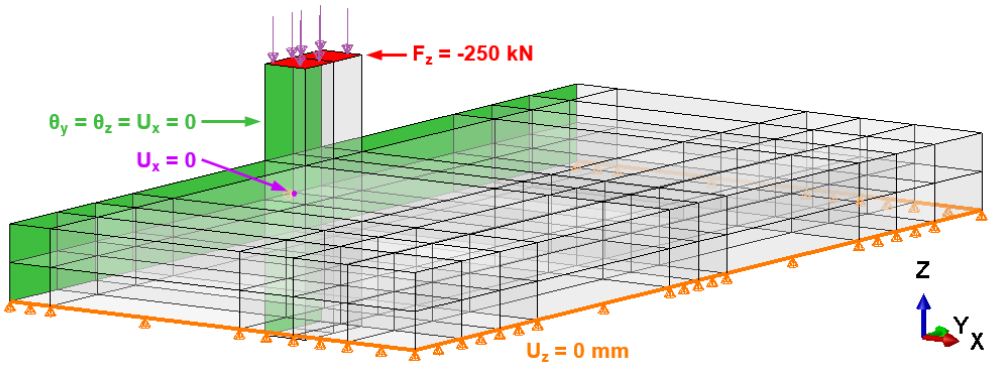

Figure 6.28: Boundary conditions used for FE analysis of specimen SB1

6.3.2 Concrete properties

The concrete mesh used for the FE analysis of specimen SB1 is shown in Figure 6.29. The concrete slab and column were meshed with C3D8R continuum elements with an element size of 20 mm.

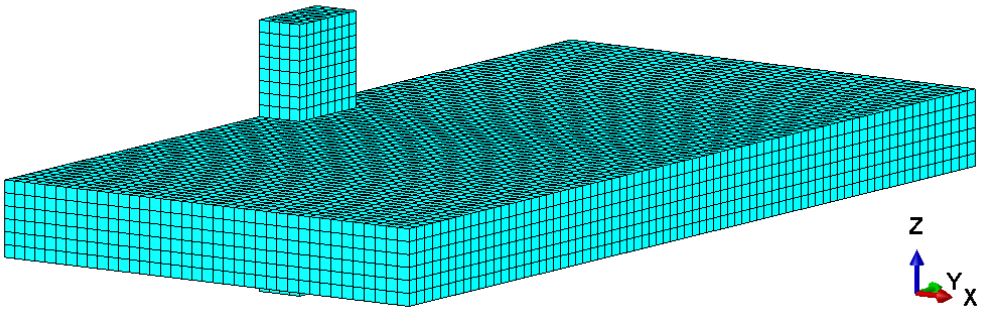

Figure 6.29: Concrete mesh used for FE analysis of specimen SB1

The concrete compression and tension stress-strain data are presented in Figure 6.30 and Figure 6.31, respectively.

Linear-elastic data

Specimen	E_c (MPa)	ε_{co}	σ_{co} (MPa)
SB1	18,561	0.0010	17.64

Plastic data

Specimen	E_t (MPa)	ε_o	f_c' (MPa)
SB1	20,918	0.0042	44.10

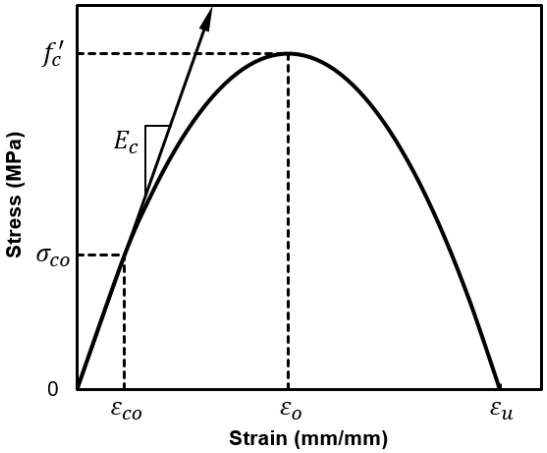

Figure 6.30: Compression stress-strain data used for FE analysis of specimen SB1

Linear-elastic data

Specimen	E_c (MPa)	ε_{cr}	f_t' (MPa)
SB1	18,561	0.0001	2.19

Plastic data

Specimen	G_f (N/mm)	ε_1	ε_u
SB1	0.143	0.0028	0.0122

Note: Element length l_c is equal to 19.44 mm

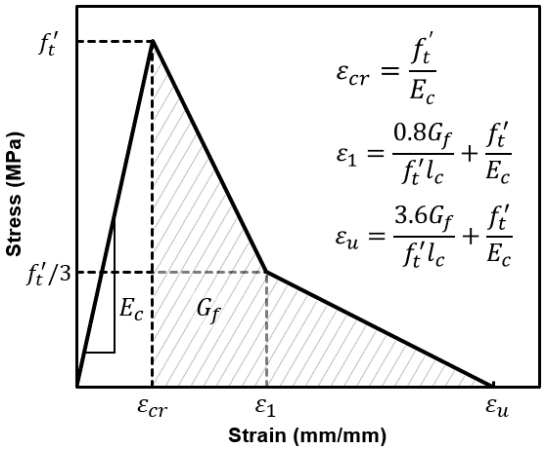

Figure 6.31: Tension stress-strain data used for FE analysis of specimen SB1

The concrete material assignments used for the FE analysis of specimen SB1 are shown in Figure 6.32. The column modulus of elasticity E_c was ten times the value presented in Figure 6.30.

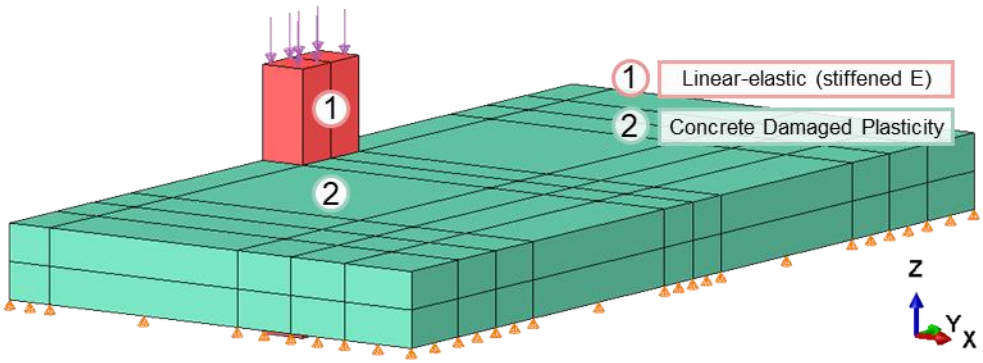

Figure 6.32: Concrete material assignments for FE analysis of specimen SB1

6.3.3 Reinforcement properties

All steel reinforcement was meshed using T3D2 truss elements with an element size of 20 mm. The compression and tension reinforcement properties are presented in Table 6.6 and Table 6.7, respectively. The column longitudinal reinforcement properties are presented in Table 6.8. The column stirrups were 5M bars with an area equal to 50 mm^2 spaced at 100 mm center-to-center.

Table 6.6: Compression reinforcement properties for FE analysis of specimen SB1

	x-direction			y-direction		
Specimen	Depth	Spacing (from centerline)	Area	Depth	Spacing (from centerline)	Area
SB1	24 mm	1-10M at 25 mm, 3-10M at 200 mm	100 mm^2	24 mm	1-10M at 25 mm, 3-10M at 200 mm	100 mm^2

Table 6.7: Tension reinforcement properties for FE analysis of specimen SB1

	x-direction			y-direction		
Specimen	Depth	Spacing (from centerline)	Area	Depth	Spacing (from centerline)	Area
SB1	90 mm	1-10M at 25 mm, 8-10M at 93 mm	100 mm^2	90 mm	1-10M at 25 mm, 8-10M at 93 mm	100 mm^2

Table 6.8: Column reinforcement properties for FE analysis of specimen SB1

	x-direction		y-direction	
Specimen	Spacing	Area	Spacing	Area (mm^2)
SB1	2-20M at 100 mm	300 mm^2	2-20M at 100 mm	300 mm^2

The true stress-strain data for the steel reinforcement is shown in Figure 6.33.

Linear-elastic data

Poisson's ratio	Modulus of elasticity
0.3	200,000 MPa

Plastic data

	Strain (mm/mm)	Stress (MPa)
Yield	0.0023	455
Ultimate	0.1777	767
Rupture	0.2358	612

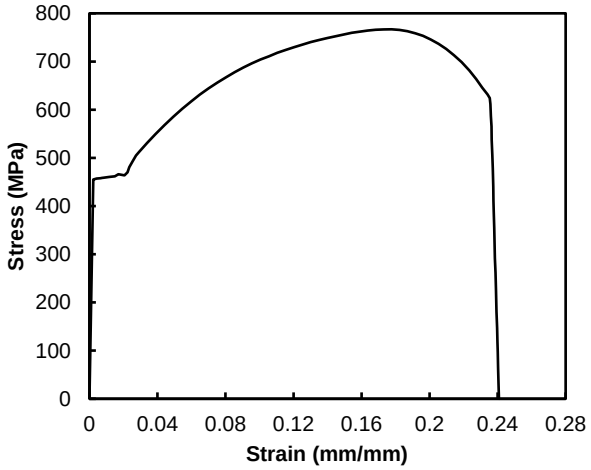

Figure 6.33: Reinforcement stress-strain data used for specimen SB1 analysis

6.3.4 Vertical load versus displacement results

The vertical load versus vertical displacement results for the experiment and the FE analysis are presented in Figure 6.34. The load-displacement data produced by the analysis was steeper than

that of the experiment for vertical loads up to 120 kN. Past 120 kN, the slope of the FE analysis load-displacement data was similar to the experiment data. The ultimate vertical loads for the analysis and the experiment were 226.3 kN and 250.4 kN, respectively.

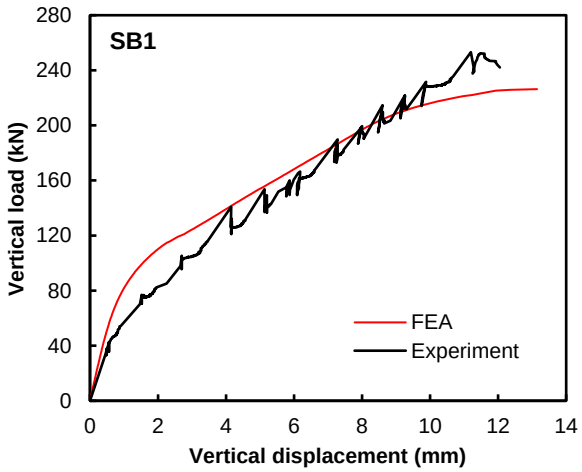

Figure 6.34: Specimen SB1 vertical load versus vertical displacement results

6.3.5 Crack patterns

The tension-side view of the specimen SB1 experiment and FEA crack patterns are presented in Figure 6.35. The FEA accurately reproduced the tangential cracks that formed midway between the column and the slab edge. Furthermore, the FEA reproduced the radial cracks that formed from the column toward the slab corners.

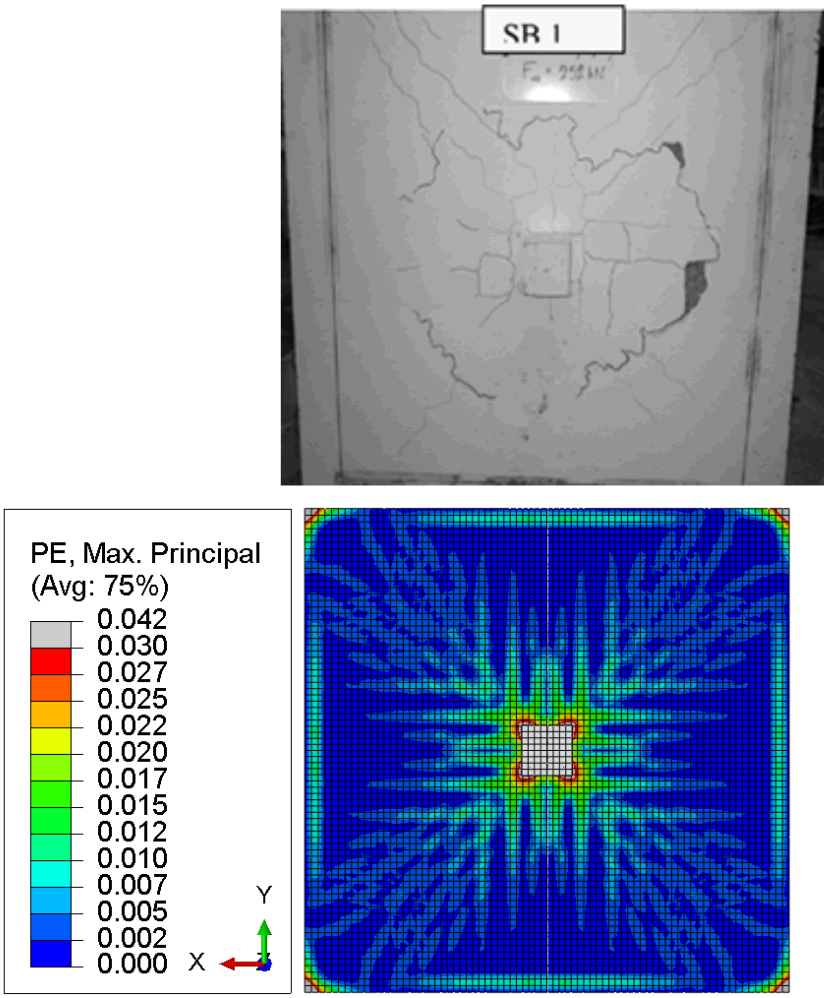

Figure 6.35: Tension-side view of specimen SB1 experiment (Adetifa & Polak, 2005) and FEA crack patterns. Authorized reprint of experiment photograph from ACI Structural Journal, Volume 102, Issue 2, March-April 2005.

Chapter 7: Parametric study using numerical modelling

Using the calibrated FE analyses of the SM specimens, a parametric study was conducted to study the effects of moment-to-shear-force ratios on load capacities and slab stress distributions at a critical perimeter $d/2$ from the column. This critical perimeter was selected because it is used by ACI 318-19, CSA A23.3-19, and *fib* Model Code 2010.

In the laboratory tests conducted by Ghali et al. (1976), the SM specimens were first subjected to a vertical load of 129 kN. The vertical load remained constant while an increasing moment was applied until failure. To conduct the parametric study, the vertical load within the calibrated FE models was modified and the models were reanalysed. Between FE analyses of each specimen, the magnitude of the vertical load varied between 0 kN (i.e. only a moment was applied) and infinite (i.e. only a vertical load was applied).

Moment versus rotation data and observations are presented in Section 7.1. Similarly, moment versus vertical load data is studied in Section 7.2. Vertical load versus eccentricity results are compared to observations by Regan (1981). Then, a moment-shear interaction diagram is presented in Section 7.4.

In Chapter 8, slab stress distributions at a critical perimeter $d/2$ are studied and compared to the linear shear distribution model used by ACI 318-19 and CSA A23.3-19.

7.1 Moment versus rotation results

Figure 7.1 shows the moment versus rotation results for specimen SM 0.5 subjected to constant vertical loads between 20 kN and 240 kN then increasing moments until failure. As the vertical load was increased between FE analyses, the ultimate moment and column rotation at ultimate moment decreased almost linearly. Similarly, increasing the vertical load resulted in lower moment-rotation stiffness. This was because higher vertical loads caused an increased number of elements to fail in tension in the vertical load step prior to the start of the moment step.

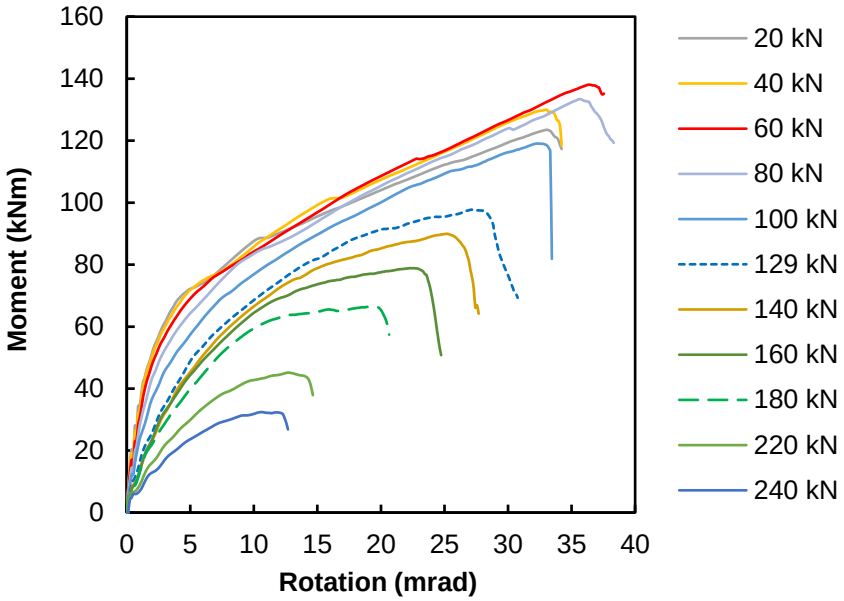

Figure 7.1: Moment-rotation results for specimen SM 0.5 subjected to varying vertical loads

Each SM 0.5 FE analysis with a vertical load of 129 kN or greater had moment-rotation data that plateaued as the analysis approached its ultimate moment. This behaviour is characteristic to slab-column connections that fail due to tension flexural reinforcement yielding. In these types of failures, the reinforcement closest to the column centerline yields. This is followed by yielding of adjacent reinforcement. This pattern continues in which adjacent bars further from the column yield until the slab-column connection ultimately fails in punching. FE analyses in which tension flexural reinforcement yielded showed concentrations of plastic strains and larger vertical column displacements as shown in Figure 7.2.

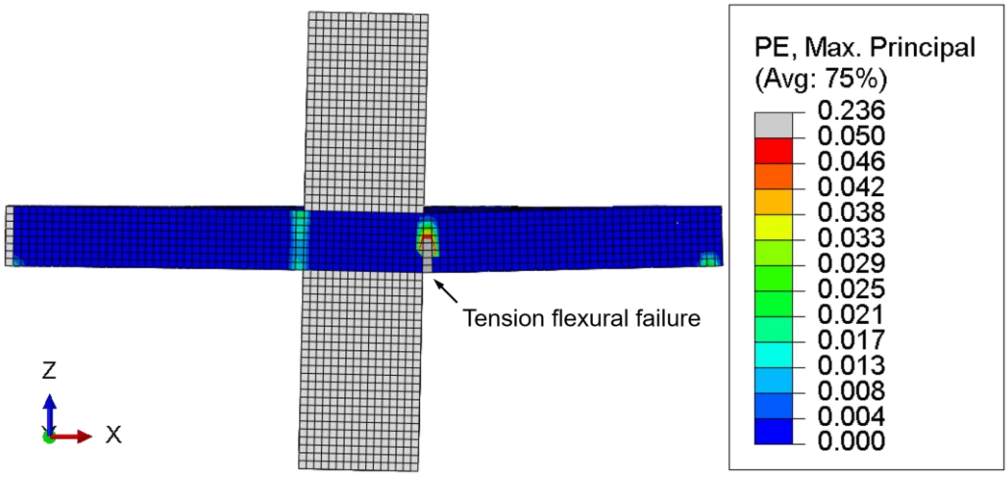

Figure 7.2: Typical tension flexural failure among SM 0.5 FE analyses under larger vertical loads (160 kN analysis shown)

FE analyses with vertical loads lower than 129 kN had kinks along each analyses moment-rotation curve. At each of these kinks, compression flexural reinforcing bars yielded due to excessive tensile stresses. These stresses were redistributed to adjacent reinforcing bars. This compression flexural failure is shown in Figure 7.3.

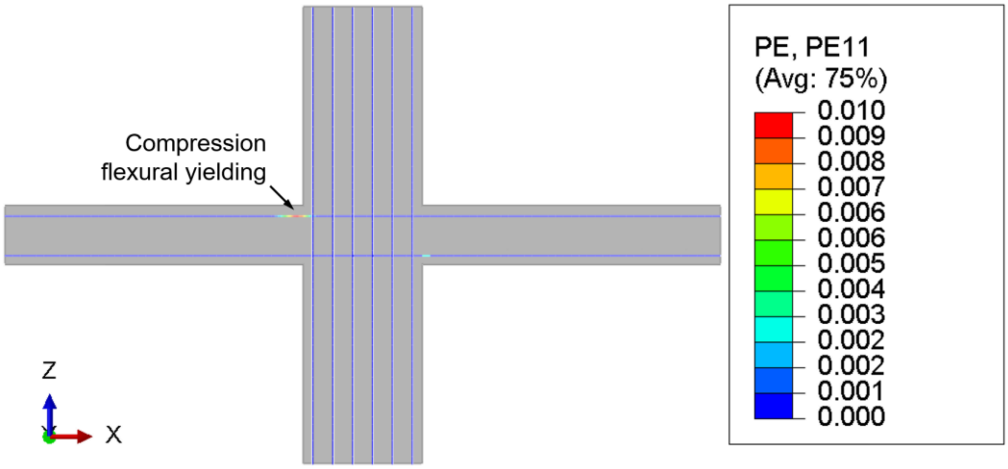

Figure 7.3: Typical compression flexural yielding among SM FE analyses under low vertical loads (60 kN analysis of SM 1.5 shown)

Figure 7.4 shows the moment versus rotation results for specimen SM 1.0 subjected to constant vertical loads between 60 kN and 360 kN then increasing moments until failure. Similar to the specimen SM 0.5 FE analyses, these FE analyses showed increasing moment capacities and rotations at ultimate moments with decreasing vertical loads. However, the moment-rotation data for each FE analysis was less ductile at fail than respective SM 0.5 FE analyses (i.e. moment-rotation data did not plateau prior to failure). Discontinuities associated with reinforcement yielding and stress redistribution was evident only in FE analyses with initial vertical loads of 129 kN or less. Even so, these redistributions occurred near each FE analyses ultimate moment. For each of these FE analyses, this suggests a partial yielding of the reinforcement mat rather the entire mat.

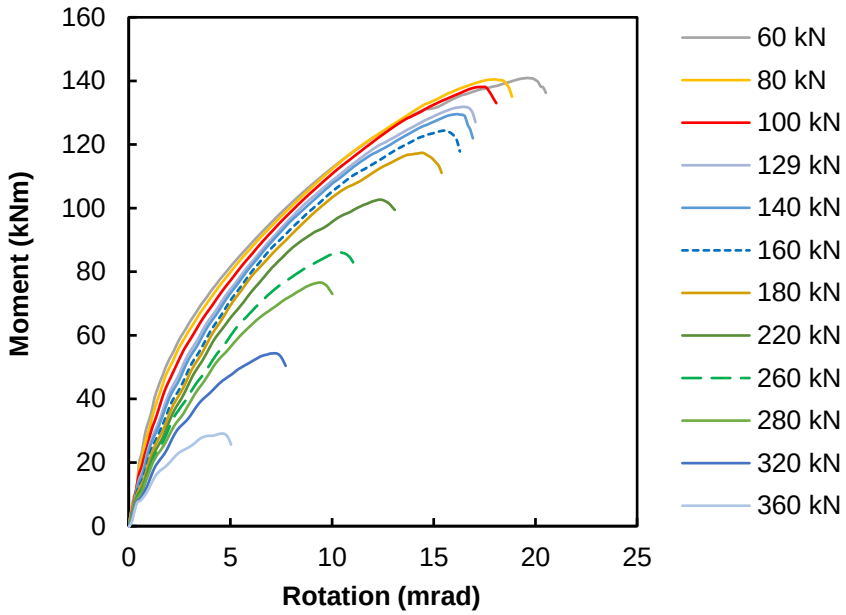

Figure 7.4: Moment-rotation results for specimen SM 1.0 subjected to varying vertical loads

Figure 7.5 shows the moment versus rotation results for specimen SM 1.5 subjected to constant vertical loads between 60 kN and 460 kN then increasing moments until failure. As observed among the FE analyses of the other SM specimens, the ultimate moment and accompanying rotation decreased almost linearly as the initial vertical load was increased. No tension flexural reinforcement yielded in any of these FE analyses. However, compression flexural reinforcement yielding was observed for specimens with initial vertical loads less than 129 kN.

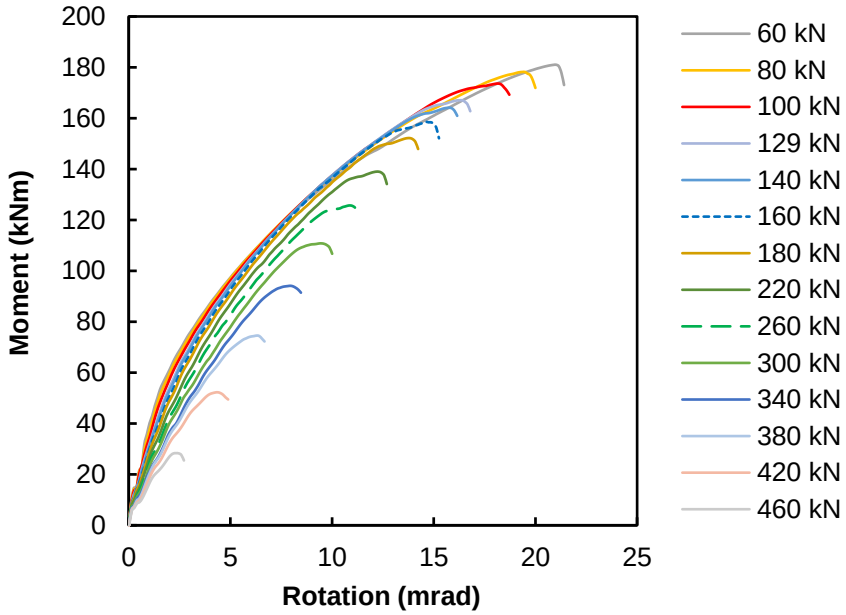

Figure 7.5: Moment-rotation results for specimen SM 1.5 subjected to varying vertical loads

7.2 Moment versus vertical load results

The combined moment versus vertical load results for specimens SM 0.5, SM 1.0, and SM 1.5 are shown in Figure 7.6.

As discussed in Section 7.1, partial yielding of the compression reinforcement mat was commonly observed for FE analyses with initial vertical loads less than 129 kN. FE analyses in which specimens were subjected to initial vertical loads less than 60 kN exhibited full yielding of their compression reinforcement mats. These compression flexural failures occurred prior to the development of the specimens respective punching shear capacities. For FE analyses with initial vertical loads less than 60 kN, the ultimate moment decreased as the initial vertical load was decreased.

Among the specimen SM 0.5 FE analyses, significant yielding of the tension flexural reinforcement occurred prior to punching. As a result, specimen SM 0.5 FE analyses results did not follow the data trends of FE analyses for specimens SM 1.0 and SM 1.5.

For predicting punching failure in following sections, only FE analyses that failed in punching were considered. All SM 0.5 FE analyses as well as SM 1.0 and SM 1.5 FE analyses with vertical loads less than 140 kN were not considered. The specimen SM 0.5 FE analyses failed due to tensile compression reinforcement yielding under lower vertical loads or due to tensile tension reinforcement yielding under higher vertical loads. It is unnecessary to predict the capacities of the SM 0.5 analyses since ACI 318-19 would not allow these flexure-driven failures to occur. ACI 318-19 requires a minimum reinforcement area within a slabs column strip to allow the slab-column connection to develop its full punching shear strength prior to failure. Similarly, the SM 1.0 and SM 1.5 FE analyses subjected to lower vertical loads failed due to compression reinforcement yielding prior to punching failure.

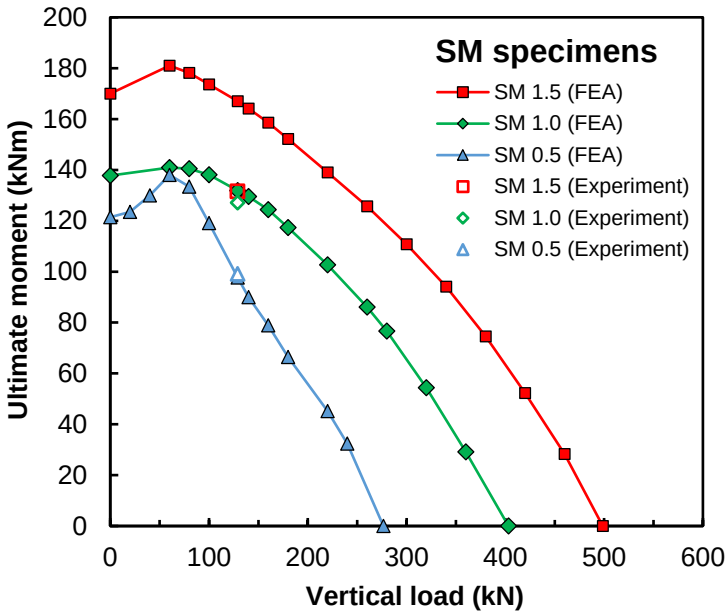

Figure 7.6: Moment versus vertical load results for SM specimens

7.3 Vertical load capacity versus eccentricity

The FEA moment versus vertical load results presented in Section 7.2 showed reduced moment capacities when specimens were subjected to low vertical loads. As discussed, the reduction in moment capacity is caused by compression reinforcement failure occurring prior to punching failure. It was stated that the FEA moment capacities for specimens subjected to low vertical loads are unrepresentative of connections with adequate compression reinforcement.

To verify the observed moment versus vertical load behaviours for large vertical loads, the FEA results are compared to a punching shear prediction equation developed by Regan (1981). Using experimental data, Regan developed an equation to predict the normalized vertical load capacity as a function of eccentricity, M/V. The normalized vertical load capacity is equal to the eccentric vertical load capacity, V, divided by the concentric vertical load capacity, V_o. More information about Regan's research is provided in Section 2.1.11.

The normalized vertical load capacities versus eccentricities for all SM specimens and Regan's predictions (as per Equation 2.36) are shown in Figure 7.7. As previously discussed, Regan stated that the constant 1.5 within his equation could be substituted with constants 1.0 or 2.0. These variations are also shown in Figure 7.7. For each SM specimen, the concentric vertical load capacity, V_o, was obtained from FEA.

Specimen SM 0.5 data did not correlate well with Regan's predictions. This is likely because this specimen failed in flexure rather than punching under all eccentricities. Specimens SM 1.0 and SM 1.5 showed good agreement with Regan's equation with a coefficient of 2.0 for eccentricities up to 2.0. For larger eccentricities, compression flexural failure occurred. This suggests that the FEA moment versus vertical load data is reasonable when the FEA specimens failed due to punching rather than flexure.

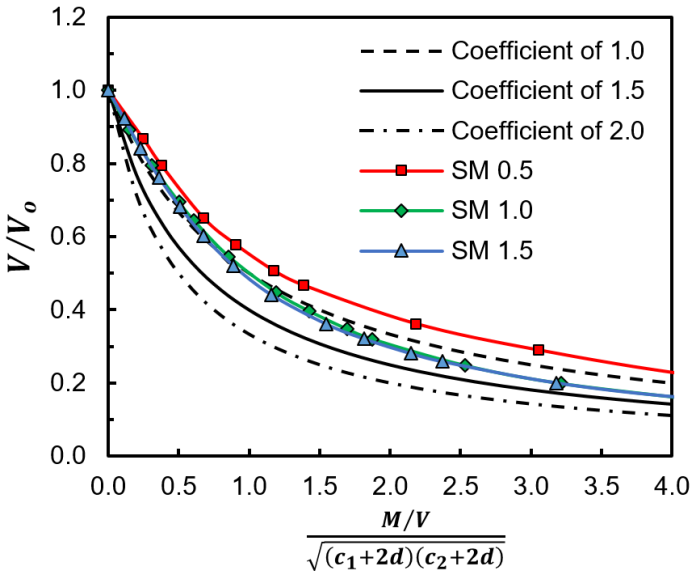

Figure 7.7: Normalized vertical load capacities versus eccentricities for SM specimens and predictions by Regan (1981)

7.4 Moment-shear interaction diagram

In this section, the linear moment-shear interaction assumed by ACI 318-19 and CSA A23.3-19 is derived. Then, the moment versus vertical load data from the parametric study FE analyses is normalized and a line is superimposed on the FEA moment-shear data. This is done to determine if a linear relation can accurately describe the interaction between moment and shear.

As shown in Section 2.2, the failure criterion for both ACI 318-19 and CSA A23.3-19 is:

$$v_c = \frac{V}{b_o d} + \frac{\gamma_v M c}{J} \tag{7.1}$$

where v_c is the two-way shear strength, V is the vertical load, b_o is the critical perimeter at d/2 from the column, d is the effective depth, γ_v is the fraction of moment transferred to shear, M

is the unbalanced moment, c is the distance from the centroid to the edge of the critical section, and J is the polar moment of inertia.

If the unbalanced moment, M, in Equation 7.1 is set to zero, an equation for the concentric vertical load required to cause punching shear failure V_o is obtained:

$$V_o = v_c b_o d \, . \tag{7.2}$$

Similarly, if the vertical load V in Equation 7.1 is set to zero, an equation is obtained for the unbalanced moment required to cause punching failure M_o:

$$M_o = v_c J/c \, . \tag{7.3}$$

A linear moment-shear relation can be obtained by dividing Equation 7.1 by v_c then substituting Equation 7.2 and Equation 7.3:

$$\frac{V}{V_o} + \frac{M}{M_o} = 1 \, . \tag{7.4}$$

For each specimen, the FEA moment-shear data was obtained by dividing the vertical load V and moment M of each datum by V_o and M_o, respectively. Both V_o and M_o were found using FE analyses.

The FEA moment-shear data for the SM specimens is presented in Figure 7.8. In the same figure, a line is plotted through moment-shear data points (0, 1) and (0.93, 0.29). The latter datum is used since the FE analyses failed due to compression flexural failure when V/V_o was less than 0.29 (i.e. when V was less than 129 kN). While ACI 318-19 and CSA A23.3-19 suggest that γ_v is a constant based on column location and geometry, it is likely that γ_v is also a function of vertical load and reinforcement ratio. This is because the moment-shear interaction was nonlinear between M/M_o values of 0 and 0.93.

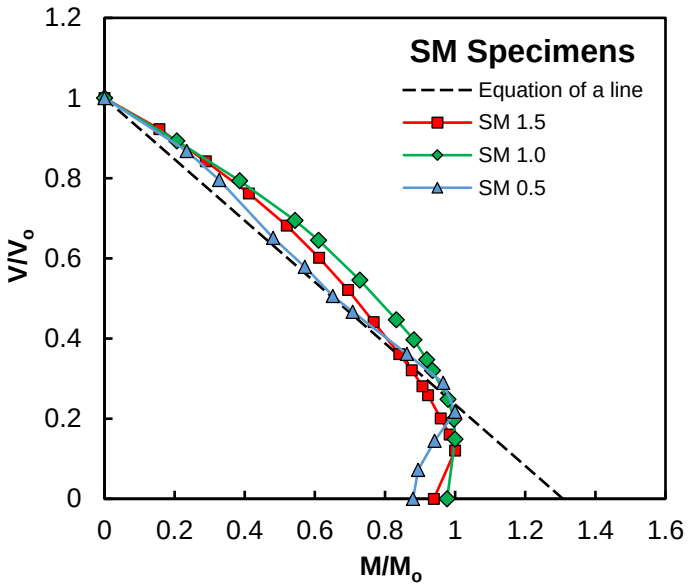

Figure 7.8: Moment-shear interaction diagram for the SM specimens

Chapter 8: Proposed method for predicting punching shear failure

Using the FE analyses from the parametric study, equations were produced to predict punching shear failure based on shear stresses within elements located at a perimeter d/2 from the column. This perimeter was chosen as it is the critical perimeter of CSA A23.3-19, ACI 318-19, and *fib* Model Code 2010 design codes. The elements studied are shown in Figure 8.1.

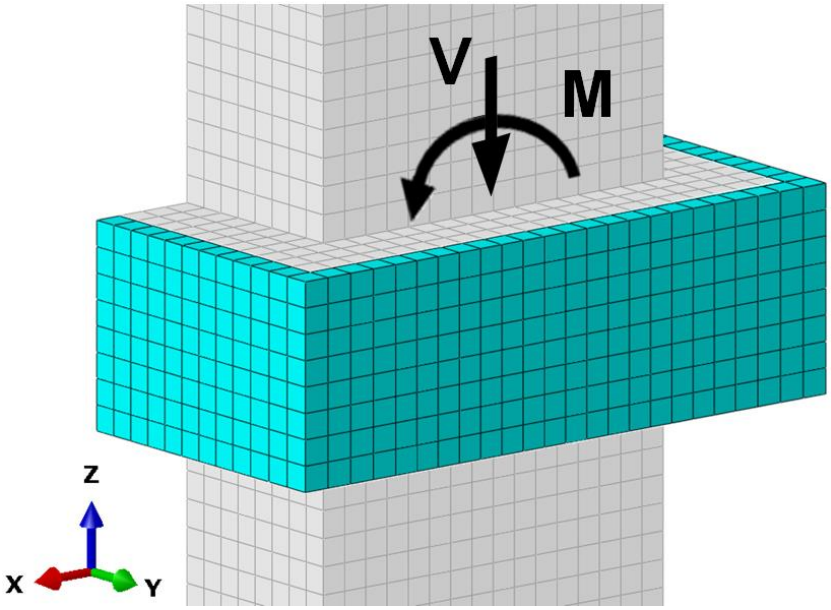

Figure 8.1: Critical perimeter elements used to develop stress-based analysis method

Since all specimen concrete slabs were meshed with 20 mm C3D8R elements, eight elements were present through the depths of the slabs. For each stress distribution, the shear stresses among the elements through the slab depth were averaged to obtain an average shear stress at each x-y coordinate. For elements along the column face parallel to the y-axis, 1-3 shear stresses were used in calculations. For elements along the column face parallel to the x-axis, 2-3 shear stresses were used in calculations. Calculations involving elements at the perimeter corners used both 1-3 and 2-3 shear stresses.

At each x-y location, the average shear stress was found by dividing the sum of element shear forces through the slab depth by the sum of element areas through the slab depth. The shear force for each element was found by multiplying the element area by its shear stress. The average shear stresses around the perimeter located $d/2$ from the column were plotted with respect to their element centroid x and y coordinates.

A typical shear stress distribution at the critical perimeter for a specimen subjected to only a vertical load is shown in Figure 8.2. A typical shear stress distribution at the critical perimeter for a specimen subjected to a vertical load and 85-percent of the ultimate moment is shown in Figure 8.3. When specimens were subjected to a combined vertical load and moment, the average shear stresses along the critical perimeter were nonlinear.

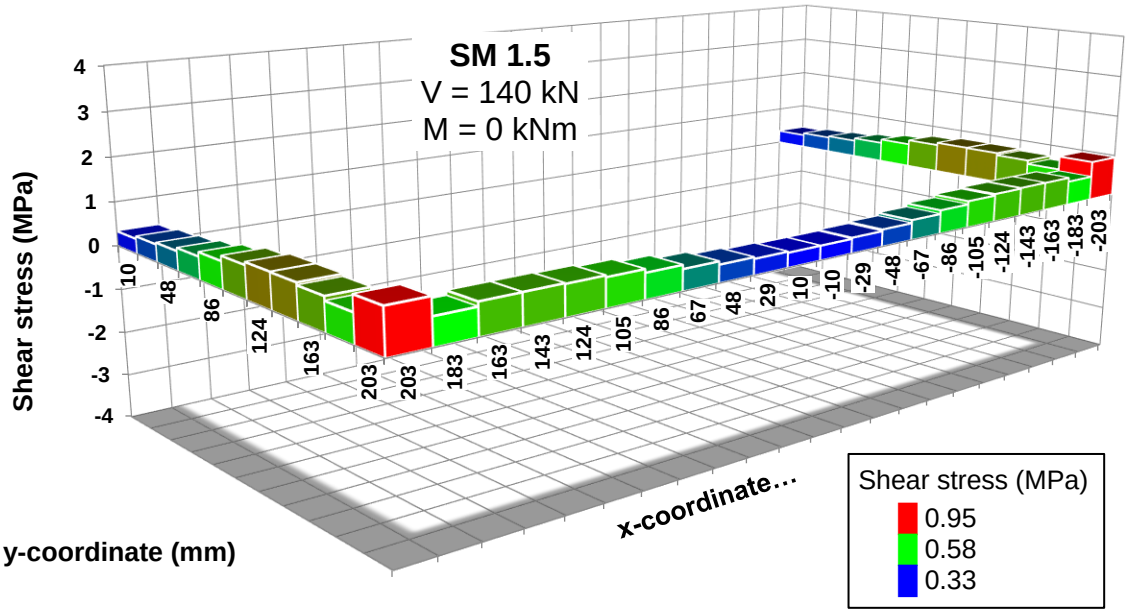

Figure 8.2: Typical shear stress distribution at critical perimeter under only vertical load

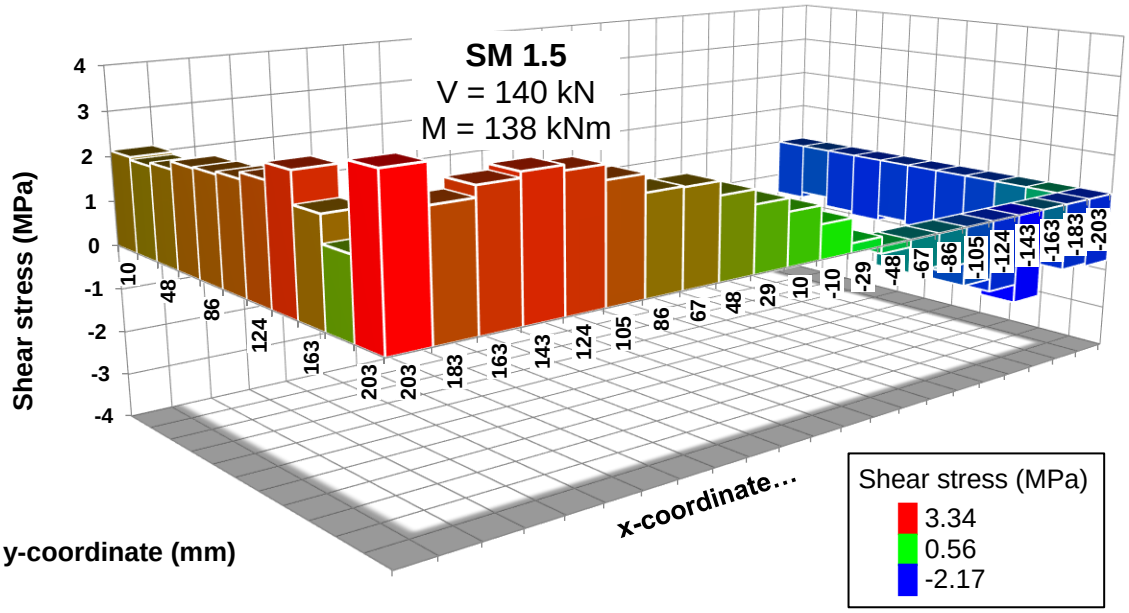

Figure 8.3: Typical shear stress distribution at critical perimeter under combined vertical load and unbalanced moment

In this approach, punching shear failure occurs when the average of the shear stresses among elements at the additive side of the critical section equal a limiting average shear stress, v_c. These elements are shown in Figure 8.4 and will be referred to as the critical elements. The average of shear stresses among the critical elements is the sum of the average shear stress caused by the vertical load, v_V, and the average shear stress caused by the unbalanced moment, v_M. The shear stress from vertical load, v_V, was estimated as a function of the vertical load, critical perimeter, and effective depth. The shear stress from the unbalanced moment, v_M, was estimated as a function of the vertical load, unbalanced moment, and reinforcement ratio. Lastly, the limiting shear stress, v_c, was estimated as a function of the vertical load and reinforcement ratio.

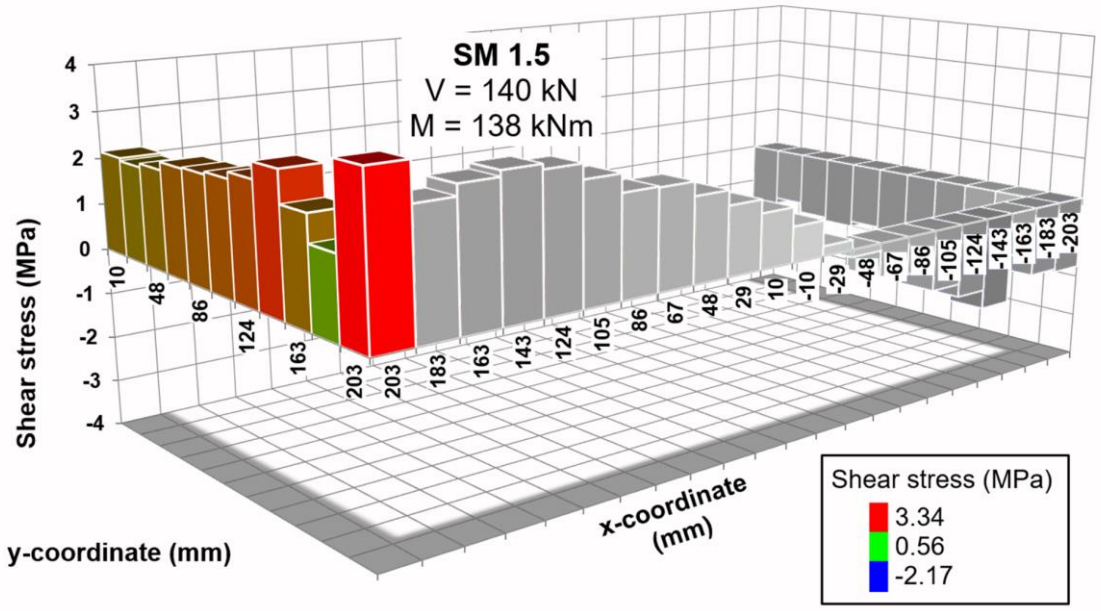

Figure 8.4: Critical elements at additive side of critical section

8.1 Average shear stresses of critical elements versus applied moment

During specimen failure, the largest shear stresses were observed within concrete slab elements located at the side of the critical section where shear stresses from the vertical load and unbalanced moment are additive. Figure 8.5, Figure 8.6, and Figure 8.7 show the average shear stresses versus applied moments for these critical elements for specimens SM 0.5, SM 1.0, and SM 1.5, respectively. Linear regressions were plotted alongside data obtained from numerical

modelling. These linear functions fit the observed data well and were used to predict average shear stresses in following sections.

Consistent between Figure 8.5, Figure 8.6, and Figure 8.7, the average shear stress caused by only the vertical load increased linearly as the vertical load was increased. Furthermore, the slope of the shear-moment data decreased as the vertical load was increased. The ultimate average shear stress varied between 1.2 MPa and 1.4 MPa for specimen SM 0.5, 1.8 MPa and 2.1 MPa for specimen SM 1.0, and 2.3 MPa and 2.6 MPa for specimen SM 1.5.

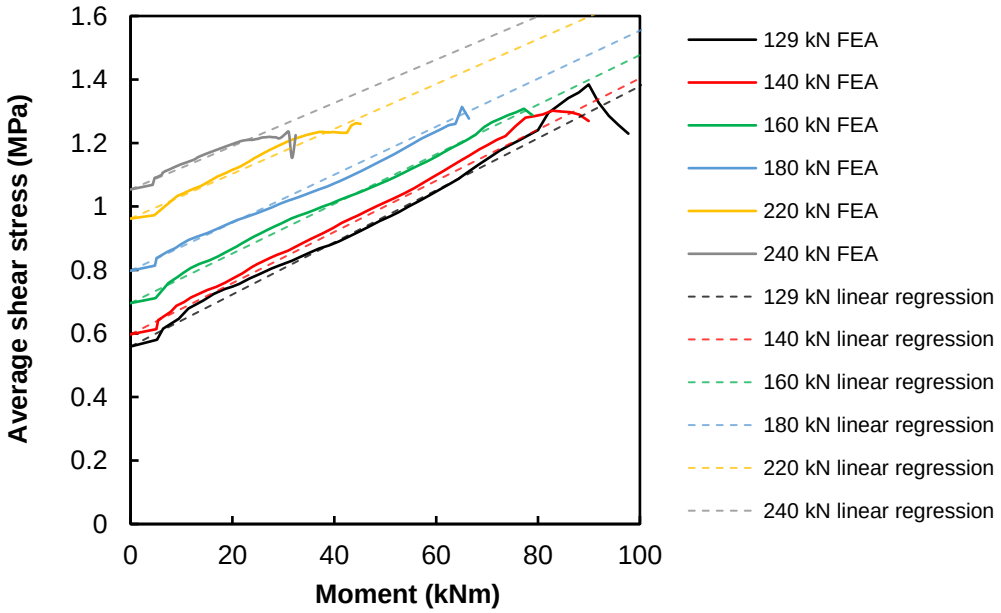

Figure 8.5: Average shear stress versus moment for specimen SM 0.5 FE analyses

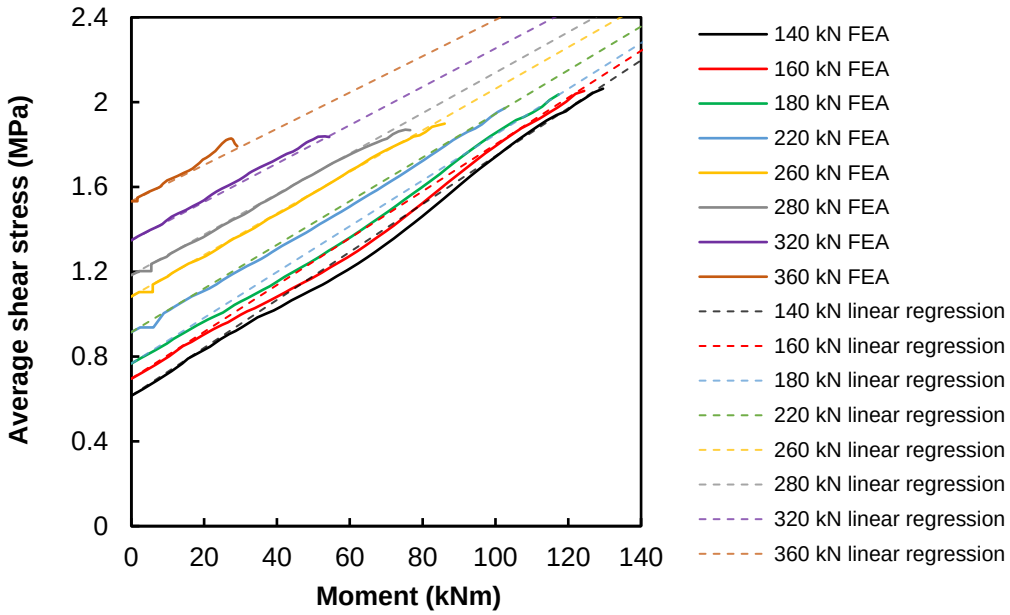

Figure 8.6: Average shear stress versus moment for specimen SM 1.0 FE analyses

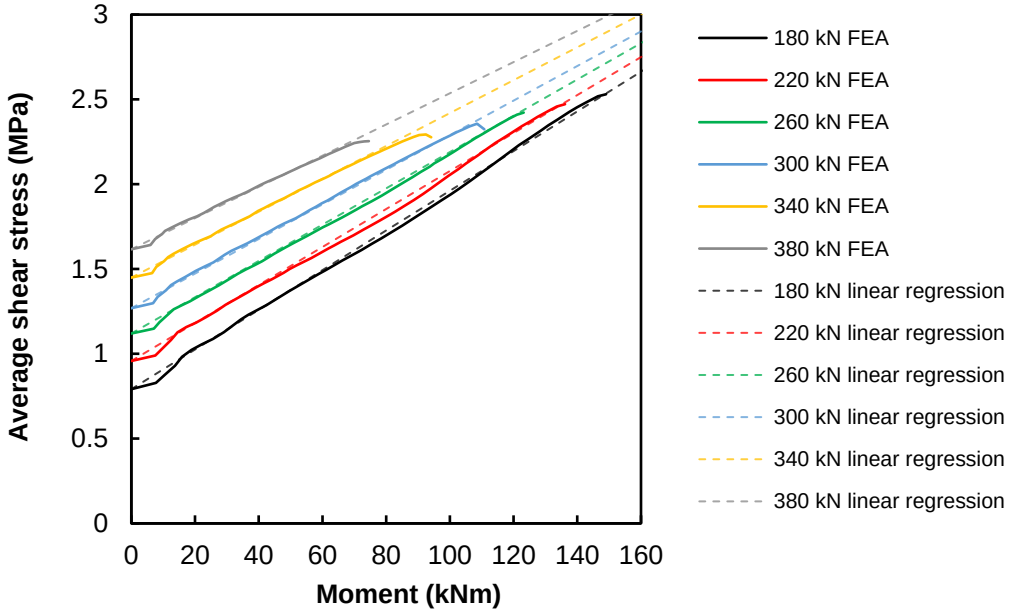

Figure 8.7: Average shear stress versus moment for specimen SM 1.5 FE analyses

8.2 Stress-based method: vertical load contribution to average shear stress

The average shear stress versus vertical load for the SM specimens subjected to only a vertical load are presented in Figure 8.8. Alongside this data, a linear function predicting the average shear stress from vertical load (MPa) as a function of vertical load (kN) is presented.

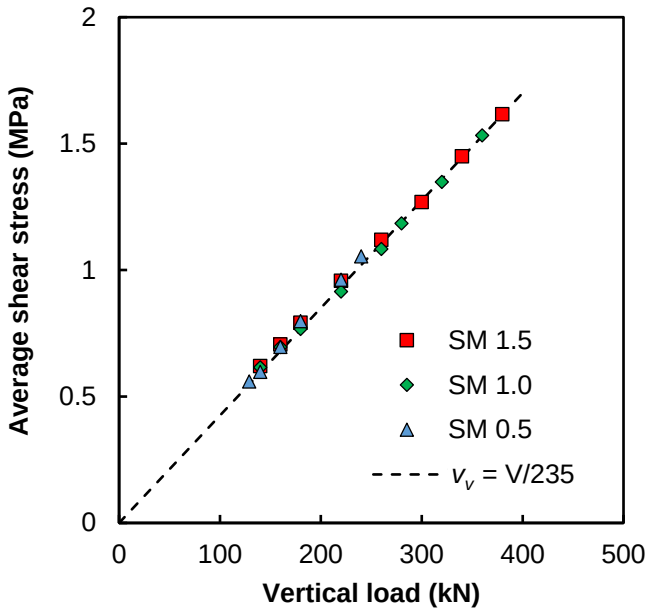

Figure 8.8: Average shear stress versus vertical load from FE analyses of SM specimens subjected to only vertical loading

Recall that ACI 318-19 and CSA A23.3-19 state that the average stress from a vertical load v_V is equal to $V/b_o d$ (where b_o is the critical perimeter at d/2 from the column and d is the effective depth). For the SM specimens, $b_o d$ is equal to $205 \cdot 10^3$ mm^3. The v_V function shown in Figure 8.8 suggests that $b_o d$ is equal to $235 \cdot 10^3$ mm^3. This is a difference of 15-percent.

Therefore, the vertical load contribution to the total shear stress v_V was estimated as

$$v_V = \frac{V}{1.15 b_o d} \quad . \tag{8.1}$$

In future work, the constant 1.15 can be studied further to determine if this was a calculation error or if the effective depth as defined by ACI 318-19 and CSA A23.3-19 should be increased to consider a larger punching shear critical section.

8.3 Stress-based method: moment contribution to average shear stress

As previously shown in Figure 8.5, Figure 8.6, and Figure 8.7, the average shear stress increased linearly as the moment was increased. However, the rate at which the average shear stress increased was greater when lower initial vertical loads were applied. As defined by the Hognestad parabola, the uniaxial compression modulus of elasticity decreases as the axial stress increases. The changes in stress given an applied strain for low and high initial stresses are

shown in Figure 8.9. If a uniaxial compressive stress σ_1 was applied followed by an applied strain of $\Delta\varepsilon$, a change in uniaxial compressive stress $\Delta\sigma_1$ would occur. If a higher uniaxial compressive stress σ_2 were applied followed by the same applied strain $\Delta\varepsilon$, the change in uniaxial compressive stress $\Delta\sigma_2$ would be less than the change in uniaxial stress $\Delta\sigma_1$ (i.e. when stress σ_1 was applied).

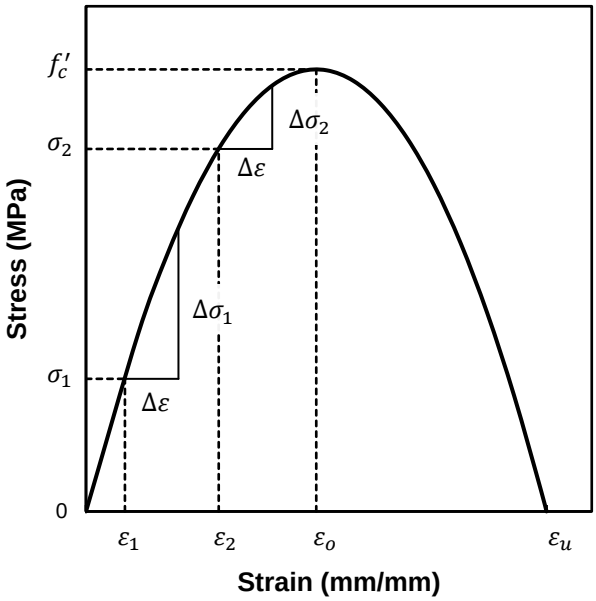

Figure 8.9: Changes in stresses given an applied strain for low and high axial forces

The moment contribution to the average shear stress, v_M, is assumed to be equal to

$$v_M = \frac{\gamma_v M c}{J} = \alpha M \ . \tag{8.2}$$

This definition is based on that provided by ACI 318-19 and CSA 23.3-19. For the work herein, the coefficient γ_v is assumed to be a function of vertical load, V, and reinforcement ratio, ρ. Parameters c (the distance from the centroid to the centroid to the edge of the critical section) and J (the polar moment of inertia) are constant since all SM specimens have identical concrete geometries. The coefficient α is the slope of average shear versus moment data as shown in Figure 8.10, which is also equal to $\gamma_v c/J$.

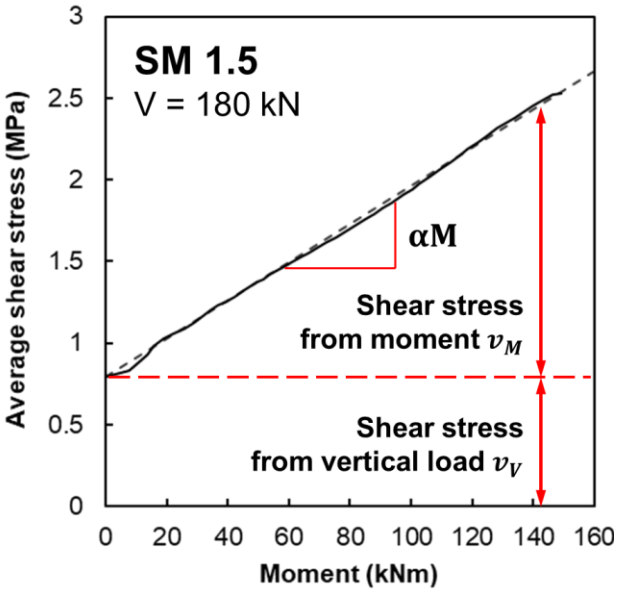

Figure 8.10: Slope α of average shear stress versus moment results from FEA (180 kN FE analysis of SM 1.5 shown)

To determine γ_v, an equation is developed to predict α based on shear-moment data previously presented in Section 8.1. Then, coefficient α is multiplied by J/c to produce γ_v.

The coefficient α is assumed to be a function of V and ρ:

$$\alpha(V, \rho) = mV + b(\rho) \tag{8.3}$$

where m is a constant, V is the vertical load, and b is a function of the reinforcement ratio ρ.

The value of coefficient α versus vertical load data for the SM specimens is presented in Figure 8.11. It is assumed that the values of α for specimen SM 0.5 would be larger if more flexural reinforcement was provided such that the specimen failed in two-way shear rather than flexure. It is assumed that additional reinforcement would reduce rotations, which would result in a higher portion of stresses to be transferred to shear rather than flexure. However, it is recommended that a slab-column connection with similar geometry and materials but with another reinforcement ratio greater than 1-percent be analysed to confirm this assumption.

Another observation from Figure 8.11 is that the α-V data for all specimens is linear and parallel to one another. This meant that the slope of α (i.e. m) is constant for all specimens and independent of reinforcement ratio.

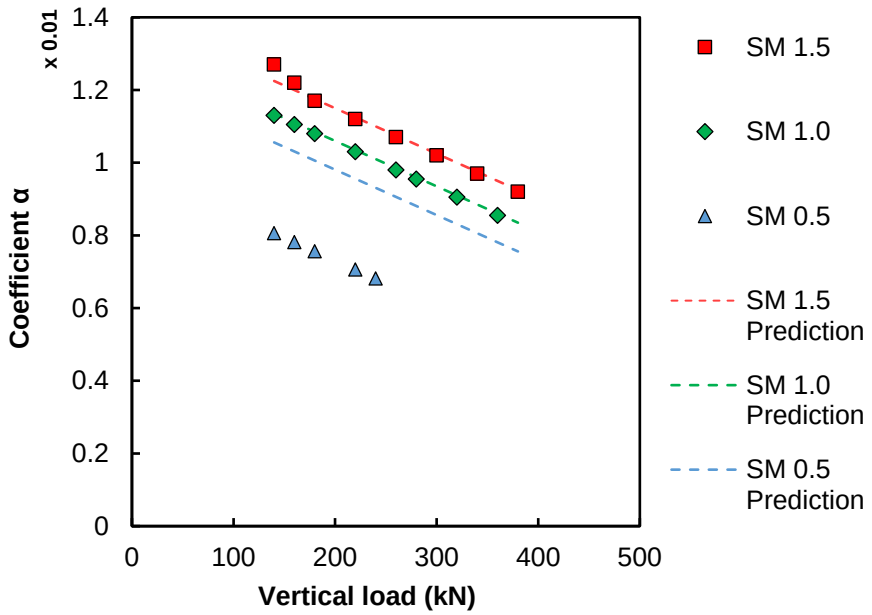

Figure 8.11: Values of α coefficient versus vertical loads

From linear regressions, the slope of the α-V data m for all specimens is determined to be

$$m = -\frac{1}{8 \cdot 10^7} \ . \qquad \text{(SI units: N, mm) (8.4)}$$

It is assumed that α increases linearly as the reinforcement ratio is increased. A linear function for the y-intercept b is developed based on the y-intercepts of the linear regressions for specimens SM 1.0 and SM 1.5:

$$b(\rho) = \frac{1}{86.15 - 9.81 \cdot 100 \cdot \rho} \ . \qquad \text{(SI units: N, mm) (8.5)}$$

Substituting Equation 8.4 and Equation 8.5 into Equation 8.3 produces the equation:

$$\alpha = \frac{1}{86.15 - 9.81 \cdot 100 \cdot \rho} - \frac{V}{8 \cdot 10^7} \ . \qquad \text{(SI units: N, mm) (8.6)}$$

For the SM specimens, the polar moment of inertia, J, is equal to $6.29 \cdot 10^9$ mm^4 and the distance from the centroid to the edge of the critical section, c, is equal to 213 mm. The equations used to calculate these values are presented in Section 2.2.1.2.

Equation 8.6 was multiplied by J/c to obtain a function for γ_v:

$$\gamma_v(V,\rho) = \frac{1}{3} - \frac{V}{2\,703\,296} + 5.3\rho \ . \qquad \text{(SI units: N, mm) (8.7)}$$

The constants within Equation 8.7 are specific to the SM specimens. Further development of Equation 8.7 is necessary before it can be applied to other slab-column connections.

In future work, average shear stress versus moment data should be obtained for connections with varying column locations, column dimensions, effective depths, and concrete strengths. This data should be studied to understand the influence of each parameter. Then, the constants within Equation 8.7 could be replaced with physical parameters to produce a general equation.

8.4 Stress-based method: ultimate shear stress

Per this method, failure occurs in a specimen when the average of shear stresses within the critical elements reaches an ultimate average shear stress, v_c. The proposed equation for predicting the ultimate average shear stress, v_c, as a function of vertical load, V, and reinforcement ratio, ρ, is

$$v_c(V,\rho) = 1.26 + 101\rho - \frac{V}{7.1 \cdot 10^5} \ . \qquad \text{(SI units: N, mm) (8.8)}$$

The ultimate average shear stress, v_c, versus vertical load results and the proposed equation are presented in Figure 8.12. For each of the specimens, the ultimate average shear stress decreases linearly as the vertical load increases. The rate at which this ultimate stress decreases is the same regardless of the reinforcement ratio. Increasing the reinforcement ratio results in increased ultimate average shear stresses for all vertical loads.

The proposed equation was obtained by performing linear regressions using the ultimate shear stress versus vertical load data for the SM specimens. The results of specimen SM 0.5 were considered outliers as it is assumed that shear stresses within specimen SM 0.5 would be larger if the specimen had failed in punching rather than flexure. As such, it is assumed that the reinforcement ratio linearly affected the ultimate average shear stress.

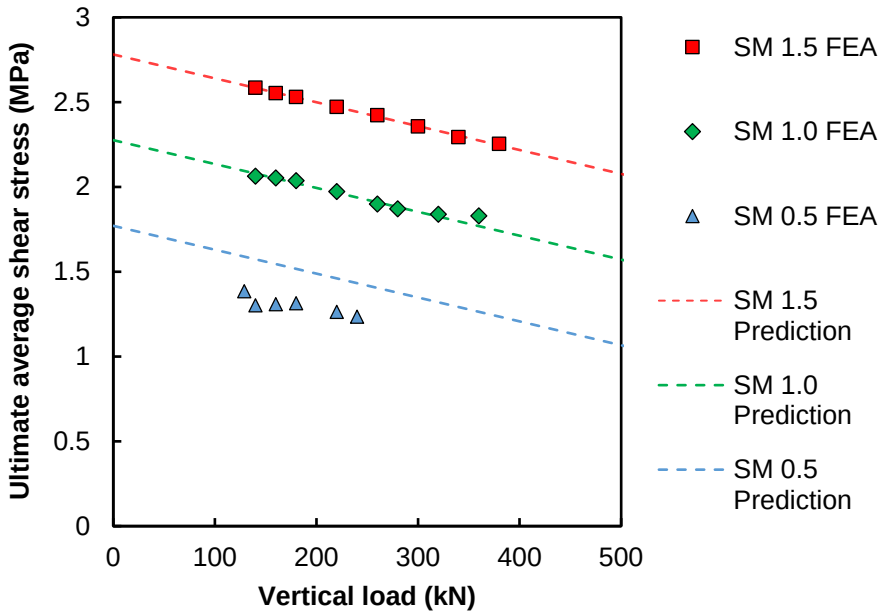

Figure 8.12: Ultimate average shear stresses versus vertical loads for SM FE analyses

As previously mentioned, it is assumed that the reinforcement ratio has a linear effect on ultimate shear stress. In future work, it is recommended that this assumption be verified by analysing a slab-column connection with similar geometry and material properties but different reinforcement ratio (preferably greater than 1-percent). It is recommended that additional numerical modelling be completed for other specimens to replace the constants in Equation 8.8 with parameters relating to connection geometries and material properties.

Chapter 9: Comparisons with current design codes

9.1 SM specimens by Ghali, Elmasri, and Dilger (1976)

In Section 9.1.1, the average shear stresses versus moments calculated using the proposed method are compared the predictions of ACI 318-19. In Section 9.1.2, the moment versus vertical load results from FE analyses are compared to the predictions of ACI 318-19, CSA A23.3-19, Eurocode 2 (2004), *fib* Model Code 2010, and the proposed method.

9.1.1 Coefficient γ_v as proposed versus ACI 318-19

In this section, the average shear stresses versus moments calculated using the proposed stress-based method are compared to ACI 318-19 predictions for SM specimens subjected to vertical loads of 140 kN, 160 kN, and 180 kN. The predicted average shear stresses are plotted alongside FEA stresses to ensure that the proposed equations were developed without errors. Then, the values of γ_v from the stress-based method are compared to ACI 318-19 predictions.

The FEA and predicted average shear stresses for the SM specimens subjected to a vertical load of 140 kN are plotted in Figure 9.1. The ultimate shear stress predicted by ACI 318-19 is dependent on the concrete compressive strength. Since all specimens were cast from concrete of similar compressive strength, the predicted ultimate average shear stresses are similar between specimens. The γ_v value of 0.4 from ACI 318-19 is closest to that of specimen SM 1.5. As per the FEA results, the γ_v values for specimens SM 0.5, SM 1.0, and SM 1.5 are 0.31, 0.33, and 0.36.

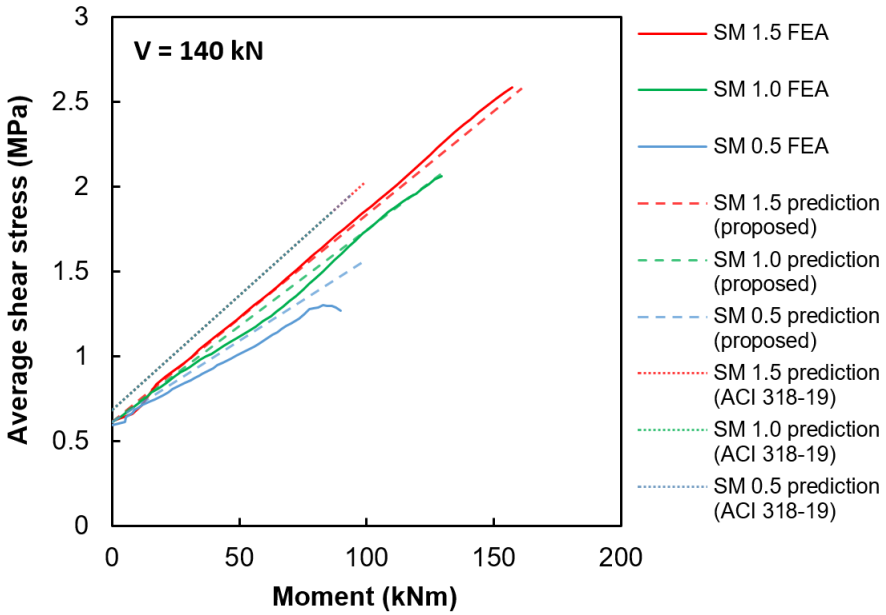

Figure 9.1: Average shear stress versus moment for SM specimens (V = 140 kN)

The FEA and predicted average shear stresses for the SM specimens subjected to a vertical load of 160 kN are plotted in Figure 9.2. As was the case with the 140 kN vertical load, the γ_v value of 0.4 from ACI 318-19 is closest to that of specimen SM 1.5. As per the FEA results, the γ_v values for specimens SM 0.5, SM 1.0, and SM 1.5 with an applied vertical load of 160 kN are 0.30, 0.33, and 0.35, respectively.

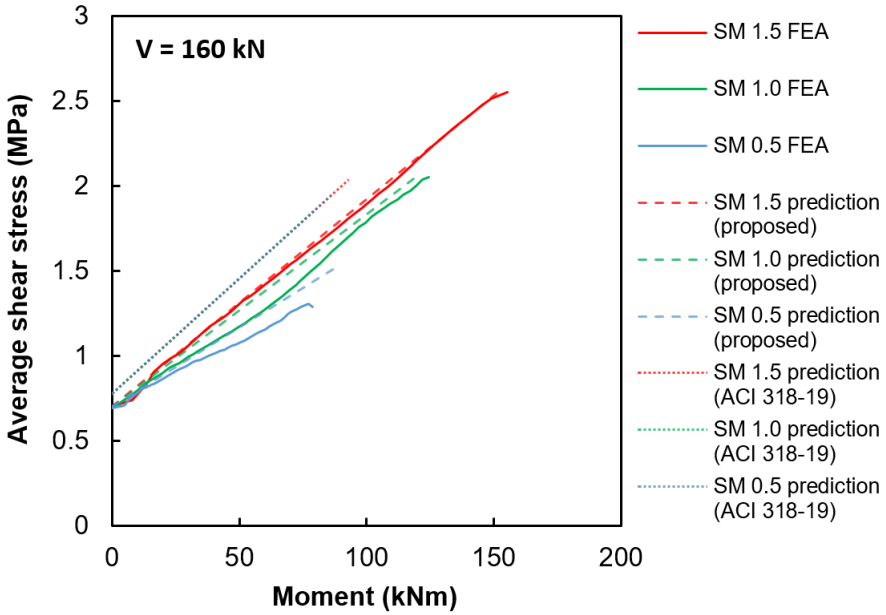

Figure 9.2: Average shear stress versus moment for SM specimens (V = 160 kN)

The FEA and predicted average shear stresses for the SM specimens subjected to a vertical load of 180 kN are plotted in Figure 9.3. As per the FEA results, the γ_v values for specimens SM 0.5, SM 1.0, and SM 1.5 with a vertical load of 180 kN are 0.29, 0.32, and 0.35, respectively.

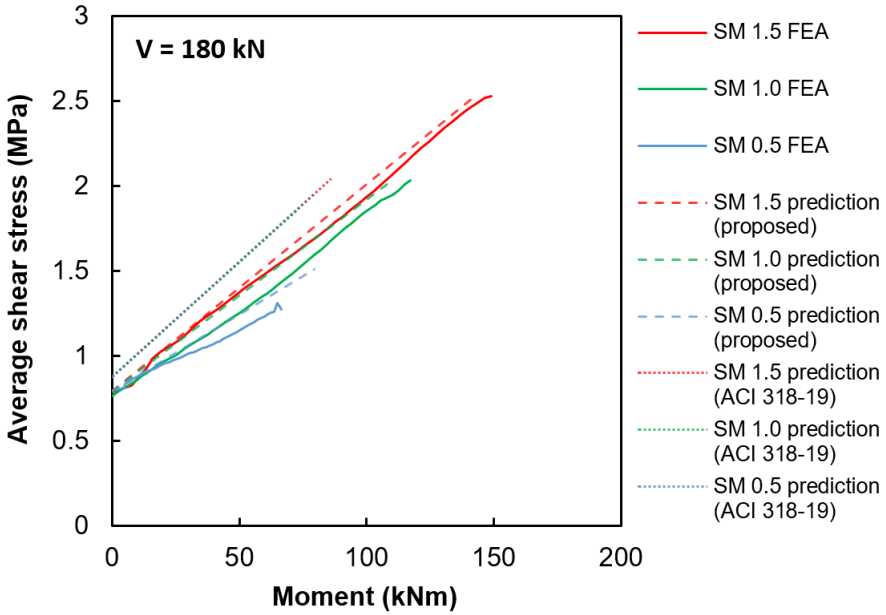

Figure 9.3: Average shear stress versus moment for SM specimens (V = 180 kN)

The proposed values of γ_v for the SM specimens using Equation 8.7 are presented in Table 9.1. Since the proposed equation is a function of vertical load and reinforcement ratio, the values of γ_v for two load cases are presented for each specimen. The first load case is when the specimen is subjected to only an unbalanced moment (i.e. the vertical load equals zero). The second load case is when the connection is subjected to its concentric vertical load capacity V_o (without any unbalanced moment). For each specimen, V_o was obtained from FE analyses. Intermediate values of γ_v may be obtained through linear interpolation.

Table 9.1: Proposed values of γ_v for SM specimens subjected to only moments or only vertical loads

Specimen	γ_v (only unbalanced moment)	Concentric vertical load capacity V_o (from FEA)	γ_v (only vertical load V_o)
SM 0.5	0.36	277 kN	0.26
SM 1.0	0.39	403 kN	0.24
SM 1.5	0.41	499 kN	0.23

Based on these results, the value of γ_v ranged between 0.23 and 0.41 depending on the reinforcement ratio and vertical load. Other parameters possibly have an influence on γ_v as well.

When Moe first introduced his version of γ_v in 1961, he found that γ_v equal to 0.27 fit his "Type A" specimens well and γ_v equal to 0.38 fit his "Type B" specimens well. Both sets of specimens had 6-ft by 6-ft slab sizes. Type A specimens used a reinforcement ratio of 1.5-percent with a square column dimension of 12-inches. Type B specimens used a reinforcement ratio of 1.34-percent with a square column dimension of 10-inches. Ultimately, he decided on a γ_v equal to 0.33, which provided adequate results for both sets of specimens. ASCE-ACI Committee 326 (1962) found that γ_v equal to 0.2 provided a good fit to available test data. Hanson and Hanson (1968) showed that γ_v equal to 0.4 provided a good fit to their experimental data.

Each of these researchers proposed a different value for γ_v varying between 0.2 and 0.4. These values are consistent with the values of the stress-based method shown in Table 9.1. In 2003, Alexander and Simmonds argued that Hanson and Hanson's specimens were subjected to substantially greater magnitudes of unbalanced moments than shears. As a result, the specimens failed due to compression crushing rather than shear failure (Alexander & Simmonds, 2003). These statements were consistent with Table 9.1, which showed that specimens subjected to no (or little) vertical loads had γ_v values close to 0.4.

In conclusion, each researcher selected a value of γ_v that worked best for their set of specimens. It is worthwhile to further study how the value of γ_v can change depending on specimen loading, geometry, and material properties. A more efficient γ_v approach would increase the accuracy of ACI 318-19 and allow for more efficient structural designs. For example, if specimen SM 1.5 is subjected to an unbalanced moment of 50 kNm, ACI 318-19 predicts a vertical load capacity of 284 kN (based on γ_v equal to 0.4). Using the proposed γ_v equation, this prediction is increased to 318 kN (based on γ_v equal to 0.3). If the connection is only required to resist 284 kN, using the proposed γ_v equation allows the column size to be reduced from 305 mm by 305 mm to 280 mm by 280 mm.

9.1.2 Moment versus vertical load results

In this section, the ultimate moments versus vertical loads of specimens SM 0.5, SM 1.0, and SM 1.5 are compared to the code predictions of ACI 318-19, CSA A23.3-19, EC2-2004, MC

2010, and the proposed method. It is expected that the predictions of CSA A23.3-19 will be similar to ACI 318-19. This is because both codes are based on the same research but CSA A23.3-19 has different safety factors combined into its constants. For all design codes, the safety factors are set equal to 1. For MC 2010 calculations, the radius of contraflexure, r_s, was assumed equal to the specimen length since the specimen was sized to the radius of contraflexure.

The level IV approximation of MC 2010 uses slab rotations obtained from FE analyses. For each combination of vertical load and ultimate moment, slab rotations were calculated using nodal vertical displacements along the slab's top and bottom faces, at the plane of symmetry, along the axis perpendicular to the moment axis. Four rotations were calculated where the slab meets the column: one rotation at each side of the column along the top slab face and one rotation at each side of the column along the bottom slab face. The maximum magnitude of these four rotations was used for the level IV approximation of MC 2010.

The FEA and predicted ultimate moment versus vertical load data for specimen SM 0.5 are shown in Figure 9.4. It is important to note that specimen SM 0.5 failed in flexure for all vertical load levels. As such, the punching shear code provisions would provide better estimates had the specimens failed in punching rather than flexure. Section 8.6.1.2 of ACI 318-19 provides an equation for the minimum reinforcement ratio (based on connection geometry) to prevent flexure-driven failure. More information about the research behind this provision is provided in Section 2.1.17. For the SM specimens, the minimum reinforcement ratio is 0.75-percent. The design codes' punching shear provisions would likely produce more accurate predictions if the reinforcement ratio of SM 0.5 was increased to 0.75-percent.

ACI 318-19 underestimated the moment capacities for all vertical loads except between 40 kN and 120 kN. CSA A23.3-19 underestimated the moment capacities for all vertical loads. EC2 was adequate for vertical loads between 20 kN and 240 kN. Level I approximations of MC 2010 were the most conservative of all analyses. As previously discussed, level I is intended to be used for regular flat slabs without significant redistribution of internal forces. For this reason, it was expected that level I would be accurate for low eccentricities (i.e. high vertical loads). However, the slope of the moment versus vertical load data was accurate to that of the FE analyses. Level II approximations of MC 2010 were the least conservative of the three MC 2010 levels compared. Level II predicted the same ultimate moment as the FE analyses when no

vertical load was applied. However, it underestimated the vertical load when no unbalanced moment was applied. The shape of level IV approximations was very similar to the shape of the FEA data. This is likely because the rotations for level IV calculations were obtained from FEA data.

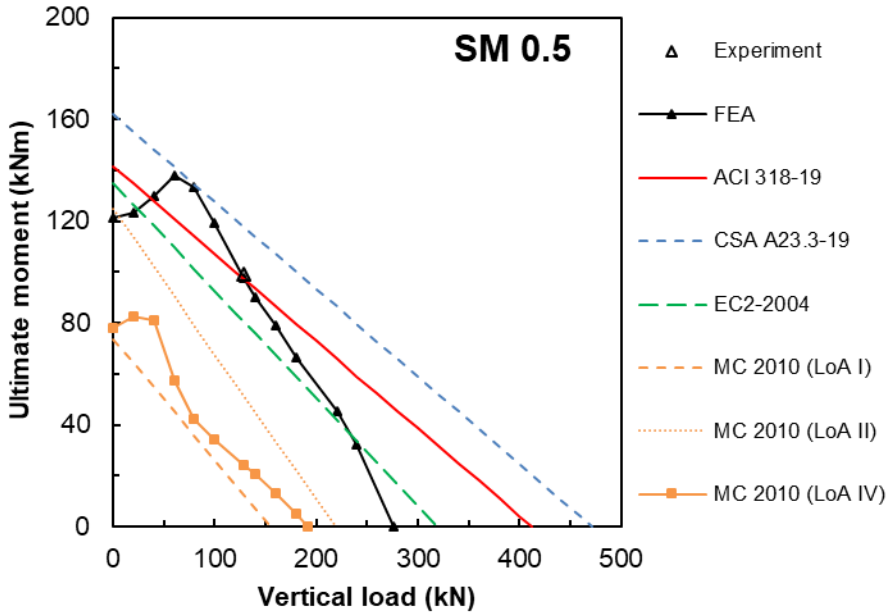

Figure 9.4: FEA and code-predicted moment capacities for specimen SM 0.5 subjected to various vertical loads

The FEA and code-predicted ultimate moment versus vertical load data for specimen SM 1.0 are shown in Figure 9.5. ACI 318-19 and CSA A23.3-19 do not consider the effects of flexural reinforcement. As such, the predictions of these design codes are the same for all three SM specimens. That being said, ACI 318-19 predicted the punching shear capacities accurately for moment-only and vertical-only load cases for specimen SM 1.0. However, it was conservative for intermediate vertical load values. Using ACI 318-19 with the proposed γ_v equation produced less conservative predictions for these intermediate values. CSA A23.3-19 predictions were non-conservative for vertical loads less than 45 kN and greater than 350 kN. EC2 accurately predicted the punching shear capacity when only a vertical load was applied. However, it underestimated the connection strength when only an unbalanced moment was applied. None of the MC 2010 levels of approximation adequately predicted the punching capacities for any vertical loads. However, level IV accurately predicted the slope of the FEA moment versus vertical load data. The proposed method demonstrated the possible moment capacities if

additional compression reinforcement been provided. Additional compression reinforcement would ensure that the specimen failed in punching shear rather than flexure under low vertical loads.

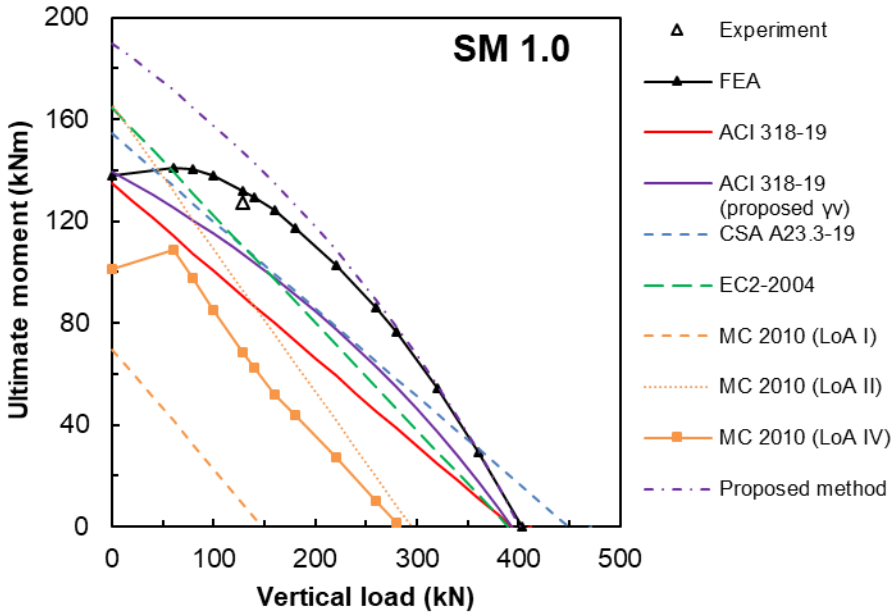

Figure 9.5: FEA and code-predicted moment capacities for specimen SM 1.0 subjected to various vertical loads

The FEA and code-predicted ultimate moment versus vertical load data for specimen SM 1.5 are shown in Figure 9.6. ACI 318-19 was conservative for all vertical loads. ACI 318-19 using the proposed γ_v equation predicted less conservative moment capacities. CSA A23.3-19 accurately predicted the punching shear capacities for the vertical load only and moment only load cases. As previously mentioned, these code predictions did not change between the SM specimens. EC2 accurately predicted the punching shear capacity for the vertical load only load case. However, its punching shear capacity prediction was non-conservative for the moment only load case. Model Code 2010 did not adequately predict the capacities of the SM specimens. However, the slope of the level IV approximation was similar to the analysis data since the rotations were obtained from the analyses. As with specimen SM 1.0, the proposed method showed the possible moment capacities if additional compression reinforcement had been provided such that the specimens did not fail in flexure.

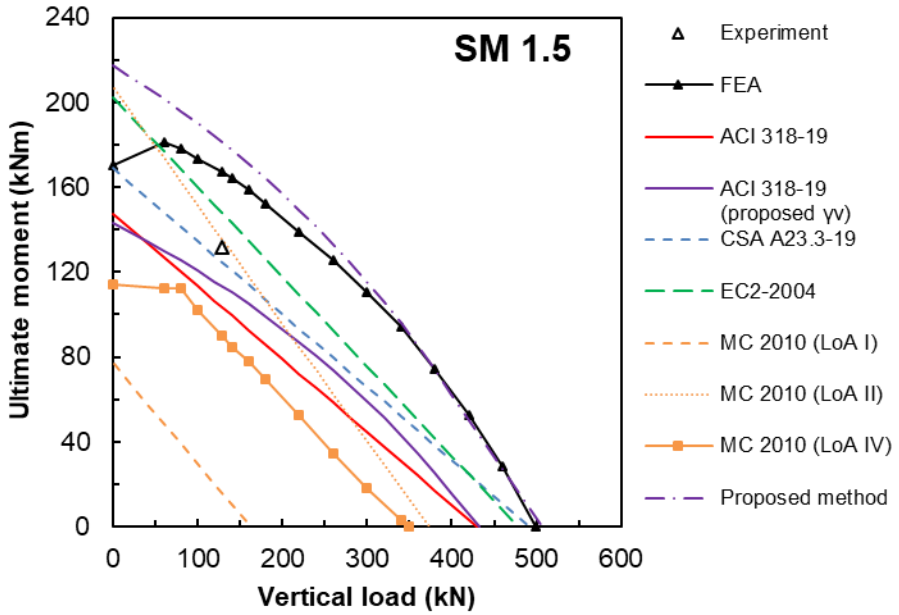

Figure 9.6: FEA and code-predicted moment capacities for specimen SM 1.5 subjected to various vertical loads

To summarize, none of the design codes' punching shear provisions accurately predicted the slope of the moment versus vertical load data for specimen SM 0.5. This is because specimen SM 0.5's moment capacities were governed by its flexural strength rather than its punching shear strength. ACI 318-19 accurately predicted the punching shear capacities of specimen SM 1.0. However, it did not acknowledge the increase in capacity due to additional reinforcement. As such, its predictions were conservative for specimen SM 1.5. For specimens SM 1.0 and SM 1.5, Eurocode 2 accurately predicted the punching shear capacities for most vertical load values. However, it was non-conservative for low vertical loads. This may be because the specimens failed in flexure under low vertical loads. Model Code 2010 did not adequately predict the moment capacities for any of the specimens but the slopes of its predictions were close to the slopes of the FE analyses. It is possible that adjusting the parameter r_s would increase the accuracy of Model Code 2010.

9.2 Specimens XXX and HXXX by El-Salakawy (1998)

The experiment, FEA, and code-predicted maximum vertical loads and moments for specimen XXX are presented in Table 9.2. The percentage differences of all vertical loads were compared to the experiment and analysis vertical loads. For all design codes, maximum vertical loads and moments were calculated while maintaining an eccentricity (i.e. M/V ratio) of 0.3 m. Relative

to the experiment, the vertical load predicted by CSA A23.3-19 was the most accurate. Relative to the FEA, the vertical load predicted by EC2-2004 was the most accurate. Unexpectedly, MC 2010 (LoA II) predicted more accurate maximum vertical loads than MC 2010 (LoA IV).

Table 9.2: Experiment, FEA, and code-predicted capacities for specimen XXX

			Vertical load percentage difference relative to	
	Vertical load (kN)	Moment (kNm)	experiment (%)	analysis (%)
Experiment	125.0	38.1	0.0	18.7
FEA	103.7	31.6	18.7	0.0
Code predictions				
ACI 318-19	113.4	34.0	9.7	9.0
CSA A23.3-19	131.3	39.4	4.9	23.5
EC2-2004	106.6	32.0	15.9	2.8
MC 2010 (LoA I)	44.7	13.4	94.7	79.5
MC 2010 (LoA II)	109.6	32.9	13.1	5.6
MC 2010 (LoA IV)	75.9	22.8	48.8	30.9

The experiment, FEA, and code-predicted maximum vertical loads and moments for specimen HXXX are presented in Table 9.3. ACI 318-19 predicted a maximum vertical load closest to that of the experiment. The next closest prediction was produced by EC2-2004 then MC 2010 (LoA IV). Relative to the FEA, MC 2010 (LoA IV) was the most accurate followed by EC2-2004 then ACI 318-19. Contrary to the specimen XXX predictions, the MC 2010 predictions increased in accuracy with increasing LoA level.

Table 9.3: Experiment, FEA, and code-predicted capacities for specimen HXXX

			Vertical load percentage difference relative to	
	Vertical load (kN)	Moment (kNm)	experiment (%)	analysis (%)
Experiment	70.0	50.7	0.0	17.9
FEA	58.5	38.4	17.9	0.0
Code predictions				
ACI 318-19	71.1	47.0	1.6	19.5
CSA A23.3-19	82.4	54.4	16.2	33.9
EC2-2004	68.5	45.2	2.2	15.7
MC 2010 (LoA I)	29.2	19.3	82.3	66.9
MC 2010 (LoA II)	85.7	56.5	20.1	37.7
MC 2010 (LoA IV)	65.1	42.9	7.3	10.6

9.3 Specimen SB1 by Adetifa (2003)

The experiment, FEA, and code-predicted maximum vertical loads and moments for specimen SB1 are presented in Table 9.4. The Critical Shear Crack Theory (CSCT) was included among the code predictions. It was not included in other specimen predictions since it is not applicable to slab-column connections subjected to unbalanced moments.

Relative to the experiment, the most accurate vertical load capacity was predicted by CSA A23.3-19 followed by EC2-2004 then ACI 318-19. The least accurate prediction as produced by MC 2010 (LoA I). Relative to the FEA, the most accurate vertical load capacity was predicted by CSA A23.3-19 followed by EC2-2004 then CSCT.

Table 9.4: Experiment, FEA, and code-predicted capacities for specimen SB1

		Percentage difference relative to:	
	Vertical load (kN)	experiment (%)	analysis (%)
Experiment	253.1	0.0	11.2
FEA	226.3	11.2	0.0
Code predictions			
ACI 318-19	186.8	30.2	19.1
CSA A23.3-19	213.7	16.9	5.7
EC2-2004	202.7	22.1	11.0
MC 2010 (LoA I)	81.2	102.8	94.4
MC 2010 (LoA II)	160.3	44.9	34.1
MC 2010 (LoA IV)	150.0	51.2	40.6
CSCT	186.0	30.6	19.6

Chapter 10: Conclusions and recommendations

10.1 Finite element model parameter calibration

In this work, finite element models of specimens SM 0.5, SM 1.0, and SM 1.5 tested by Ghali et al. (1976) were created. The preliminary parameters were based on past research by Genikomsou (2015) and boundary condition, material, and geometry information provided by Ghali et al. (1976). It was necessary to calibrate the finite element model parameters to ensure the analyses accurately reproduced behaviour observed during laboratory testing. This was done by changing one parameter at a time and selecting the parameter value that best reproduced experimental results. The moment-rotation data, load-displacement data, and crack patterns obtained from analyses were compared to those of obtained from laboratory testing when evaluating the accuracy of analyses.

The calibrated finite element analyses of the SM specimens showed good agreement with experimental results. The FE analyses produced moment-rotation data with similar slopes to the experimental data. The percentage differences between analysis and experiment ultimate moments for specimens SM 0.5, SM 1.0, and SM 1.5 were 1.4-percent, 3.7-percent, and 23.8-percent, respectively. It was predicted that specimen SM 1.5 was an outlier and would produce a higher moment if recast and retested. This is because the dynamically-loaded specimens DM 0.5 and DM 1.0 produced ultimate moments which were 20 kNm larger than statically-loaded specimens SM 0.5 and SM 1.0; however, specimens DM 1.5 and SM 1.5 had a difference in ultimate moment of 50 kNm.

The finite element analyses did not accurately reproduce the slopes of experimental column displacement versus rotation data. It was predicted that modelling neoprene bearing pads (instead of restraining the nodes of slab edge elements) would increase the accuracy of the analyses displacements. However, no information about the dimensions or material properties of the bearing pads was included in the publication by Ghali et al. (1976). Furthermore, creep during the application of vertical loads would have increased the deformations of the specimens. However, creep effects were not captured by the finite element analyses. The FEA crack patterns of specimens SM 0.5 and SM 1.5 showed good agreement with the photographed crack patterns.

Photographs of specimen SM 1.0 crack patterns were not published. FEA crack patterns of specimen SM 1.0 and SM 1.5 were nearly identical to one another.

10.2 Verification of calibrated finite element model parameters

The finite element model parameters were verified by conducting finite element analyses of specimens XXX and HXXX tested by El-Salakawy (1998) and specimen SB1 tested by Adetifa (2003). Specimens XXX and HXXX were edge slab-column sub-assemblage specimens with eccentricities of 0.30-meters and 0.66-meters, respectively. Specimen SB1 was an interior slab-column sub-assemblage specimen subjected to concentric loading.

Finite element analyses of specimens XXX and HXXX underestimated the ultimate moments of the experiments. Furthermore, the FEA moment-rotation data was softer than the experimental data. The percentage differences between FEA and experiment ultimate moments for specimens XXX and HXXX were 18.4-percent and 27.6-percent. Similarly, the FE analyses underestimated the ultimate vertical loads of the experiments. However, the slopes of the load-displacement data were accurately predicted by the FE analyses. The percentage differences between the FEA and experiment ultimate vertical loads for specimens XXX and HXXX were 18.6-percent and 17.9-percent, respectively. The FEA accurately reproduced the photographed experiment crack patterns.

The finite element analysis of specimen SB1 showed good agreement with experimental results. The ultimate vertical load percentage difference between the FEA and the experiment was 10.1-percent. The FEA accurately reproduced the slope of the load-displacement data. Lastly, the crack patterns showed good agreement between the FE analysis and the experiment.

10.3 Accuracy of national design codes

Using the calibrated finite element models of the SM specimens, a parametric study was conducted on the effect of varying eccentricities on the strengths of slab-column connections. FE analyses were conducted in which the SM specimens were subjected to varying initial vertical loads prior to the application of a displacement-couple, which was ramped until failure. For each specimen, moment capacities were plotted as a function of the initial vertical loads. On the same figures, moment capacities predicted by ACI 318-19, CSA A23.3-19, EC2-2004, and *fib* Model Code 2010 were plotted for the same range of vertical loads.

ACI 318-19 and CSA A23.3-19 do not consider increases in punching shear strengths resulting from increases in flexural reinforcement area. For this reason, the predictions of ACI 318-19 and CSA A23.3-19 did not change between the three SM specimens.

None of the design codes' punching shear provisions accurately predicted the punching shear strength of specimen SM 0.5. This was expected since specimen SM 0.5 had a flexure-driven failure rather than a punching failure (i.e. flexural failure occurred before its shear capacity was developed). However, ACI 318-19 introduced a provision that requires a minimum area of flexural reinforcement to be provided to allow for slab-columns to develop their full shear capacity. By this provision, the minimum allowable reinforcement ratio for the SM specimens is 0.75-percent. It was expected that the design codes' punching shear provisions would produce more accurate predictions if the reinforcement ratio of SM 0.5 was increased to 0.75-percent.

ACI 318-19 accurately predicted the punching shear strength for specimen SM 1.0 subjected to eccentricities equal to zero (i.e. only gravity load applied) and infinity (i.e. only unbalanced moment applied). For intermediate eccentricities, these predictions were conservative. This is because ACI 318 assumes a linear interaction between unbalanced moment and shear, while the parametric study analyses produced a nonlinear moment-shear interaction. Since the predictions of ACI 318-19 were not affected by the reinforcement ratio, these predictions were conservative for specimen SM 1.5.

CSA A23.3-19, which is based on the same research as ACI 318-19, produced non-conservative punching shear predictions for specimen SM 1.0. However, its predictions were accurate for specimen SM 1.5 subjected to eccentricities of zero and infinity. Like ACI 318-19, CSA A23.3-19 assumes a linear moment-shear interaction.

EC2-2004 accurately predicted the punching shear strengths for both specimens subjected to eccentricities equal to zero. However, it was non-conservative for eccentricities equal to infinity. Analyses in which SM specimens were subjected to large eccentricities failed due to flexural failure. This is because the reinforcement ratios of these specimens' compression mats were one-third of their tension mats. It is possible that EC2-2004 would produce more accurate predictions if sufficient compression reinforcement were provided to prevent flexural failures at

larger eccentricities. Like ACI 318-19 and CSA A23.3-19, EC2 assumes a linear moment-shear interaction.

Level I, II, and IV approximations of *fib* Model Code 2010 (MC 2010) predicted conservative punching shear capacities for all SM specimens. As expected, level I predictions were more conservative than level II predictions. Unexpectedly, level II predictions were less conservative than level IV predictions. However, level IV predictions accurately reproduced the shape of the moment-shear interaction of the finite element analyses. This is because slab rotations used to predict the ultimate vertical load were obtained from the finite element analyses. It was predicted that the radius of contraflexure r_s may need to be modified to improve the accuracy of MC 2010 predictions for the SM specimens.

With the exception of MC 2010 level IV predictions, all aforementioned design codes assumed a linear interaction between moment and shear. However, the finite element analyses produced moment-shear data that was nonlinear. As such, if the codes accurately predicted punching shear capacities for eccentricities of zero and infinity, they were non-conservative for intermediate values of shear.

10.4 Study of shear stresses at critical perimeter of ACI 318-19

Using the parametric study FE analyses, shear stresses were studied at a distance of d/2 from the column as defined by ACI 318-19 and CSA A23.3-19. The shear stresses along the critical periphery did not vary linearly as assumed by these design codes. Furthermore, the FEA average shear stress at failure varied depending on the eccentricity of the loading. Both ACI 318-19 and CSA A23.3-19 assume that failure occurs when the average shear stress reaches a limiting value, which is a function of the concrete compressive strength.

The maximum average shear stress along the critical section was compared to the average shear stress predicted by the design codes. This maximum average shear stress was separated into vertical load and unbalanced moment components. The vertical load component had good agreement with the assumptions of the design codes. With respect to unbalanced moment shear component, the coefficient γ_v was found to vary as a function of eccentricity with some influence from the reinforcement ratio. When the loading eccentricity was equal to zero, the

coefficient γ_v was approximately 0.25 for all three specimens. When the loading eccentricity was equal to infinity, the coefficient γ_v was approximately 0.40 for all three specimens.

10.5 Recommendations

The calibrated finite element model was capable of accurately predicting punching shear capacities and crack patterns of slab-column connections subjected to varying magnitudes of unbalanced moments. As is, the model may be used to study stresses at any location depending on the purpose of the study. The model may be further developed to improve the accuracy of deflections and rotations if necessary. This can be done through more advanced modelling of boundary conditions or contact conditions between the concrete and reinforcement.

In this work, an equation specific to the SM specimens was presented to calculate the coefficient γ_v as a function of vertical load and reinforcement ratio. In its current form, the γ_v equation includes constants that are based on geometry properties of the analysed specimens. The finite element model presented herein may be used to study shear stresses of other slab-column sub-assemblages along the same critical perimeter. The resulting average shear stresses can be compared to shear stresses presented herein to develop a universal equation for predicting the coefficient γ_v. To do so, additional experimental data are required, in which slab-column sub-assemblages, of varying reinforcement ratios, are subjected to varying monotonically-applied eccentric loads until failure.

The finite element model presented herein was developed to work for specimens without transverse reinforcement. The research of Genikomsou (2015) may be used to extend the finite element model to include shear reinforcement.

Letters of copyright

The letters/agreements granting permission to reproduce figures from previously published literature are provided on the following pages.

Re: Request for permission to reproduce crack pattern figures (specimens XXX and HXXX) in Master's thesis

Ehab El-Salakawy <Ehab.El-Salakawy@umanitoba.ca>

Sun 2020-03-08 7:47 PM

To: Mikhail Laguta <mikhail.laguta@uwaterloo.ca>;

Hi Mikhail
Good to hear that you are working on the punching shear of slab-column connections.
Yes, you have my permission to reproduce the said figures.
Regards,

Ehab El-Salakawy, Ph.D., P.Eng., FCSCE
Professor of Structural Engineering
Department of Civil Engineering
University of Manitoba
Room E1-434 (EITC), 15 Gillson St.
Winnipeg, Manitoba R3T 5V6
Tel: (204) 474-8319
Fax: (204) 474-7513
Home page: http://home.cc.umanitoba.ca/~elsalaka/

From: Mikhail Laguta <mikhail.laguta@uwaterloo.ca>
Sent: March 8, 2020 2:14:02 PM
To: Ehab El-Salakawy
Subject: Request for permission to reproduce crack pattern figures (specimens XXX and HXXX) in Master's thesis

Good afternoon Dr. El-Salakawy,

My name is Mikhail Laguta and I am one of Dr. Polak's graduate students at the University of Waterloo. I am preparing my Master's thesis and I would like permission to include the crack pattern photographs of your specimens XXX and HXXX in my thesis. I would like to reproduce the following figures from your PhD thesis:

- specimen XXX of Figure 5.1 from page 115,
- specimen XXX of Figure 5.8 from page 122,
- specimen HXXX of Figure 5.36 from page 143, and
- specimen HXXX of Figure 5.39 from page 146.

My thesis will be published in the institutional repository at the University of Waterloo (Waterloo, Ontario, Canada). Proper citation would be included with the reproduction of the figures.

Please let me know if you need any other information.

Thank you for considering this request,
Mikhail Laguta

RE: Request for permission to reproduce ACI figures in master's thesis

Barry M. Bergin <Barry.Bergin@concrete.org>

Fri 2020-03-13 12:21 PM

To: Mikhail Laguta <mikhail.laguta@uwaterloo.ca>;

Hi,

Yes, you can use these 3 items for your thesis.

Be well!

Barry

Barry M. Bergin
Manager, Publishing Services
p +1.248.848.3749

American Concrete Institute | *Always advancing*
www.concrete.org

From: Mikhail Laguta <mikhail.laguta@uwaterloo.ca>
Sent: Thursday, March 12, 2020 4:46 PM
To: Barry M. Bergin <Barry.Bergin@concrete.org>
Subject: Request for permission to reproduce ACI figures in master's thesis

Hi Barry,

My name is Mikhail Laguta and I am a graduate student at the University of Waterloo. I am emailing to follow up on a voicemail I left earlier today.

I am preparing my master's thesis and I would like permission to reproduce ACI figures in my thesis. I spoke to Mary Meeks who recommended that I contact you about this.

I would like to include one table from ACI 318-19 and two figures from the ACI Structural Journal in my thesis:

- *Table 8.4.2.2.4 Maximum modified values of yf for nonprestressed two-way slabs* from page 106 of "Building Code Requirements for Structural Concrete (ACI 318-19)" (June 2019);

- *Figure 5 Cracks after failure* from page 571 of "Punching of Flat Plates under Static and Dynamic Horizontal Forces" (ACI Journal, Vol. 73 No. 10, October 1976); and

- *Figure 13 Final crack patterns for SB1 and SB4 with no openings and four rows of shear bolts, and SB6 with two openings and four rows of shear bolts* from page 274 of "Retrofit of slab column interior connections using shear bolts" (ACI Structural Journal, Vol. 102 No. 2, March-April 2005).

My thesis will be published in the institutional repository at the University of Waterloo (Waterloo, Ontario, Canada). Proper citation would be included with the reproduction of the figures.

Please let me know if you need any other information.

Thank you for considering this request,
Mikhail Laguta

RE: Request for permission to reproduce PCA figure in Master's thesis

Rick Bohan <rbohan@cement.org>

Mon 2020-03-09 12:14 PM

To: Mikhail Laguta <mikhail.laguta@uwaterloo.ca>;

Mikhail,

You have permission to use the referenced document in the manner described in your email with appropriate attribution as noted.

Please contact me if you have any other questions.

Best regards,

Rick Bohan

PCA Since 1916 America's Cement Manufacturers™

Richard Bohan, P.E. Senior Director, Research and Technology
Portland Cement Association
t. 847.972.9038 **c.** 847.528.2068
e. rbohan@cement.org **w.** cement.org

From: Mikhail Laguta <mikhail.laguta@uwaterloo.ca>
Sent: Sunday, March 8, 2020 12:03 PM
To: Rick Bohan <rbohan@cement.org>
Subject: Request for permission to reproduce PCA figure in Master's thesis

Good afternoon Rick,

My name is Mikhail Laguta and I am a graduate student at the University of Waterloo. I am preparing my Master's thesis and I would like permission to include

> *Figure 8.1 Elimination of the Possibility of Shear Failure in Slabs* from page 101 of *Shearing Strength of Reinforced Concrete Slabs and Footings under Concentrated Loads* (Development Department Bulletin D47, Portland Cement Association, April 1961)

in my thesis.

My thesis will be published in the institutional repository at the University of Waterloo (Waterloo, Ontario, Canada). Proper citation would be included with the reproduction of the figure.

Please let me know if you need any other information or if I should be directing my request toward someone else.

Thank you very much,
Mikhail Laguta

References

ACI-ASCE Committee 326. (1962). Shear and diagonal tension: Part 3—slabs and footings. *Journal of American Concrete Institute, 59*(3), 353–396.

ACI Committee 318. (1956). *Building code requirements for reinforced concrete (ACI 318-56)*. Detroit, Michigan: American Concrete Institute.

ACI Committee 318. (1965). *SP-010: Commentary on Building Code Requirements for Reinforced Concrete (ACI 318-63)*. Detroit, Michigan: American Concrete Institute.

ACI Committee 318. (1970). *Proposed Revision of ACI 318-63 Building Code Requirements for Reinforced Concrete*. *ACI Journal*. American Concrete Institute.

ACI Committee 318. (1971). *Building code requirements for reinforced concrete (ACI 318-71)*. American Concrete Institute.

ACI Committee 318. (1977). *Building code requirements for reinforced concrete (ACI 318-77)*. American Concrete Institute.

ACI Committee 318. (1986). *Building code requirements for reinforced concrete (ACI 318-86)*. American Concrete Institute.

ACI Committee 318. (1989). *Building code requirements for reinforced concrete (ACI 318-89)*. American Concrete Institute.

ACI Committee 318. (1995). *Building code requirements for structural concrete (ACI 318-95)*. American Concrete Institute.

ACI Committee 318. (2019). *Building code requirements for structural concrete (ACI 318-19) and commentary*. Farmington Hills, Michigan: American Concrete Institute.

Adetifa, B. (2003). *A new punching shear strengthening technique for reinforced concrete slabs at interior slab-column connections*. Master's Thesis, University of Waterloo, Waterloo, Ontario.

Adetifa, B., & Polak, M. A. (2005). Retrofit of slab column interior connections using shear bolts. *ACI Structural Journal, 102*(2), 268–274.

Alexander, S. D. B., & Simmonds, S. H. (1987). Ultimate Strength of Slab-Column Connections. *ACI Structural Journal, 84*(3), 255–261.

Alexander, S. D. B., & Simmonds, S. H. (2003). Moment Transfer at Interior Slab-Column Connections. *ACI Structural Journal, 100*(2), 197–202.

Anderson, J. (1966). *Preliminary Summary of Punching Shear of Concrete Slabs with Edge Columns*. *Bulletin d'Information No. 58*. Paris, France: Comité Européen du Béton.

ASCE-ACI Committee 426. (1974). The Shear Strength of Reinforced Concrete Members—Slabs. *Journal of the Structural Division, 100*(8), 1543–1591.

ASTM International. (1968). ASTM A 615-68: standard specification for deformed billet-steel bars for concrete reinforcement. In *Annual book of ASTM standards 1968* (pp. 98–103). Philadelphia, PA: American Society for Testing and Materials.

Bollinger, K. (1985). *Load-Carrying Behaviour and Reinforcement of Axisymmetrically Loaded Reinforced Concrete Plates*. PhD Thesis, Abteilung Bauwesen der Universität Dortmund, Dortmund, Germany.

British Standards Institution. (2004). *Eurocode 2: design of concrete structures — Part 1-1: General rules and rules for buildings*. London: BSi.

Clément, T., Pinho Ramos, A., Fernández Ruiz, M., & Muttoni, A. (2014). Influence of prestressing on the punching strength of post-tensioned slabs. *Engineering Structures*, *72*, 56–69.

Comité Euro-International du Béton. (1993). *CEB-FIP Model Code 1990: Design Code*. London: Thomas Telford.

Corley, B. W. G., & Hawkins, N. M. (1968). Shearhead Reinforcement for Slabs. *ACI Journal Proceedings*, *65*(10), 811–824.

CSA Group. (1973). *CSA A23.3-73: Code for the Design of Concrete Structures for Buildings*. Ottawa, Ontario: Canadian Standards Association.

CSA Group. (2019). *CSA A23.3-19: Design of Concrete Structures*. Toronto, Ontario: Canadian Standards Association.

Dabaon, M., El-Khoriby, S., El-Boghdadi, M., & Hassanein, M. F. (2009). Confinement effect of stiffened and unstiffened concrete-filled stainless steel tubular stub columns. *Journal of Constructional Steel Research*, *65*(8–9), 1846–1854.

Dam, T. X., Wight, J. K., & Parra-Montesinos, G. J. (2017). Behavior of Monotonically Loaded Slab-Column Connections Reinforced with Shear Studs. *ACI Structural Journal*, *114*(1), 221–232.

Dassault Systèmes. (2012). *Abaqus Documentation*. Providence, RI, USA.

Di Stasio, J., & Van Buren, M. P. (1960). Transfer of Bending Moment Between Flat Plate Floor and Column. *ACI Journal Proceedings*, *57*(9), 299–314.

Drakatos, I. S., Muttoni, A., & Beyer, K. (2018). Mechanical model for drift-induced punching of slab-column connections without transverse reinforcement. *ACI Structural Journal*, *115*(2), 463–474.

Earij, A., Alfano, G., Cashell, K., & Zhou, X. (2017). Nonlinear three–dimensional finite–element modelling of reinforced–concrete beams: Computational challenges and experimental validation. *Engineering Failure Analysis*, *82*, 92–115.

Einpaul, J., Ruiz, M. F., & Muttoni, A. (2015). Influence of moment redistribution and compressive membrane action on punching strength of flat slabs. *Engineering Structures*, *86*, 43–57.

El-Salakawy, E. F. (1998). *Shear behaviour of reinforced concrete flat slab-column edge connections with openings*. PhD Thesis, University of Waterloo, Waterloo, Ontario.

Elstner, R. C., & Hognestad, E. (1956). Shearing Strength of Reinforced Concrete Slabs. *ACI Journal Proceedings*, *28*(1), 29–58.

federation internationale du béton (fib). (2013). *Model Code for Concrete Structures 2010*. Lausanne, Switzerland.

FEMA 274. (1997). *NEHRP Commentary on the Guidelines for the Seismic Rehabilitation of Buildings*. *FEMA-274*. Federal Emergency and Management Agency (FEMA), Washington, D.C.

Fernández Ruiz, M., & Muttoni, A. (2009). Applications of the critical shear crack theory to punching of R/C slabs with transverse reinforcement. *ACI Structural Journal*, *106*(4), 485–494.

Flathau, W. (1971). *Dynamic Tests of Large Reinforcing Bar Splices*. Vicksburg, Mississippi: Army Engineer Waterways Experiment Station.

Genikomsou, A. (2015). *Nonlinear finite element analysis of punching shear of reinforced concrete slab-column connections*. PhD Thesis, University of Waterloo, Waterloo, Ontario.

Ghali, A., Elmasri, M. Z., & Dilger, W. (1976). Punching of Flat Plates Under Static and Dynamic Horizontal Forces. *ACI Journal Proceedings*, *73*(10), 566–572.

Hanson, N. W., & Hanson, J. M. (1968). Shear and Moment Transfer Between Concrete Slabs and Columns. *Journal of the PCA, Research and Development Laboratories*, *10*(1), 2–16.

Hawkins, N., & Corley, G. (1971). Transfer of Unbalanced Moment and Shear from Flat Plates to Columns. *ACI Special Publication*, *30*, 147–176.

Hawkins, N. M., Fallsen, H. B., & Hinojosa, R. C. (1971). Influence of Column Rectangularity on the Behavior of Flat Plate Structures. *ACI Special Publication*, *30*, 127–146.

Hawkins, N. M., & Ospina, C. E. (2017). Effect of slab flexural reinforcement and depth on punching strength. *ACI Symposium Publication*, *315*, 117–140.

Hillerborg, A., Modéer, M., & Petersson, P. E. (1976). Analysis of crack formation and crack growth in concrete by means of fracture mechanics and finite elements. *Cement and Concrete Research*, *6*(6), 773–781.

Hognestad, E. (1951). *Study of Combined Bending and Axial Load in Reinforced Concrete Members*. University of Illinois at Urbana Champaign, College of Engineering. Engineering Experiment Station.

Hu, H. T., Huang, C. S., Wu, M. H., & Wu, Y. M. (2003). Nonlinear analysis of axially loaded concrete-filled tube columns with confinement effect. *Journal of Structural Engineering*, *129*(10), 1322–1329.

Langohr, P. H., Ghali, A., & Dilger, W. H. (1976). Special Shear Reinforcement for Concrete Flat Plates. *ACI Journal Proceedings*, *73*(3), 141–146.

Lee, J., & Fenves, G. L. (1998). Plastic-Damage Model for Cyclic Loading of Concrete Structures. *Journal of Engineering Mechanics*, *124*(8), 892–900.

Lubliner, J., Oliver, J., & Onate, E. (1989). A plastic-damage model for concrete. *International Journal of Solids and Structures*, *25*(3), 299–326.

Moe, J. (1961). *Shearing Strength of Reinforced Concrete Slabs and Footings Under Concentrated Loads*. *Development Department Bulletin D47*. Skokie, Illinois: Portland Cement Association.

Moehle, J. P. (1988). Strength of Slab-Column Edge Connections. *ACI Structural Journal*, *13*(14), 89–98.

Moehle, J. P., Kreger, M. E., & Leon, R. (1988). Background to recommendations for design of reinforced concrete slab-column connections. *ACI Structural Journal*, *85*(6), 636–644.

Muttoni A., Fernández Ruiz M., S. J. T. (2018). Recent improvements of the Critical Shear Crack Theory for punching shear design and its simplification for code provisions. In *fib Congress* (pp. 485–494). Melbourne, Australia.

Muttoni, A. (2003). Shear and punching strength of slabs without shear reinforcement, (in German, "Schubfestigkeit und Durchstanzen von Platten ohne Querkraftbewehrung"). *Beton Und Stahlbetonbau*, *98*, 74–84.

Muttoni, A. (2008). Punching Shear Strength of Reinforced Concrete Slabs without Transverse Reinforcement. *ACI Structural Journal*, *105*(4), 440–450.

Muttoni, A., Ruiz, M. F., Bentz, E., Foster, S., & Sigrist, V. (2013). Background to fib Model Code 2010 shear provisions — part II: punching shear. *Structural Concrete*, *14*(3), 204–214.

Muttoni, A., & Schwartz, J. (1991). Behavior of Beams and Punching in Slabs without Shear Reinforcement. In *IABSE Colloquium* (Vol. 62, pp. 703–708). Zurich, Switzerland.

Natário, F., Fernández Ruiz, M., & Muttoni, A. (2014). Shear strength of RC slabs under concentrated loads near clamped linear supports. *Engineering Structures*, *76*, 10–23.

Neth, V. W., de Paiva, H. A. R., & Long, A. E. (1981). Behavior of Models of a Reinforced Concrete Flat Plate Edge-Column Connection. *ACI Structural Journal*, *78*(4), 269–275.

Peiris, C., & Ghali, A. (2011). Flexural reinforcement essential for punching shear resistance of slabs. *ACI Special Publication*, *287*, 83–97.

Petersson, P. E. (1981). *Crack growth and development of fracture zones in plain concrete and similar materials*. PhD Thesis, Lund Institute of Technology, Lund, Sweden.

Regan, P. E. (1981). *Behaviour of Reinforced Concrete Flat Slabs*. *CIRIA Report No. 89*. London: Construction Industry Research and Information Association.

Reineck, K. H., Kuchma, D. A., Kim, K. S., & Marx, S. (2003). Shear database for reinforced concrete members without shear reinforcement. *ACI Structural Journal*, *100*(2), 240–249.

SIA. (2003). *262 Code for Concrete Structures*. *Swiss Society of Engineers and Architects*. Zurich, Switzerland.

Stamenkovic, A. (1969). *Local strength of flat slab at column heads*. PhD Thesis, University of London, London, England.

Vanderbilt, M. D. (1972). Shear Strength of Continuous Plates. *ACI Structural Journal*, *11*(62), 961–973.

Vecchio, F. J., & Collins, M. P. (1986). The Modified Compression-Field Theory for Reinforced Concrete Elements Subjected to Shear. *ACI Structural Journal*, *83*(2), 219–231.

Walraven, J. C. (1981). Fundamental Analysis of Aggregate Interlock. *Journal of Structural Engineering*, *107*(11), 2245–2270.

Widianto, Bayrak, O., & Jirsa, J. O. (2009). Two-Way Shear Strength of Slab-Column Connections: Reexamination of ACI 318 Provisions. *ACI Structural Journal*, *106*(2), 160–170.

Zaghlool, E. E. D. R. F. (1971). *Strength and behaviour of corner and edge column-slab connections in reinforced concrete flat plates*. PhD Thesis, University of Calgary, Calgary, Alberta.